ISSN 2500-316X (Online)

RUSSIAN TECHNOLOGICAL JOURNAL

РОССИЙСКИЙ ТЕХНОЛОГИЧЕСКИЙ ЖУРНАЛ

Information systems.
Computer sciences.
Issues of information security

Multiple robots (robotic centers) and systems.
Remote sensing and non-destructive testing

Modern radio engineering and telecommunication systems

Micro- and nanoelectronics.
Condensed matter physics

Analytical instrument engineering and technology

Mathematical modeling

Economics of knowledge-intensive and high-tech enterprises and industries.
Management in organizational systems

Product quality management. Standardization

Philosophical foundations of technology and society

12+
www.rtj-mirea.ru

МИРЭА
Российский технологический университет

10(3) 2022

ISSN 2500-316X (Online)

RUSSIAN TECHNOLOGICAL JOURNAL

РОССИЙСКИЙ ТЕХНОЛОГИЧЕСКИЙ ЖУРНАЛ

- Information systems. Computer sciences. Issues of information security
- Multiple robots (robotic centers) and systems. Remote sensing and non-destructive testing
- Modern radio engineering and telecommunication systems
- Micro- and nanoelectronics. Condensed matter physics
- Analytical instrument engineering and technology
- Mathematical modeling
- Economics of knowledge-intensive and high-tech enterprises and industries. Management in organizational systems
- Product quality management. Standardization
- Philosophical foundations of technology and society

- Информационные системы. Информатика. Проблемы информационной безопасности
- Роботизированные комплексы и системы. Технологии дистанционного зондирования и неразрушающего контроля
- Современные радиотехнические и телекоммуникационные системы
- Микро- и наноэлектроника. Физика конденсированного состояния
- Аналитическое приборостроение и технологии
- Математическое моделирование
- Экономика наукоемких и высокотехнологичных предприятий и производств. Управление в организационных системах
- Управление качеством продукции. Стандартизация
- Мировоззренческие основы технологии и общества

Russian Technological Journal
2022, Vol. 10, No. 3

Russian Technological Journal
2022, том 10, № 3

https://www.rtj-mirea.ru

https://doi.org/10.32362/2500-316X

ISSN 2500-316X (Online)

Russian Technological Journal
2022, Vol. 10, No. 3

Publication date May 31, 2022.

The peer-reviewed scientific and technical journal highlights the issues of complex development of radio engineering, telecommunication and information systems, electronics and informatics, as well as the results of fundamental and applied interdisciplinary researches, technological and economical developments aimed at the development and improvement of the modern technological base.

Periodicity: bimonthly.
The journal was founded in December 2013. The titles were «Herald of MSTU MIREA» until 2016 (ISSN 2313-5026) and «Rossiiskii tekhnologicheskii zhurnal» from January 2016 until July 2021 (ISSN 2500-316X).

Founder and Publisher:
Federal State Budget
Educational Institution
of Higher Education
«MIREA – Russian Technological University»
78, Vernadskogo pr., Moscow, 119454 Russia.

The Journal is included in RSL (Russian State Library), Russian citation index, elibrary, Socionet, Directory of Open Access Journals (DOAJ), Directory of Open Access Scholarly Resources (ROAD), Google Scholar, Open Archives Initiative, Ulrich's International Periodicals Directory.

The registration number ПИ № ФС 77 - 81733 was issued in August 19, 2021 by the Federal Service for Supervision of Communications, Information Technology, and Mass Media of Russia.

The subscription index of *Pressa Rossii*: **79641**.

Russian Technological Journal
2022, том 10, № 3

Дата опубликования 31 мая 2022 г.

Научно-технический рецензируемый журнал освещает вопросы комплексного развития радиотехнических, телекоммуникационных и информационных систем, электроники и информатики, а также результаты фундаментальных и прикладных междисциплинарных исследований, технологических и организационно-экономических разработок, направленных на развитие и совершенствование современной технологической базы.

Периодичность: один раз в два месяца.
Журнал основан в декабре 2013 года. До 2016 г. издавался под названием «Вестник МГТУ МИРЭА» (ISSN 2313-5026), а с января 2016 г. по июль 2021 г. под названием «Российский технологический журнал» (ISSN 2500-316X).

Учредитель и издатель:
федеральное государственное бюджетное
образовательное учреждение
высшего образования
«МИРЭА – Российский технологический университет»
119454, РФ, г. Москва, пр-т Вернадского, д. 78.

Журнал индексируется в РГБ, РИНЦ, elibrary, Соционет, Directory of Open Access Journals (DOAJ), Directory of Open Access Scholarly Resources (ROAD), Google Scholar, Open Archives Initiative, Ulrich's International Periodicals Directory.

Регистрационный номер и дата принятия решения о регистрации СМИ ПИ № ФС 77 - 81733 от 19.08.2021 г. СМИ зарегистрировано Федеральной службой по надзору в сфере связи, информационных технологий и массовых коммуникаций (Роскомнадзор).

Индекс по объединенному каталогу «Пресса России» **79641**.

https://www.rtj-mirea.ru

Editorial Board

Редакционная коллегия

Contents

Содержание

Information systems. Computer sciences. Issues of information security
Информационные системы. Информатика. Проблемы информационной безопасности

UDC 004.02+004.4+004.891+004.91
https://doi.org/10.32362/2500-316X-2022-10-3-7-23

RESEARCH ARTICLE

Pedagogical design of a digital teaching assistant in massive professional training for the digital economy

Elena G. Andrianova @,
Liliya A. Demidova,
Petr N. Sovetov

MIREA – Russian Technological University, Moscow, 119454 Russia
@ *Corresponding author, e-mail: andrianova@mirea.ru*

Abstract

Objectives. The active digitalization of the Russian economy has resulted in a shortage of IT personnel; this is particularly true of software developers. Thus, the Russian university education is faced with the task of undertaking the large-scale professional training of such specialists. The purpose of the present work was to support the large-scale ("massive") professional training of programmers through the creation and implementation of Digital Teaching Assistant (DTA) computer system, allowing teachers working under stressful conditions to concentrate on functions that require a creative approach, namely, drawing up and discussing nontrivial programming tasks.

Methods. Pedagogical methods for the personification of learning processes were employed. The general approach was based on satisfying the constraints for creating programming task generators. Tasks were generated using methods for generating random programs and data based on probabilistic context-sensitive grammars, along with translation methods using an abstract syntax tree. The declarative representation of the task generator was performed using functional programming methods, allowing the creation of a domain-specific language using combinators. The solutions were checked using automated testing methods.

Results. The developed structure of the proposed DTA system was presented. Considering the automatic generation of programming tasks, classes of practical tasks that reflected the modern specifics of software development were identified along with examples of their generation. A diagram of the programming task generator was provided along with a description of the procedure for automatically checking the solutions of the tasks using a set of program tests generated by the task generator. The presented procedure for comprehensive assessment of a student's solution included verification of the correctness of the result and plagiarism checks in the case of tasks created manually by the teacher; this also involved validation for compliance with coding style standards, along with metrics for assessing program complexity, etc. The means for recording of statistics of academic achievement of students was characterized along with the interface of interaction between students and teachers.

Conclusions. The experience of introducing a DTA into the learning process of teaching programming in Python confirmed the possibility of personifying the learning process in the form of individual learning paths.

Keywords: massive programming learning, Digital Teaching Assistant, task generation, individual learning path, student motivation

• **Submitted:** 29.12.2021 • **Revised:** 03.03.2022 • **Accepted:** 11.05.2022

For citation: Andrianova E.G., Demidova L.A., Sovetov P.N. Pedagogical design of a digital teaching assistant in massive professional training for the digital economy. *Russ. Technol. J.* 2022;10(3):7–23. https://doi.org/10.32362/2500-316X-2022-10-3-7-23

Financial disclosure: The authors have no a financial or property interest in any material or method mentioned.

The authors declare no conflicts of interest.

НАУЧНАЯ СТАТЬЯ

«Цифровой ассистент преподавателя» в массовом профессиональном обучении для цифровой экономики

Е.Г. Андрианова [@], **Л.А. Демидова**, **П.Н. Советов**

МИРЭА – Российский технологический университет, Москва, 119454 Россия
[@] *Автор для переписки, e-mail: andrianova@mirea.ru*

Резюме

Цели. Активная цифровизация российской экономики вызывает дефицит ИТ-кадров и, в первую очередь, дефицит разработчиков программного обеспечения. Для российского университетского образования актуальной является задача массовой профессиональной подготовки таких специалистов. Цель работы – повышение качества массовой профессиональной подготовки программистов путем создания, внедрения и развития функциональности компьютерной системы «Цифровой ассистент преподавателя» (ЦАП). Эта система позволяет преподавателю в условиях массового обучения сконцентрироваться на функциях, требующих творческого подхода – составлении и обсуждении нетривиальных задач по программированию.

Методы. Использованы педагогические методы персонификации учебного процесса. Общий подход основан на удовлетворении ограничениям для создания генераторов задач по программированию. При генерации задач применены методы порождения случайных программ и данных на основе вероятностных контекстно-зависимых грамматик, а также методы трансляции с использованием дерева абстрактного синтаксиса. Для декларативного представления генератора задач применены методы функционального программирования, позволяющие создать предметно-ориентированный язык с помощью комбинаторов. Для проверки решений использованы методы автоматического тестирования.

Результаты. Разработана структура системы ЦАП. Рассмотрена автоматическая генерация задач по программированию, выделены классы практических задач, отражающие современную специфику разработки программного обеспечения, приведены примеры их генерации. Приведена схема генератора задач по программированию. Описана процедура автоматической проверки решения задач, осуществляемая с помощью набора программных тестов, сформированного генератором задач. Приведена процедура комплексной оценки решения обучающегося, включающая проверку корректности результата и проверку на плагиат решений в случае задач, созданных преподавателем вручную; соответствие стандарту стиля написания программы, метрикам оценки сложности программы и т.д. Рассмотрены ведение статистики успеваемости обучающихся и интерфейс взаимодействия обучающихся и преподавателей.

Выводы. Опыт внедрения ЦАП в учебный процесс курса «Программирование на языке Python» подтвердил возможность обеспечения персонификации учебного процесса для обучающихся в виде индивидуальных образовательных траекторий.

Ключевые слова: массовое обучение программированию, цифровой ассистент преподавателя, генерация заданий, индивидуальная траектория обучения, мотивация обучающихся

• **Поступила:** 29.12.2021 • **Доработана:** 03.03.2022 • **Принята к опубликованию:** 11.05.2022

Для цитирования: Андрианова Е.Г., Демидова Л.А., Советов П.Н. «Цифровой ассистент преподавателя» в массовом профессиональном обучении для цифровой экономики. *Russ. Technol. J*. 2022;10(3):7–23. https://doi.org/10.32362/2500-316X-2022-10-3-7-23

Прозрачность финансовой деятельности: Авторы не имеют финансовой заинтересованности в представленных материалах или методах.

Авторы заявляют об отсутствии конфликта интересов.

INTRODUCTION

The digitalization of the economy, which has the potential to radically transform all fields of human activity, generates an urgent need for a large number of professionals with IT or digital competences. Thus, a significant challenge facing learning providers concerns how to provide massive professional training of personnel for the digital economy, in the first place, software developers. In the medium term, the Russian labor market anticipates an increase in the demand for software developers in such promising areas as artificial intelligence, big data analytics, robotics, virtual reality, and the Internet-of-things[1] [1, 2].

Technologies of massive training of software developers require the active implementation of intelligent and IT technologies in the organization of learning process and use of electronic educational resources to support convenient and rapid communications between participants in learning process and apply advanced pedagogical innovations and practices.

However, there is a concern that the digitalization of the learning process for massive training of software developers might imply the unification of approaches to all students. On the contrary, it is necessary to provide a student with wide opportunities to create and support personification of learning, first of all, by creating individual learning paths, which imply the active individual work of the student. According to Yaroslavtseva, in making digital technologies available for massive use, which structures the social system and social relationships, electronic culture implies the formation of new views of the world and methods of perceiving it. The human in digital space thus becomes a continuously developing "open anthroposystem," an interactive system, which "rapidly expands its capabilities and creates the corresponding parameters of the future" [3]. Meanwhile, some pedagogical experts note a decrease in the motivation of students for individual work. There is even an opinion that this is due to educational labor now having the "traits of forced labor" [4]. Thus, existing standards and training materials are failing to provide students with personally significant learning results but are instead perceived as motivated by the requirements imposed by the education system. Students do not feel as of their actions are independent; rather, they are forced to conform to the learning objectives, contents and methods of an external control system. "Motives for learning are replaced by motives for responsibility, social need and enforcement: 'you should,' 'you must'" [5].

Various concepts of learning approaches aimed at increasing the motivation of students have been proposed. For example, the heuristic learning concept, which is based on an exteriorization model, is aimed at the self-actualization of a student [6, 7]. Conversely, the developmental learning concept, which is based on an interiorization model, is targeted at the development of a student [6, 7]. Whether proceeding according to the heuristic or developmental learning approaches, the purpose of the teacher lies not so much in the development of course content (e.g., lectures and practical exercises) as the search and monitoring of available educational resources, which can comprise materials for the learning content of the course. By taking this approach, it is possible to support a student in creating an individual learning path. However, it should be noted that the important issue of providing support of the motivation of a student to software development competence cannot be reduced only to the material aspect.

When carrying out training of software developers, technical universities using a classical form of programming training have long competed in the provision of high-quality massive open online course at leading companies and educational institutions and with specialized online educational platforms, such as Stepik [8] and JetBrains Academy [9], which provide tools for the efficient learning of programming languages that are currently in demand by employers in software development.

The increased use of online technologies in the learning processes as part of recent epidemic control measures resulted in blended learning becoming a standard part of the learning process at universities. This has changed the duties of the teacher by supplementing them with a tutoring function, which obviously increases the scope of the teacher's creative functions related to

[1] Rynok truda v Rossii (The labor market in Russia). *Tadviser. Gosudarstvo. Biznes. Tekhnologii* (in Russ.). https://clck.ru/ZD5AU. Accessed November 28, 2021.

the tutorship due to the necessity to take into account the individual traits of a student in practice-oriented training in programming. Due to the resultant significant increase in the teacher's workload, it has become necessary to automate the routine part of the teacher's duties by creating and using a Digital Teaching Assistant (DTA). Comprising a kind of intelligent learning system, a DTA can take on functions of delivery and creation of practical programming tasks, generation of tasks and checking of results, monitoring of the attendance and work of students, digital footprint acquisition, etc.

Thus, the development of a DTA, as well as its realization and implementation in teaching a training course in programming at a technical university, becomes an urgent problem.

1. PEDAGOGICAL DESIGN AND MAIN ELEMENTS OF COMPUTERIZATION OF PROGRAMMING TRAINING

The state of the art in the educational system of programming training provides a teacher with significant opportunities for setting learning objectives and undertaking pedagogical design of a training course, which determines means for achieving the set objectives. Pedagogical design is a systematized approach to creating learning solutions, which uses pedagogical principles and theories to ensure high quality of learning [10].

In the context of digitalization of education, pedagogical design represents an efficient tool for developing learning content aimed at ensuring a reasonable combination of online and offline learning (blended learning), creating an intelligent environment within the programming training course and supporting the realization of an individual learning path.

The main principles of pedagogical design are to provide a clear explanation of the goals and objectives of learning, attraction and retention of student's attention, awaken interest in topic being learned or learning methods applied, ensure rapid testing of obtained knowledge in practice, receive feedback from students, deliver assessments (including self-assessment) of academic achievement and general assessment of efficiency of training course, and help to student in preserving and correctly using obtained knowledge [10].

By using pedagogical design principles in developing the content of a training course, it becomes possible to determine optimal conditions for achieving learning goals: model of interactive interaction of participants in the learning process, forms of representation of the learning content of the training course and methods of increasing the motivation of students for independent work on the materials of the course (cognitive function). For example, using crowdsourcing methods identifies learning needs and deficits that are significant for students trained in this programming training course.

The pedagogical design of the programming training course encapsulates not only the format of representation of the learning content, but also methodological guidelines for students and teachers, tasks and exercises on the developed content, as well as test assignments and student self-assessment forms. Test assignments, their performance, and the subsequent self-assessment of academic achievement in the course by students can partially be based on gamification. Student self-assessment of competence can correspond to events in an electronic system, e.g., such as evaluation of a performed task on a pass/no pass or letter-grade basis, and so on. For the content of the training course to be of high quality, motivating stimuli should necessarily be included, e.g., as creative tasks, tasks for determining the problematic area of the course, etc.

The pedagogical design of a practice-oriented programming training course has the following mandatory elements:

- interactive materials available online (a student can run examples directly in a study guide, can use elements of a built-in graphical interface to update the contents of graphs, etc.);
- presentation of the materials in a personalized form: as a dependency graph (knowledge graph);
- online system for reception and verification of tasks;
- automatic adaptation of the complexity of tasks and theoretical materials to the level of a student;
- automatic task generation;
- automatic generation of hints and comments on the solutions of the tasks.

2. CONTEMPORARY PROGRAMMING LEARNING TOOLS

A promising trend in the pedagogical design of a university course of massive training in programming consists in the use of learning tools and blended learning (a combination of offline and online learning). The asynchrony of the online part of the learning process provides a student with the space to select the material and time to learn it. Of particular relevance here is the flipped classroom model based on online self-directed online learning of students in the main theoretical knowledge in the course. In this case, classroom lectures become more interactive to include discussions of the topics self-learned by students; such lectures widely feature additional materials, as well as involving collaborative solution of tasks.

For students to better retain the training material, a conventional 1½-hour-long lecture is more and more often represented online as a set of short (5–15 min) videos [11]. Using virtual reality technologies in learning

process becomes increasingly popular [11]. For prompt assessment of academic achievement, feedback with students can be organized directly during the online lecture as brief test questions and test tasks. A special role in ensuring the deep retention of the lecture material by students can be played by such interactive elements of the lecture as executable code fragments and various apparent dynamic models, which are controlled by a graphical interface (explorable explanation) [12]. In particular, the Online Python Tutor [13] visualizes details of the execution of a Python program in a dynamic mode.

In organizing a massive programming training course, it is important to personalize learning by creating an individual learning path to adapt the learning process to an individual student's needs. For lectures, the material of the course can be represented as a knowledge graph with the freedom of choice between topic nodes taking into account dependency edges [14].

During performing practical exercises and under quantitative constraints on instructional personnel, an intelligent tutoring system (ITS) can be employed to obtain feedback from students, transfer an individual instruction or provide a response to the actions of students on a real-time basis without teacher intervention. ITS are computer systems that combine a knowledge domain model with a student model and a teacher model. Such integrated systems often use machine learning methods and have a complex design [15].

The complexity of the design of an ITS as a single system integrating all the situations and scenarios of interaction led to propagation of computer tools, which solve individual problems related to an ITS. In particular, they comprise automated grading systems [16], data-driven hint generation systems [17], as well as automatic generators of exercises of a given complexity [18] and systems for checking solutions for plagiarism [19].

A disadvantage of such systems is that they focus only on a student's individual work along with a limited, formally defined set of tasks. In this context, specialized forums such as Piazza[2], which may include rewards for students who help their colleagues, can be useful. An important role is also played by using learning projects developed collaboratively by students (project-based learning) and using technologies to provide the gamification of learning processes [20].

3. DIGITAL TEACHING ASSISTANT

3.1. DTA structure

In university massive programming training courses, much of the teaching workload is borne by teacher assistants, who create programming tasks and check the correctness of their solution by students. In this context, a new approach is proposed for organizing the learning process of training of software developers based on a DTA computer system. DTA helps teachers working under massive learning conditions to concentrate on functions that require a creative approach, in particular, creating and discussing nontrivial programming tasks and also developing the DTA functionality.

The main DTA functions (Fig. 1) are:

- generation of individual tasks;
- check of tasks with informative answer for a student;
- recording student academic achievement statistics;
- interface of interaction between learning process participants.

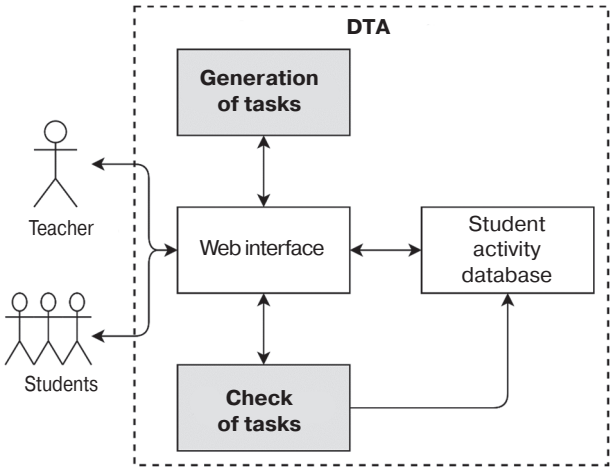

Fig. 1. DTA structure

Unlike an ITS [21], a DTA is not intended to completely replace a teacher or resemble a "black box" that automatically select tasks during learning or evaluates solutions according to parameters hidden from a student. The model of a tutor used in ITS is replaced in DTA by real teacher's settings.

3.2. Automatic generation of programming tasks

The automatic generation of programming tasks provides each of students with an individual set of tasks. This inherently laborious function is difficult for teachers to perform alone, especially if the number of students is large. Automatic task generation also partially solves the problem of plagiarism of solutions.

The following requirements are imposed on a task generator;

- support of the main topics of the course and language constructs;
- interest and practical utility of tasks;

[2] https://piazza.com/. Accessed January 13, 2022.

- clarity and univocality of the text of a task statement and its resemblance to a human-composed text;
- identical complexity of all the generated variants of a task at fixed settings of the task generator;
- absence of obvious cliché solutions to different variants of a task;
- possibility of automatic check of solution.

A DTA contains a large number of task generators $G = \{g_1, \ldots, g_n\}$, each generating variants of tasks of its own type. The inputs of the task generator function $g_i(h, s)$ consist in the hash value h of the individual data of a student and parameter s of complexity or size of the task.

Approaches to automatic generation remain to be developed for all the types of programming tasks. The types of tasks for which generators have already been created are discussed below.

In a course of programming in a certain language, one can identify the following classes of practical tasks reflecting the modern specificity of software development:

- creation of a new program;
- analysis of the existing program;
- creation of unit tests for the existing program.

Among the tasks involved in creating a new program, there are generators of tasks of such types as [18]:

- translation of a certain representation into a program code;
- data format conversion.

In tasks of the former type, the input representation can be a mathematical formula. Thereby, a student learns a practically important skill to translate a mathematical language into a programming language. Another example of a task of the former type is to translate a program from one programming language into another. The input representation can also be graphic notation. Examples of tasks using graphic notation including converting a finite-state machine graph or a UML diagram into a program code.

Tasks to convert input data format into output data format can use both text and binary data formats.

In the general form, generators of tasks of the considered types can be created using approaches from the field of combinatorial problems of artificial intelligence. In particular, a promising approach is to use the constraint satisfaction method [22]. Using this approach, a set of variables and a set of their values describe a space of generated programs or data formats, and a set of constraints enables one to filter off only the results that correspond to given characteristics for a chosen type of tasks.

Random configuration p (program or data format description) from a space of configurations P is defined as

$$p \in \mathrm{P} \wedge \phi_c(p) \wedge \phi_t(p).$$

Here, the specification predicate ϕ_c determines the conditions of choosing p, while the predicate ϕ_t characterizes the possibility to create for p a set of nondegenerate (i.e., with different values within given limits) program tests.

Random generations can be generated using probabilistic grammars, in which each rule is supplemented with the probability of using it in the process of generation of the result. The same approach is used in fuzzing [23].

Of special interest are probabilistic context-sensitive grammars, which not only enable a syntactically correct result to be achieved in the event of obtaining a random result, but also carry out a number of semantic checks. An example of such a check is correct use of a previously defined variable in its scope.

In generating a task, it is insufficient to formulate its statement. It is also necessary to obtain a set of program tests, against which the correctness of students' solutions is evaluated. The step of test generation is part of the total process generating the task. If the quality of the obtained tests is unsatisfactory, the statement of the task should be changed.

Along with simple unit tests, which contain set of pairs $\{(x_1, y_1), \ldots, (x_n, y_n)\}$, where x_i is the vector of input values and y_i is the computation result, tests with monitoring the state for responding systems can be used. The input data in this case are a trace of calls (methods, messages) and the responses of the system to each of the calls.

Among typical programming tasks for analyzing the correctness of the existing programs, generators that allow the creation of variations using a set of program templates could be of interest, as well as those for introducing an error to a program code, whose correction is delegated to a student.

A class of tasks related to the creation of program tests is characterized by using mutation testing [24] to determine the quality of program tests composed by students for an automatically generated program.

3.3. Realization of task generators

Figure 2 presents a general flowchart of a programming task generator. The statement of a task is formulated based on the hash code of information on a student and the task complexity parameter, along with program tests for automatic check of solutions.

The possible realization of the random configuration generator described below forms a random program or a random data format. The configuration is further subjected to a sequence of simplifications of its structure. In the case of a generated program, they can consist of conventional compiler-side optimizations, such as constant folding and simplification of expressions.

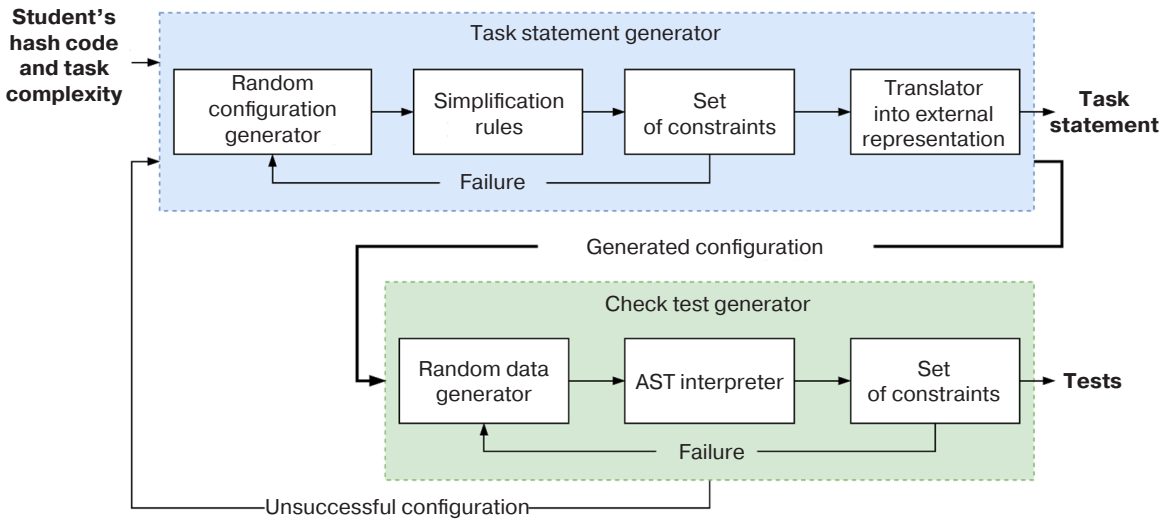

Fig. 2. Flowchart of programming task generator

The characteristics of the configuration are evaluated using a set of constraints according to which the uniform complexity of the generated tasks is maintained. The well-generated configuration is translated into an external representation, which comprises the task statement for a student.

The check test generator creates random data according to the type of a task being formed. The previously obtained configuration is evaluated using a set of tests. In the case of a program configuration, its internal representation is interpreted as an abstract syntax tree (AST) using random data as program inputs. In the case of a data format configuration, the corresponding structures are filled with random values. If no set of tests with given characteristics is successfully formed (e.g., after making a given number of attempts), then the return to the generation of a new configuration is performed.

To realize a random configuration generator, it is proposed to use a special grammar-describing language—configuration generation rules. This language is an extension of probabilistic context-sensitive grammars and is a set of combinators in the spirit of functional programming.

Combinators are higher-order functions used to create embedded domain-specific languages (eDSL). In particular, numerous realizations of parser combinators are known [25]. In the case under consideration, the combinator after computation of the arguments returns the lexical closure *f*:

$$f: c \to c'.$$

This uses a computation model in which combinators receive context c and return a new version of it. The context $c = \{(a_1, v_1), \ldots, (a_n, v_n)\}$ comprises a set consisting of n pairs of the attribute–value form. The context always contains the following attributes: computation result a_{val} and Boolean error value a_{err}. If an error emerges during the computation, a local rollback occurs from combinators: this is a return to one of the calling combinators, which processes this error.

The basis of the considered combinator language are combinators realizing operations known from the theory of formal languages: concatenation (*seq*) and union (*alt*). The basic combinator *seq* computes a sequence of its combinator arguments, thus updating the context. If an error emerges, there is a return from the combinator with restoration of the state of the context at the beginning of the execution of *seq*. The basic combinator *alt* computes, among its arguments, a randomly chosen combinator. For each of the arguments, the probability that it has been selected can be given. The combinator *check* checks the argument expression for truth using the current context as an argument. It the expression is false, then the unit value of a_{err} in the context indicates an error. The combinator *find* repeats the execution of the argument combinator until the computation result is good.

A variant of a combinatorial language developed in Python is considered. Using combinators, a random polynomial generator can be developed as shown in Fig. 3. This generator is realized according to three rules. The *coeff* rule in Fig. 3a determines the value of the coefficient. A choice is made between a random value in a given range and zero with the probability given in *prob*. The *term* rule forms an AST representation for an expression of the form kx^n. The *main* rule forms an AST representation of a polynomial to the third degree. The combinator *let* is used to name the results, while *ref* provides a means for their subsequent reference. Using the combinator *check*, a constraint is imposed that the generated polynomial should have at least one nonzero coefficient at x.

```
coeff = alt(randint(-100, 100), 0, prob=[0.3, 0.7])

term = λ k, n: mul(k, power('x', n))

main = find(seq(
    let(a=coeff), let(b=coeff),
    let(c=coeff), let(d=coeff),
    add(
        term(ref('a'), 3),
        term(ref('b'), 2),
        term(ref('c'), 1),
        term(ref('d'), 0),
    ),
    check(λ c: c.a != 0 or c.b != 0 or c.c != 0)
))
```

(a)

$$86x^3 + 20x^2 + -27$$
$$-85x$$
$$-98x$$
$$86x^3 + -47x^2 + 51x$$
$$40x + 44$$
$$93x$$
$$-63x + -66$$
$$-62x^3 + -17x$$
$$-97x^2$$
$$94x^2$$

(b)

Fig. 3. Random polynomial generator:
(a) realization in eDSL and (b) examples of the results of generation in the LaTeX format

The search for the correct result is made by the combinator *find*. Thus, a simple declarative constraint programming system is realized. This approach is much less productive than, e.g., SMT solvers and specialized solvers for constraint programming tasks. Nevertheless, the considered declarative language allows constraints of arbitrary complexity to be used. Moreover, the generation rate typically is not the most important characteristic of creating learning tasks. Finally, SMT solvers and other third-party tools can be used together with the considered combinatorial language.

Figure 4 presents a more extended example of the realization of generation of random functions in C++ for array handling. Here, a task in the spirit of finite-impulse-response filters is imitated.

In the generated random functions, the data types and the variable names are consistent. A cycle can be realized using both *for* and *while*, whose realization is similar to that of *for*. The realization of the combinator *expr* is not shown because it presents nothing new in comparison with the previous example of polynomial generation.

```
args = shuffle_list(
    decl_ptr(ref('ty'), ref('buf1')), decl_ptr(ref('ty'), ref('buf2')),
    decl('int', ref('size'))
)
for_array = λ *body: for_loop(
    eq(decl('int', ref('idx')), ref('mtap')), lt(ref('idx'), ref('size')),
    postop('++', ref('idx')),  block(*body)
)
memset = call('memset',
    lst(ref('buf2'), 0, mul(call('sizeof', ref('ty')), ref('size')))
)
loop_body = stmt(eq(load(ref('buf2'), ref('idx')), expr))
main = seq(
    let(ty=one_of('int float double')),
    let(name=one_of('data buf arr x y')),
    let(buf1=to(λ c: c.name + '1')), let(buf2=to(λ c: c.name + '2'))
    let(size=to(λ c: c.buf1 + '_size')),
    let(idx=one_of('i j k n')),
    let(taps=to(λ c: sorted(sample(range(1, 5), randint(1, 3))))),
    let(mtap=to(λ c: max(c.taps))),
    function(
        one_of('calculate process compute perform'),
        'void', args, block(stmt(memset),
            alt(for_array(loop_body), while_array(loop_body))
        )
    )
)
```

Fig. 4. Realization of a generator of random functions of array handling

Figure 5 gives some examples of the generated random functions.

```
void process(int x_size, double *y, double *x) {
  memset(y, 0, sizeof(double) * x_size);
  for (int i = 4; i < x_size; i++) {
    y[i] = 8 * x[i] + 2 * x[i - 1] + -4 * x[i - 3] + -5 * x[i - 4];
  }
}
void perform(float *arr1, int arr1_size, float *arr2) {
  memset(arr2, 0, sizeof(float) * arr1_size);
  int k = 2;
  while (k < arr1_size) {
    arr2[k] = 5 * arr1[k] + 8 * arr1[k - 2];
    k++;
  }
}
void compute(int y1_size, float *y2, float *y1) {
  memset(y2, 0, sizeof(float) * y1_size);
  for (int k = 3; k < y1_size; k++) {
    y2[k] = -6 * y1[k] + -7 * y1[k - 3];
  }
}
```

Fig. 5. Examples of the generated random functions of array handling in C++

3.4. Automatic check of tasks

The correctness of the obtained solution was checked using a set of program tests, which is formed by a task generator. For testing, a "sandbox", representing a medium of safe execution of program code, is realized.

It is also expedient to make a comprehensive evaluation of a student's solution without restricting only to checking the correctness of the result. Elements of such evaluation made automatically can include:

- check of solutions for plagiarism in the case of tasks created manually by teachers;
- check for compliance with the program writing style standard;
- analysis of the metrics for assessing the program complexity;
- evaluation of the correctness of the result, the computational complexity of the program, and the memory size used by the program.

The first three items in the list can be realized using statistical analysis tools, while the last item, requires the use of program profiling tools.

In the case of an incorrect solution, the answer of DTA should include at least a massage of the compiler and an indication of the nonexecuted test.

A more informative answer includes an indication of a typical error made by a student. Such a mechanism can be realized by seeking templates in the AST of the incorrect program. Rules of the template-message form are added to DTA by the teacher. There are also approaches that enable the generation, based on an incorrect solution, of automatic hints directing the student toward the correct result [26].

3.5. Recording of statistics of academic achievement of students

By storing solutions received from students in a DTA database, the teacher can dispense with the requirement to manually fill out a gradebook. Furthermore, by comprehensively evaluating solutions using the DTA, it is possible to abandon simplified formulas for calculating the final grade or ready sets of tasks. As a result, the teacher can satisfy him- or herself with indicating the minimum necessary number of solved tasks for each of the topics of the course. At the same time, a DTA allows a student to carry out an unlimited number, complexity and type of training tasks.

3.6. Interface of interaction between students and teachers

For a DTA, it is preferable to use a web interface that provides access to the system from any device with an Internet connection.

From a student's standpoint, the interface should allow the student to choose the types and parameters of tasks on the current topic of the course. By providing the results of the integrated assessment together with the history of the previous results, the student is empowered to evaluate his or her progress.

From a teacher's standpoint, an important role is played by the analysis of students' activity data. Using the DTA interface, the teacher can promptly assess the situation and make the necessary decisions. This concerns, e.g., a situation in which a task turned out to be too easy or too difficult to solve for the majority of students. Here, data analysis can be used to identify underachievers or predict a student's final grade.

4. EXPERIENCE OF DEVELOPMENT OF PYTHON PROGRAMMING TRAINIUNG COURSE

The Python programming training course at the MIREA – Russian Technological University, Moscow, Russia, is organized as a blended learning environment. Figure 6 presents online tools used in this course.

The instructional personnel of the course comprise 4 lecturers and 13 tutors of practical exercises. Since more than 1500 students participated in the training, a Telegram channel was created for their prompt notification of important events during the course. In terms of a duplex communication channel, the MantisBT bug tracker was used. This was already known to the

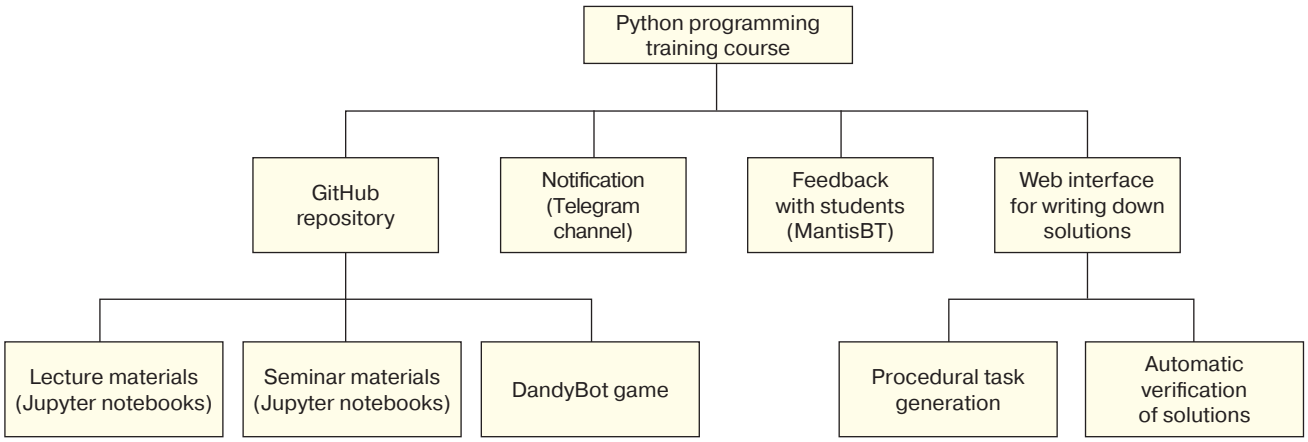

Fig. 6. Structure of the inline part of the Python programming training course

students from a configuration management course and was used as a replacement of conventional interaction tools (electronic mail and forum).

The basic part of the course, which includes issues of using the main constructs of the language and introduces students to the object-oriented programming style accepted in Python, was presented in the form of lectures. The final lectures consider a number of special issues, in particular:

- test automation: test coverage metrics, mutation testing, design by contract, property- and model-based testing;
- functional programming: higher-order functions, closures, decorators, generators, immutable data types, functools and itertools modules, and NumPy library.

The main materials of the course are stored in a separate GitHub repository. The students are rewarded for errors found in the materials. Messages about the found errors are received as pull requests.

The use of Jupyter notebooks increased the interactivity of the online lectures delivered in a webinar format. During the lecture, the students directly experiment with brief proposed programs; responding inter alia to the students' questions, the lecturer can modify and run examples of programs in cells of a Jupyter notebook. The representation of lecture material in the conventional slide form supplemented with the interactivity provided by cells is performed using the RISE extension for Jupyter notebooks.

The classroom lectures include an interactive theoretical part, which allows:

- assessment of the retention of the lecture material by the students online and, if necessary, timely addressing of gaps in the students' knowledge;
- introduce the students to the subject domain of the tasks considered in the exercise.

In seminar classes, tasks of several types are used:

- procedure-generated tasks;
- tasks from Jupyter notebooks;
- tasks related to DandyBot game;
- individual and group creative projects on tutors' topics.

Among the main problems involved in the design of the considered course were the creation and organization of rapid checks of practical tasks under massive learning conditions given a shortage of tutors. It was decided to use an approach based on procedural generation: an individual set of tasks was automatically formed for each of the students [18]. As well as solving the problem of plagiarism among the students, this approach also reduced the tutors' workload due to the automatic checking of solutions.

For example, variants of the following tasks are generated automatically:

1) conversion of mathematical notation into code: arithmetic expression;
2) conversion of mathematical notation into code: branching;
3) conversion of mathematical notation into code: cycles;
4) conversion of mathematical notation into code: recursion;
5) conversion of solution tree into code;
6) realization of bit field swapping in a bit word;
7) tabular data format conversion (Fig. 7);
8) binary file format parsing (Fig. 8);
9) realization of finite-state machine by object-oriented programming features.

For a given generated task, the degree of complexity can be set along with the number of formed tests to allow a student to check the correctness of his or her solution.

An important part is played by the informativeness of messages received by the students from the system submitting task solutions. For some types of tasks, there is a support of rules according to which a detailed error message is generated and accompanied by a reference to methods for obtaining the correct solution using the template found in the solution code. The pattern-matching search is performed at the level of the representation of a student's program as an AST. In the bit field swapping

task, such rules allow an incorrect solution approach to be identified (the presence of a number-to-string conversion function) as well as hints given concerning the correct direction (using bitwise operations).

The exam in the Python programming training course also uses procedure-generated tasks. Figure 9 presents the web interface via which the students send their solutions of tasks of this type.

For the majority of the seminar class, practical tasks from Jupyter notebooks are discussed and solved. Some of such tasks are considered "at the blackboard": the tutor invites someone of the students to take a seat at a computer connected to the room's projector. Using such a format, other students can keep track of the solution and the tutor's comments. Better-prepared students during the classroom learning solve tasks by themselves and send the solutions to the tutor for checking through the bug tracking system. Such a workflow allows the tutor to actively participate in the learning without continuously moving over the room from computer to computer and, thereby, to respect COVID-19 restrictions more rigorously. A sudden transition to offline learning using such a workflow of practical exercise is not a serious problem because the students send their task solutions using the same bug tracking system.

Task 3. Realize a tabular data conversion function. The input and output tables are given in row-by-row form. Filled cells have a row data type. Empty cells have the None value.

Make the following conversions of the input tables:
– remove empty columns;
– divide column 1 by divider "!";
– convert cell contents by examples;
– transpose the table.

Examples of table conversions:

1. Initial table:

		+78694947943!03-08-2003	No
		+79774177489!27-03-2002	Yes
		+77571568485!05-12-2001	Yes
		+73113372701!21-07-2003	No

Conversion result:

8694947943	9774177489	7571568485	3113372701
false	true	true	false
03-08-03	02-03-27	01-12-05	03-07-21

2. Initial table:

		+76058136232!11-04-2001	No
		+72178434337!02-10-2000	No
		+76826857881!25-11-2003	Yes

Conversion result:

6058136232	2178434337	6826857881
false	false	true
01-04-11	00-10-02	03-11-25

Fig. 7. Example of an automatically generated task of tabular data conversion

Task 3.1. Realize binary file format parsing (in the spirit of the WAD format of the Doom game or the graphic PNG format). The data begin with the signature 0 × 42, 0 × 58, 0 × 59, 0 × 9a followed by the structure A. Byte order: big-endian. The addresses are expressed as the offsets from the data origin. In the solution, it is allowed using the struct module.

Structure A:

1	Structure array B, size 4
2	int16
3	int16
4	int16
5	Structure C
6	Size (uint32) and address (uint32) of the double array
7	uint32
8	Structure D

Structure B:

1	uint32
2	double
3	Size (uint32) and address (uint32) of the char array

Structure C:

1	Int16 array, size 5
2	uint64
3	int16
4	int8

Structure D:

1	int16
2	int8
3	int8
4	uint64
5	Size (uint32) and address (uint32) of the uint16 array

Fig. 8. Example of an automatically generated task of binary file format parsing (test data are not shown)

Exam in the Python programming training course

Group B1 Variant 25

Solution:

```
import struct

def f31(x):
    res = {}
    res['A1'] = struct.unpack('f', x[3:7:])[0]
    res['A2'] = struct.unpack('q', x[7:15:])[0]
    res['A3'] = {}
    addr = x[15] + x[16] * 16 + x[17] * 16 * 16 + x[18] * 16 * 16 * 16
    res['A3']['B1'] = struct.unpack('q', x[addr : addr + 8])[0]
    res['A3']['B2'] = struct.unpack('H', x[addr + 8 : addr+ 10])[0]
    res['A3']['B3'] = struct.unpack('b', x[addr + 10 : addr + 11])[0]
    res['A4'] = struct.unpack('h', x[19:21:])[0]
    res['A5'] = {}
    res['A5']['C1'] = ''
    size = x[21] + x[22] * 16 + x[23] * 16 * 16 + x[24] * 16 * 16 * 16
    addr = x[25] + x[26] * 16 + x[27] * 16 * 16 + x[28] * 16 * 16 * 16
    for i in range(addr, addr + size):
        res['A5']['C1'] += chr(x[i])
    res['A5']['C2'] = [] # = ''
    size = x[29] + x[30] * 16
    addr = x[31] + x[32] * 16
    for i in range(size):
        res['A5']['C2'].append({})
        res['A5']['C2'][i]['D1'] = struct.unpack('H', x[addr + 4 * i : addr + 2 + 4 * i :])[0]
        res['A5']['C2'][i]['D2'] = struct.unpack('H', x[addr + 2 + 4 * i : addr + 4 + 4 * i :])
```

Send

Table of results

Error log

Fig. 9. Web interface for receiving the solutions of automatically generated tasks

Practical tasks from Jupyter notebooks, which belong to different subject domains, are developed so that they are of interest for students and in such a way as to permit a solution to be obtained within a single practical exercise. The topics of the practical tasks are as follows: random digital economy report generator; Burrows–Wheeler transform; ASCII banner generator; Schelling's model of segregation; graph imaging by physical modeling; stack language interpreter; hierarchical clustering algorithm; formal verification of computer game puzzles; undo/redo mechanism in graphic editor; SQL-like query language; Julia fractal; Floyd–Steinberg algorithm.

A special type of practical tasks is constituted by tasks of simple data analysis based on information collected by a web tool for receiving the students' solutions of procedure-generated tasks. Here, in the reflection mode, the students learn their own activity in the course. Figures 10 and 11 show the results of such an analysis.

Additional tasks for practical exercises are provided via the DandyBot game, which was developed especially for the considered course. It belongs to the genre of games for programmers in which, for success in the game, it is necessary to write a program code. The DandyBot game, an example of a level of which is shown in Fig. 12, is presented in the style of Roguelike games to allow the "intelligence" of player characters to be programmed in Python.

At the first levels, the players should write the simplest programs; therefore, even the students with minimum programming experience can be involved in writing a code in Python in a playful way.

The DandyBot game used by the students is a semi-product presented in the form of a GitHub repository requiring numerous improvements. This stimulates the students to develop the program code of the DandyBot project as well as to create additional levels.

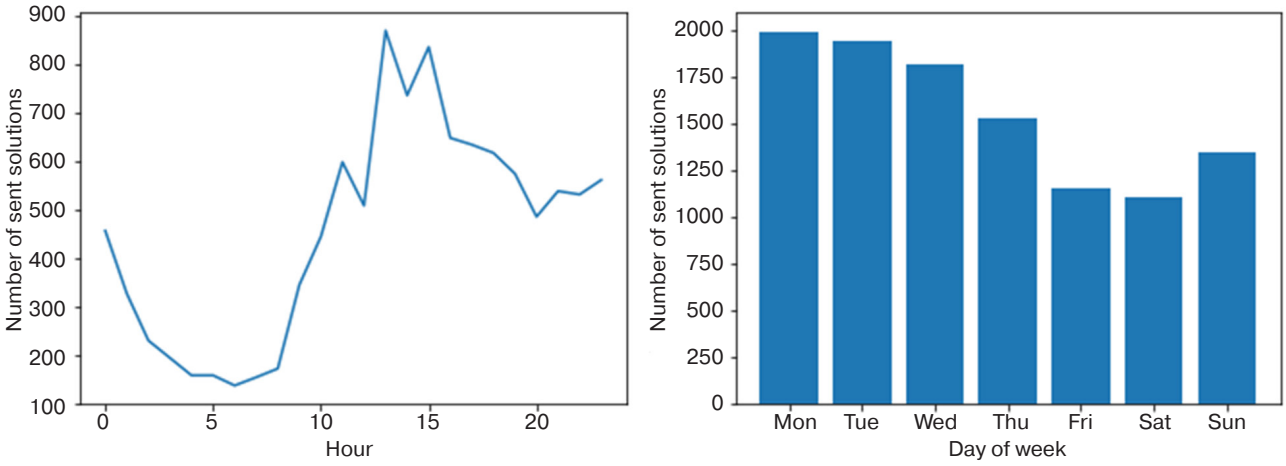

Fig. 10. Students' activity over the day and the days of the week

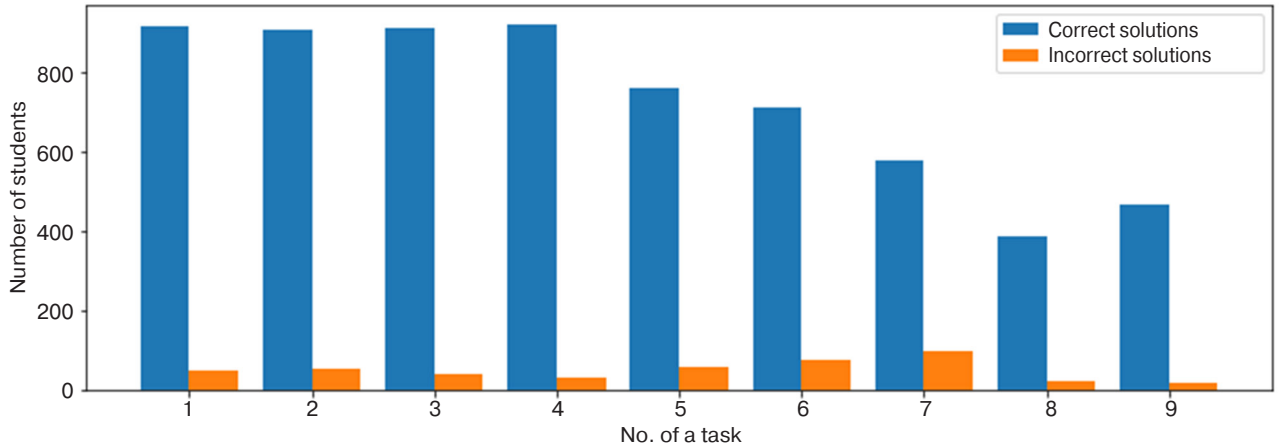

Fig. 11. Statistics of solutions of procedure-generated tasks that were sent by the students

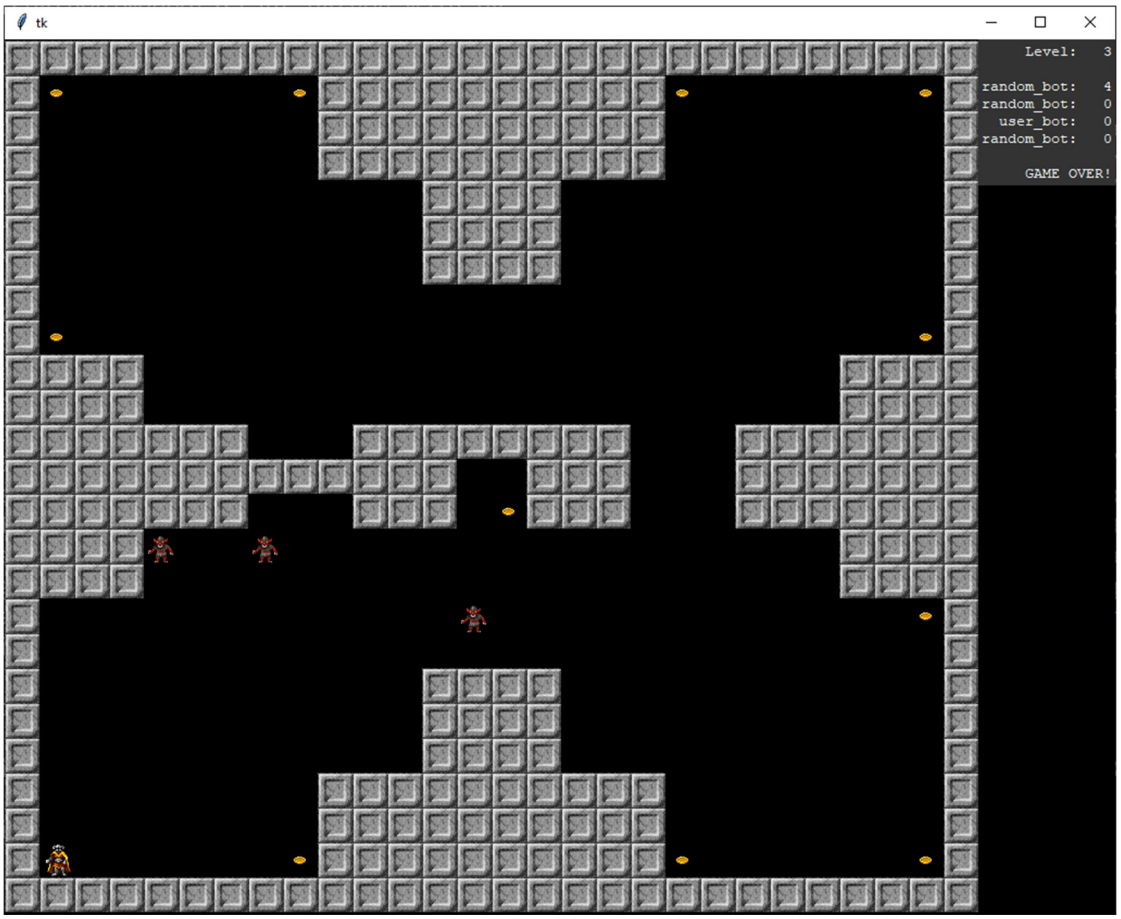

Fig. 12. A level of the DandyBot game with a player controlled by a program in Python language

CONCLUSIONS

Under present-day conditions (massive programming learning, transition from classroom learning to distant/blended learning and back within a semester, and competition with specialized courses and platforms of learning of programming languages), teachers at university programming teaching courses encounter a significant increase in the workload, which is mostly related to performing routine activities.

The developed DTA automates such procedures as generating individual tasks and checking their solutions, as well as providing an informative answer to the student and recording the academic achievement of students. This allows the teacher to devote more time and attention to functions requiring creative input—in particular, to creation and discussion of nontrivial programming tasks.

The experience of implementing the DTA in the learning process of the Python Programming course confirmed the possibility of personifying the learning process for students in the form of individual learning paths.

Authors' contributions:

E.G. Andrianova: The urgency of automating the process of massive programming training was substantiated. The personification methods for the massive programming training process were investigated and adapted. Types of practical tasks reflecting the contemporary specifics of software development were highlighted.

L.A. Demidova: A procedure for a comprehensive assessment of the student's solution was proposed. This procedure included checking the correctness of the result and checking for plagiarism of solutions in the case of tasks created by the teacher manually, as well as compliance of the program style with the standard and metrics for assessing the program complexity, etc. The maintenance of statistics of students' progress and the interface of interaction between students and teachers are described.

P.N. Sovetov: Algorithms satisfying the constraints for creating generators of programming tasks were developed, the Digital Teaching Assistant computer system architecture was built, and the implementation of this system was completed. A procedure for automatic verification of task solutions was developed and described. This procedure is realized using software tests generated by the task generator.

All authors took part in the development and implementation of the Digital Teaching Assistant computer system in the practice of the RTU MIREA educational process in the Programming in Python discipline.

REFERENCES

1. Gudov M.M., Ermakova E.R. Structural transformations of the Russian economy in the conditions of acceleration digitalization of industrial relations. *Teoreticheskaya i prikladnaya ekonomika = Theoretical and Applied Economics*. 2020;2:1–8 (in Russ.). https://doi.org/10.25136/2409-8647.2020.2.32625
2. Novikova E.S. Risks and perspectives of higher school transformation for the Russian economy in conditions of gobalization and digitalization. *Mezhdunarodnaya torgovlya i torgovaya politika = International Trade and Trade Policy*. 2021;7(4):147–162 (in Russ.). https://doi.org/10.21686/2410-7395-2021-3-147-162
3. Yaroslavtseva E.I. Humanitarian aspects of digital technologies. *Vestnik Rossiiskogo filosofskogo obshchestva = Russian Philosophical Society*. 2020;1–2(91–92): 248–251 (in Russ.). Available from URL: https://rfo1971.ru/wp-content/uploads/2020/03/09-03_248-251.pdf
4. Yaroslavtseva E.I. The potential of digital technologies and the problems of human creativity. *Voprosy Filosofii*. 2020;11:58–66 (in Russ.). https://doi.org/10.21146/0042-8744-2020-11-58-66.
5. Strokov A.A. Digitalization of education: problems and prospects. *Vestnik Mininskogo universiteta = Vestnik of Minin University*. 2020;8(2):15 (in Russ.). https://doi.org/10.26795/2307-1281-2020-8-2-15
6. Khutorskoi A.V. Pedagogical prerequisites for student self-realization in heuristic learning. *Vestnik Instituta Obrazovaniya Cheloveka*. 2020;1:1 (in Russ.). Available from URL: http://eidos-institute.ru/journal/2020/100/Eidos-Vestnik2020-101-Khutorskoy.pdf
7. Khutorskoi A.V. Interiorization and exteriorization – two approaches to human education. *Narodnoe obrazovanie*. 2021;1(1484):37–49 (in Russ.).
8. Khalyapina L., Kuznetsova O. Multimedia professional content foreign language competency formation in a digital educational system exemplified by STEPIK framework. *Lecture Notes in Networks and Systems*. 2020;131: 357–366. https://doi.org/10.1007/978-3-030-47415-7_38
9. Panova I.V., Kolivnyk A.A. An overview of the content of online courses on teaching the basics of programming in the Python language. In: *Sovremennye obrazovatel'nye Web-tekhnologii v realizatsii lichnostnogo potentsiala obuchayushchikhsya* (*Contemporary Educational Web-technologies in the Realization of the Personal Potential of Students*): Collection of research articles of international scientific and practical conference. Arzamas; 2020. P. 523–528 (in Russ).
10. Vorob'eva N.A., Oboeva S.V., Bernadiner M.I. Using pedagogical design technologies in the context of digitalization of education. *Vestnik Moskovskogo gorodskogo pedagogicheskogo universiteta. Seriya: Informatika i informatizatsiya obrazovaniya = The academic Journal of Moscow City University, series Informatics and Informatization of Education*. 2020;1(51):34–37 (in Russ).
11. Guo P.J., Kim J., Rubin R. How video production affects student engagement: An empirical study of MOOC videos. In: *Proceedings of the First ACM Conference on Learning @ Scale Conference*. 2014. P. 41–50. https://doi.org/10.1145/2556325.2566239

СПИСОК ЛИТЕРАТУРЫ

1. Гудов М.М., Ермакова Э.Р. Структурные преобразования российской экономики в условиях форсированной цифровизации производственных отношений. *Теоретическая и прикладная экономика*. 2020;2:1–8. https://doi.org/10.25136/2409-8647.2020.2.32625
2. Новикова Е.С. Риски и перспективы трансформации высшей школы для российской экономики в условиях глобализации и цифровизации. *Международная торговля и торговая политика*. 2021;7(4):147–162. https://doi.org/10.21686/2410-7395-2021-3-147-162
3. Ярославцева Е.И. Гуманитарные аспекты цифровых технологий. *Вестник Российского философского общества*. 2020;1–2(91–92):248–251. URL: https://rfo1971.ru/wp-content/uploads/2020/03/09-03_248-251.pdf
4. Ярославцева Е.И. Потенциал цифровых технологий и проблемы творчества человека. *Вопросы философии*. 2020;11:58–66. https://doi.org/10.21146/0042-8744-2020-11-58-66
5. Строков А.А. Цифровизация образования: проблемы и перспективы. *Вестник Мининского университета*. 2020;8(2):15. https://doi.org/10.26795/2307-1281-2020-8-2-15
6. Хуторской А.В. Педагогические предпосылки самореализации ученика в эвристическом обучении. *Вестник Института образования человека*. 2020;1:1. URL: http://eidos-institute.ru/journal/2020/100/Eidos-Vestnik2020-101-Khutorskoy.pdf
7. Хуторской А.В. Интериоризация и экстериоризация – два подхода к образованию человека. *Народное образование*. 2021;1(1484):37–49.
8. Khalyapina L., Kuznetsova O. Multimedia professional content foreign language competency formation in a digital educational system exemplified by STEPIK framework. *Lecture Notes in Networks and Systems*. 2020;131:357–366. https://doi.org/10.1007/978-3-030-47415-7_38
9. Панова И.В., Коливнык А.А. Обзор содержания онлайн курсов по обучению основам программирования на языке Python. В: *Современные образовательные Web-технологии в реализации личностного потенциала обучающихся*. сборник статей участников Международной научно-практической конференции. Арзамас; 2020. С. 523–528.
10. Воробьева Н.А., Обоева С.В., Бернадинер М.И. Использование технологий педагогического дизайна в условиях цифровизации образования. *Вестник Московского городского педагогического университета. Серия: Информатика и информатизация образования*. 2020;1(51):34–37.
11. Guo P.J., Kim J., Rubin R. How video production affects student engagement: An empirical study of MOOC videos. In: *Proceedings of the First ACM Conference on Learning @ Scale Conference*. 2014. P. 41–50. https://doi.org/10.1145/2556325.2566239
12. Lau S., Guo P.J. Data theater: a live programming environment for prototyping data-driven explorable explanations. *Workshop on Live Programming* (*LIVE*). 2020. 6 p. URL: https://www.samlau.me/pubs/Data-Theater-prototyping-explorable-explanations_LIVE-2020.pdf

12. Lau S., Guo P.J. Data Theater: A live programming environment for prototyping data-driven explorable explanations. *Workshop on Live Programming* (*LIVE*). 2020. 6 p. Available from URL: https://www.samlau.me/pubs/Data-Theater-prototyping-explorable-explanations_LIVE-2020.pdf
13. Guo P.J. Online python tutor: embeddable web-based program visualization for cs education. In: *Proceeding of the 44th ACM Technical Symposium on Computer Science Education*. 2013. P. 579–584. https://doi.org/10.1145/2445196.2445368
14. Miller H., Willcox K., Huang L. Crosslinks: Improving course connectivity using online open educational resources. *The Bridge*. 2016;43(3):38–45. Available from URL: http://hdl.handle.net/1721.1/117022
15. Utterberg M.M., et al. Intelligent tutoring systems: Why teachers abandoned a technology aimed at automating teaching processes. In: *Proceedings of the 54th Hawaii International Conference on System Sciences*. 2021. P. 1538. Available from URL: http://hdl.handle.net/10125/70798
16. Sherman M., et al. Impact of auto-grading on an introductory computing course. *J. Comput. Sci. Coll.* 2013;28(6):69–75.
17. Rivers K., Koedinger K.R. Data-driven hint generation in vast solution spaces: a self-improving python programming tutor. *Int. J. Artif. Intell. Educ*. 2017;27(1):37–64. https://doi.org/10.1007/s40593-015-0070-z
18. Sovietov P. Automatic generation of programming exercises. In: *2021 1st International Conference on Technology Enhanced Learning in Higher Education* (*TELE*). IEEE. 2021. P. 111–114. https://doi.org/10.1109/TELE52840.2021.9482762
19. Schleimer S., Wilkerson D.S., Aiken A. Winnowing: local algorithms for document fingerprinting. In: *Proceedings of the 2003 ACM SIGMOD International Conference on Management of Data* (*SIGMOD'03*). 2003. P. 76–85. https://doi.org/10.1145/872757.872770
20. Rogers M., et al. Exploring Personalization of gamification in an Introductory programming course. In: *Proceedings of the 52nd ACM Technical Symposium on Computer Science Education* (*SIGCSE'21*). 2021. P. 1121–1127. https://doi.org/10.1145/3408877.3432402
21. Putnam V., Conati C. Exploring the need for explainable artificial intelligence (XAI) in intelligent tutoring systems (ITS). *IUI Workshops*. 2019. V. 19. Available from URL: https://explainablesystems.comp.nus.edu.sg/2019/wp-content/uploads/2019/02/IUI19WS-ExSS2019-19.pdf
22. Shcherbina O.A. Constraint satisfaction and constraint programming. *Intellektual'nye sistemy = Intelligent Systems*. 2011;15(1–4):53–170 (in Russ.).
23. Wang J., Chen B., Wei L., Liu Y. Skyfire: Data-driven seed generation for fuzzing. In: *2017 IEEE Symposium on Security and Privacy* (*SP*). IEEE. 2017. P. 579–594. https://doi.org/10.1109/SP.2017.23
24. Papadakis M., et al. Mutation testing advances: an analysis and survey. *Adv. Comput*. 2019;112:275–378. https://doi.org/10.1016/bs.adcom.2018.03.015

13. Guo P.J. Online python tutor: embeddable web-based program visualization for cs education. In: *Proceeding of the 44th ACM Technical Symposium on Computer Science Education*. 2013. P. 579–584. https://doi.org/10.1145/2445196.2445368
14. Miller H., Willcox K., Huang L. Crosslinks: Improving course connectivity using online open educational resources. *The Bridge*. 2016;43(3):38–45. URL: http://hdl.handle.net/1721.1/117022
15. Utterberg M.M., et al. Intelligent tutoring systems: Why teachers abandoned a technology aimed at automating teaching processes. In: *Proceedings of the 54th Hawaii International Conference on System Sciences*. 2021. P. 1538. URL: http://hdl.handle.net/10125/70798
16. Sherman M., et al. Impact of auto-grading on an introductory computing course. *J. Comput. Sci. Coll.* 2013;28(6):69–75.
17. Rivers K., Koedinger K.R. Data-driven hint generation in vast solution spaces: a self-improving python programming tutor. *Int. J. Artif. Intell. Educ*. 2017;27(1):37–64. https://doi.org/10.1007/s40593-015-0070-z
18. Sovietov P. Automatic generation of programming exercises. In: *2021 1st International Conference on Technology Enhanced Learning in Higher Education* (*TELE*). IEEE. 2021. P. 111–114. https://doi.org/10.1109/TELE52840.2021.9482762
19. Schleimer S., Wilkerson D.S., Aiken A. Winnowing: local algorithms for document fingerprinting. In: *Proceedings of the 2003 ACM SIGMOD International Conference on Management of Data* (*SIGMOD'03*). 2003. P. 76–85. https://doi.org/10.1145/872757.872770
20. Rogers M., et al. Exploring personalization of gamification in an introductory programming course. In: *Proceedings of the 52nd ACM Technical Symposium on Computer Science Education* (*SIGCSE'21*). 2021. P. 1121–1127. https://doi.org/10.1145/3408877.3432402
21. Putnam V., Conati C. Exploring the need for explainable artificial intelligence (XAI) in intelligent tutoring systems (ITS). *IUI Workshops*. 2019. V. 19. URL: https://explainablesystems.comp.nus.edu.sg/2019/wp-content/uploads/2019/02/IUI19WS-ExSS2019-19.pdf
22. Щербина О.А. Удовлетворение ограничений и программирование в ограничениях. *Интеллектуальные системы*. 2011;15(1–4):53–170.
23. Wang J., Chen B., Wei L., Liu Y. Skyfire: Data-driven seed generation for fuzzing. In: *2017 IEEE Symposium on Security and Privacy* (*SP*). IEEE. 2017. P. 579–594. https://doi.org/10.1109/SP.2017.23
24. Papadakis M., et al. Mutation testing advances: an analysis and survey. *Adv. Comput*. 2019;112:275–378. https://doi.org/10.1016/bs.adcom.2018.03.015
25. Hutton G., Meijer E. *Monadic Parser Combinators*. Technical Report NOTTCS-TR-96-4. Department of Computer Science, University of Nottingham. 1996. 38 p. URL: https://www.cs.nott.ac.uk/~pszgmh/monparsing.pdf
26. Phothilimthana P.M., Sridhara S. High-coverage hint generation for massive courses: Do automated hints help CS1 students? In: *Proceedings of the 2017 ACM Conference on Innovation and Technology in Computer Science Education* (*ITiCSE'17*). 2017. P. 182–187. https://doi.org/10.1145/3059009.3059058

25. Hutton G., Meijer E. *Monadic Parser Combinators*. Technical Report NOTTCS-TR-96-4. Department of Computer Science, University of Nottingham. 1996. 38 p. Available from URL: https://www.cs.nott.ac.uk/~pszgmh/monparsing.pdf
26. Phothilimthana P.M., Sridhara S. High-coverage hint generation for massive courses: Do automated hints help CS1 students? In: *Proceedings of the 2017 ACM Conference on Innovation and Technology in Computer Science Education* (*ITiCSE'17*). 2017. P. 182–187. https://doi.org/10.1145/3059009.3059058

About the authors

Elena G. Andrianova, Cand. Sci. (Eng.), Associated Professor, Head of the Department of Corporate Information Systems, Institute of Information Technologies, MIREA – Russian Technological University (78, Vernadskogo pr., Moscow, 119454 Russia). E-mail: andrianova@mirea.ru. Scopus Author ID 57200555430, ResearcherID T-7908-2018, SPIN-code RSCI 9858-3229, http://orcid.org/0000-0001-6418-6797

Liliya A. Demidova, Dr. Sci. (Eng.), Professor, Professor of the Department of Corporate Information Systems, Institute of Information Technologies, MIREA – Russian Technological University (78, Vernadskogo pr., Moscow, 119454 Russia). E-mail: demidova@mirea.ru. Scopus Author ID 56406258800, ResearcherID R-6077-2016, SPIN-code RSCI 9447-3568, http://orcid.org/0000-0003-4516-3746

Petr N. Sovetov, Cand. Sci. (Eng.), Associated Professor, Department of Corporate Information Systems, Institute of Information Technologies, MIREA – Russian Technological University (78, Vernadskogo pr., Moscow, 119454 Russia). E-mail: sovetov@mirea.ru. Scopus Author ID 57221375427, SPIN-code RSCI 9999-1460, http://orcid.org/0000-0002-1039-2429

Об авторах

Андрианова Елена Гельевна, к.т.н., доцент, заведующий кафедрой корпоративных информационных систем Института информационных технологий ФГБОУ ВО «МИРЭА – Российский технологический университет» (119454, Россия, Москва, пр-т Вернадского, д. 78). E-mail: andrianova@mirea.ru. Scopus Author ID 57200555430, ResearcherID T-7908-2018, SPIN-код РИНЦ 9858-3229, http://orcid.org/0000-0001-6418-6797

Демидова Лилия Анатольевна, д.т.н., профессор, профессор кафедры корпоративных информационных систем Института информационных технологий ФГБОУ ВО «МИРЭА – Российский технологический университет» (119454, Россия, Москва, пр-т Вернадского, д. 78). E-mail: demidova@mirea.ru. Scopus Author ID 56406258800, ResearcherID R-6077-2016, SPIN-код РИНЦ 9447-3568, http://orcid.org/0000-0003-4516-3746

Советов Петр Николаевич, к.т.н., доцент кафедры корпоративных информационных систем Института информационных технологий, ФГБОУ ВО «МИРЭА – Российский технологический университет» (119454, Россия, Москва, пр-т Вернадского, д. 78). E-mail: sovetov@mirea.ru. Scopus Author ID 57221375427, SPIN-код РИНЦ 9999-1460, http://orcid.org/0000-0002-1039-2429

Translated by V. Glyanchenko
Edited for English language and spelling by Thomas Beavitt

Information systems. Computer sciences. Issues of information security
Информационные системы. Информатика. Проблемы информационной безопасности

UDC 004.2
https://doi.org/10.32362/2500-316X-2022-10-3-24-33

RESEARCH ARTICLE

Prospects for using soft processors in systems-on-a-chip based on field-programmable gate arrays

Ilya E. Tarasov @, Dmitry S. Potekhin, Olga V. Platonova

MIREA – Russian Technological University, Moscow, 119454 Russia
@ Corresponding author, e-mail: tarasov_i@mirea.ru

Abstract

Objectives. Developing the element base of field-programmable gate arrays (FPGA) may significantly affect the design of electronic devices due to the enhanced logical capacity of such chips and the general tendency towards increased subsystem integration. The system-on-a-chip (SoC) concept is aimed at combining receiving, processing, and exchange subsystems onto a single chip, as well as at implementing control, diagnostic, and other auxiliary subsystems. The study aimed at developing a method for soft processor applications, i.e., processors based on configurable logical resources, for implementing control functions in an FPGA-based SoC.

Methods. A digital system design methodology was used.

Results. For soft processors, a unified design route based on selecting architectural parameters qualitatively corresponding to control tasks was considered. In particular, such parameters as instruction set addressness, number of pipeline cycles, and arithmetic logic unit configuration are adjustable at the design stage to allow the optimization of the soft processor in the discrete parameter space. An approach to rapid prototyping of the assembler based on stack-oriented programming language with regular grammar was also considered. The control of digital signal processing hardware as part of an SoC is the promising application area for soft processors. An implementation is considered on the example of an SoC based on Xilinx Virtex-7 FPGA containing several processor cores developed using the proposed methodology.

Conclusions. The considered approaches to soft processor design allow the rapid prototyping of the control processor core for operation as part of an FPGA-based SoC.

Keywords: processor, field-programmable gate array, system-on-a-chip, digital signal processing, compiler

• **Submitted:** 10.01.2022 • **Revised:** 21.03.2022 • **Accepted:** 22.04.2022

For citation: Tarasov I.E., Potekhin D.S., Platonova O.V. Prospects for using soft processors in systems-on-a-chip based on field-programmable gate arrays. *Russ. Technol. J.* 2022;10(3):24–33. https://doi.org/10.32362/2500-316X-2022-10-3-24-33

Financial disclosure: The authors have no a financial or property interest in any material or method mentioned.

The authors declare no conflicts of interest.

НАУЧНАЯ СТАТЬЯ

Перспективы применения софт-процессоров в системах на кристалле на базе программируемых логических интегральных схем

И.Е. Тарасов [@], Д.С. Потехин, О.В. Платонова

МИРЭА – Российский технологический университет, Москва, 119454 Россия
[@] Автор для переписки, e-mail: tarasov_i@mirea.ru

Резюме

Цели. Развитие элементной базы программируемых логических интегральных схем (ПЛИС) качественно меняет требования к маршруту проектирования электронных средств вследствие роста логической емкости этих микросхем и тенденции к повышению степени интеграции подсистем. Преимущественным направлением применения данной платформы является концепция системы на кристалле (СнК), направленная на совмещение в одном кристалле подсистем приема, обработки и обмена данными, а также реализацию управляющих, диагностических и других вспомогательных подсистем. Цель работы – разработка методики применения софт-процессоров, т.е. процессоров, создаваемых на базе конфигурируемых логических ресурсов, для реализации функций управления в составе СнК на базе ПЛИС.

Методы. Использованы методы проектирования цифровых систем.

Результаты. Для софт-процессоров рассмотрен унифицированный маршрут проектирования, основанный на выборе архитектурных параметров, качественно соответствующих задачам управления. В частности, такие параметры, как адресность системы команд, количество тактов конвейера, конфигурация арифметико-логического устройства, являются регулируемыми на этапе проектирования, что позволяет проводить оптимизацию софт-процессора в дискретном пространстве параметров. Рассмотрен также подход к быстрому прототипированию ассемблера на основе стекового языка программирования с регулярной грамматикой. Перспективным направлением применения софт-процессоров является управление аппаратными компонентами цифровой обработки сигналов в составе СнК. В статье рассмотрен пример реализации СнК на базе ПЛИС Xilinx Virtex-7, в составе которого применены несколько процессорных ядер, разработанных по предложенной методике.

Выводы. Рассмотренные подходы к проектированию софт-процессоров позволяют проводить быстрое прототипирование управляющего процессорного ядра для работы в составе СнК на базе ПЛИС.

Ключевые слова: процессор, ПЛИС, система на кристалле, цифровая обработка сигналов, компилятор

• **Поступила:** 10.01.2022 • **Доработана:** 21.03.2022 • **Принята к опубликованию:** 22.04.2022

Для цитирования: Тарасов И.Е., Потехин Д.С., Платонова О.В. Перспективы применения софт-процессоров в системах на кристалле на базе программируемых логических интегральных схем. *Russ. Technol. J.* 2022;10(3):24–33. https://doi.org/10.32362/2500-316X-2022-10-3-24-33

Прозрачность финансовой деятельности: Авторы не имеют финансовой заинтересованности в представленных материалах или методах.

Авторы заявляют об отсутствии конфликта интересов.

INTRODUCTION

Disadvantages inherent to programmable logic cell arrays in digital system designs based on field-programmable gate arrays (FPGA) include inferior clock rate, chip area, and power consumption characteristics. However, such disadvantages may be compensated by combining hardware architectures to allow the reconfiguration of circuits, as well as the development of devices having optimized architectures for particular tasks [1]. Moreover, since FPGA functionality involves a number of digital nodes and subsystems, hardware architecture has evolved to progressively add specialized non-reconfigurable hardware components embedded in logic cell design. For example, dual-port static memory blocks and hardware multipliers of independent operands later converted into digital signal processing (DSP) modules were added to the FPGA architecture at the turn

of 2000s [2]. Later on, the PowerPC (Xilinx Virtex-II Pro, Virtex-4, Virtex-5)[1] and Advanced RISC Machine (ARM) (Xilinx Zynq-7000, Xilinx Zynq UltraScale+, Xilinx Versal[2], Intel Cyclone V[3]) hardware processor cores were added to FPGAs. By separating the ARM processor subsystem into an independently operating part of the chip, the Xilinx Zynq-7000 family became a fully programmable system-on-a-chip (SoC)[4] rather than FPGA.

The practical use of fully programmable SoCs has demonstrated the increasingly auxiliary role of processors due to the significant lag in their performance as compared with the overall performance of the array of configurable logic elements supplemented with DSP components. However, attempts to build a system around a processor core with configurable peripheral devices resulted in economically inefficient solutions as compared to similar capabilities provided by a wide element base range of microcontrollers based on ARM, MIPS (microprocessor without interlocked pipeline stages), RISC-V (reduced instruction set computer) cores, etc. Thus, the key factor determining the competitive technical and economic performance of FPGAs is the demand for reconfigurable resources as the main element of a computing system.

Among the main areas of application for high-performance computing are video processing systems, virtual and augmented reality, robotics, industrial automation, digital radio communication, and measurement equipment systems [3, 4]. Current areas of signal processing include digital filtering [5], spectral analysis [6], and machine learning algorithms [7], including those based on specialized neuroprocessors [8] or FPGA-based reconfigurable accelerators.[5]

ARCHITECTURE OF DIGITAL SoC BASED ON PROCESSOR

The requirements for a processor used as part of an SoC are determined by its tasks and role in the system. Since the main computational load is provided by hardware accelerators implemented on the basis of logic cells, static memory blocks, and DSP hardware modules, it becomes hard to ensure the continuous participation of a processor (or even several processor cores) in dataflow computing. Therefore, hardware accelerators implemented in FPGA should provide dataflow computing that does not require constant processor participation, but instead allows the processing of parameters, reconfiguration, monitoring, and similar tasks, to be controlled by software. The implementation of complex software protocols for data exchange, such as support for wired and wireless networks, user interfaces, etc., also becomes a significant challenge. The flowchart illustrating interaction between the processor and hardware acceleration subsystem is shown in Fig. 1.

Figure 1 shows that the main computational performance is determined by a hardware accelerator implemented based on reconfigurable FPGA resources. At the same time, the control of low-speed peripherals may be assigned to the soft processor, while its low capacity allows the use of a second (and, if necessary, the third, fourth, etc.) processor core for simplifying software development. Here, a significant factor is the need to reduce response time to events generated by peripheral controllers.

Two significant tasks may arise in the development of control processors:

- providing an efficient topological implementation;
- tool support by software development tools.

The design route of an FPGA-based digital device can be divided into principal stages of synthesis and topological implementation. At the synthesis stage, the main part of circuit design is performed to convert the design source code into a hardware-independent netlist. The predicted clock rate may be significantly reduced by the subsequent placing of components and tracing of configurable connections. Achieving a high clock rate usually involves additional efforts by developers to clarify the mutual arrangement of the processor subsystems and even its individual digital nodes. Therefore, newly developed processors, even with implementing additional features, are initially disadvantaged compared to widespread processor cores optimized at the FPGA topology level.

The second significant factor hindering the active spread of using new soft processors optimized for the combined action with hardware accelerators is the requirement for tool support. Since additional instructions entered into the processor are not automatically supported by universal compilers, the basic soft processor model can additionally be defined by focusing on common retargetable compilers, such as GNU compiler collection (GCC) and low-level virtual machine (LLVM). This may drastically reduce the value

[1] Virtex-4 FPGA. User Guide. UG070 (v2.6). December 1, 2008. URL: https://www.xilinx.com/support/documentation/user_guides/ug070.pdf. Accessed December 27, 2021.

[2] Versal ACAP Technical Reference Manual. AM011 (v1.3). October 27, 2021. URL: https://www.xilinx.com/support/documentation/architecture-manuals/am011-versal-acap-trm.pdf. Accessed December 27, 2021.

[3] Cyclone® V FPGA и SoC FPGA. URL: https://www.intel.ru/content/www/ru/ru/products/details/fpga/cyclone/v.html. Accessed December 27, 2021.

[4] Xilinx Adaptive SoCs. URL: https://www.xilinx.com/products/silicon-devices/soc.html. Accessed December 27, 2021.

[5] Versal Architecture and Product Data Sheet: Overview DS950 (v1.0). October 2, 2018. Advance Product Specification. URL: https://www.xilinx.com/support/documentation/data_sheets/ds950-versal-overview.pdf. Accessed December 27, 2021.

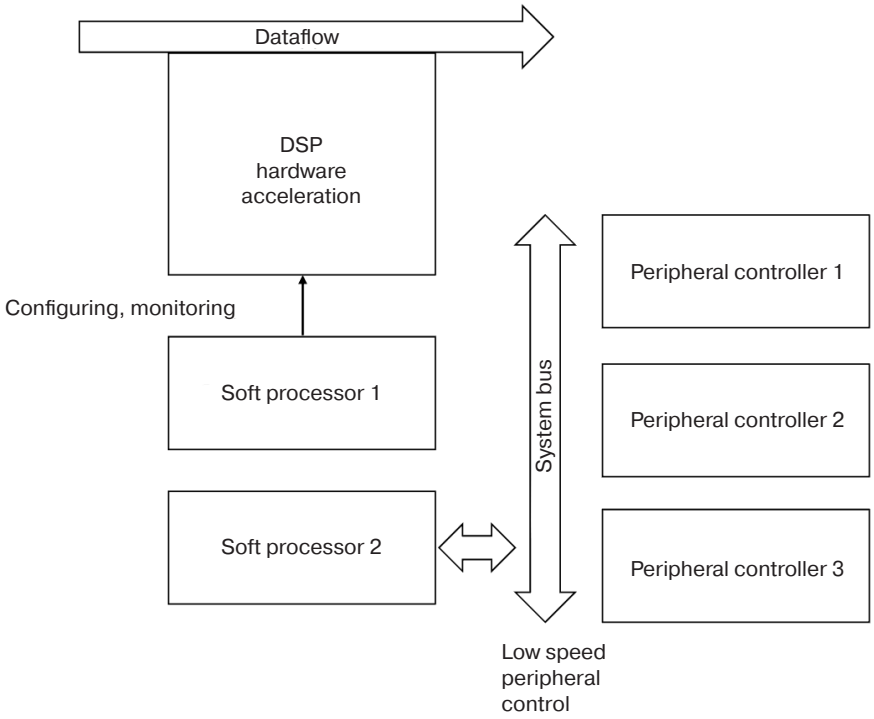

Fig. 1. Interaction between processor and hardware acceleration subsystem in SoC class device

of hardware modifications by allowing the efficient use of low-level programming.

SOFT PROCESSOR ARCHITECTURES

The reconfigurable nature of the programmable cell array defines a sufficient range of possibilities for implementing soft processors. On the other hand, using FPGA for processor layout intended for subsequent implementation in very large-scale integration (VLSI) should be distinguished from developing SoC components intended primarily for control, monitoring, and interface support functions. In this case, the soft processor added to the system should not overload it in terms of occupying logical resources or unnecessarily reduce the clock rate of the design due to excessive trace complexity.

The selection of soft processor architecture is strongly dependent on the hardware architecture. For example, ARM[6], MIPS[7], and RISC-V[8] solutions are currently widely used. Nevertheless, implementing processors based on FPGA configurable logic cells is only trivially less efficient as compared with a hardware solution. At the same time, the widespread MicroBlaze soft processor has been strongly influenced by the PowerPC and then ARM hardware core architecture. Here, a significant advantage of a soft processor has been software compatibility with corresponding hardware solutions present in the market. Therefore, for early FPGA families with PowerPC hardware cores, MicroBlaze cores were considered as a lower performance alternative suitable for low-cost FPGAs allowing the transfer of partially methodological developments and program code for PowerPC.

Thus, the implementation of widespread processor architectures based on logic cells aims at preserving methodological and tool support, but does not fully meet the requirements for the adaptation of the soft processor to the system architecture of the design. A possible solution to this problem may be the implementation of architecture features better adapted to FPGA, as well as to those designed for specific tasks.

It may be noted that the machine code density is the significant parameter for soft processors. This is due to the relatively low specific capacity of the FPGA on-chip static memory. In addition, since static memory blocks may be also used by hardware accelerators, memory saved for storing programs may be significant when selecting the processor architecture.

The general approach to instruction coding distinguishes between the two fundamental trends of strong and weak coding [9]. In strong coding, the binary representation of the instruction and its action is not accessible requiring transformation of machine code. In weak coding, conversely, some binary representation fields are directly responsible for particular processor devices encoding the operation, operands, and additional features.

[6] URL: https://www.arm.com/products/silicon-ip-cpu. Accessed December 27, 2021.

[7] URL: https://www.mips.com/products/architectures. Accessed December 27, 2021.

[8] URL: https://riscv.org/risc-v-foundation/16. Accessed December 27, 2021.

The generalized instruction format may be represented as follows:

<Dest> = <Operand1> op <Operand2>

where Dest is the destination device (register) for placing the operation result; Operand1 is the first operand; op is the type of operation; and Operand2 is the second operand.

For the instruction set, the notion of addressness reflecting the number of registers described in the instruction code is used. The representation of instructions having different addressness is shown in Fig. 2.

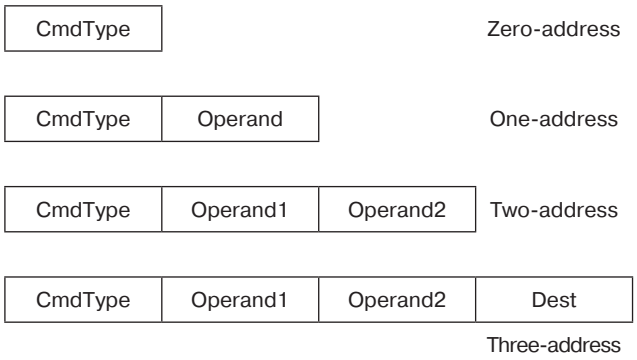

Fig. 2. Representation of instructions with different addressness

Figure 2 shows that, although an overall increase in the addressness results in increased tool software capabilities, the control word length is also increased. Therefore, the memory size required for storing the program also increases. The absence of a reference to a particular type of resource follows implicitly from the type of operation being performed or coincides with specified resources. For example, in the x86 processor instruction set, the destination register coincides with the first operand, while, in accumulator architectures, the accumulator is always the destination register and the first operand. In stack architectures, the operands are always positioned at the top of the data stack along with the result.

The instruction set architecture may be supplemented with hardware microarchitecture defining the interaction of the main circuitry components forming the processor core. While the instruction set architecture and microarchitecture are generally designed independently, the list of permitted operations is largely determined by the presence of hardware components and communication between them. Basic versions of the processor microarchitecture limited to the 5-cycle architecture are depicted in Fig. 3.

As well as supporting a number of instruction formats, raising the number of pipeline stages allows the clock rate to be increased. For example, only one data memory operation (read or write) may be performed in 3-cycle architecture. Here, the synchronous data memory interface conditions the outcome of the read instruction to be available at the "execution" stage only, while one additional cycle would be required for writing the read data to the destination register. However, 5-cycle architecture is free from this limitation.

While soft processors do not permit a further increase in the number of the pipeline clock cycles, the introduction of pipelining in an arithmetic logic unit (ALU) may reduce

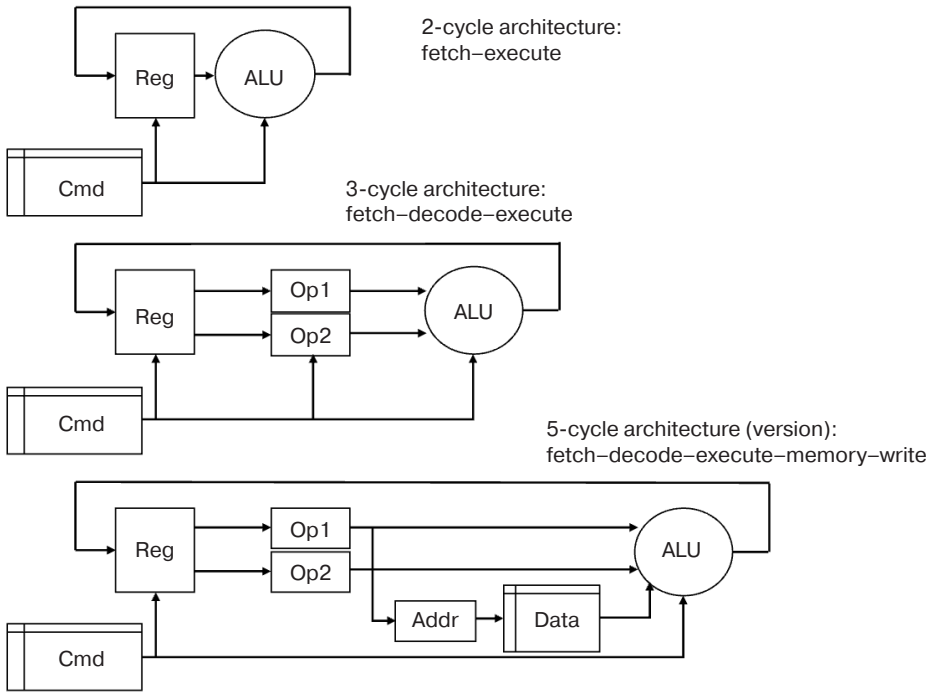

Fig. 3. Basic versions of the processor microarchitecture. ALU is the arithmetic logic unit

the critical path length in this module. Nevertheless, this approach may be less efficient for FPGAs where computational implementation is based on logic cells due to the larger granularity of cells compared with some of VLSI gates.

Considering the reconfigurable nature of FPGAs and the possibility of creating an instruction set optimized for a subclass of tasks, attention should be drawn to the possibilities of describing ALU. For example, in [10], a unified description of a computational node through four parameters (I, O, D, and S) is considered, where I is the number of instructions executed per clock cycle, O is the number of operations defined by instruction, D is the number of operands (pairs of operands) related to operations, and S is the degree of pipelining.

For SIMD (single instruction, multiple data) architectures, $D > 1$; for MIMD (multiple instruction, multiple data) architectures, $I > 1$, $D > 1$. Datapaths at the level of a separate computational node may be additionally considered for mass parallelism, thus allowing the architecture to be described according to the node in the form of four (R, $<O>$, $<D>$, and $<S>$), where: R is the number of independently calculated results, $<O>$ is the vector of the number of operations performed by the instruction for each of the data paths, $<D>$ is the vector of the number of operands (pairs of operands) for each of the datapaths, and $<S>$ is the vector of pipelining for each of the datapaths.

This approach implies the replacement of parameters O, D, and S by vectors describing the characteristics of the corresponding datapaths forming R outputs.

The examples of ALU implementation are shown in Fig. 4. This description does not consider possible variations in the composition of computational nodes shown as ALU1, ALU2, and ALU3, although their functionality may differ both within a single path and for separate paths.

The datapath design route may be as follows:

1) selecting an architecture model in space (R, $<O>$, $<D>$, and $<S>$);
2) compiling pseudocode by the set of model tasks, identifying the most frequent sequences of operations along with creating computational nodes for their single-cycle execution, checking the result using emulator, and creating the processor element nodes at the register transfer level description;
3) checking the synthesizability of the obtained scheme and performing functional verification at the system level;
4) evaluating the topological implementation in the selected technological basis.

USE OF STACKED PROCESSORS IN FPGA-BASED DESIGNS

When providing tools for designing systems for new processor architectures, an important component consists in the design of compilers [11, 12]. Although so-called regular grammar imposes significant limitations on the input language, its low implementation complexity is of interest. A regular grammar may be conveniently supported by a stack-oriented computational model.

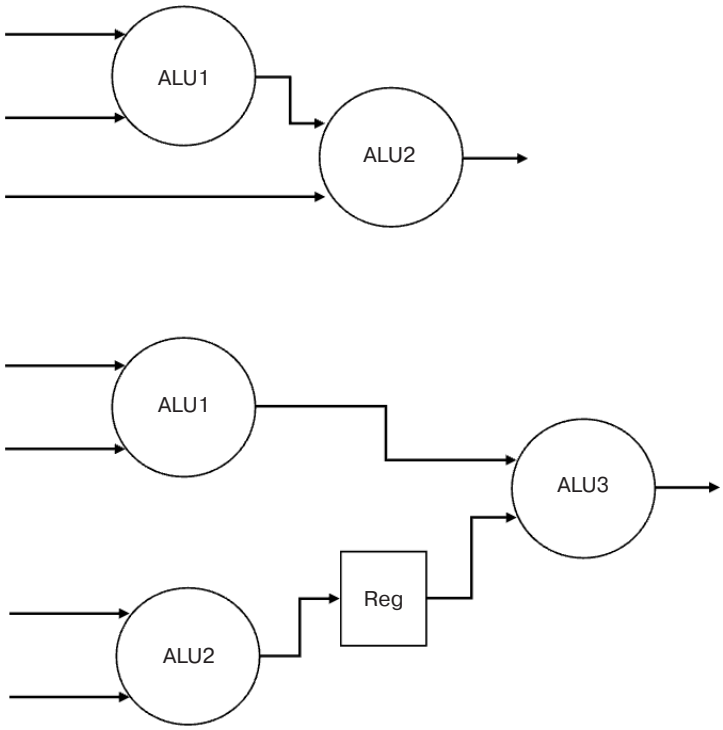

Fig. 4. Examples of the ALU architecture implementation based on unified representation

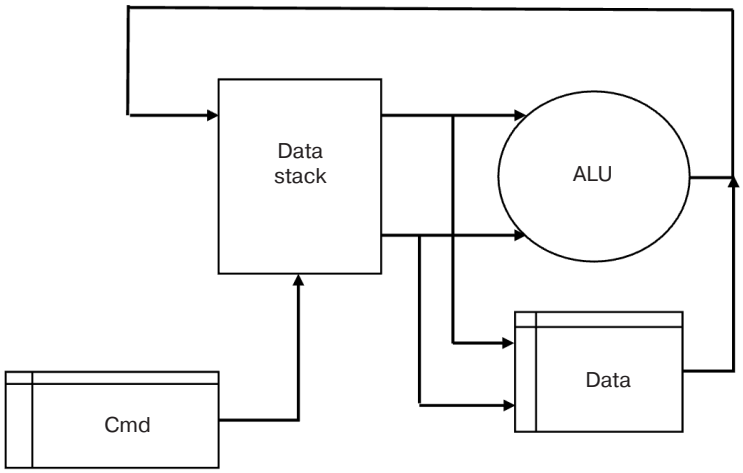

Fig. 5. Stacked processor microarchitecture

The stacked processor is an example of a zero-address architecture allowing the reduction of instruction size. This feature may be useful for FPGA-based systems in which on-chip static memory size is limited. Such a stacked processor microarchitecture is shown in Fig. 5.

Formalized approaches to program code generation for the stack-oriented computing model include those originally developed during the 1970s in the Forth programming language [13] and implemented, e.g., in the Java Virtual Machine, the intermediate code representation of .NET technology, and others. Although the Forth programming language itself is no longer widely used, the stack-oriented computing principles it embodies allow this approach to be used for low-level programming of stacked processor cores for efficient use as auxiliary processors in SoCs due to their compact code requirement and relatively low hardware costs. When combined with regular grammar, such a stack-oriented computing model supports rapid prototyping of tool software. This may be relevant for enabling the ALU rapid reconfiguration and the instruction set modification.

The external appearance of the developed 16-channel spectrum analyzer based on FPGA with multiprocessor control subsystem based on stacked processor cores is shown in Fig. 6.

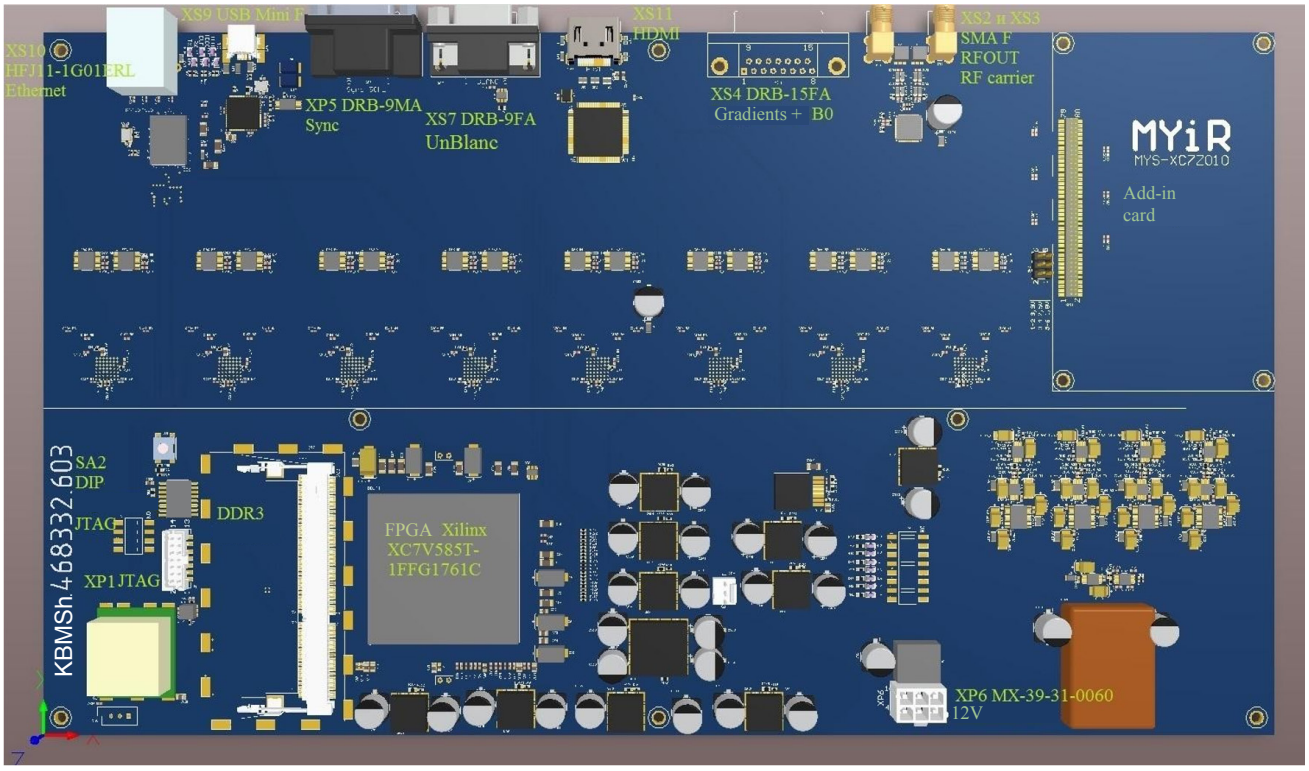

Fig. 6. External appearance of the developed 16-channel spectrum analyzer based on FPGA with multiprocessor control subsystem

Along with their positive impact on the system performance, the characteristics of stacked processor cores have been noted in the process of spectrum analyzer development and pilot operation. In particular, the selection of processor cores for auxiliary and communication tasks has allowed the complex programming requirement to be significantly simplified by focusing auxiliary cores on main computational processes without allocating resources of the main computational node for processing rarely occurring events. Combined with the large size used by FPGA (more than 500 000 logic cells), this confirms the feasibility of extensive use of soft processors for computational load distribution in complex computer systems.

CONCLUSIONS

In the paper, described approaches to the use of soft processors are aimed at accelerating the design of FPGA-based systems having medium and high logical capacity. The design methods allow the selection of microarchitecture versions and approaches to designing the processor instruction set intended mainly for supporting main hardware auxiliaries and performing auxiliary tasks as a part of an SoC. The use of stacked soft processors to reduce program memory size is relevant for solving auxiliary tasks associated with a deficit of on-chip FPGA memory.

Authors' contributions. All authors equally contributed to the research work.

REFERENCES

1. Hennessy J.L., Patterson D.A. A new golden age for computer architecture: Domain-specific hardware/software co-design, enhanced security, open instruction sets, and agile chip development. In: *Proceedings of the 2018 ACM/IEEE 45th Annual International Symposium on Computer Architecture* (*ISCA*). Los Angeles, CA, USA, June 1–6, 2018. https://doi.org/10.1109/ISCA.2018.00011
2. Tarasov I.E. *PLIS Xilinx. Yazyki opisaniya apparatury VHDL i Verilog, SAPR, priemy proektirovaniya* (*FPGA Xilinx. Hardware description languages VHDL and Verilog, CAD, design techniques*). Moscow: Goryachaya liniya – Telekom; 2020. 538 p. (in Russ.). ISBN: 978-5-9912-0802-4
3. Sesin I.Yu., Bolbakov R.G. Comparative analysis of software optimization methods in context of branch predication on GPUs. *Russ. Technol. J.* 2021;9(6):7–15 (in Russ.). https://doi.org/10.32362/2500-316X-2021-9-6-7-15
4. Sleptsov V.V., Afonin V.L., Ablaeva A.E., Dinh B. Development of an information measuring and control system for a quadrocopter. *Russ. Technol. J.* 2021;9(6):26–36 (in Russ.). https://doi.org/10.32362/2500-316X-2021-9-6-26-36
5. Smirnov A.V. Optimization of digital filters performances simultaneously in frequency and time domains. *Russ. Technol. J.* 2020;8(6):63–77 (in Russ.). https://doi.org/10.32362/2500-316X-2020-8-6-63-77
6. Umnyashkin S.V. *Osnovy teorii tsifrovoi obrabotki signalov* (*Fundamentals of the theory of digital signal processing*). Moscow: Tekhnosfera; 2017. 528 p. (in Russ.). ISBN 978-5-94836-424-7
7. Abadi M., et al. TensorFlow: A system for large-scale machine learning. In: *Proceedings of the 12th USENIX Symposium on Operating Systems Design and Implementation* (*OSDI'16*). 2016. P. 265–283. Available from URL: https://www.usenix.org/system/files/conference/osdi16/osdi16-abadi.pdf
8. Nurvitadhi E., et al. Accelerating Binarized Neural Networks: Comparison of FPGA, CPU, GPU, and ASIC. In: *2016 International Conference on Field-Programmable Technology*. 2016. P. 77–84. https://doi.org/10.1109/fpt.2016.7929192

СПИСОК ЛИТЕРАТУРЫ

1. Hennessy J.L., Patterson D.A. A new golden age for computer architecture: Domain-specific hardware/software co-design, enhanced security, open instruction sets, and agile chip development. In: *Proceedings of the 2018 ACM/IEEE 45th Annual International Symposium on Computer Architecture* (*ISCA*). Los Angeles, CA, USA, June 1–6, 2018. https://doi.org/10.1109/ISCA.2018.00011
2. Тарасов И.Е. *ПЛИС Xilinx. Языки описания аппаратуры VHDL и Verilog, САПР, приемы проектирования*. М.: Горячая линия – Телеком; 2022. 538 с. ISBN 978-5-9912-0802-4
3. Сесин И.Ю., Болбаков Р.Г. Сравнительный анализ методов оптимизации программного обеспечения для борьбы с предикацией ветвлений на графических процессорах. *Russ. Technol. J.* 2021;9(6):7–15. https://doi.org/10.32362/2500-316X-2021-9-6-7-15
4. Слепцов В.В., Афонин В.Л., Аблаева А.Е., Динь Б. Разработка информационно-измерительной и управляющей системы квадрокоптера. *Russ. Technol. J.* 2021;9(6):26–36. https://doi.org/10.32362/2500-316X-2021-9-6-26-36
5. Смирнов А.В. Оптимизация характеристик цифровых фильтров одновременно в частотной и временной областях. *Russ. Technol. J.* 2020;8(6):63–77. https://doi.org/10.32362/2500-316X-2020-8-6-63-77
6. Умняшкин С.В. *Основы теории цифровой обработки сигналов*. М.: Техносфера; 2017. 528 с. ISBN 978-5-94836-424-7
7. Abadi M., et al. TensorFlow: A system for large-scale machine learning. In: *Proceedings of the 12th USENIX Symposium on Operating Systems Design and Implementation* (*OSDI'16*). 2016. P. 265–283. URL: https://www.usenix.org/system/files/conference/osdi16/osdi16-abadi.pdf
8. Nurvitadhi E., et al. Accelerating Binarized Neural Networks: Comparison of FPGA, CPU, GPU, and ASIC. In: *2016 International Conference on Field-Programmable Technology*. 2016. P. 77–84. https://doi.org/10.1109/fpt.2016.7929192

9. Korneev V., Kiselev A. *Sovremennye mikroprotsessory* (*Modern microprocessors*). St. Petersburg: BHV-Petersburg; 2003. 448 p. (in Russ.).
10. Sima D., Fountain T., Kacsuk P. *Advanced Computer Architectures: A Design Space Approach*. Addison-Wesley; 1997. 790 p.
11. Akho A.V., Lam M.S., Seti R., Ul'man D.D. *Kompilyatory: printsipy, tekhnologii i instrumentarii* (*Compilers: Principles, Techniques, and Tools*). Transl. from Engl. Moscow: Vil'yams; 2017. 1184 p. (in Russ.). ISBN 978-5-8459-1932-8.
12. Pratt T., Zelkovits M. *Yazyki programmirovaniya: razrabotka i realizatsiya* (*Programming Languages: Design and Implementation*). Matrosov A. (Ed.). St. Petersburg: Piter; 2002. 688 p. (in Russ.). ISBN 5-318-00189-0
13. Baranov S.N., Nozdrunov N.R. *Yazyk Fort i ego realizatsii* (*The Forth Language and its Implementations*). Leningrad: Mashinostroenie; 1988. 157 p. (in Russ.). ISBN 5-217-00324-3
14. Sovetov P.N. Synthesis of linear programs for a stack machine. *Vysokoproizvoditel'nye vychislitel'nye sistemy i tekhnologii = High-performance computing systems and technologies*. 2019;3(1):17–22 (in Russ.).
15. Tarasov I.E., Potekhin D.S., Khrenov M.A., Sovetov P.N. Computer-aided design of multicore system for embedded applications. *Ekonomika i menedzhment sistem upravleniya*. 2017;25(3–1):179–185 (in Russ.).

9. Корнеев В., Киселев А. *Современные микропроцессоры*. СПб.: БХВ-Петербург; 2003. 448 с.
10. Sima D., Fountain T., Kacsuk P. *Advanced Computer Architectures: A Design Space Approach*. Addison-Wesley; 1997. 790 p.
11. Ахо А.В., Лам М.С., Сети Р., Ульман Д.Д. *Компиляторы: принципы, технологии и инструментарий*: пер. с англ. М.: «И.Д. Вильямс»; 2017. 1184 с. ISBN 978-5-8459-1932-8.
12. Пратт Т., Зелковиц М. *Языки программирования: разработка и реализация*: под ред. А. Матросова. СПб.: Питер; 2002. 688 с. ISBN 5-318-00189-0
13. Баранов С.Н., Ноздрунов Н.Р. *Язык Форт и его реализации*. Л.: Машиностроение; 1988. 157 с. ISBN 5-217-00324-3
14. Советов П.Н. Синтез линейных программ для стековой машины. *Высокопроизводительные вычислительные системы и технологии*. 2019;3(1):17–22.
15. Тарасов И.Е., Потехин Д.С., Хренов М.А., Советов П.Н. Автоматизация проектирования многопроцессорной системы на базе ПЛИС для управления во встраиваемых приложениях. *Экономика и менеджмент систем управления*. 2017;25(3–1):179–185.

About the authors

Ilya E. Tarasov, Dr. Sci. (Eng.), Associated Professor, Professor, Department of Corporate Information Systems, Institute of Information Technologies, MIREA – Russian Technological University (78, Vernadskogo pr., Moscow, 119454 Russia). E-mail: tarasov_i@mirea.ru. Scopus Author ID 57213354150, http://orcid.org/0000-0001-6456-4794

Dmitry S. Potekhin, Dr. Sci. (Eng.), Associated Professor, Professor, Computer Technology Department, Institute of Information Technologies, MIREA – Russian Technological University (78, Vernadskogo pr., Moscow, 119454 Russia). E-mail: potehin@mirea.ru. Scopus Author ID 57213839310.

Olga V. Platonova, Cand. Sci. (Eng.), Associated Professor, Head of the Computer Technology Department, Institute of Information Technologies, MIREA – Russian Technological University (78, Vernadskogo pr., Moscow, 119454 Russia). E-mail: platonova@mirea.ru. Scopus Author ID 57222119478.

Об авторах

Тарасов Илья Евгеньевич, д.т.н., доцент, профессор кафедры корпоративных информационных систем Института информационных технологий ФГБОУ ВО «МИРЭА – Российский технологический университет» (119454, Россия, Москва, пр-т Вернадского, д. 78). E-mail: tarasov_i@mirea.ru. Scopus Author ID 57213354150, http://orcid.org/0000-0001-6456-4794

Потехин Дмитрий Станиславович, д.т.н., доцент, профессор кафедры вычислительной техники Института информационных технологий ФГБОУ ВО «МИРЭА – Российский технологический университет» (119454, Россия, Москва, пр-т Вернадского, д. 78). E-mail: potehin@mirea.ru. Scopus Author ID 57213839310.

Платонова Ольга Владимировна, к.т.н., доцент, заведующий кафедрой вычислительной техники Института информационных технологий ФГБОУ ВО «МИРЭА – Российский технологический университет» (119454, Россия, Москва, пр-т Вернадского, д. 78). E-mail: platonova@mirea.ru. Scopus Author ID 57222119478.

Translated by K. Nazarov
Edited for English language and spelling by Thomas Beavitt

Modern radio engineering and telecommunication systems

Современные радиотехнические и телекоммуникационные системы

UDC 681.2.0821.083:535.2:543.063
https://doi.org/10.32362/2500-316X-2022-10-3-34-44

RESEARCH ARTICLE

Solution of topical spectroradiometric problems using synchrotron radiation

Alexander S. Sigov,
Nataliya B. Golovanova,
Olga A. Minaeva [@],
Sergei I. Anevsky,
Roman V. Shamin,
Olga I. Ostanina

MIREA – Russian Technological University, Moscow, 119454 Russia
[@] Corresponding author, e-mail: minaeva_o@mirea.ru

Abstract

Objectives. In order to solve fundamental metrological problems concerning the reproduction and transmission of spectral radiometry units, as well as developing methods and tools for metrological support of modern technologies such as nanophotolithography in the electronics industry, synchrotron radiation can be used. When developing solid-state sources and receivers of radiation, new topical problems arise in connection with the metrological characteristics of light-emitting diodes (LEDs), multi-element array receivers, charge-coupled device (CCD) cameras and telescopes, whose successful solution depends on the properties of a reference source of synchrotron radiation. Therefore, the purpose of the present work is to develop spectral radiometry methods for obtaining metrological channels using an electron storage ring in order to control the characteristics of electronics components, as well as for studying and calibrating radiometers, photometers, and emitters operating in the visible, ultraviolet and infrared regions of the electromagnetic spectrum.

Methods. Methods for transmitting spectroradiometric units on an electron storage ring are based on the classical theory of Julian Schwinger, which describes the electromagnetic radiation of a relativistic electron to calculate the spectral and energetic synchrotron radiation characteristics taking polarization components into account.

Results. The possibility of developing methods for transmitting spectral radiometric units using synchrotron radiation was evaluated by means of a test setup, which included a monochromator-based comparator, a telescope with a CCD array, a spectroradiometer, a radiometer, a photometer, a goniometer, and an integrating sphere. This allowed the full set of spectroradiometric and photometric characteristics of radiation sources and receivers to be measured: from the most differential distribution of the spectral radiance density of the emitting region to the integral radiation flux. The results were compared with the reference synchrotron radiation source.

Conclusions. Among possible approaches for determining the metrological characteristics of LED emitters, multi-element array receivers, CCD cameras, and telescopes, synchrotron radiation seems to be the most promising. This approach allows the small size of the emitting region of synchrotron radiation, the Gaussian distribution of radiance over the emitting region of the synchrotron electron bunch, as well as the wide dynamic range of spectrum tuning due to changes in the energy and number of accelerated electrons, to be taken into account.

Keywords: spectral radiometry, synchrotron radiation, radiance, radiation intensity, LED, photometer, radiometer

• **Submitted:** 15.02.2022 • **Revised:** 28.02.2022 • **Accepted:** 18.04.2022

For citation: Sigov A.S., Golovanova N.B., Minaeva O.A., Anevsky S.I., Shamin R.V., Ostanina O.I. Solution of topical spectroradiometric problems using synchrotron radiation. *Russ. Technol. J.* 2022;10(3):34–44. https://doi.org/10.32362/2500-316X-2022-10-3-34-44

Financial disclosure: The authors have no a financial or property interest in any material or method mentioned.

The authors declare no conflicts of interest.

НАУЧНАЯ СТАТЬЯ

Решение актуальных задач спектрорадиометрии с использованием синхротронного излучения

А.С. Сигов,
Н.Б. Голованова,
О.А. Минаева [@],
С.И. Аневский,
Р.В. Шамин,
О.И. Останина

МИРЭА – Российский технологический университет, Москва, 119454 Россия
[@] Автор для переписки, e-mail: minaeva_o@mirea.ru

Резюме

Цели. Использование синхротронного излучения позволяет решать фундаментальные метрологические задачи воспроизведения и передачи единиц спектрорадиометрии, разрабатывать методы и средства метрологического обеспечения современных технологий, таких как нанофотолитография в электронной промышленности. Развитие твердотельных источников и приемников излучения формирует новые актуальные задачи исследования метрологических характеристик светодиодов, многоэлементных матричных приемников, ПЗС-камер и телескопов, успешное решение которых зависит от использования свойств эталонного источника синхротронного излучения. Целью работы является развитие методов спектрорадиометрии для метрологических каналов электронного накопительного кольца при контроле характеристик компонентов в электронной промышленности, при исследованиях и калибровках радиометров, фотометров, излучателей в видимой, ультрафиолетовой и инфракрасной областях спектра.

Методы. Методы передачи единиц спектрорадиометрии на электронном накопительном кольце основаны на использовании классической теории Ю. Швингера, описывающей электромагнитное излучение релятивистского электрона, для расчета спектральных энергетических характеристик синхротронного излучения с учетом поляризационных компонентов.

Результаты. Рассмотрены возможности развития методов передачи единиц спектрорадиометрии с использованием синхротронного излучения и создания испытательной установки. Эта установка включает в себя компаратор на основе монохроматора, телескопа с ПЗС-матрицей, спектрорадиометра, радиометра, фотометра, гониометра и интегрирующей сферы, позволяющих проводить измерения полного набора спектрорадиометрических и фотометрических характеристик источников и приемников излучения – от наиболее дифференциального распределения спектральной плотности энергетической яркости по излучающей области до интегрального потока излучения с прослеживаемостью к эталонному источнику синхротронного излучения.

Выводы. Определение метрологических характеристик светодиодных излучателей, многоэлементных матричных приемников, ПЗС-камер и телескопов с использованием синхротронного излучения представляется наиболее перспективным направлением с учетом малых размеров излучающей области синхротронного излучения, Гауссова распределения энергетической яркости по излучающей области электронного сгустка синхротрона, широкого динамического диапазона перестройки спектра за счет изменения энергии и числа ускоренных электронов.

Ключевые слова: спектрорадиометрия, синхротронное излучение, энергетическая яркость, сила излучения, светодиод, фотометр, радиометр

• **Поступила:** 15.02.2022 • **Доработана:** 28.02.2022 • **Принята к опубликованию:** 18.04.2022

Для цитирования: Сигов А.С., Голованова Н.Б., Минаева О.А., Аневский С.И., Шамин Р.В., Останина О.И. Решение актуальных задач спектрорадиометрии с использованием синхротронного излучения. *Russ. Technol. J.* 2022;10(3):34–44. https://doi.org/10.32362/2500-316X-2022-10-3-34-44

Прозрачность финансовой деятельности: Авторы не имеют финансовой заинтересованности в представленных материалах или методах.

Авторы заявляют об отсутствии конфликта интересов.

INTRODUCTION

The unique synchrotron radiation properties of accelerated relativistic electrons in cyclic accelerators opened up significant opportunities for metrology, allowing electron storage rings (ESRs) to be used as primary reference sources of electromagnetic radiation. This results in a clean, plasma-free, continuous spectrum, which is free of spectral lines and easily tunable by changing the energy and number of electrons in orbit [1].

Synchrotron radiation is widely used in fundamental metrological research and developing metrological support for modern nanophotolithography technologies used in the electronics industry [2]. The Decree of the President of the Russian Federation[1] and the Decree of the Government of the Russian Federation[2] pay great attention to the development of optical radiation spectroradiometry using synchrotron radiation.

The first work on spectroradiometry carried out at the DESY[3] synchrotron in Hamburg was aimed at measuring the spectral density of energy brightness of ultraviolet (UV) radiation using the relative spectral distribution of synchrotron radiation with absolute referencing in the visible region to the standard black body model. By this means, the spectral range of the deuterium continuum could be calibrated up to the vacuum ultraviolet (VUV) limit—that is, up to photon energies of 6 eV, which is not possible using the black body model. Electron storage rings and synchrotrons are used in Russia, Germany, and the USA to expand the range of absolute spectral measurements to the VUV region, first to the Schumann region up to 10 eV, and then to the Lyman region to 30 eV. With the development of extreme VUV for nanoelectronics based on contemporary advances in nanophotolithography, synchrotron radiation metrology can be used to determine the dimensions of microcircuit elements down to several nanometers at photon energies of about 100 eV [3, 4]. With the creation of the Metrological Light Source (MLS) storage ring at the National Metrological Institute RTV (Berlin), spectroradiometric work began on the use of synchrotron radiation to access the terahertz range for photon energies ranging from 10^{-2} to 10^{-3} eV [5]. Meanwhile, the Siberia-1 and Siberia-2 ESRs hosted at the Kurchatov Institute in Russia are also engaged in developing spectroradiometric methods using synchrotron radiation. Thus, synchrotron radiation has been instrumental in providing absolute spectral measurements at the world's leading national metrological centers across a wide range of wavelengths from radio frequencies to X-rays.

In national metrological centers, fundamental and applied metrological research is not only carried out using synchrotron radiation in the extreme VUV and terahertz ranges, but also in the visible and near infrared (IR) regions of the spectrum, where the successful solution of certain challenging metrological problems involved in the study of the metrological characteristics of LEDs, multi-element array receivers, as well as

[1] Decree of the President of the Russian Federation of July 25, 2019 No. 356 "On measures to develop synchrotron and neutron research and research infrastructure in the Russian Federation" (in Russ.).

[2] Decree of the Government of the Russian Federation of March 16, 2020 No. 287 "On Approval of the Federal Scientific and Technical Program for the Development of Synchrotron and Neutron Research and Research Infrastructure for 2019–2027" (in Russ.).

[3] Deutsches Elektronen-Synchrotron—German electronic synchrotron (National Research Center DESY, Germany).

CCD[4] cameras and telescopes, depends directly on the properties of a reference source of synchrotron radiation.

METHODOLOGY AND APPARATUS FOR MEASUREMENTS

In accordance with the existing GOST 8.888-2015[5], GOST R 54814-2018[6], and GOST R.8.749-2011[7] standards, the main tasks in the study of the metrological characteristics of LEDs involve measurements of the spectral power density of the radiation and the total radiation flux. Measurements of the metrological characteristics of LEDs are especially important for carrying out technological control in the production of emitters of white cold, neutral, and warm colors for the development of illumination and indication equipment used in land, aviation, and marine transport, as well as lighting products used for office, street and domestic purposes. The study of the electro-optical, luminosity, and thermal characteristics of semiconductor nanoheterostructures of solid-state radiation sources also requires the development of spectroradiometric methods. To determine the radiation characteristics of sources used in units of the spectral power density of radiation (SPDR), spectral comparators are used to integrate the spectral density of energy brightness (SDEB) within the radiating region and at a fixed solid angle [6].

When using synchrotron radiation in spectral radiometry, the main problem involves the need to take into account the complex angular dependence of the intensity of the polarization components [1]. The comparator for calibrating the SPDR of LEDs comprises focusing optics, a spectral device, light filters, and a radiation receiver. The method of transmitting a unit of SPDR on an electron storage ring should take into account two polarization components of synchrotron radiation whose oscillations lie in the electron orbit and perpendicular planes, respectively. The equation describing the comparator signal $i_{SR}(\lambda)$, which is proportional to the SPDR [7, 8] in the polarization components of the synchrotron radiation, is written as follows:

$$i_{SR}(\lambda) = \int_{\Psi_0} I_{SR}^{\parallel}(\psi,\lambda)\tau^{\parallel}(\psi,\lambda)S^{\parallel}(\lambda)\Delta\lambda\Delta\varphi d\psi + \int_{\Psi_0} I_{SR}^{\perp}(\psi,\lambda)\tau^{\perp}(\psi,\lambda)S^{\perp}(\lambda)\Delta\lambda\Delta\varphi d\psi, \quad (1)$$

where Ψ is the angle of deviation from the plane of the electron orbit; Ψ_0 is the aperture angle of deviation from the plane of the electron orbit; λ is the wavelength; $I_{SR}^{\parallel}(\psi,\lambda)$, $I_{SR}^{\perp}(\psi,\lambda)$ are the spectral power densities of synchrotron radiation polarized in the orbit and perpendicular planes, respectively; $\tau^{\parallel}(\psi,\lambda)$ and $\tau^{\perp}(\psi,\lambda)$ are the transmission coefficients of the comparator spectral device for radiation polarized in the orbital plane and perpendicular planes, respectively; $S^{\parallel}(\lambda)$, $S^{\perp}(\lambda)$ are the spectral sensitivities of the comparator detector for radiation polarized in the orbit and perpendicular planes, respectively; $\Delta\lambda$ is the spectral resolution of the comparator; $\Delta\varphi$ is the aperture angle of the comparator in the plane of the electron orbit.

As follows from Equation (1), metrological analysis is complicated when using a monochromator, photomultiplier, or spectral radiometer as part of a comparator, whose efficiency depends on the plane of polarization of the incident radiation. While a photodiode or CCD array can be used to eliminate the complex dependence of the signal on the degree of polarization, for spectral measurements, a normal incidence monochromator or set of interference filters is used [9, 10].

This allows Equation (1) for the comparator signal to be reduced to:

$$i_{SR}(\lambda) = S(\lambda)\Delta\lambda\Delta\varphi\Delta\tau\left[\int_{\Psi_0} I_{SR}^{\parallel}(\psi,\lambda)d\psi + \int_{\Psi_0} I_{SR}^{\perp}(\psi,\lambda)d\psi\right]. \quad (2)$$

For an LED, the equation describing the comparator signal $i_{LED}(\Omega, \lambda)$ in a fixed solid angle Ω, which is proportional to the spectral power density of the unpolarized radiation $I_{LED}(\Omega, \lambda)$ [11], has the form:

$$I_{LED}(\Omega, \lambda) = S(\lambda)\Delta\lambda\Delta\tau\Omega I_{LED}(\Omega, \lambda). \quad (3)$$

In order to take the polarization components into account in the system of equations (1) and (3) on the synchrotron radiation metrological channel of the ESR BESSY-II[8] in Berlin, the monochromator is rotated

[4] CCD is a charge-coupled device.

[5] GOST 8.888-2015. National Standard of the Russian Federation. State system for ensuring the uniformity of measurements. Reference Light-emitting diodes (LED) of noncoherent radiation. Technical requirements. Moscow: Standartinform; 2019 (in Russ.).

[6] GOST R 54814-2018. National Standard of the Russian Federation. Light emitting diodes (LED) and LED modules for general lighting and related equipment. Terms and definitions. Moscow: Standartinform; 2018 (in Russ.).

[7] GOST R 8.749-2011. National Standard of the Russian Federation. State system for ensuring the uniformity of measurements. Light-emitting diodes. Methods of photometric measurements. Moscow: Standartinform; 2019 (in Russ.).

[8] BESSY-II Electron storage ring is a third-generation synchrotron radiation source (Helmholtz-Zentrum Berlin, Germany). URL: https://www.helmholtz-berlin.de/forschung/quellen/bessy/index_en.html. Accessed December 10, 2021.

around the optical axis without violating the alignment. For a comparator with a small aperture angle relative to the plane of the electron orbit, only the polarization sigma-component of the synchrotron radiation is considered, which makes it possible to obtain a relatively simple solution for the spectral density of the radiation intensity of the LED in accordance with the Schwinger formula [12].

$$I_{\mathrm{LED}}(\Omega,\lambda) = 0.0273N(i_{\mathrm{LED}} / i_{\mathrm{SR}})\Delta\varphi(e^2c / \Omega R^3) \times \\ \times (\lambda_c / \lambda)^4 \gamma^8 \int_{\Psi_0} K_{2/3}^2(\lambda_c / 2\lambda)d\psi, \quad (4)$$

where N is the number of electrons in the orbit; γ is the relativistic factor; e is the electron charge; R is the radius of the electron orbit; c is the speed of light; $K_{2/3}$ is MacDonald function; $\lambda_c = (4/3)\pi R\gamma^{-3}$ is the critical wavelength.

For determining the electron energy and the relativistic factor on storage rings, electron bunch backscattered laser radiation allows the magnetic field induction to be measured in orbit alongside methods based on relative spectral measurements of the synchrotron radiation flux. The most accurate method for determining the number of electrons is based on the use of a telescope with a CCD array to isolate an individual electron in the orbit of the accelerator. The radius of the orbit is determined by the frequency of the accelerating field of the electron storage rings. To fulfill the condition $\Omega = \Delta\varphi\Psi_0$, the sizes of aperture diaphragms and the distance to the radiating point of the orbit are determined.

At wavelengths much greater than the critical λ_c (i.e., in the visible-, near UV-, and near IR regions of the spectrum), along with an increase in the aperture angle of the optical system of the comparator in the plane of the electron orbit Ψ_0 for the synchrotron radiation source, the integrated values of the SPDR in the total angle of deviation from the plane of the orbit (normalized to one electron) can only be determined by the radius of the orbit at the point of emission. This means that in the visible-, near UV-, and near IR regions of the spectrum, the accurate calculation of the spectral density integral of the synchrotron radiation intensity across all angles of deviation from the orbital plane is constant for each synchrotron radiation source and does not depend on the electron energy. This conclusion is especially important for metrological studies when creating primary spectroradiometric standards based on fundamental physical constants.

By integrating the SPDR of LEDs over different wavelengths, it is possible to determine the radiant and luminous intensity in a fixed solid angle taking into account the relative spectral luminous efficiency in accordance with GOST 8.332-2013[9]. In accordance with the recommendations of the International Commission on Illumination (CIE 127:2007[10]), the measurement of the radiation intensity in regime A is carried out at a distance of 316 mm in a solid angle of 0.001 sr; in regime B—at a distance of 100 mm in a solid angle of 0.01 sr. To determine the radiation intensity and luminous intensity of LEDs, integrated comparators including radiometers, photometers, or spectroradiometers are used [13]. Here the main difficulties are associated with the need of accurate measurements of the spectral correction coefficients of the comparator sensitivity in accordance with the recommendations of CIE 053-1982[11].

Spectral correction of the sensitivity of the luxmeter in accordance with regulatory documents is only carried out for five types of control emitters. This means that the spectral correction of the sensitivity of the luxmeter is mainly carried out at the maximum sensitivity in the “green” region, as well as on the falling wings in the “blue” and “red” regions of the spectrum. Since the relative spectral sensitivity of the luxmeter can differ from the relative spectral light efficiency by an order of magnitude, significant errors can occur, for example, when assessing the hazardous effects of radiation when using bright blue LEDs [14].

When using an integral radiometer, significant difficulties are encountered due to the practical impossibility of realizing the required top-hat profile in the relative spectral sensitivity of the radiometer. Therefore, the creation of universal integral radiometers and photometers for determining the radiation intensity and luminous intensity of a LED comprises a nontrivial metrological problem [14]. When using ESR, radiometers and photometers are calibrated in accordance with expression (4), while spectral correction coefficients are determined for specific types of emitters and comparators. The use of spectroradiometers calibrated with respect to synchrotron radiation allows the values of the radiation intensity and luminous intensity to be obtained by integrating signals proportional to the SPDR of LEDs. However, here it is necessary to consider the level of scattered radiation, higher diffraction orders, and the impact of the degree of polarization of synchrotron radiation [16].

[9] GOST 8.332-2013. Interstate Standard. State system for ensuring the uniformity of measurements. Light measurements. Values of relative spectral luminous efficiency function of monochromatic radiation for photopic vision. Moscow: Kodeks; 2015 (in Russ.).

[10] CIE 127:2007. Technical report “Measurement of LEDs”. ISBN 978-3-901906-58-9.

[11] CIE 053-1982. Methods of characterizing the performance of radiometers and photometers. ISBN 978-92-9034-053-9.

When determining the total standard uncertainty of measurements of radiation intensity and luminous intensity, it is also necessary to consider the linearity range of sensitivity and noise, as well as the sensitivity threshold of the spectroradiometer's detectors.

The main difficulties encountered in measuring the characteristics of solid-state emitters are associated with the complex angular dependence of the SPDR and the high energy brightness of solid-state LED emitters [17]. When measuring the angular distribution of the radiation intensity of LEDs in metrological laboratories, goniometers are used to obtain the value of the radiation flux and luminous flux. Goniometer detectors include radiometers, photometers, spectroradiometers, and CCD arrays calibrated against a synchrotron radiation source.

When measuring the total flux, the detector is mounted on the movable arm of the goniometer and adjusted in horizontal and vertical planes to obtain the maximum signal. With step-by-step fixation of signals, the angular distribution of radiation intensity is determined. To improve the accuracy of measurements, the minimum step of the angle of rotation relative to the geometric axis of the LED is used. Depending on the angle of deviation from the geometric axis of the emitter and when the emitter is rotated around the geometric axis, the signals of the radiometer or photometer are normalized to the maximum signal of the angular distribution and measured in a solid angle fixed during calibration at the synchrotron radiation source.

By integrating the angular dependence of the normalized goniometer signals, it is possible to calculate the total radiation flux or luminous flux of the LED. However, this requires the processing of a large amount of information on measurements involving angle gradations of several thousand points, as well as involving significant measurement time due to the need to stabilize the LED power regime and maintain the thermal regime. Measurement of the total radiation flux using a goniometer is characterized by a significant systematic error due to the absolute calibration of the reference radiometer or photometer while taking into account the spectral sensitivity correction, setting the angle of rotation of the goniometer arm, measuring the distance from the detector to the center of rotation, angular resolution and angular step, noise of the radiometer or photometer, high scanning speed at the corners of the scattered radiation, and instability of the radiation source [18].

The use of highly sensitive multi-element detectors allows the measurement time to be reduced while maintaining the requirements of spectral sensitivity correction. A 3D computer diagram illustrating the results of measurements of the angular dependence of the LED radiation intensity is shown in Fig. 1.

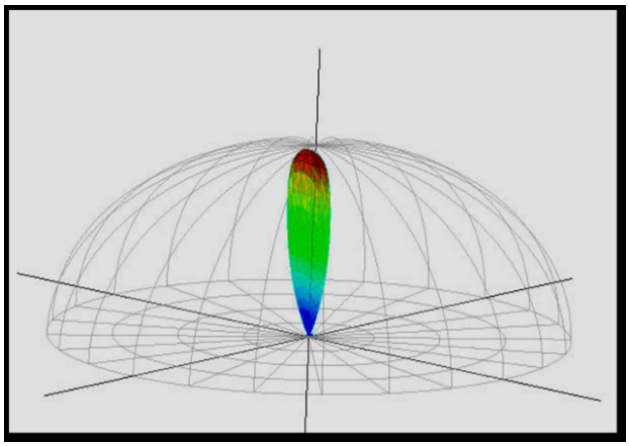

Fig. 1. 3D computer diagram depicting the results of measuring the angular dependence of the LED radiation intensity

The above example shows that the maximum of the radiation intensity angular distribution can be shifted relative to the axis of the LED, while the radiation flux is concentrated in a small solid angle. The resulting angular distribution allows the radiation intensity and flux to be determined in an arbitrary solid angle.

The corresponding 2D diagram is presented in Fig. 2. Here, the red line represents the half-width of the angular distribution of the LED radiation with a shift relative to the geometric axis.

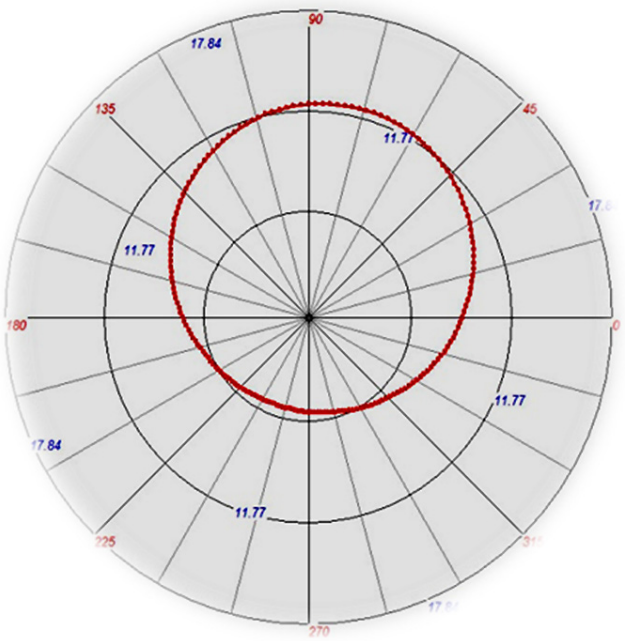

Fig. 2. 2D diagram of the half-width of the angular distribution of the LED radiation

In order to measure the luminous flux of high-power LEDs used for illumination, it is necessary to investigate the angular distribution of the radiation

intensity according to the regime in which LEDs are used in working modules. A controllable heat sink is used to ensure the desired temperature when measuring the characteristics of high-power LEDs.

In spectroradiometry, it is particularly important to accurately measure the most differential characteristics of radiation, involving the spatial distribution of brightness and radiance of LEDs over the emitting region. The radiance comparator includes an optical system, a set of corrective filters and a cooled CCD matrix.

The calibration of the relative sensitivity of the pixels of the CCD array and measurement of the distribution of the radiance of various emitters is possible due to the Gaussian distribution of the radiance over the emitting region of the ESR electron bunch, which comprises a fundamental property of synchrotron radiation.

Figure 3 shows the results of registration of the Gaussian distribution of energy brightness over the radiating region of the ESR. Fig. 4 depicts the energy brightness across the emitting region of the LED [19].

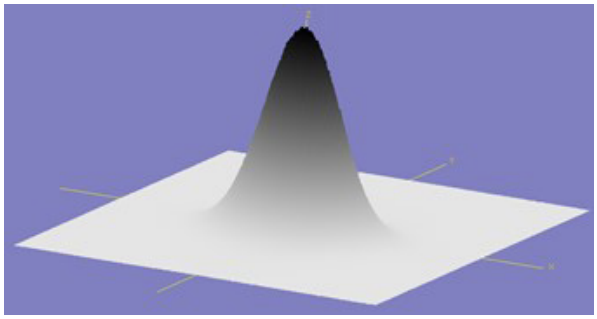

Fig. 3. Registered Gaussian distribution of brightness for emitting region of ESR

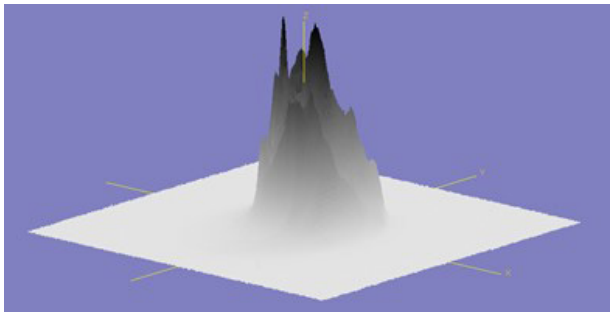

Fig. 4. Registered distribution of brightness for emitting region of the LED

The significant inhomogeneity of the LED's spatial brightness distribution is associated with the distortion of the distribution due to the focusing lens [20]. To eliminate this distortion over the radiating region, secondary reference LEDs featuring a specially shaped surface and temperature control using a Peltier element were developed (Fig. 5).

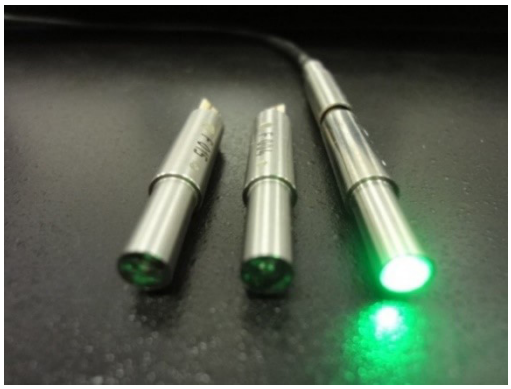

Fig. 5. Specially designed secondary reference LEDs

Figure 6 shows the results of measurements of the brightness distribution over the emitting area of the reference LED.

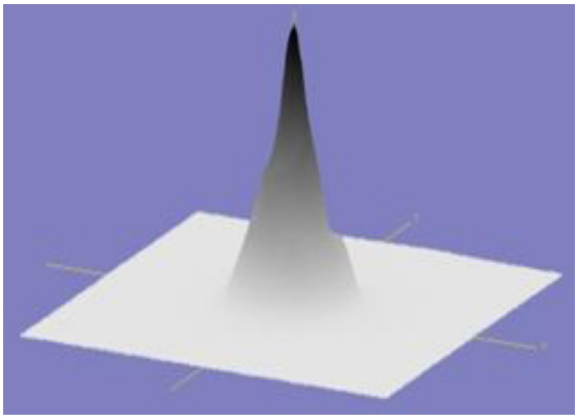

Fig. 6. Brightness distribution over the emitting area of the reference LED

To obtain the sensitivity of the comparator based on a telescope with a CCD array in accordance with the relative light efficiency, a set of corrective filters is used. This allows the spatial brightness distribution and average overall brightness to be measured to determine indicators of glare and visual discomfort of a light environment formed by super bright LED emitters.

The standard method for measuring the total radiation flux of an LED is based on an integrating sphere. This involves a correction of the spatial inhomogeneity of the diffuse reflection coefficient of the sphere surface, as well as the angular and spectral correction of the detector sensitivity [21]. To increase measurement accuracy, large diameter integrating spheres with a high ratio of sphere area to emitter size are used. In this case, the LED should be installed in the center of the integrating sphere in accordance with the CIE recommendations.

The LED calibration scheme and general view of the integrating sphere used are shown in Figs. 7 and 8. The radiation of an external reference source *6* or *7* enters the integrating sphere *1* through the aperture diaphragm

and is detected by the radiation detector *2*. A photodiode or a CCD array with corrective filters, a photometer, a radiometer, or a spectroradiometer are used as the radiation detector *2*. The radiation of the calibrated LED *4* installed in the center of the integrating sphere is prevented from directly hitting the radiation receiver by screens *3*. The receiver *5* is used to detect radiation at the aperture diaphragm of the integrating sphere. External reference sources of radiation *6*, *7* and the receiver *5* are placed at an angle of 90°.

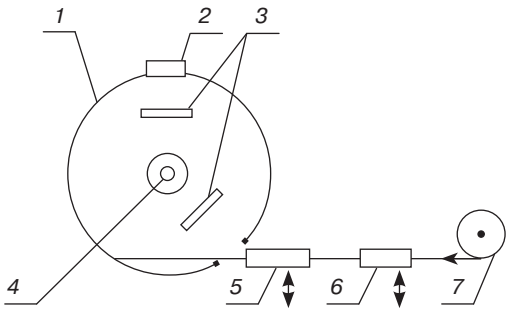

Fig. 7. Scheme for calibrating a LED on an integrating sphere using synchrotron radiation

Fig. 8. General view of the integrating sphere

The radiation flux from an external reference source is determined by integrating the radiation intensity within a solid angle fixed during the calibration against the synchrotron radiation source. The radiation flux from an internal LED source is determined by the ratio of the signals of the radiation receiver from external and internal sources along with correction factors that account for the imperfection of the integrating sphere [22].

In accordance with the CIE recommendations, correction factors are used during calibration to account for the spectral correction error relative to type A source, the inhomogeneity of the integrating sphere for internal and external radiation sources, and the difference in diffuse reflection coefficients of the sphere coating at different angles of incidence. The zonal inhomogeneity coefficient of the sensitivity of the sphere is determined by the angular dependence of the receiver signals, which allows the effects of screens, uneven coating thickness, and the state of the inner surface to be taken into account [23]. The sensitivity of the integrating sphere, which is calibrated according to the reproducibility of the metrological characteristics of ESR synchrotron radiation, is determined by the ratio of the signal received by the detector to the radiation flux at the input diaphragm.

CONCLUSIONS

In conclusion, the development of spectroradiometry methods developed for ESR metrological channels in Russia and abroad demonstrates synchrotron radiation source to comprise a high-precision primary standard used by national metrological centers to provide metrological support for the production of components in the electronics industry, as well as research and calibrations of radiometers, photometers and emitters (including LEDs), in the visible, UV, and IR regions of the electromagnetic spectrum.

Spectroradiometry methods based on the use of the fundamental properties of synchrotron radiation with a small emitting region and high radiation intensity and brightness controlled over a wide dynamic range can be used to provide absolute calibration of CCD-based telescopes and cameras, integrating spheres, goniophotometers, and spectroradiometers.

The spectroradiometric setup, which comprises a comparator based on a set of emitters, monochromator, telescope with a CCD array, spectroradiometer, radiometer, and photometer, allows the measurement of the full set of spectroradiometric and photometric characteristics of emitters used in the electronics industry—from the most differential SDEB distribution over the emitting region to integral total radiation flux.

When using a source of synchrotron radiation at wavelengths much longer than the critical one—that is, in the visible, near UV, and near IR regions of the spectrum—the integral values of SPDR in the full angle of deviation from the orbital plane normalized to the number of accelerated electrons are determined only by the radius of the orbit at the radiation point. These values, which do not depend on the energy of electrons

and are calculated with high accuracy from fundamental physical constants, thus comprise invariable metrological characteristics for each source of synchrotron radiation.

Synchrotron radiation appears to be the most promising metrological approach for determining the metrological characteristics of LEDs, allowing the small size of the emitting region of synchrotron radiation compared to the emitting region of LEDs to be taken into account, as well as the Gaussian distribution of the brightness over the emitting region of the electron bunch of the synchrotron, the wide dynamic range of SPDR tuning due to changes in the energy and the number of accelerated electrons at wavelengths near critical.

Authors' contributions

A.S. Sigov—choice of the prospect area of research based on the use of methods and means of metrological support of modern technologies, such as nanophotolithography in the electronic industry; analysis and assessment of the results obtained.

N.B. Golovanova—assessment of the chosen research method effectiveness, participation in the choice of the experimental setup optimal composition in the study of characteristics of the electronics industry components, as well as in the calibration of radiometers and photometers of optical radiation.

O.A. Minaeva—conducting theoretical and experimental studies, participating in the development of a spectroradiometric installation for measuring the characteristics of radiation sources and receivers with traceability to a reference source of synchrotron radiation, estimating measurement errors.

S.I. Anevsky—conducting experimental spectroradiometric studies to solve fundamental metrological problems of reproduction and transmission of spectroradiometry units using the theoretical foundations of synchrotron radiation.

R.V. Shamin—theoretical justification for the use of a synchrotron radiation reference source to assess the characteristics of radiation sources and receivers.

O.I. Ostanina—participation in the measuring installation design, conducting measurements, and evaluation of metrological and technical characteristics of the developed measuring installation.

REFERENCES

1. Richter M., Ulm G. Metrology with Synchrotron Radiation. In: Jaeschke E., Khan S., Schneider J.R., Hastings J.B. (Eds.). *Synchrotron Light Sources and Free-Electron Lasers*. Springer; 2020. P. 1–35. https://doi.org/10.1007/978-3-319-04507-8_63-1
2. Li H., Li B., Wang S., Li Z., Qi J., Yu M., Huang Y., Li Y., Barboutis A., Lubeck J., Klein R., Kroth S., Paustian W., Ressin M., Thornagel R. Research on the irradiance calibration of a VUV dual-grating spectrometer based on synchrotron radiation. *Opt. Commun*. 2020;475:126254. https://doi.org/10.1016/j.optcom.2020.126254
3. Hurdax P., Hollerer M., Egger L., Koller G., Yang X., Haags A., Soubatch S., Tautz F.S., Richter M., Gottwald A., Puschnig P., Sterrer M., Ramsey M.G. Controlling the electronic and physical coupling on dielectric thin films. *Beilstein J. Nanotechnol*. 2020;11:1492–1503. https://doi.org/10.3762/bjnano.11.132
4. Chkhalo N.I., Gusev S.A., Nechay A.N., Pariev D.E., Polkovnikov V.N., Salashchenko N.N., et al. High-reflection Mo/Be/Si multilayers for EUV lithography. *Optic. Lett*. 2017;42(24):5070–5073. https://doi.org/10.1364/ol.42.005070
5. Steiger A., Kehrt M., Deninger A. A reference material for accurate THz measurements. In: *2018 43rd International Conference on Infrared, Millimeter, and Terahertz Waves* (*IRMMW-THz*). 2018:8510011. https://doi.org/10.1109/IRMMW-THz.2018.8510011
6. Sperling A., Meyer M., Pendsa S., Jordan W., Revtova E., Poikonen T., Renaux D., Blattner P. Multiple Transfer Standard for calibration and characterization of the setups for LED lamps and luminaires in industry. *Metrologia*. 2018;55(2):S37–S42. https://doi.org/10.1088/1681-7575/aaa173
7. Sigov A.S., Minaeva O.A., Anevsky S.I., Lebedev A.M., Minaev R.V. Metrological studies of the characteristics of multilayer surface coatings using synchrotron radiation. *Rossiiskii tekhnologicheskii zhurnal = Russian Technological Journal*. 2021;9(1):38–47 (in Russ.). https://doi.org/10.32362/2500-316X-2021-9-1-38-47
8. Schneider P., Salffner K., Sperling A., Nevas S., Kröger I., Reiners T. Improved calibration strategy for luminous intensity. *J. Phys.: Conf. Series*. 2018;972(1):012016. https://doi.org/10.1088/1742-6596/972/1/012016
9. Klein R., Kroth S., Paustian W., Richter M., Thornagel R. PTB's radiometric scales for UV and VUV source calibration based on synchrotron radiation. *Metrologia*. 2018;55(3):386. https://doi.org/10.1088/1681-7575/aab803
10. Reichel T., Gottwald A., Kroth U., Laubis C., Scholze F. Developments in calibration of EUV and VUV detectors for solar orbiter instrumentation using synchrotron radiation. In: *Proc. SPIE 9905, Space Telescopes and Instrumentation 2016: Ultraviolet to Gamma Ray*, 990547990547-6. https://doi.org/10.1117/12.2231405
11. Sildoja M., Nevas S., Pape S., Pendsa S., Sperfeld P., Kemus F. LED-based UV monitoring source. In: *13th International Conference on New Developments and Applications in Optical Radiometry* (*NEWRAD 2017*), Proceedings. 2017: 92–93.
12. Schwihys J. On the classical radiarion of accelerated electrons. *Phys. Rev*. 1949;75(12):1912–1925. https://doi.org/10.1103/PhysRev.75.1912
13. Sildoja M., Nevas S., Kouremeti N., Gröbner J., Pape S., Pendsa S., Sperfeld P., Kemus F. LED-based UV source for monitoring spectroradiometer properties. *Metrologia*. 2018;55(3):97–103. https://doi.org/10.1088/1681-7575/aab639

14. Schmähling F., Wuebbeler G., Krueger U., Ruggaber B., Schmidt F., Taubert R.D., Sperling A., Elster C. Uncertainty evaluation and propagation for spectral measurements. *Color Reseach & Application*. 2018;43(1):6–16. https://doi.org/10.1002/col.22185
15. McEvoy H.C., Martin M-J., Steiner A., Schreiber E., Girard F., Battuello M., Sadli M., Ridoux P., Gutschwager B., Hollandt J., Diril A., Pehlivan Ö. Report on the measurement results for the EURAMET 658 extension: project to examine underlying parameters in radiance scale realization. *Metrologia*. 2018;55(1A):03001. https://doi.org/10.1088/0026-1394/55/1A/03001
16. Zuber R., Sperfeld P., Nevas S., Sildoja M. A stray light corrected array spectroradiometer for complex high dynamic range measurements in the UV spectral range. In: *13th International Conference on New Developments and Applications in Optical Radiometry* (*NEWRAD 2017*), Proceedings. 2017:65–66.
17. Kokka F., Poikonen T., Blattner P., Jost S., Ferrero S., Pulli T., Ngo M., Thorseth A., Gerloff T., Dekker P., Stuker F., Klej A., Ludwig K., Schneider M., Reiners T., Ikonen E. Development of LED illuminants for colorimetry and recommendation of white LED reference spectrum for photometry. *Metrologia*. 2018;55(4):526–534. https://doi.org/10.1088/1681-7575/aacae7
18. Ferrero A., Velázquez J.L., Pons A., Campos J. Index for the evaluation of the general photometric performance of photometers. *Opt. Express*. 2018;26(14):18633–18643. https://doi.org/10.1364/OE.26.018633
19. Gutschwager B., Hollandt J. Nonuniformity correction of infrared cameras by reading radiance temperatures with a spatially nonhomogeneous radiation source. *Meas. Sci. Technol*. 2017;28(1):015401. https://doi.org/10.1088/1361-6501/28/1/015401
20. Strothkämper C., Ferrero A., Koo A., Jaanson P., Ged G., Obein G., Källberg S., Audenaert J., Leloup F.B., Martínez-Verdú F.M., Perales E., Schirmacher A., Campos J. Multilateral spectral radiance factor scale comparison. *Appl. Opt.* 2017;56(7):1996–2006. https://doi.org/10.1364/ao.56.001996
21. Kokka A., Pulli T., Poikonen T., Askola J., Ikonen E. Fisheye camera method for spatial non-uniformity corrections in luminous flux measurements with integrating spheres. *Metrologia*. 2017;54(4):577–583. https://doi.org/10.1088/1681-7575/aa7cb7
22. Kokka A., Pulli T., Ferrero A., Dekker P., Thorseth A., Kliment P., Klej A., Gerloff T., Ludwig K., Poikonen T., Ikonen E. Validation of the fisheye camera method for spatial non-uniformity corrections in luminous flux measurements with integrating spheres. *Metrologia*. 2019;56(4):045002. https://doi.org/10.1088/1681-7575/ab17fe

About the authors

Alexander S. Sigov, Academician at the Russian Academy of Sciences, Dr. Sci. (Phys.–Math.), Professor, President, MIREA – Russian Technological University (78, Vernadskogo pr., Moscow, 119454 Russia). E-mail: sigov@mirea.ru. Scopus Author ID 35557510600, ResearcherID L-4103-2017, https://www.researchgate.net/profile/A_Sigov

Nataliya B. Golovanova, Dr. Sci. (Econ.), Professor, Deputy First Vice-Rector, MIREA – Russian Technological University (78, Vernadskogo pr., Moscow, 119454 Russia). E-mail: golovanova@mirea.ru. Scopus Author ID 57191447039, https://orcid.org/0000-0002-9901-8897

Olga A. Minaeva, Dr. Sci. (Eng.), Head of the Department of Metrology and Standardization, Institute for Advanced Technologies and Industrial Programming, MIREA – Russian Technological University (78, Vernadskogo pr., Moscow, 119454 Russia). E-mail: minaeva_o@mirea.ru. Scopus Author ID 6603019847, https://orcid.org/0000-0001-9465-3210

Sergei I. Anevsky, Dr. Sci. (Eng.), Professor, Department of Metrology and Standardization, Institute for Advanced Technologies and Industrial Programming, MIREA – Russian Technological University (78, Vernadskogo pr., Moscow, 119454 Russia). E-mail: anevskij@mirea.ru. https://orcid.org/0000-0001-9197-0034

Roman V. Shamin, Dr. Sci. (Phys.-Math.), Director, Institute for Advanced Technologies and Industrial Programming, MIREA – Russian Technological University (78, Vernadskogo pr., Moscow, 119454 Russia). E-mail: shamin@mirea.ru. Scopus Author ID 6506250832, https://orcid.org/0000-0002-3198-7501

Olga I. Ostanina, Cand. Sci. (Chem.), Assistant Professor, Department of Metrology and Standardization, Institute for Advanced Technologies and Industrial Programming, MIREA – Russian Technological University (78, Vernadskogo pr., Moscow, 119454 Russia). E-mail: ostanina@mirea.ru. Scopus Author ID 9249650700, https://orcid.org/0000-0002-5455-0046

Об авторах

Сигов Александр Сергеевич, академик Российской академии наук, д.ф.-м.н., профессор, президент ФГБОУ ВО «МИРЭА – Российский технологический университет» (119454, Россия, Москва, пр-т Вернадского, д. 78). E-mail: sigov@mirea.ru. Scopus Author ID 35557510600, Researcher ID L-4103-2017, https://www.researchgate.net/profile/A_Sigov

Голованова Наталия Борисовна, д.э.н., профессор, заместитель первого проректора ФГБОУ ВО «МИРЭА – Российский технологический университет» (119454, Россия, Москва, пр-т Вернадского, д. 78). E-mail: golovanova@mirea.ru. Scopus Author ID 57191447039, https://orcid.org/0000-0002-9901-8897

Минаева Ольга Александровна, д.т.н., заведующий кафедрой метрологии и стандартизации Института перспективных технологий и индустриального программирования ФГБОУ ВО «МИРЭА – Российский технологический университет» (119454, Россия, Москва, пр-т Вернадского, д. 78). E-mail: minaeva_o@mirea.ru. Scopus Author ID 6603019847, https://orcid.org/0000-0001-9465-3210

Аневский Сергей Иосифович, д.т.н., профессор кафедры метрологии и стандартизации Института перспективных технологий и индустриального программирования ФГБОУ ВО «МИРЭА – Российский технологический университет» (119454, Россия, Москва, пр-т Вернадского, д. 78). E-mail: anevskij@mirea.ru. https://orcid.org/0000-0001-9197-0034

Шамин Роман Вячеславович, д.ф.-м.н., директор Института перспективных технологий и индустриального программирования ФГБОУ ВО «МИРЭА – Российский технологический университет» (119454, Россия, Москва, пр-т Вернадского, д. 78). E-mail: shamin@mirea.ru. Scopus Author ID 6506250832, https://orcid.org/0000-0002-3198-7501

Останина Ольга Ивановна, к.х.н., доцент кафедры метрологии и стандартизации, Институт перспективных технологий и индустриального программирования ФГБОУ ВО «МИРЭА – Российский технологический университет» (119454, Россия, Москва, пр-т Вернадского, д. 78). E-mail: ostanina@mirea.ru. Scopus Author ID 9249650700, https://orcid.org/0000-0002-5455-0046

Translated by E. Shklovskii
Edited for English language and spelling by Thomas Beavitt

Micro- and nanoelectronics. Condensed matter physics

Микро- и наноэлектроника. Физика конденсированного состояния

UDC 535.015
https://doi.org/10.32362/2500-316X-2022-10-3-45-55

RESEARCH ARTICLE

High-temperature terahertz quantum-cascade lasers: design optimization and experimental results

Dmitry V. Ushakov [1], Alexander A. Afonenko [1], Igor A. Glinskiy [2], Rustam A. Khabibullin [2, 3, @]

[1] *Belarusian State University, Minsk, 220030 Belarus*
[2] *Institute of Ultra High Frequency Semiconductor Electronics, Russian Academy of Sciences, Moscow, 117105 Russia*
[3] *Ioffe Institute, St. Petersburg, 194021 Russia*
[@] *Corresponding author, e-mail: khabibullin@isvch.ru*

Abstract

Objectives. Terahertz quantum-cascade lasers (THz QCLs) are compact solid-state lasers pumped by electrical injection to generate radiation in the range from 1.2 to 5.4 THz. The THz QCL operating frequency band contains absorption lines for a number of substances that are suitable for biomedical and environmental applications. In order to reduce the size and cost of THz QCLs and simplify the use of THz sources in these applications, it is necessary to increase the operating temperature of lasers.

Methods. To calculate electron transport in THz QCLs, we used a system of balance equations based on wave functions with reduced dipole moments of tunnel-bound states.

Results. As a result of the calculations, an original band design with a period based on three GaAs/$Al_{0.18}Ga_{0.82}As$ quantum wells (QWs) and a gain maximum at about 3.3 THz was proposed. Based on the developed design, a THz QCL was fabricated, including the growth of a laser structure by molecular beam epitaxy, postgrowth processing to form strip lasers with a double metal waveguide, as well as an assembly of lasers mounted on a heat sink. The developed THz QCLs was capable of lasing at temperatures of up to 125 K as predicted by the performed calculations. We also studied band designs based on two GaAs/$Al_xGa_{1-x}As$ QWs having varying aluminum contents in the barrier layers (x = 0.20, 0.25, and 0.30).

Conclusions. The calculated temperature dependences of the peak gain for two-QW designs with $x > 0.2$ confirm the possibility of creating THz QCLs operating at temperatures above 200 K. Thus, we have proposed two-QW band designs that outperform existing high-temperature designs in terms of maximum operating temperature.

Keywords: quantum cascade laser, terahertz range, quantum well, molecular beam epitaxy

• **Submitted:** 17.11.2021 • **Revised:** 28.02.2022 • **Accepted:** 15.04.2022

For citation: Ushakov D.V., Afonenko A.A., Glinskiy I.A., Khabibullin R.A. High-temperature terahertz quantum-cascade lasers: design optimization and experimental results. *Russ. Technol. J.* 2022;10(3):45–55. https://doi.org/10.32362/2500-316X-2022-10-3-45-55

Financial disclosure: The authors have no a financial or property interest in any material or method mentioned.

The authors declare no conflicts of interest.

НАУЧНАЯ СТАТЬЯ

Высокотемпературные квантово-каскадные лазеры терагерцового диапазона: оптимизация дизайнов и экспериментальные результаты

Д.В. Ушаков [1],
А.А. Афоненко [1],
И.А. Глинский [2],
Р.А. Хабибуллин [2, 3, @]

[1] *Белорусский государственный университет, Минск, 220030 Республика Беларусь*
[2] *Институт сверхвысокочастотной полупроводниковой электроники им. В.Г. Мокерова Российской академии наук, Москва, 117105 Россия*
[2] *Физико-технический институт им. А.Ф. Иоффе Российской академии наук, Санкт-Петербург, 194021 Россия*
[@] *Автор для переписки, e-mail: khabibullin@isvch.ru*

Резюме

Цели. Квантово-каскадные лазеры терагерцового диапазона (ТГц ККЛ) являются компактными твердотельными приборами с инжекционной накачкой, которые позволяют генерировать излучение в диапазоне от 1.2 до 5.4 ТГц. В полосе рабочих частот ТГц ККЛ находятся линии поглощения для ряда веществ, актуальных для медико-биологических и экологических приложений. Для широкого применения ТГц ККЛ в данных приложениях необходимо увеличивать рабочую температуру лазеров, что позволит уменьшить размеры и стоимость ТГц ККЛ, а также упростит использование данных ТГц-источников.

Методы. В работе для расчета электронного транспорта в ТГц ККЛ использовалась система балансных уравнений на основе базиса волновых функций с уменьшенными дипольными моментами туннельно-связанных состояний.

Результаты. В результате расчетов предложен оригинальный зонный дизайн с периодом на основе трех GaAs/$Al_{0.18}Ga_{0.82}As$ квантовых ям (КЯ) и максимумом усиления около 3.3 ТГц. На основе разработанного дизайна был экспериментально изготовлен ТГц ККЛ, что включало рост лазерной структуры методом молекулярно-лучевой эпитаксии, постростовой процессинг для формирования полосковых лазеров с двойным металлическим волноводом и сборку лазеров на теплоотводе. Изготовленные ТГц ККЛ продемонстрировали генерацию вплоть до температуры 125 K, что согласуется с проведенными расчетами. Также в работе проведено исследование зонных дизайнов на основе двух GaAs/$Al_xGa_{1-x}As$ КЯ с различным содержанием алюминия в барьерных слоях (x = 0.20, 0.25 и 0.30).

Выводы. Рассчитанные температурные зависимости пикового усиления для двух-КЯ дизайнов с $x > 0.2$ подтверждают возможность создания ТГц ККЛ, работающих при температурах свыше 200 K. Таким образом, в работе предложены двух-КЯ зонные дизайны, которые превосходят по максимальной рабочей температуре существующие рекордные высокотемпературные дизайны ТГц ККЛ.

Ключевые слова: квантово-каскадный лазер, терагерцовый диапазон, квантовая яма, молекулярно-лучевая эпитаксия

• **Поступила:** 17.11.2021 • **Доработана:** 28.02.2022 • **Принята к опубликованию:** 15.04.2022

Для цитирования: Ушаков Д.В., Афоненко А.А., Глинский И.А., Хабибуллин Р.А. Высокотемпературные квантово-каскадные лазеры терагерцового диапазона: оптимизация дизайнов и экспериментальные результаты. *Russ. Technol. J.* 2022;10(3):45–55. https://doi.org/10.32362/2500-316X-2022-10-3-45-55

Прозрачность финансовой деятельности: Авторы не имеют финансовой заинтересованности в представленных материалах или методах.

Авторы заявляют об отсутствии конфликта интересов.

INTRODUCTION

Both in terms of fundamental science and as comprising a potential solution to a large number of applied problems, the terahertz frequency range (1–10 THz) remains one of the most intriguing regions of the electromagnetic spectrum. For a long time, the lack of compact solid-state sources of THz radiation with an average power level measured in mW remained a limiting factor for realizing the advantages of THz waves in spectroscopy, visualization, and remote sensing applications. The possibility of "transferring" the operational scheme of quantum-cascade lasers (QCLs) in the mid-infrared (mid-IR) range to the THz region demonstrated the possibility of tuning the generation frequency from 1.2 to 5.4 THz to create a unique source of THz radiation by changing the thickness of the semiconductor layers without using large magnetic fields. However, in comparison with mid-IR QCLs, where operating temperatures of more than 300 K have been demonstrated, the operation of THz QCLs required long periods of cryogenic cooling. Thus, the task of raising THz QCL operating temperatures using thermoelectric cooling based on the Peltier effect becomes highly relevant in order to for THz QCLs to find practical application in medicine, biology, agriculture, ecology, the fight against terrorism, and wireless communication [1–8].

The cryogenic cooling used with the first THz QCLs, which required the laser chip to be mounted on the cold finger of a flooded cryostat or a closed cycle cryocooler, significantly affected the size and energy efficiency of such THz sources, complicating the use of this type of laser outside laboratories. The optimization of THz QCL band designs and use of low-loss waveguides led to an increase in the operating temperature of these lasers, allowing the use of compact electric cryocoolers operating according to the Stirling cycle, which do not require cryogenic liquids and have a service life of more than 30 000 hours. However, the main disadvantage of this approach is the high cost of Stirling cryocoolers (tens of thousands of US dollars), which also limited the widespread use of THz QCLs.

Studies into electron transport [9] and the creation of more efficient band designs of the THz QCL active region [10] led to the revolutionary demonstration in 2019 of the first thermoelectrically cooled lasers operating at a maximum temperature of 210.5 K (−63°C). By the end of 2020, data had been published demonstrating a THz QCL having a maximum operating temperature of 250 K (about −23°C) [11], which permitted the use for cooling of a single-stage Peltier element costing less than USD 100. Meanwhile, research featuring similar band designs whose active region period was based on two quantum wells (QWs), differing in the height of potential barriers $Al_xGa_{1-x}As_x$ = 0.25 ([10], 2019) and x = 0.30 ([11], 2020), was published. Here, the band design and approach to increasing the height of potential barriers are primarily aimed at suppressing parasitic channels of electron leakage into the continuum, since the presence of such parasitic conduction channels in the active region adversely affects the operation of THz QCLs at high temperatures [12]. The increase in the height of potential barriers results in the need to reduce their thickness in order to maintain tunneling transparency, which in turn leads to even higher requirements for the epitaxial growth of such heterostructures having extremely thin barrier layers with a thickness of a few monolayers [13].

Despite work on the creation of THz QCLs in Russia having begun with a 10–15-year delay relative to the work of foreign groups, THz QCLs exclusively fabricated in Russia include the use of molecular beam epitaxy (MBE) to grow heterostructures and post-growth processing of stripe lasers with a double metal waveguide [14, 15]. In this paper, we present the experimental results of a study into THz QCLs based on an original active region design whose period contains three GaAs/$Al_{0.18}Ga_{0.82}As$ QWs. The results of the band design optimization of THz QCLs having a period based on two GaAs/$Al_xGa_{1-x}As$ QWs with x = 0.20, 0.25, and 0.30 for operation at high temperatures (greater than 200 K) are also presented.

EXPERIMENTAL STUDY OF THz QCL WITH A PERIOD BASED ON THREE GaAs/$Al_{0.18}Ga_{0.82}As$ QWs

The highest THz QCL operating temperatures to date have been demonstrated by a resonant phonon (RP) design featuring successive resonant tunneling of electrons to the upper laser level and emission of a THz photon, along with the depopulation of the lower laser level due to electron scattering on longitudinal optical phonons (longitudinal-optical phonons, LO-phonons). By means of diagonal radiative transitions, it was possible to significantly reduce the rate of nonradiative recombination of "hot" electrons from upper to lower laser levels due to the temperature activation of the emission of LO-phonons. Based on the foregoing, in order to optimize the active region of a high-temperature THz QCL, we selected a resonant-phonon design having a period of three GaAs/$Al_{0.18}Ga_{0.82}As$ QWs and a generation frequency of about 3.3 THz.

In order to achieve the maximum operating temperature, numerical optimization of the design of the THz QCL active region was carried out according to the previously developed method based on a system of balance equations [16, 17]. In the course of optimization, the thicknesses of all layers of the period were scanned over a wide range (thicknesses

of the QWs and barriers) with a step equal to half the constant of the GaAs crystal lattice. When selecting optimal designs, there was a condition for ensuring maximum gain on the positive branch of the current-voltage characteristic in order to avoid electrical instabilities that prevent the formation of electric field domains. The maximum operating temperature of the design corresponded to the intersection point of the temperature dependences of the gain and losses in the resonator, which were calculated earlier for a THz QCL with a double metal waveguide [16].

In the course of the optimization, an original GaAs/$Al_{0.18}Ga_{0.82}As$ band design was developed based on a period comprising a sequence of layer thicknesses starting from the injector barrier: 4.23/**16.09**/3.95/**8.75**/2.54/**8.18** (in units of nm, GaAs QWs are in bold). Doping of the active module with a Si donor impurity was $3.0 \cdot 10^{10}$ cm^{-2}. In the model, the height of $Al_{0.18}Ga_{0.82}As$ potential barriers in the conduction band was assumed to be $\Delta E_c = 164$ meV.

An illustration of electronic transport in the developed band design is shown in Fig. 1; here, the current flow through the electron levels in two periods is indicated by arrows. The number of arrows between levels is proportional to the current density (the current density through the period corresponds to five arrows). During optimization, spurious conduction channels having current densities of less than one arrow were minimized (not shown in Fig. 1). The diagonal laser transition E_{43} with a matrix element of dipole transitions Z_{43} = 3.8 nm corresponds to a generation frequency of 3.3–3.4 THz. In the insert, Fig. 1 shows the gain spectrum of the developed design (red line) and the loss spectrum in the resonator (blue dot-dash line).

A laser structure based on the developed GaAs/$Al_{0.18}Ga_{0.82}As$ band design was grown by MBE

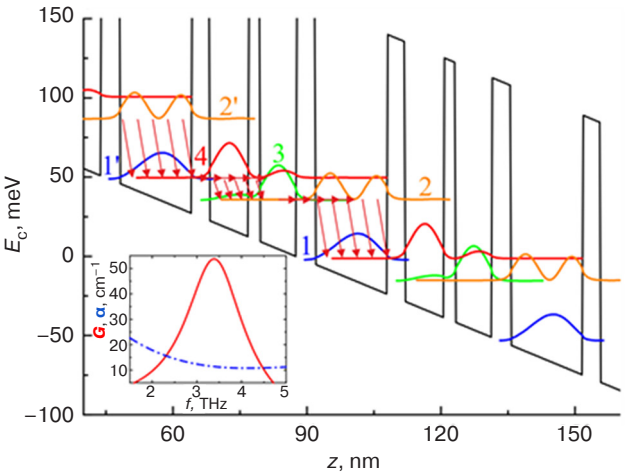

Fig. 1. Energy profile of the bottom of the conduction band E_c; energy levels (numbered) and basis wave functions after the localization procedure (tight coupling model) for two successive active modules at voltage V_1 = 51 mV and temperature 77 K

on a Riber Compact 21T setup at the National Research Nuclear University "MEPhI" (group of Prof. I.S. Vasilevsky). When developing optimal growth parameters, special attention was paid to the selection of technological growth conditions (substrate temperature, As_4 arsenic flow), accurate calibration of the growth rates of GaAs and AlAs compounds, as well as their stability during the growth of thick structures. Excluding the time taken for the growth of gauge superlattices, which were grown before and after the growth of the laser structure, the growth time of one laser structure was more than 10 h. The deviation of the thickness of the period of the structure grown from the nominal thickness (specified in the design) did not exceed 1%.

Based on the grown laser structure, THz QCLs with a double metal waveguide (DMW) were fabricated. The fabrication procedure for stripe lasers with Au–Au DMW is described in detail in [18, 19]. The cleaved THz QCLs with a Fabry–Perot resonator were assembled at the M.F. Stelmakh Polyus Research Institute (group of S.M. Sapozhnikov) on C-mount radiators; electrical contact was made by welding to the upper metal of the laser strip a large number of gold wires with a diameter of 30 μm, distributed evenly along the entire length of the strip to improve electrical injection over the entire surface of the laser [20].

The radiation characteristics of the fabricated lasers were measured at the Institute of Physics of Microstructures of the Russian Academy of Sciences (group of Prof. V.I. Gavrilenko). The current-voltage characteristics (*I–V*) and the dependences of the integral radiation intensity on the pump current and temperature of the fabricated THz lasers were studied in a pulsed mode (pulse duration 500 ns, repetition frequency 100 Hz). The structures were powered by a specially made electronic key, which made it possible to obtain pulses of a given duration, duty cycle, and amplitude, as well as to measure the voltage and current passing through the laser. When measuring the voltage-current characteristics and the integral dependences of radiation on current/temperature, the signal from the detector was fed to a Stanford Research Systems SR250 two-channel strobe integrator (Sunnyvale, California, USA).

In order to determine the maximum operating temperature, we measured the dependences of the integrated radiation intensity on the pump current. Figure 2 shows that an increase in temperature from 8 to 60 K has little effect on the output power or threshold current values. When approaching 100 K, the intensity of the optical signal begins to decrease sharply. The rapid increase in the threshold current at temperatures above 100 K is most likely due to the activation of parasitic conduction channels. The maximum temperature at which lasing was observed was about 125–130 K. A metal tube having its own loss level in the THz range was used as a waveguide system for extracting THz QCL

radiation from the cryostat. It can be assumed that the actual maximum operating temperature of the THz QCL is higher by 5–10 K; that is, about 140 K.

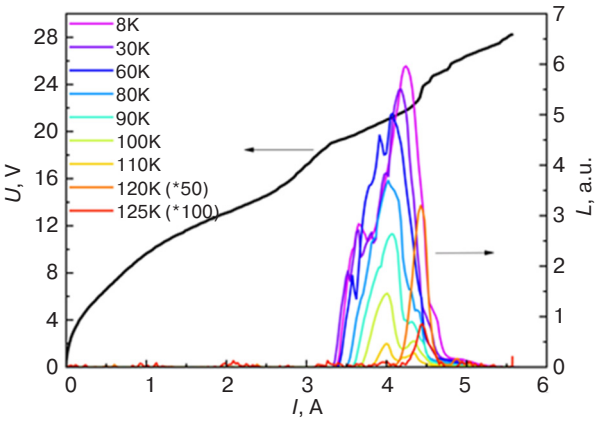

Fig. 2. *I–V* (black line) and current dependences of the integrated radiation intensity for QCL #52111 in the temperature range from 8 to 125 K. The amplitude of the integrated signal for temperatures of 120 and 125 K is multiplied by 50 and 100, respectively

OPTIMIZATION OF THz QCL BAND DESIGN BASED ON TWO GaAs/Al$_x$Ga$_{1-x}$As QUANTUM WELLS WITH x = 0.20, 0.25, AND 0.30

To further improve the high-temperature characteristics of THz QCLs, it is necessary to develop new concepts for the band design of active regions for reducing losses in the resonator. Approaches for reducing losses in THz QCLs proposed earlier include those based on the use of a double silver metal waveguide [21, 22]. In order to increase the maximum operating temperature of THz QCLs, we proposed to study band designs based on two GaAs/Al$_x$Ga$_{1-x}$As QWs with different potential barrier heights: x = 0.20, 0.25, and 0.30.

A system of balance equations with a basis of wave functions in the tight-coupling approximation was used to calculate the THz QCL characteristics. This basis was obtained as a superposition of the eigenstates of the Schrödinger equation for the entire THz QCL active region by minimizing the spatial expansion of the wave functions of the tunnel-coupled states. Due to the small wave function overlap (and accordingly low scattering rate) of degenerate ground states with $\Delta E \lesssim 3$ meV, the localized basis of wave functions in the tight-coupling approximation is more resistant to the influence of the dephasing effect. After analyzing band designs of THz QCLs based on two GaAs/Al$_x$Ga$_{1-x}$As QWs, we optimized the height of potential barriers by varying the aluminum contents (see Table).

The depiction of the proposed designs in Fig. 3 shows the current through the energy levels (red arrows). Several conduction channels can be seen between the electronic levels, including the 3–2 transition between the upper and lower laser levels, as well as parasitic transitions between levels 3 and 1. The temperature dependences of the maximum gain at a frequency of 3.9 THz shown in Fig. 4 demonstrate the possibility of operation at temperatures above 200 K for designs with $x > 0.2$. As a comparison, the calculated dependence of the gain on temperature (blue line) is shown for the band design based on three GaAs/A$_{10.25}$Ga$_{0.75}$As QWs proposed in [10], along with the experimental maximum operating temperature T_{max} = 210.5 K.

Table. Parameters of optimized band designs of an active module THZ QCL based on two quantum wells GaAs/Al$_x$Ga$_{1-x}$As

Design	x	Barrier heigh ΔE_c, meV	Sequences of barriers in a period: **Potential barrier** / quantum well, nm
Bosco [10]	0.25	212.5	**1.98**/16.37/**3.39**/7.91
A	0.20	178.5	**2.3**/16.4/**4.2**/7.3
B	0.25	212.5	**2.0**/17.2/**3.4**/7.9
C	0.30	244.5	**1.7**/17.0/**3.1**/7.9

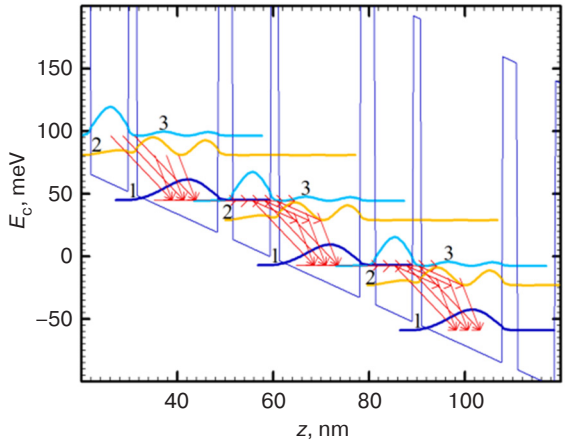

Fig. 3. Band diagram for design C

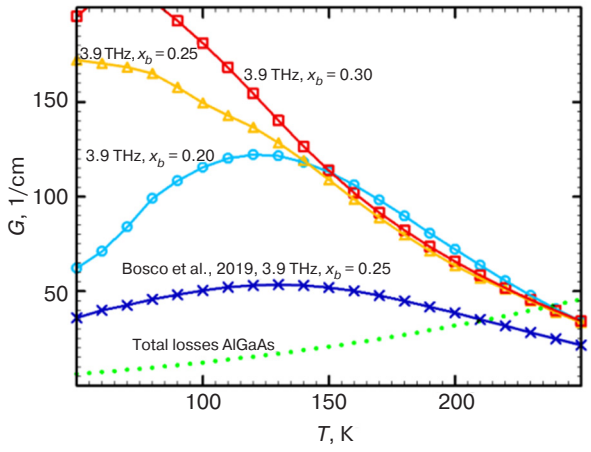

Fig. 4. Temperature dependences of the maximum gain G for the GaAs/Al$_x$Ga$_{1-x}$As structure with different Al content in the barriers

Designs with gain exceeding losses at high temperatures (210–240 K) were optimized by scanning the thickness of the active module in the range from 24 to 36 nm. In this case, the thickness of the $Al_xGa_{1-x}As$ barrier layers was varied in the range of 1.4–4.0 nm, while that of the GaAs quantum wells was in the range of 6.3–20.0 nm; here, a step was equal to half the lattice constant of GaAs. The parameters of optimized designs of active modules for different compositions of barrier layers (x contents) are presented in Table. In the sequence of period layers, GaAs quantum wells are shown in bold type. The central part of the wide GaAs QW is doped with silicon having a layer concentration of $4.5 \cdot 10^{10}$ cm^{-2}, as in [3].

The main factors affecting the gain in QCLs are the effective electron mass m_e, population inversion n_{32} of laser levels, and matrix elements of dipole transitions Z_{32} [23–25]. Thus, the gain of the QCL active module can be represented as the product of these parameters $G \sim m_c^{-3/2} n_{32} Z_{32}^2$. This means that effective amplification in a QCL requires a small effective electron mass combined with a large population inversion and dipole transition matrix elements. The temperature dependences of these values for the optimized active modules compared to the Bosco design [3] are shown in Fig. 5, while Fig. 5a depicts the effective electron mass increases in designs with higher potential barriers (higher aluminum content in $Al_xGa_{1-x}As$) due to the non-parabolic effect. For all designs under study, m_c can be seen to decrease at elevated temperatures. In optimized designs B and C (Fig. 5b), the population inversion is larger at temperatures above 200 K. As can be seen from Fig. 5c, the matrix elements of the dipole junctions of these designs increase with rising temperature from 50 to 250 K: from 4.9 to 5.2 nm (design Bosco 2019), from 4.7 to 5.0 nm (design A), from 4.4 to 4.7 nm (design B), and from 4.7 to 5.0 nm (design C). Thus, by combining all three factors for all optimized designs A (x_b = 0.20), B (x_b = 0.25) and C (x_b = 0.30), we can expect a maximum operating temperature of 238 K.

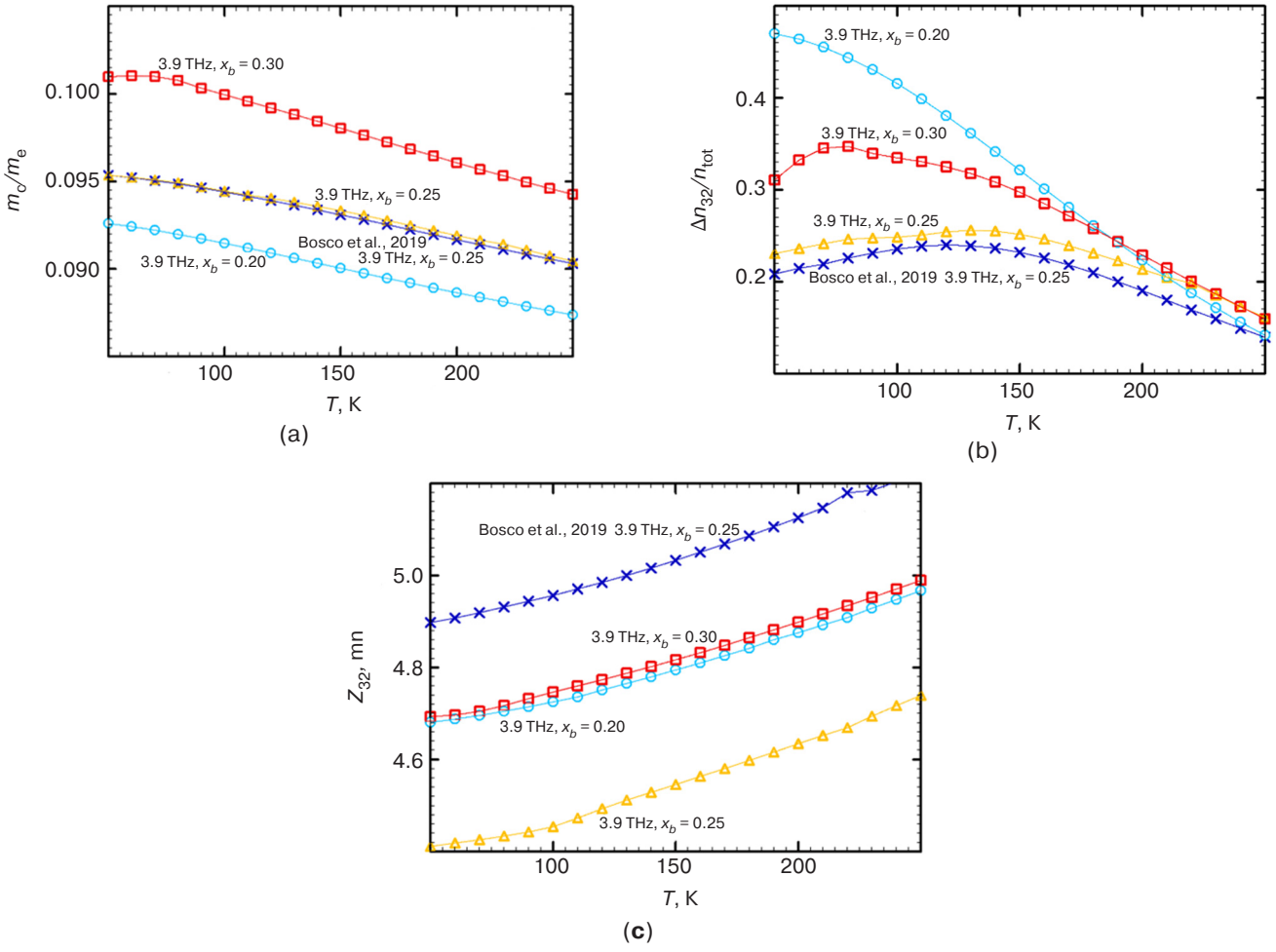

Fig. 5. Temperature dependences of the effective electron mass m_c (a), Δn_{32} are population inversions, n_{tot} is the total electron concentration in a period (b), and matrix elements of dipole transitions Z_{32} (c) for the optimized design A (x_b = 0.20), B (x_b = 0.25), and C (x_b = 0.30)

CONCLUSIONS

A THz QCL based on an original band design having a period based on three GaAs/$Al_{0.18}Ga_{0.82}As$ quantum wells has been experimentally demonstrated at a maximum operating temperature of more than 125 K. Band designs based on two GaAs/$Al_xGa_{1-x}As$ quantum wells with varying aluminum contents of x = 0.20, 0.25, and 0.30 were studied. The calculated temperature dependences of the peak gain for two-QW designs with $x > 0.2$ confirm the possibility of creating a THz QCL operating at temperatures above 200 K.

ACKNOWLEDGMENTS

The study was supported by grant of MIREA – Russian Technological University "Innovations in the implementation of priority areas in the science and technology development" (Research part 28/21) in the framework of theoretical research and with the support of the Russian Science Foundation, grant No. 21-72-30020, for the THz QCL fabrication.

Authors' contributions

D.V. Ushakov—numerical optimization of THz QCL designs.

A.A. Afonenko—numerical optimization of THz QCL designs.

I.A. Glinskiy—calculation of losses in the THz QCL resonator.

R.A. Khabibullin—fabrication and measurement of the emission characteristics of THz QCLs.

REFERENCES

1. Sampaolo A., Yu C., Wei T., Zifarelli A., Giglio M., Patimisco P., Zhu H., Zhu H., He L., Wu H., Dong L., Xu G., Spagnolo V. H_2S quartz-enhanced photoacoustic spectroscopy sensor employing a liquid-nitrogen-cooled THz quantum cascade laser operating in pulsed mode. *Photoacoustics*. 2021;21:100219. https://doi.org/10.1016/j.pacs.2020.100219
2. Consolino L., Nafa M., De Regis M., Cappelli F., Garrasi K., Mezzapesa F.P., Li L., Davies A.G., Linfield E.H., Vitiello M.S., Bartalini S., De Natale P. Quantum cascade laser based hybrid dual comb spectrometer. *Commun. Phys*. 2020;3(1):69. https://doi.org/10.1038/s42005-020-0344-0
3. Irimajiri Y., Morohashi I., Kawakami A. Multifrequency heterodyne detection of molecules using a hot electron bolometer mixer pumped by two phase-locked THz-quantum cascade lasers. *IEEE Trans. Terahertz Sci. Technol*. 2020;10(5):474–479. https://doi.org/10.1109/TTHZ.2020.2990358
4. Jin Y., Reno J.L., Kumar S. Phase-locked terahertz plasmonic laser array with 2 W output power in a single spectral mode. *Optica*. 2020;7(6):708–715. https://doi.org/10.1364/OPTICA.390852
5. Rakić A.D., Taimre T., Bertling K., Lim Y.L., Dean P., Valavanis A., Indjin D. Sensing and imaging using laser feedback interferometry with quantum cascade lasers. *Appl. Phys. Rev*. 2019;6(2):021320. https://doi.org/10.1063/1.5094674
6. Dunn A., Poyser C., Dean P., Demić A., Valavanis A., Indjin D., Salih M., Kundu I., Li L., Akimov A., Davies A.G., Linfield E., Cunningham J., Kent A. High-speed modulation of a terahertz quantum cascade laser by coherent acoustic phonon pulses. *Nat. Commun*. 2020;11:835. https://doi.org/10.1038/s41467-020-14662-w
7. Hagelschuer T., Richter H., Wienold M., Lü X., Röben B., Schrottke L., Biermann K., Grahn H., Hübers H. A compact 4.75-THz source based on a quantum-cascade laser with a back-facet mirror. *IEEE Trans. Terahertz Sci. Technol*. 2019;9(6):606–612. https://doi.org/10.1109/TTHZ.2019.2935337

СПИСОК ЛИТЕРАТУРЫ

1. Sampaolo A., Yu C., Wei T., Zifarelli A., Giglio M., Patimisco P., Zhu H., Zhu H., He L., Wu H., Dong L., Xu G., Spagnolo V. H_2S quartz-enhanced photoacoustic spectroscopy sensor employing a liquid-nitrogen-cooled THz quantum cascade laser operating in pulsed mode. *Photoacoustics*. 2021;21:100219. https://doi.org/10.1016/j.pacs.2020.100219
2. Consolino L., Nafa M., De Regis M., Cappelli F., Garrasi K., Mezzapesa F.P., Li L., Davies A.G., Linfield E.H., Vitiello M.S., Bartalini S., De Natale P. Quantum cascade laser based hybrid dual comb spectrometer. *Commun. Phys*. 2020;3(1):69. https://doi.org/10.1038/s42005-020-0344-0
3. Irimajiri Y., Morohashi I., Kawakami A. Multifrequency heterodyne detection of molecules using a hot electron bolometer mixer pumped by two phase-locked THz-quantum cascade lasers. *IEEE Trans. Terahertz Sci. Technol*. 2020;10(5):474–479. https://doi.org/10.1109/TTHZ.2020.2990358
4. Jin Y., Reno J.L., Kumar S. Phase-locked terahertz plasmonic laser array with 2 W output power in a single spectral mode. *Optica*. 2020;7(6):708–715. https://doi.org/10.1364/OPTICA.390852
5. Rakić A.D., Taimre T., Bertling K., Lim Y.L., Dean P., Valavanis A., Indjin D. Sensing and imaging using laser feedback interferometry with quantum cascade lasers. *Appl. Phys. Rev*. 2019;6(2):021320. https://doi.org/10.1063/1.5094674
6. Dunn A., Poyser C., Dean P., Demić A., Valavanis A., Indjin D., Salih M., Kundu I., Li L., Akimov A., Davies A.G., Linfield E., Cunningham J., Kent A. High-speed modulation of a terahertz quantum cascade laser by coherent acoustic phonon pulses. *Nat. Commun*. 2020;11:835. https://doi.org/10.1038/s41467-020-14662-w
7. Hagelschuer T., Richter H., Wienold M., Lü X., Röben B., Schrottke L., Biermann K., Grahn H., Hübers H. A compact 4.75-THz source based on a quantum-cascade laser with a back-facet mirror. *IEEE Trans. Terahertz Sci. Technol*. 2019;9(6):606–612. https://doi.org/10.1109/TTHZ.2019.2935337

8. Schrottke L., Ropcke J., Grahn H.T., Lu X., Röben B., Drude P., Biermann K., Hagelschuer T., Wienold M., Hübers H.-W., Hannemann M., Hubertus van Helden J.-P. High-performance GaAs/AlAs terahertz quantum-cascade lasers for spectroscopic applications. *IEEE Trans. Terahertz Sci. Technol.* 2020;10(2):133–140. https://doi.org/10.1109/TTHZ.2019.2957456
9. Franckié M., Bosco L., Beck M., Bonzon C., Mavrona E., Scalari G., Wacker A., Faist J. Two-well quantum cascade laser optimization by non-equilibrium Green's function modelling. *Appl. Phys. Lett*. 2018;112:021104. https://doi.org/10.1063/1.5004640
10. Bosco L., Franckié M., Scalari G., Beck M., Wacker A., Faist J. Thermoelectrically cooled THz quantum cascade laser operating up to 210 K. *Appl. Phys. Lett*. 20194;115:010601. https://doi.org/10.1063/1.5110305
11. Khalatpour A., Paulsen A.K., Deimert C., Wasilewski Z.R., Hu Q. High-power portable terahertz laser systems. *Nat. Photonics*. 2021;15:16–20. https://doi.org/10.1038/s41566-020-00707-5
12. Kainz M.A., Schönhuber S., Andrews A.M., Detz H., Limbacher B., Strasser G., Unterrainer K. Barrier height tuning of THz quantum cascade lasers for high temperature operation. *ACS Photonics*. 2018;5(11):4687–4693. https://doi.org/10.1021/acsphotonics.8b01280
13. Yachmenev A.E., Pushkarev S.S., Reznik R., Khabibullin R.A., Ponomarev D.S. Arsenides-and related III-V materials-based multilayered structures for terahertz applications: various designs and growth technology. *Prog. Cryst. Growth Charact. Mater.* 2020;66(2):100485. https://doi.org/10.1016/j.pcrysgrow.2020.100485
14. Khabibullin R.A., Shchavruk N.V., Pavlov A.Yu., Ponomarev D.S., Tomosh K.N., Galiev R.R., Maltsev P.P., Zhukov A.E., Cirlin G.E., Zubov F.I., Alferov Z.I. Fabrication of terahertz quantum cascade laser with a double metal waveguide based on multilayer GaAs/AlGaAs heterostructures. *Semiconductors*. 2016;50(10):1377–1382. https://doi.org/10.1134/S1063782616100134
[Original Russian Text: Khabibullin R.A., Shchavruk N.V., Pavlov A.Yu., Ponomarev D.S., Tomosh K.N., Galiev R.R., Maltsev P.P., Zhukov A.E., Cirlin G.E., Zubov F.I., Alferov Z.I. Fabrication of terahertz quantum cascade laser with a double metal waveguide based on multilayer GaAs/AlGaAs heterostructures. *Fizika i Tekhnika Poluprovodnikov*. 2016;50(10):1395–1400 (in Russ.).]
15. Ikonnikov A.V., Maremyanin K.V., Morozov S.V., Gavrilenko V.I., Pavlov A.Yu., Shchavruk N.V., Khabibullin R.A., Reznik R.R., Cirlin G.E., Zubov F.I., Zhukov A.E., Alferov Zh.I. Generation of terahertz radiation in multilayer quantum-cascade heterostructures. *Tech. Phys. Lett*. 2017;43(7):362–365. https://doi.org/10.1134/S1063785017040083
[Original Russian Text: Ikonnikov A.V., Maremyanin K.V., Morozov S.V., Gavrilenko V.I., Pavlov A.Yu., Shchavruk N.V., Khabibullin R.A., Reznik R.R., Cirlin G.E., Zubov F.I., Zhukov A.E., Alferov Zh.I. Generation of terahertz radiation in multilayer quantum-cascade heterostructures. *Pis'ma v Zhurnal Tekhnicheskoi Fiziki*. 2017;43(7):86–94 (in Russ.). https://doi.org/10.21883/PJTF.2017.07.44473.16602]

8. Schrottke L., Ropcke J., Grahn H.T., Lu X., Röben B., Drude P., Biermann K., Hagelschuer T., Wienold M., Hübers H.-W., Hannemann M., Hubertus van Helden J.-P. High-performance GaAs/AlAs terahertz quantum-cascade lasers for spectroscopic applications. *IEEE Trans. Terahertz Sci. Technol.* 2020;10(2):133–140. https://doi.org/10.1109/TTHZ.2019.2957456
9. Franckié M., Bosco L., Beck M., Bonzon C., Mavrona E., Scalari G., Wacker A., Faist J. Two-well quantum cascade laser optimization by non-equilibrium Green's function modelling. *Appl. Phys. Lett*. 2018;112:021104. https://doi.org/10.1063/1.5004640
10. Bosco L., Franckié M., Scalari G., Beck M., Wacker A., Faist J. Thermoelectrically cooled THz quantum cascade laser operating up to 210 K. *Appl. Phys. Lett*. 20194;115:010601. https://doi.org/10.1063/1.5110305
11. Khalatpour A., Paulsen A.K., Deimert C., Wasilewski Z.R., Hu Q. High-power portable terahertz laser systems. *Nat. Photonics*. 2021;15:16–20. https://doi.org/10.1038/s41566-020-00707-5
12. Kainz M.A., Schönhuber S., Andrews A.M., Detz H., Limbacher B., Strasser G., Unterrainer K. Barrier height tuning of THz quantum cascade lasers for high temperature operation. *ACS Photonics*. 2018;5(11):4687–4693. https://doi.org/10.1021/acsphotonics.8b01280
13. Yachmenev A.E., Pushkarev S.S., Reznik R., Khabibullin R.A., Ponomarev D.S. Arsenides-and related III-V materials-based multilayered structures for terahertz applications: various designs and growth technology. *Prog. Cryst. Growth Charact. Mater*. 2020;66(2):100485. https://doi.org/10.1016/j.pcrysgrow.2020.100485
14. Хабибуллин Р.А., Щаврук Н.В., Павлов А.Ю., Пономарев Д.С., Томош К.Н., Галиев Р.Р., Мальцев П.П., Жуков А.Е., Цырлин Г.Э., Зубов Ф.И., Алфёров Ж.И. Изготовление терагерцового квантово-каскадного лазера с двойным металлическим волноводом на основе многослойных гетероструктур GaAs/AlGaAs. *Физика и техника полупроводников*. 2016;50(10):1395–1400.
15. Иконников А.В., Маремьянин К.В., Морозов С.В., Гавриленко В.И., Павлов А.Ю., Щаврук Н.В., Хабибуллин Р.А., Резник Р.Р., Цырлин Г.Э., Зубов Ф.И., Жуков А.Е., Алфёров Ж.И. Генерация терагерцового излучения в многослойных квантово-каскадных гетероструктурах. *Письма в ЖТФ*. 2017;43(7):86–94. https://doi.org/10.21883/PJTF.2017.07.44473.16602
16. Ушаков Д.В., Афоненко А.А., Дубинов А.А., Гавриленко В.И., Васильевский И.С., Щаврук Н.В., Пономарев Д.С., Хабибуллин Р.А. Спектры модовых потерь в ТГц квантово-каскадных лазерах с двойным металлическим волноводом на основе Au и Ag. *Квантовая электроника*. 2018;48(11):1005–1008. https://doi.org/10.1070/QEL16806
17. Ушаков Д.В., Афоненко А.А., Дубинов А.А., Гавриленко В.И., Волков О.Ю., Щаврук Н.В., Пономарев Д.С., Хабибуллин Р.А. Моделирование квантово-каскадных лазеров терагерцевого диапазона частот методом балансных уравнений на основе базиса волновых функций с уменьшенными дипольными моментами туннельно-связанных состояний. *Квантовая электроника*. 2019;49(10):913–918. https://doi.org/10.1070/QEL17068

16. Ushakov D.V., Afonenko A.A., Dubinov A.A., Gavrilenko V.I., Vasil'evskii I.S., Shchavruk N.V., Ponomarev D.S., Khabibullin R.A. Mode loss spectra in THz quantum-cascade lasers with gold- and silver-based double metal waveguides. *Quantum Electronics*. 2018;48(11): 1005–1008. https://doi.org/10.1070/QEL16806
17. Ushakov D.V., Afonenko A.A., Dubinov A.A., Gavrilenko V.I., Volkov O.Yu., Shchavruk N.V., Ponomarev D.S., Khabibullin R.A. Balance-equation method for simulating terahertz quantum-cascade lasers using a wave-function basis with reduced dipole moments of tunnel-coupled states. *Quantum Electronics*. 2019;49(10):913–918. https://doi.org/10.1070/QEL17068
18. Khabibullin R.A., Shchavruk N.V., Ponomarev D.S., Ushakov D.V., Afonenko A.A., Vasil'evskii I.S., Zaycev A.A., Danilov A.I., Volkov O.Y., Pavlovskiy V.V., Maremyanin K.V., Gavrilenko V.I. Temperature dependences of the threshold current and output power of a quantum-cascade laser emitting at 3.3 THz. *Semiconductors*. 2018;52(11):1380–1385. https://doi.org/10.1134/S1063782618110118
[Original Russian Text: Khabibullin R.A., Shchavruk N.V., Ponomarev D.S., Ushakov D.V., Afonenko A.A., Vasil'evskii I.S., Zaycev A.A., Danilov A.I., Volkov O.Y., Pavlovskiy V.V., Maremyanin K.V., Gavrilenko V.I. Temperature dependences of the threshold current and output power of a quantum-cascade laser emitting at 3.3 THz. *Fizika i Tekhnika Poluprovodnikov*. 2018;52(11):1268–1273 (in Russ.). https://doi.org/10.21883/FTP.2018.11.46581.03]
19. Khabibullin R.A., Shchavruk N.V., Ponomarev D.S., Ushakov D.V., Afonenko A.A., Maremyanin K.V., Volkov O.Yu., Pavlovskiy V.V., Dubinov A.A. The operation of THz quantum cascade laser in the region of negative differential resistance. *Opto-Electronics Review*. 2019;27(4):329. https://doi.org/10.1016/j.opelre.2019.11.002
20. Dolgov A.K., Ponomarev D.S., Khabibullin R.A., Ushakov D.V., Afonenko A.A., Dyuzhikov I.N., Glinskiy I.A. Simulation on the nonuniform electrical pumping efficiency of THz quantum-cascade lasers. *Quantum Electronics*. 2021;51(2):164–168. https://doi.org/10.1070/QEL17431
21. Khabibullin R., Ushakov D., Afonenko A., Shchavruk N., Ponomarev D., Vasil'evskii I., Safonov D., Dubinov A. Spectra of mode loss in THz quantum cascade laser with double metal waveguide based on Au, Cu and Ag. *Proc. SPIE*. 2018;11066:1106613. https://doi.org/10.1117/12.2523284
22. Khabibullin R., Ushakov D., Afonenko A., Shchavruk N., Ponomarev D., Volkov O., Pavlovskiy V., Vasil'evskii I., Safonov D., Dubinov A. Silver-based double metal waveguide for terahertz quantum cascade laser. *Proc. SPIE*. 2019;11022:1102204. https://doi.org/10.1117/12.2521774
23. Khabibullin R.A., Shchavruk N.V., Klochkov A.N., Glinskiy I.A., Zenchenko N.V., Ponomarev D.S., Maltsev P.P., Zaycev A.A., Zubov F.I., Zhukov A.E., Cirlin G.E., Alferov Zh.I. Energy spectrum and thermal properties of terahertz quantum-cascade laser based on the resonant-phonon depopulation scheme. *Semiconductors*. 2017;51(4): 514–519. https://doi.org/10.1134/S106378261704008X
18. Хабибуллин Р.А., Щаврук Н.В., Пономарев Д.С., Ушаков Д.В., Афоненко А.А., Васильевский И.С., Зайцев А.А., Данилов А.И., Волков О.Ю., Павловский В.В., Маремьянин К.В., Гавриленко В.И. Температурная зависимость порогового тока и выходной мощности квантово-каскадного лазера с частотой генерации 3.3 ТГц. *Физика и техника полупроводников*. 2018;52(11):1268–1273. https://doi.org/10.21883/FTP.2018.11.46581.03
19. Khabibullin R.A., Shchavruk N.V., Ponomarev D.S., Ushakov D.V., Afonenko A.A., Maremyanin K.V., Volkov O.Yu., Pavlovskiy V.V., Dubinov A.A. The operation of THz quantum cascade laser in the region of negative differential resistance. *Opto-Electronics Review*. 2019;27(4):329. https://doi.org/10.1016/j.opelre.2019.11.002
20. Долгов А.К., Ушаков Д.В., Афоненко А.А., Дюжиков И.Н., Глинский И.А., Пономарев Д.С., Хабибуллин Р.А. Моделирование эффективности электрической накачки квантово-каскадного терагерцевого лазера при неоднородном питании током. *Квантовая электроника*. 2021;51(2):164–168. https://doi.org/10.1070/QEL17431
21. Khabibullin R., Ushakov D., Afonenko A., Shchavruk N., Ponomarev D., Vasil'evskii I., Safonov D., Dubinov A. Spectra of mode loss in THz quantum cascade laser with double metal waveguide based on Au, Cu and Ag. *Proc. SPIE*. 2018;11066:1106613. https://doi.org/10.1117/12.2523284
22. Khabibullin R., Ushakov D., Afonenko A., Shchavruk N., Ponomarev D., Volkov O., Pavlovskiy V., Vasil'evskii I., Safonov D., Dubinov A. Silver-based double metal waveguide for terahertz quantum cascade laser. *Proc. SPIE*. 2019;11022:1102204. https://doi.org/10.1117/12.2521774
23. Хабибуллин Р.А., Щаврук Н.В., Клочков А.Н., Глинский И.А., Зенченко Н.В., Пономарев Д.С., Мальцев П.П., Зайцев А.А., Зубов Ф.И., Жуков А.Е., Цырлин Г.Э., Алфёров Ж.И. Энергетический спектр и тепловые свойства терагерцового квантово-каскадного лазера на основе резонансно-фононного дизайна. *Физика и техника полупроводников*. 2017;51(4): 540–546. https://doi.org/10.21883/FTP.2017.04.44349.8414
24. Цырлин Г.Э., Резник Р.Р., Жуков А.Е., Хабибуллин Р.А., Маремьянин К.В., Гавриленко В.И., Морозов С.В. Особенности роста наноструктур для терагерцовых квантово-каскадных лазеров и их физические свойства. *Физика и техника полупроводников*. 2020;54(9):902–905. https://doi.org/10.21883/FTP.2020.09.49829.21
25. Ushakov D., Afonenko A., Khabibullin R., Ponomarev D., Aleshkin V., Morozov S., Dubinov A. HgCdTe-based quantum cascade lasers operating in the GaAs phonon Reststrahlen band predicted by the balance equation method. *Opt. Express*. 2020;28(17):25371–25382. https://doi.org/10.1364/oe.398552

[Original Russian Text: Khabibullin R.A., Shchavruk N.V., Klochkov A.N., Glinskiy I.A., Zenchenko N.V., Ponomarev D.S., Maltsev P.P., Zaycev A.A., Zubov F.I., Zhukov A.E., Cirlin G.E., Alferov Zh.I. Energy spectrum and thermal properties of terahertz quantum-cascade laser based on the resonant-phonon depopulation scheme. *Fizika i Tekhnika Poluprovodnikov*. 2017;51(4):540–546 (in Russ.). https://doi.org/10.21883/FTP.2017.04.44349.8414]

24. Cirlin G.E., Reznik R.R., Zhykov A.E., Khabibullin R.A., Marem'yanin K.V., Gavrilenko V.I., Morozov S.V. Specific growth features of nanostructures for terahertz quantum cascade lasers and their physical properties. *Semiconductors*. 2020;54:1092–1095. http://dx.doi.org/10.1134/S1063782620090298
[Original Russian Text: Cirlin G.E., Reznik R.R., Zhykov A.E., Khabibullin R.A., Marem'yanin K.V., Gavrilenko V.I., Morozov S.V. Specific growth features of nanostructures for terahertz quantum cascade lasers and their physical properties. *Fizika i Tekhnika Poluprovodnikov*. 2020;54(9):902–905 (in Russ.). https://doi.org/10.21883/FTP.2020.09.49829.21]
25. Ushakov D., Afonenko A., Khabibullin R., Ponomarev D., Aleshkin V., Morozov S., Dubinov A. HgCdTe-based quantum cascade lasers operating in the GaAs phonon Reststrahlen band predicted by the balance equation method. *Opt. Express*. 2020;28(17):25371–25382. https://doi.org/10.1364/oe.398552

About the authors

Dmitrii V. Ushakov, Cand. Sci. (Phys.-Math.), Associate Professor, Dean of the Faculty of Radiophysics and Computer Technologies, Belarusian State University (4, Nezavisimosti pr., Minsk, 220030 Belarus). E-mail: ushakovDVU@gmail.com. Scopus Author ID 6701760232, ResearcherID K-4878-2013, https://orcid.org/0000-0002-2108-7024

Alexander A. Afonenko, Dr. Sci. (Phys.-Math.), Associate Professor, Head of the Department of Quantum Radiophysics and Optoelectronics, Belarusian State University (4, Nezavisimosti pr., Minsk, 220030 Belarus). E-mail: afonenko@bsu.by. Scopus Author ID 6603664811.

Igor A. Glinskiy, Junior Researcher, V.G. Mokerov Institute of Ultra High Frequency Semiconductor Electronics, Russian Academy of Sciences (7/5, Nagorny pr., Moscow, 117105 Russia). E-mail: glinskiy.igor@yandex.ru. Scopus Author ID 57190616854, ResearcherID I-4334-2015, https://orcid.org/0000-0002-0477-608X

Rustam A. Khabibullin, Cand. Sci. (Phys.-Math.), Associate Professor, Leading Researcher, V.G. Mokerov Institute of Ultra High Frequency Semiconductor Electronics, Russian Academy of Sciences (7/5, Nagorny pr., Moscow, 117105 Russia); Leading Researcher, Ioffe Institute (26, Politekhnicheskaya ul., St. Petersburg, 194021 Russia). E-mail: khabibullin@isvch.ru. Scopus Author ID 55018400000, ResearcherID B-6594-2012, https://orcid.org/0000-0002-8414-7653

Об авторах

Ушаков Дмитрий Владимирович, к.ф.-м.н., доцент, декан факультета радиофизики и компьютерных технологий, Белорусский государственный университет (220030, Беларусь, Минск, пр-т Независимости, д. 4). E-mail: ushakovDVU@gmail.com. Scopus Author ID 6701760232, ResearcherID K-4878-2013, https://orcid.org/0000-0002-2108-7024

Афоненко Александр Анатольевич, д.ф.-м.н., доцент, заведующий кафедрой квантовой радиофизики и оптоэлектроники, Белорусский государственный университет (220030, Беларусь, Минск, пр-т Независимости, д. 4). E-mail: afonenko@bsu.by. Scopus Author ID 6603664811.

Глинский Игорь Андреевич, младший научный сотрудник, Институт сверхвысокочастотной полупроводниковой электроники им. В.Г. Мокерова Российской академии наук (117105, Россия, Москва, Нагорный пр., д. 7, стр. 5). E-mail: glinskiy.igor@yandex.ru. Scopus Author ID 57190616854, ResearcherID I-4334-2015, https://orcid.org/0000-0002-0477-608X

Хабибуллин Рустам Анварович, к.ф.-м.н., доцент, ведущий научный сотрудник, Институт сверхвысокочастотной полупроводниковой электроники им. В.Г. Мокерова Российской академии наук (117105, Россия, Москва, Нагорный пр., д. 7, стр. 5); ведущий научный сотрудник, Физико-технический институт им. А.Ф. Иоффе Российской академии наук (194021, Россия, Санкт-Петербург, Политехническая ул., д. 26). E-mail: khabibullin@isvch.ru. Scopus Author ID 55018400000, ResearcherID B-6594-2012, https://orcid.org/0000-0002-8414-7653

Translated by E. Shklovskii
Edited for English language and spelling by Thomas Beavitt

Micro- and nanoelectronics. Condensed matter physics

Микро- и наноэлектроника. Физика конденсированного состояния

UDC 538.915
https://doi.org/10.32362/2500-316X-2022-10-3-56-63

RESEARCH ARTICLE

Modeling of two-dimensional $Mo_xW_{1-x}S_{2y}Se_{2(1-y)}$ alloy band structure

Nikita Yu. Pimenov [@], Sergey D. Lavrov, Andrey V. Kudryavtsev, Artur Yu. Avdizhiyan

MIREA – Russian Technological University, Moscow, 119454 Russia
[@] Corresponding author, e-mail: nikitapimenov13@gmail.com

Abstract

Objectives. Two-dimensional transition metal dichalcogenides (TMDs) are utilized for various optical applications due to the presence in these materials of a direct band gap corresponding to the visible and near-infrared spectral regions. However, a limited set of existing TMDs makes the region of the used spectral range discrete. The most effective way to solve this problem is to use two-dimensional TMD films based on multicomponent alloys, including three or more different chemical elements (while TMDs consist of two). By varying their morphological composition, one can control the value of the band gap and thus their optical absorption spectrum. However, since the band gap in such structures is highly nonlinear as far as their chemical composition is concerned, it can be challenging to select the required concentration in order to achieve uniform absorption. In this regard, the purpose of this work is to theoretically determine the dependence of the band gap of four-component two-dimensional $Mo_xW_{1-x}S_{2y}Se_{2(1-y)}$ alloys on their morphological composition.

Methods. The calculations were performed within the framework of the density functional theory using the Quantum Espresso software package. Flakes of two-dimensional TMDs alloys were prepared from bulk TMDs crystals by mechanical exfoliation on a Si/SiO_2 substrate. An experimental study of the photoluminescence characteristics was carried out using photoluminescence microscopy-spectroscopy.

Results. In this work, the dependence of the band gap on the morphological composition of two-dimensional $Mo_xW_{1-x}S_{2y}Se_{2(1-y)}$ alloys was determined. Upon varying the composition of TMDs alloys, it was found that the band gap changes from 1.43 to 1.83 eV. The obtained theoretical results are in qualitative agreement with the experimental data.

Conclusions. The minimum band gap is observed in alloys close to $MoSe_2$, while alloys close to WS_2 have the maximum band gap value.

Keywords: transition metal dichalcogenides, two-dimensional semiconductors, band structure, band gap, density functional theory

• **Submitted:** 17.11.2021 • **Revised:** 24.02.2022 • **Accepted:** 19.04.2022

For citation: Pimenov N.Yu., Lavrov S.D., Kudryavtsev A.V., Avdizhiyan A.Yu. Modeling of two-dimensional $Mo_xW_{1-x}S_{2y}Se_{2(1-y)}$ alloy band structure. *Russ. Technol. J.* 2022;10(3):56–63. https://doi.org/10.32362/2500-316X-2022-10-3-56-63

Financial disclosure: The authors have no a financial or property interest in any material or method mentioned.

The authors declare no conflicts of interest.

НАУЧНАЯ СТАТЬЯ

Моделирование зонной структуры двумерных твердых растворов $Mo_xW_{1-x}S_{2y}Se_{2(1-y)}$

Н.Ю. Пименов [@], **С.Д. Лавров**, **А.В. Кудрявцев**, **А.Ю. Авдижиян**

МИРЭА – Российский технологический университет, Москва, 119454 Россия
[@] *Автор для переписки, e-mail: nikitapimenov13@gmail.com*

Резюме

Цели. Благодаря наличию прямозонного перехода с шириной запрещенной зоны, соответствующей видимой и ближней инфракрасной областям спектра, двумерные дихалькогениды переходных металлов (ДПМ) находят применение в различных оптических приложениях. Однако ограниченный набор существующих ДПМ делает область используемого спектрального диапазона дискретной. Наиболее эффективным способом решения этой проблемы является использование двумерных пленок ДПМ на основе многокомпонентных твердых растворов, в состав которых входят три и более различных химических элемента (в то время, как ДПМ состоят из двух). Варьируя их морфологический состав, можно управлять значением ширины запрещенной зоны, и, таким образом, их оптическим спектром поглощения. Так как ширина запрещенной зоны в таких структурах сильно нелинейна по отношению к их химическому составу, это затрудняет подбор необходимой концентрации для достижения равномерного поглощения. В связи с этим целью данной работы является теоретическое определение зависимости ширины запрещенной зоны четырехкомпонентных двумерных твердых растворов $Mo_xW_{1-x}S_{2y}Se_{2(1-y)}$ от их морфологического состава.

Методы. Расчеты выполнены в рамках теории функционала плотности с использованием программного пакета *Quantum Espresso*. Двумерные кристаллиты твердых растворов ДПМ были изготовлены из объемных кристаллов ДПМ методикой механической эксфолиации на подложку Si/SiO_2. Экспериментальное исследование фотолюминесцентных характеристик было проведено при помощи фотолюминесцентной микроскопии-спектроскопии.

Результаты. В работе была определена зависимость ширины запрещенной зоны от морфологического состава двумерных твердых растворов $Mo_xW_{1-x}S_{2y}Se_{2(1-y)}$. Установлено, что при варьировании состава твердых растворов ДПМ ширина запрещенной зоны изменяется от 1.43 до 1.83 эВ. Показано, что полученные теоретические результаты качественно совпадают с экспериментальными данными.

Выводы. Минимальной шириной запрещенной зоны обладают твердые растворы, близкие по своему составу к $MoSe_2$, в то время как максимальной – структуры, близкие по своему составу к WS_2.

Ключевые слова: дихалькогениды переходных металлов, двумерные полупроводники, зонная структура, запрещенная зона, теория функционала плотности

• **Поступила:** 17.11.2021 • **Доработана:** 24.02.2022 • **Принята к опубликованию:** 19.04.2022

Для цитирования: Пименов Н.Ю., Лавров С.Д., Кудрявцев А.В., Авджиян А.Ю. Моделирование зонной структуры двумерных твердых растворов $Mo_xW_{1-x}S_{2y}Se_{2(1-y)}$. *Russ. Technol. J.* 2022;10(3):56–63. https://doi.org/10.32362/2500-316X-2022-10-3-56-63

Прозрачность финансовой деятельности: Авторы не имеют финансовой заинтересованности в представленных материалах или методах.

Авторы заявляют об отсутствии конфликта интересов.

INTRODUCTION

The discovery by Novoselov and Geim of a method for obtaining graphene in 2004 [1] aroused great interest in the study of various two-dimensional materials demonstrating unique physical properties. Transition metal dichalcogenides (TMDs) can be distinguished among such materials. TMDs comprise materials having the formula MX_2, where M is a transition metal (Mo, W, etc.) while X is a chalcogen (S, Se, etc.). The metal and chalcogen atoms have a predominantly covalent bond forming a hexagonal lattice. Bulk crystals have a layered structure with weak Van der Waals interactions between layers [2]. Unlike graphene, which has the characteristics of a semimetal, two-dimensional TMDs have a band gap. The key feature of such materials is a strong change in the configuration of their band structure with a change in thickness: for example, bulk TMD crystals are indirect-gap semiconductors, while two-dimensional crystals are referred to as direct-gap semiconductors [3]. Due to their direct transition-, high charge carrier mobility-, and a number of other properties [4], two-dimensional TMDs can be used as materials for creating photodetectors [5], phototransistors [6], solar cells [7], and other opto- and nanoelectronic devices [8].

The parameters of devices made on the basis of TMDs can be altered by varying the number of layers, as well as their composition, deformation, etc. The direct-gap transition in two-dimensional TMDs promotes efficient absorption and generation of light, which is important in optical applications. An important characteristic that determines the optical absorption of a material is the band gap. In two-dimensional TMDs, the band gap is on the order of 1–2 eV, which corresponds to the visible and near infrared regions of the spectrum. Since the number of available TMDs is very limited, the region of the spectral range used is discrete. One approach to solving this problem, which involves the synthesis of various structures comprising more than two types of atoms is possible due to the similar atomic structure of various TMDs, allowing the creation of alloys based on them (for example, $MoS_{2x}Se_{2(1-x)}$ or $Mo_xW_{x-1}S_2$) [9]. In addition, many works have been devoted to the creation and study of heterostructures consisting of two TPM layers of different composition (for example, MoS_2/WS_2) [10] and "Janus monolayers" (materials having the formula MXY, where M is a transition metal atom enclosed between two homogeneous layers of different chalcogens X and Y), such as MoSSe or WSSe [11].

The use of alloys of two-dimensional TMDs is due to the fact that, by changing the morphological composition, one can quite accurately control the band gap. This, in turn, allows for controlling the absorption spectrum over the entire range of possible values. The non-linear nature of the dependence of the band gap on the morphological composition of the solid solution makes it difficult to select the required concentration to achieve the required parameters. In this regard, there is a need to determine this dependence.

At present, although there is a large number of works devoted to the study of three-component structures [12, 13], more complex structures remain poorly studied. In this regard, within the framework of the present work, a theoretical calculation of the band structure of two-dimensional $Mo_xW_{1-x}S_{2y}Se_{2(1-y)}$ alloys at $x, y \in 0–1$ was carried out to determine the dependence of the band gap on the morphological composition.

METHODS

All calculations in this work were carried out from first principles (*ab inito*) within the framework of density functional theory (DFT) involving the Perdue–Burke–Eisernhoff exchange-correlation functional [14] and ultrasoft pseudopotentials. The calculations were performed in the Quantum Espresso software environment [15]. The minimum cutoff kinetic energy was selected as 80 Ry, while the dimensions of the *k*-point sampling grid were 8 × 8 × 1. The generation of singular *k*-points in the first Brillouin zone was performed by the Monkhrust–Pack method [16]. The unit cell of a monolayer TMD contains 1 metal atom and 2 chalcogen atoms. For calculations, a supercell was generated with a dimension of 2 × 2 unit cells and including 4 metal atoms and 8 chalcogen atoms. The supercell structure is shown in Fig. 1.

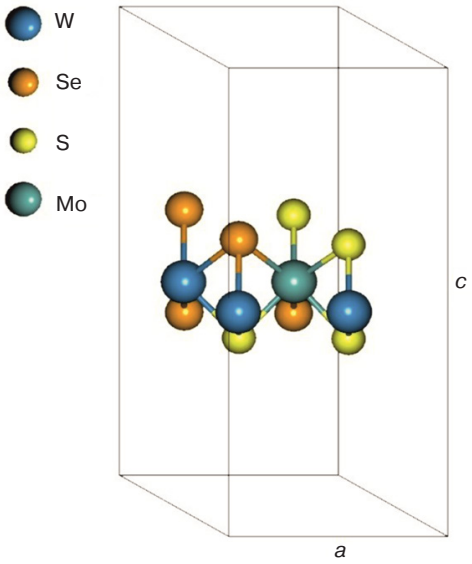

Fig. 1. Structure of the 2 × 2 $Mo_xW_{1-x}S_{2y}Se_{2(1-y)}$ supercell

In order to eliminate the influence of neighboring layers, the cell parameter ratio *c*/*a* was set to about 2.5.

Two-dimensional TMD alloy crystallites were fabricated from commercially available bulk TMD crystals (6Carbon Technology, Shenzhen, China)[1] by mechanical exfoliation onto a Si/SiO_2 substrate. The initial samples were a series of $MoS_{2x}Se_{2(x-1)}$ with different chalcogen concentrations. The parameter *x* in the series varied from 0 to 1 with a step of 0.1–0.2. The presence of interference effects allowed the thickness of the created two-dimensional crystallites to be estimated using optical confocal microscopy [17].

An experimental study of the photoluminescent characteristics of the created two-dimensional solid solutions of semiconductors was carried out using photoluminescent microscopy-spectroscopy. A solid-state laser having a wavelength of 532 nm was used as a laser pump source. Next, the radiation was focused by an objective on the sample fixed on the scanning stage. The power density of the optical pump radiation was approximately 15 mW/μm^2. A photomultiplier coupled to an optical monochromator was used for detecting optical radiation.

RESULTS AND DISCUSSION

The band structures of two-dimensional $Mo_xW_{1-x}S_{2y}Se_{2(1-y)}$ alloys were calculated in several stages. First, the two-component TMDs—MoS_2, WS_2, $MoSe_2$, and WSe_2—were calculated using the corresponding unit cells. After that, the obtained results were compared with the calculations carried out earlier using a similar method. At the second stage, three-component TMDs $Mo_xW_{1-x}S_2$, $Mo_xW_{1-x}Se_2$, $MoS_{2y}Se_{2(1-y)}$, and $WS_{2y}Se_{2(1-y)}$ of various morphological compositions were calculated. At the final stage, the four-component TMDs $Mo_xW_{1-x}S_{2y}Se_{2(1-y)}$ were calculated and a general graph of the dependence of the band gap on the morphological composition of the structures under study was constructed.

The band structures of two-dimensional MoS_2, MoS_{e2}, WS_2, and WSe_2 calculated at the first stage are shown in Fig. 2.

In all calculated structures, a direct-gap transition is observed at the K point of the Brillouin zone. The band gap E_g, the unit cell parameter *a* obtained in the course of calculations, and the results obtained using a similar technique [18] are shown in Table.

Table. Theoretical results for two-component TMDs

TMD	a_{theor}, Å	*a*, Å [18]	$E_{g\ theor}$, eV	E_g, eV [18]
MoS_2	3.18	3.18	1.69	1.68
$MoSe_2$	3.32	3.32	1.44	1.45
WS_2	3.19	3.18	1.79	1.82
WSe_2	3.33	3.32	1.55	1.55

The calculation of three-component TMD alloys was carried out for two cases, the first when the concentration of transition metal atoms changes and the second at an altered concentration of chalcogen atoms. Figure 3 shows the dependences of the band gap E_g and the supercell parameter *a* for two-dimensional $Mo_xW_{1-x}S_2$ and $Mo_xW_{1-x}Se_2$ alloys on changes in the concentration of transition metals in their composition.

Both cases are characterised by a decrease in the band gap with the predominance of Mo. The $Mo_xW_{1-x}S_2$ alloys are also characterized by a larger band gap than $Mo_xW_{1-x}Se_2$ by 0.3 eV on average. The supercell parameter varies insignificantly (within a few hundredths of Å) and is on average 6.36 Å and 6.64 Å for $Mo_xW_{1-x}S_2$ and $Mo_xW_{1-x}Se_2$, respectively.

Similar calculation results for the dependences $MoS_{2y}Se_{2(1-y)}$ and $WS_{2y}Se_{2(1-y)}$ having different chalcogen ratios are shown in Fig. 4.

For both alloys, an increase in the concentration of S in the composition leads to an increased the band gap; in this case, the supercell parameter decreases with the predominance of S in the composition (by about 0.3 Å when going from Se to S).

To experimentally verify the theoretical results, the luminescence spectra of two-dimensional TMD alloys created by mechanical exfoliation were obtained. The obtained luminescence spectra are shown in Fig. 5a. It can be seen that all spectra have a characteristic

[1] URL: http://www.6carbon.com/index-en.php. Accessed August 3, 2021.

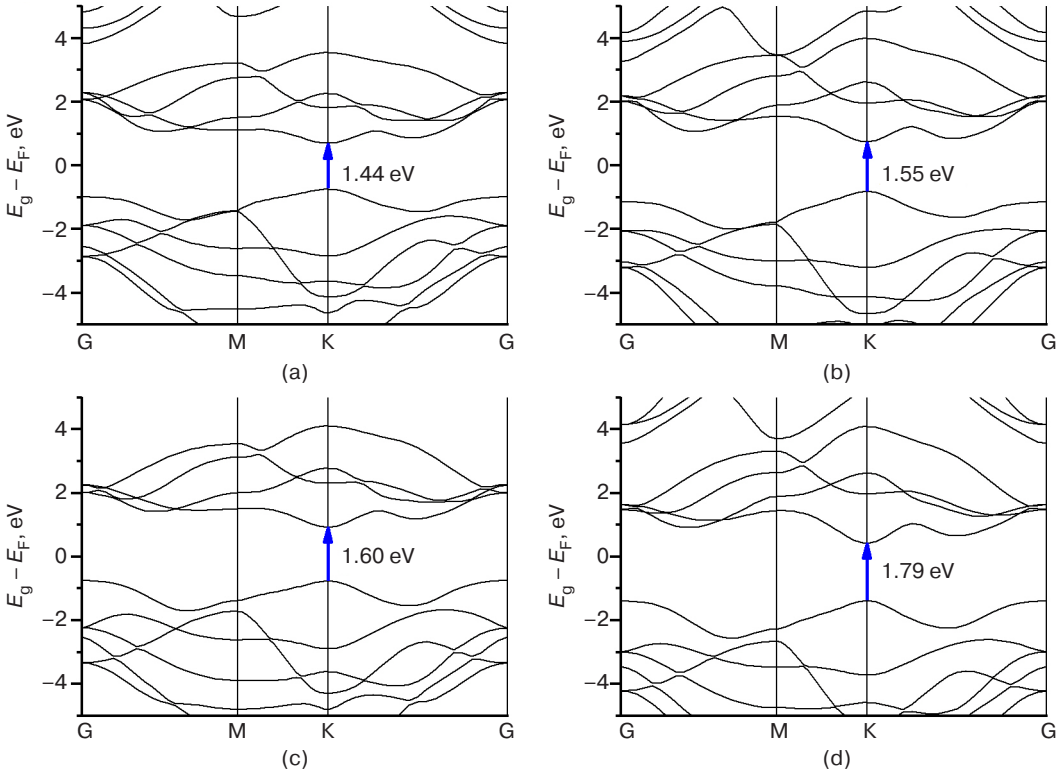

Fig. 2. Calculated band structures of (a) $MoSe_2$, (b) WSe_2, (c) MoS_2, and (d) WSe_2. G, K, and M are the characteristic points of the Brillouin zone

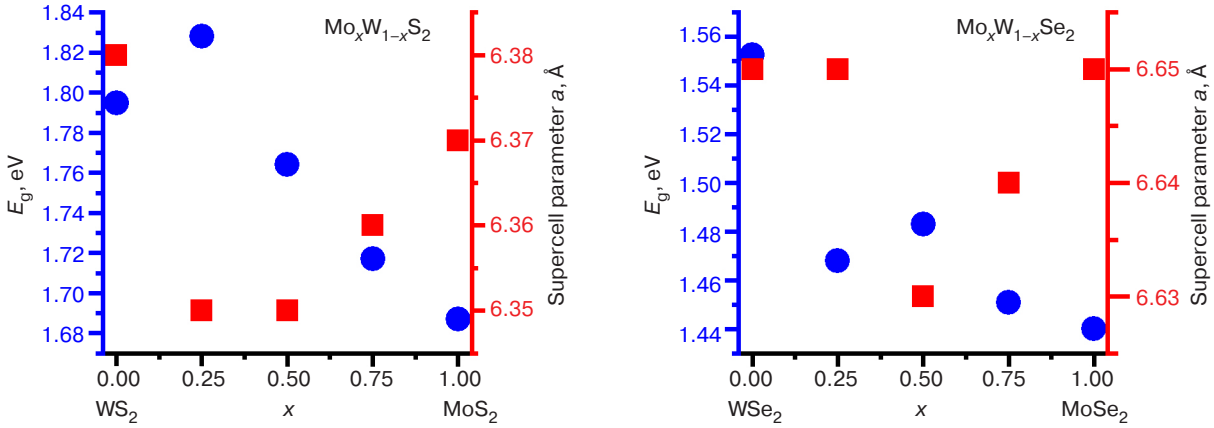

Fig. 3. Dependence of the band gap (circle) and the supercell parameter (square) on the ratio of transition metals for $Mo_xW_{1-x}S_2$ and $Mo_xW_{1-x}Se_2$, where x is the relative concentration of Mo atoms in the composition

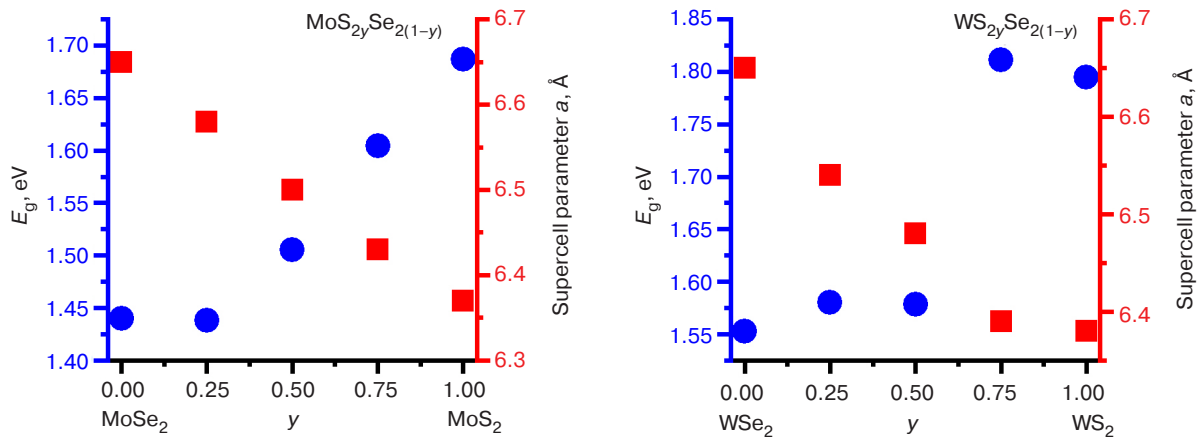

Fig. 4. Dependence of the band gap (circle) and the supercell parameter (square) on the ratio of chalcogens for $MoS_{2y}Se_{2(1-y)}$ and $WS_{2y}Se_{2(1-y)}$, where y is the relative concentration of S atoms in the composition

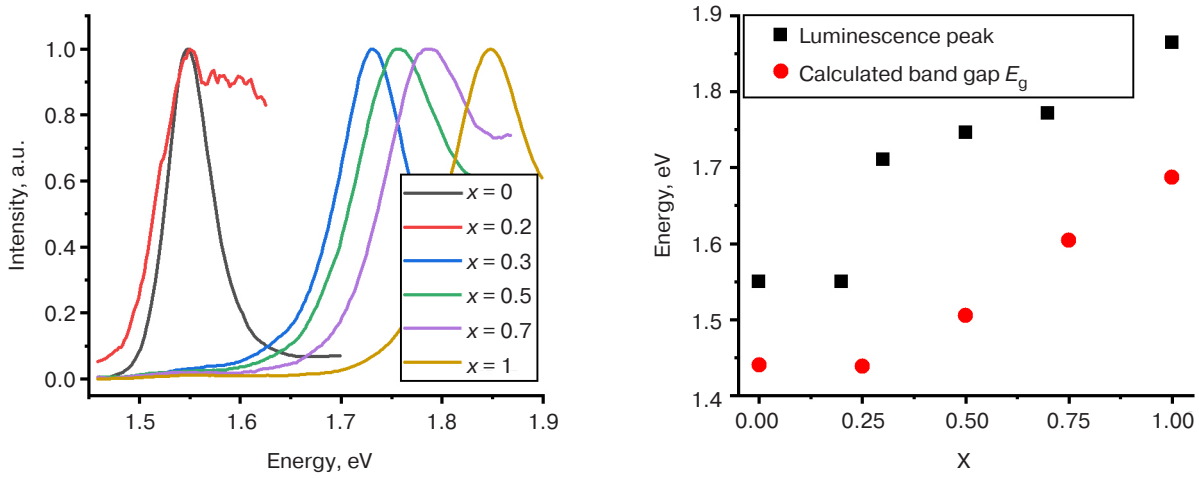

Fig. 5. (a) Luminescence spectra of alloys of two-dimensional TPM crystallites of $MoS_{2x}Se_{2(x-1)}$; (b) comparison of the theoretically calculated band gap of $MoS_{2x}Se_{2(x-1)}$ and the position of the maximum of their luminescence peak. X is the *x* value for $MoS_{2x}Se_{2(x-1)}$

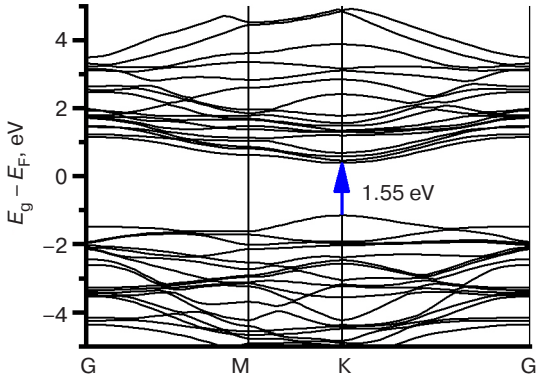

Fig. 6. Calculated band structure of the $Mo_{0.25}W_{0.75}S_{0.5}Se_{1.5}$ alloy

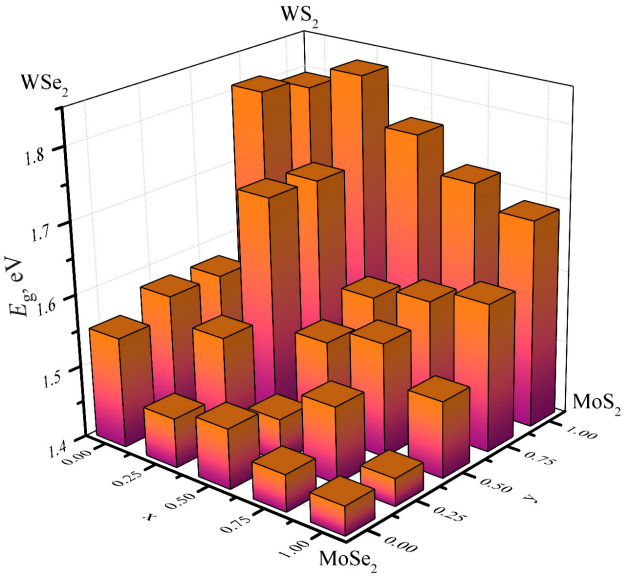

Fig. 7. Dependence of the band gap on the morphological composition of two-dimensional $Mo_xW_{1-x}S_{2y}Se_{2(1-y)}$ alloys, where *x* is the relative concentration of Mo atoms and *y* is the relative concentration of S atoms in the composition

maximum in the range from 1.55 to 1.85 eV. The positions of the maxima for each of the studied compositions are plotted together with the obtained theoretical results of the band gap in Fig. 5b. It can be seen from the presented results that the theoretical and experimental values at all TMD concentrations differ by a fixed value of approximately 0.2 eV. This is because DFT systematically underestimates the band gap; as a result, the data obtained by calculations are somewhat smaller than the experimental data [19].

The last step was the calculation of four-component $Mo_xW_{1-x}S_{2y}Se_{2(1-y)}$ alloys of various compositions. The band gap values were determined from the obtained band structures. An example of the calculated band structure for the $Mo_{0.25}W_{0.75}S_{0.5}Se_{1.5}$ alloy is shown in Fig. 6.

As in two-component alloys, a direct-gap transition is observed in all calculated four-component $Mo_xW_{1-x}S_{2y}Se_{2(1-y)}$ alloys at the K point of the Brillouin zone. Figure 7 shows the dependence of the band gap on the morphological composition of alloys of $Mo_xW_{1-x}S_{2y}Se_{2(1-y)}$ for $x, y \in 0–1$.

The results show that in two-dimensional $Mo_xW_{1-x}S_{2y}Se_{2(1-y)}$ alloys of various morphological compositions, the band gap can be varied within the range of 1.83 eV to 1.43 eV. In this case, the minimum values of the band gap have similar morphological composition structures to the $MoSe_2$ monolayer, while the maximum values are similar to those of the WS_2 monolayer.

CONCLUSIONS

In this work, a theoretical calculation of the band structure of monolayer $Mo_xW_{1-x}S_{2y}Se_{2(1-y)}$ alloys was carried out. It was determined that all the calculated structures are direct-gap semiconductors with a transition to the K point of the Brillouin zone. It is shown that the

supercell parameter depends weakly on the change in the concentration of transition metals (Mo and W) but is determined to a greater extent by the concentration of chalcogens (i.e., it decreases when going from Se to S). In two-dimensional $Mo_xW_{1-x}S_{2y}Se_{2(1-y)}$ alloys, it is possible to obtain structures having a band gap ranging from 1.43 eV (for alloys with the compositions close to that of $MoSe_2$) to 1.83 eV (for alloys with the compositions close to WS_2). A comparison of the theoretical results with the experimental data showed a qualitative agreement of the dependences. In this case, it is important to take into account that DFT systematically underestimates the band gap by approximately 0.2 eV. Further improvement of the obtained results implies an increase in the dimension of the supercell, making it possible to obtain band gap values for a larger set of $Mo_xW_{1-x}S_{2y}Se_{2(1-y)}$ structures of various morphological compositions.

ACKNOWLEDGMENTS

This work was supported by the Russian Science Foundation (grant No. 19-72-10165). Experimental studies were carried out using the equipment of the Center for Collective Use at the MIREA – Russian Technological University.

Authors' contributions

N.Yu. Pimenov and **A.V. Kudryavtsev**—zone structure simulation of the alloys under study.

S.D. Lavrov and **A.Yu. Avdizhiyan**—experimental study of photoluminescent characteristics of alloys.

REFERENCES

1. Novoselov K.S., Geim A.K., Morozov S.V., Jiang D., Zhang Y., Dubonos S.V., Grigorieva I.V., Firsov A.A. Electric field effect in atomically thin carbon films. *Science*. 2004;306(5696):666–669. https://doi.org/10.1126/science.1102896
2. Chernozatonskii L.A., Artyukh A.A. Quasi-two-dimensional transition metal dichalcogenides: structure, synthesis, properties, and applications. *Phys.-Usp.* 2018;61(1):2–28. https://doi.org/10.3367/UFNe.2017.02.038065
3. Yun W.S., Han S.W., Hong S.C., Kim I.G., Lee J.D. Thickness and strain effects on electronic structures of transition metal dichalcogenides: 2H-MX_2 semiconductors (M = Mo, W; X = S, Se, Te). *Phys. Rev. B*. 2012;85(3):033305. https://doi.org/10.1103/PhysRevB.85.033305
4. Huo N., Yang Y., Wu Y.-N., Zhang X.-G., Pantelides S.T., Konstantatos G. High carrier mobility in monolayer CVD-grown MoS_2 through phonon suppression. *Nanoscale*. 2018;10(31):15071–15077. https://doi.org/10.1039/C8NR04416C
5. Taffelli A., Dirè S., Quaranta A., Pancheri L. MoS_2 Based photodetectors: a review. *Sensors*. 2021;21(8):2758. https://doi.org/10.3390/s21082758
6. Shin G. H., Park C., Lee H.J., Jin H.J., Choi S.-Y. Ultrasensitive phototransistor based on WSe_2-MoS_2 van der Waals heterojunction. *Nano Lett*. 2020;20(8):5741–5748. https://doi.org/10.1021/acs.nanolett.0c01460
7. Wang T., Zheng F., Tang G., Cao J., You P., Zhao J., Yan F. 2D WSe_2 flakes for synergistic modulation of grain growth and charge transfer in tin-based perovskite solar cells. *Adv. Sci.* 2021;8(11):2004315. https://doi.org/10.1002/advs.202004315
8. Choi W., Choudhary N., Han G.H., Park J., Akinwande D., Lee Y.H. Recent development of two-dimensional transition metal dichalcogenides and their applications. *Mater. Today*. 2017;20(3):116–130. https://doi.org/10.1016/j.mattod.2016.10.002
9. Su S.-H., Hsu W.-T., Hsu C.-L., Chen C.-H., Chiu M.-H., Lin Y.-C., Chang W.-H., Suenaga K., He J.-H., Li L.-J. Controllable synthesis of band-gap-tunable and monolayer transition-metal dichalcogenide alloys. *Front. Energy Res.* 2014;2:27. https://doi.org/10.3389/fenrg.2014.00027
10. Li M.-Y., Chen C.-H., Shi Y., Li L.-J. Heterostructures based on two-dimensional layered materials and their potential applications. *Mater. Today*. 2016;19(6):322–335. https://doi.org/10.1016/j.mattod.2015.11.003
11. Petrić M.M., Kremser M., Barbone M., Qin Y., Sayyad Y., Shen Y., Tongay S., Finley J.J., Botello-Méndez A.R., Müller K. Raman spectrum of Janus transition metal dichalcogenide monolayers WSSe and MoSSe. *Phys. Rev. B.* 2021;103(3):035414. https://doi.org/10.1103/PhysRevB.103.035414
12. Ernandes C., Khalil L., Almabrouk H., Pierucci D., Zheng B., Avila J., Dudin P., Chaste J., Oehler F., Pala M., Bisti F., Brulé T., Lhuillier E., Pan A., Ouerghi A. Indirect to direct band gap crossover in two-dimensional $WS_{2(1-x)}Se_{2x}$ alloys. *npj 2D Mater. Appl.* 2021;5(1):7. https://doi.org/10.1038/s41699-020-00187-9
13. Wang Z., Sun J., Wang H., Lei Y., Xie Y., Wang G., Zhao Y., Li X., Xu H., Yang X., Feng L., Ma X. 2H/1T′ phase $WS_{2(1-x)}Te_{2x}$ alloys grown by chemical vapor deposition with tunable band structures. *Appl. Surf. Sci.* 2020;504:144371. https://doi.org/10.1016/j.apsusc.2019.144371
14. Perdew J.P., Burke K., Ernzerhof M. Generalized gradient approximation made simple. *Phys. Rev. Lett*. 1996;77(18):3865–3868. https://doi.org/10.1103/PhysRevLett.77.3865
15. Giannozzi P., Baroni S., Bonini N., Calandra M., Car R., Cavazzoni C., Ceresoli D., Chiarotti G.L., Cococcioni M., Dabo I., Corso A.D., Gironcoli S., Fabris S., Fratesi G., Gebauer R., Gerstmann U., Gougoussis C., Kokalj A., Lazzeri M., Martin-Samos L., Marzari N., Mauri F., Mazzarello R., Paolini S., Pasquarello A., Paulatto L., Sbraccia C., Scandolo S., Sclauzero G., Seitsonen A. P., Smogunov A., Umari P., Wentzcovitch R.M. QUANTUM ESPRESSO: a modular and open-source software project for quantum simulations of materials. *J. Phys.: Condens. Matter.* 2009;21(39):395502. https://doi.org/10.1088/0953-8984/21/39/395502
16. Monkhorst H.J., Pack J.D. Special points for Brillouin-zone integrations. *Phys. Rev. B.* 1976;13(12):5188–5192. https://doi.org/10.1103/PhysRevB.13.5188

17. Li S.-L., Miyazaki H., Song H., Kuramochi H., Nakaharai S., Tsukagoshi K. Quantitative Raman spectrum and reliable thickness identification for atomic layers on insulating substrates. *ACS Nano*. 2012;6(8):7381–7388. https://doi.org/10.1021/nn3025173
18. Zhuang H.L., Henning R.G. Computational search for single-layer transition-metal dichalcogenide photocatalysts. *J. Phys. Chem. C*. 2013;117(40):20440–20445. https://doi.org/10.1021/jp405808a
19. Huang J., Wang W., Fu Q., Yang L., Zhang K., Zhang J., Xiang B. Stable electrical performance observed in large-scale monolayer $WSe_{2(1-x)}S_{2x}$ with tunable band gap. *Nanotechnology*. 2016;27(13):13LT01. https://doi.org/10.1088/0957-4484/27/13/13LT01

About the authors

Nikita Yu. Pimenov, Postgraduate Student, Department of Nanoelectronics, Institute for Advanced Technologies and Industrial Programming, MIREA – Russian Technological University (78, Vernadskogo pr., Moscow, 119454 Russia). E-mail: nikitapimenov13@gmail.com. ResearcherID ABB-2465-2021, https://orcid.org/0000-0001-9882-8647

Sergey D. Lavrov, Cand. Sci. (Phys.-Math.), Associate Professor, Senior Researcher, Department of Nanoelectronics, Institute for Advanced Technologies and Industrial Programming, MIREA – Russian Technological University (78, Vernadskogo pr., Moscow, 119454 Russia). E-mail: sdlavrov@mail.ru. Scopus Author ID 55453548100, ResearcherID G-2912-2016, https://orcid.org/0000-0002-9432-860X

Andrey V. Kudryavtsev, Cand. Sci. (Phys.-Math.), Associate Professor, Researcher, Department of Nanoelectronics, Institute for Advanced Technologies and Industrial Programming, MIREA – Russian Technological University (78, Vernadskogo pr., Moscow, 119454 Russia). E-mail: kudryavcev_a@mirea.ru. Scopus Author ID 55219889700, ResearcherID O-1457-2016, https://orcid.org/0000-0002-2126-7404

Artur Yu. Avdizhiyan, Cand. Sci. (Phys.-Math.), Junior Researcher, Department of Nanoelectronics, Institute for Advanced Technologies and Industrial Programming, MIREA – Russian Technological University (78, Vernadskogo pr., Moscow, 119454 Russia). E-mail: avdizhiyan@mirea.ru. Scopus Author ID 57200646355, ResearcherID C-2190-2018, https://orcid.org/0000-0003-1766-5482

Об авторах

Пименов Никита Юрьевич, аспирант кафедры наноэлектроники Института перспективных технологий и индустриального программирования ФГБОУ ВО «МИРЭА – Российский технологический университет» (119454, Россия, Москва, пр-т Вернадского, д. 78). E-mail: nikitapimenov13@gmail.com. ResearcherID ABB-2465-2021, https://orcid.org/0000-0001-9882-8647

Лавров Сергей Дмитриевич, к.ф.-м.н., доцент, старший научный сотрудник кафедры наноэлектроники Института перспективных технологий и индустриального программирования ФГБОУ ВО «МИРЭА – Российский технологический университет» (119454, Россия, Москва, пр-т Вернадского, д. 78). E-mail: sdlavrov@mail.ru. Scopus Author ID 55453548100, ResearcherID G-2912-2016, https://orcid.org/0000-0002-9432-860X

Кудрявцев Андрей Владимирович, к.ф.-м.н., доцент, научный сотрудник кафедры наноэлектроники Института перспективных технологий и индустриального программирования ФГБОУ ВО «МИРЭА – Российский технологический университет» (119454, Россия, Москва, пр-т Вернадского, д. 78). E-mail: kudryavcev_a@mirea.ru. Scopus Author ID 55219889700, ResearcherID O-1457-2016, https://orcid.org/0000-0002-2126-7404

Авджиян Артур Юрьевич, к.ф.-м.н., младший научный сотрудник кафедры наноэлектроники Института перспективных технологий и индустриального программирования ФГБОУ ВО «МИРЭА – Российский технологический университет» (119454, Россия, Москва, пр-т Вернадского, д. 78). E-mail: avdizhiyan@mirea.ru. Scopus Author ID 57200646355, ResearcherID C-2190-2018, https://orcid.org/0000-0003-1766-5482

Translated by E. Shklovskii
Edited for English language and spelling by Thomas Beavitt

Micro- and nanoelectronics. Condensed matter physics

Микро- и наноэлектроника. Физика конденсированного состояния

UDC 537.6
https://doi.org/10.32362/2500-316X-2022-10-3-64-73

RESEARCH ARTICLE

Magnetoelectric effects in stripe- and periodic heterostructures based on nickel–lead zirconate titanate bilayers

Fedor A. Fedulov [@], Dmitriy V. Saveliev, Dmitriy V. Chashin, Vladimir I. Shishkin, Yuri K. Fetisov

MIREA – Russian Technological University, Moscow, 119454 Russia
[@] Corresponding author, e-mail: ostsilograf@ya.ru

Abstract

Objectives. A topical task in the design of magnetoelectric (ME) devices based on composite ferromagnetic–piezoelectric heterostructures involves reducing their dimensions to increase their operating frequencies and optimize their integration in modern electronics. The study set out to investigate the influence of in-plane dimensions on the characteristics of ME effects in stripe and periodic nickel–lead zirconate titanate heterostructures manufactured via electrolytic deposition.

Methods. Lead zirconate titanate disks with Ag-electrodes were used for manufacturing the ME heterostructures; Ni was deposited on one Ag-electrode only.

Results. While a reduction in stripe size leads to an increase in the frequency of the resonant ME effect, it is followed by a decrease in ME conversion efficiency. The ME coefficient for the periodic heterostructures is about ~1 V/(Oe·cm). By increasing the angle between the magnetic field H and the Ni-stripe axis from 0° to 90°, a 2.5-fold increase in the optimal field H_m and a 4-fold drop in the maximum amplitude of ME voltage $u_{max}(H_m)$ was achieved.

Conclusions. In periodic heterostructures, the frequency of the resonant ME effect is determined by the substrate's size, while ME conversion efficiency depends on the width of the Ni stripes and the distance between them. The observed anisotropy of the ME effects in the investigated heterostructures is explained in terms of demagnetization effects. In the future, the anisotropic ME effect in the periodic heterostructures could be used to develop magnetic field sensors that are sensitive to field orientation.

Keywords: magnetoelectric effect, magnetostriction, piezoelectric effect, anisotropy, magnetic field sensor

• **Submitted:** 24.11.2021 • **Revised:** 18.02.2022 • **Accepted:** 18.04.2022

For citation: Fedulov F.A., Saveliev D.V., Chashin D.V., Shishkin V.I., Fetisov Y.K. Magnetoelectric effects in stripe- and periodic heterostructures based on nickel–lead zirconate titanate bilayers. *Russ. Technol. J.* 2022;10(3):64–73. https://doi.org/10.32362/2500-316X-2022-10-3-64-73

Financial disclosure: The authors have no a financial or property interest in any material or method mentioned.

The authors declare no conflicts of interest.

НАУЧНАЯ СТАТЬЯ

Магнитоэлектрический эффект в двухслойных полосковых и периодических гетероструктурах никель – цирконат-титанат свинца

Ф.А. Федулов [@], **Д.В. Савельев**, **Д.В. Чашин**, **В.И. Шишкин**, **Ю.К. Фетисов**

МИРЭА – Российский технологический университет, Москва, 119454 Россия
[@] *Автор для переписки, e-mail: ostsilograf@ya.ru*

Резюме

Цели. Актуальной задачей при создании магнитоэлектрических (МЭ) устройств на основе композитных гетероструктур ферромагнетик-пьезоэлектрик является уменьшение их размеров, что позволит повысить рабочие частоты устройств и интегрировать их в современную электронику. Цель работы – исследование влияния размеров на характеристики МЭ эффектов в полосковых и периодических гетероструктурах никель – цирконат-титанат свинца, изготовленных методом электролитического осаждения.

Методы. Для изготовления образцов использовали диски циркоината-титаната свинца с Ag-электродами. На одну поверхность диска электролитически наносили слой Ni. Исследовали резонансную частоту МЭ эффекта, коэффициент МЭ преобразования на этой частоте и величину оптимального магнитного поля смещения для полученных образцов.

Результаты. Показано, что уменьшение размера в плоскости полосковых структур до ~1 мм приводит к росту частоты резонансного МЭ эффекта до ~1 МГц и одновременно к снижению эффективности МЭ преобразования. МЭ коэффициент для периодических гетероструктур с шириной Ni-полосок ~100 мкм и расстоянием между ними 20–100 мкм составляет ~1 В/(Э · см). Показано, что при увеличении угла φ между направлением постоянного поля H и осью Ni-полосок от 0° до 90° величина оптимального поля H_m возрастает в ~2.5 раза, а максимальная амплитуда напряжения $u_{max}(H_m)$ падает в 4 раза.

Выводы. В периодических структурах частота резонансного МЭ эффекта определяется размером подложки и может составлять единицы кГц, а эффективность преобразования полей зависит от ширины Ni-полосок и расстояния между ними. Обнаружена и объяснена анизотропия характеристик МЭ эффектов в исследованных гетероструктурах, возникающая из-за эффектов размагничивания. Анизотропия МЭ эффекта в периодических гетероструктурах может быть использована для создания датчиков постоянных магнитных полей, чувствительных к ориентации поля.

Ключевые слова: магнитоэлектрический эффект, магнитострикция, пьезоэлектрический эффект, анизотропия, датчик магнитного поля

• **Поступила:** 24.11.2021 • **Доработана:** 18.02.2022 • **Принята к опубликованию:** 18.04.2022

Для цитирования: Федулов Ф.А., Савельев Д.В., Чашин Д.В., Шишкин В.И., Фетисов Ю.К. Магнитоэлектрический эффект в двухслойных полосковых и периодических гетероструктурах никель – цирконат-титанат свинца. *Russ. Technol. J.* 2022;10(3):64–73. https://doi.org/10.32362/2500-316X-2022-10-3-64-73

Прозрачность финансовой деятельности: Авторы не имеют финансовой заинтересованности в представленных материалах или методах.

Авторы заявляют об отсутствии конфликта интересов.

INTRODUCTION

In recent years, much research attention has been attracted to the study of magnetoelectric (ME) effects in composite heterostructures containing ferromagnetic (FM) and piezoelectric (PE) layers due to the possibility of developing valuable devices based on these structures. Prototypes of highly sensitive ME sensors for determining constant and variable magnetic fields can be used in electrically controlled devices for processing radio signals, as well as in autonomous electrical energy sources [1–3]. It has been shown that ME effects arising in FM–PE structures due to mechanical coupling between the FM (magnetostriction) and PE (layers piezoelectricity) [4] are manifested in the generation of an alternating electrical voltage u by the structure under the action of an alternating magnetic field h (direct effect) or a change in the magnetization of the structure m under the action of an alternating electric field e (reverse effect). It has been shown that the efficiency of the ME field conversion increases by ~2 orders of magnitude when the frequency of the exciting field coincides with the acoustic resonance frequency of the structure [5]. At present, the main challenge lies in miniaturizing the ME elements to increase the operating frequencies of devices and integrate them into modern electronics and microsystems technologies. In addition, it is necessary to study the interaction of ME elements as part of spatially distributed structures for measuring magnetic fields in biology and medicine [6]. It has been experimentally shown that a decrease in the size of FM–PE heterostructures in the plane to ~0.5–1.0 cm leads to an increase in the acoustic resonance frequency of the structure f_0 and a decrease in the amplitude of the generated ME voltage $u(f_0)$ at this frequency [7].

In addition, the increased optimal bias magnetic field H_m arising due to demagnetization effects must be applied to the structure [8]. When using heterostructures having the form of long stripes, shape anisotropy becomes strong [9], which can be used to develop sensors for determining constant magnetic fields taking field direction into account [10]. To the best of the present authors' knowledge, no studies of the characteristics of ME effects in periodic structures containing a set of ME elements have been carried out to date.

The purpose of this work was to study the characteristics of ME effects in stripe and periodic heterostructures with an FM layer of nickel (Ni) and a PE layer of piezoceramic lead zirconate titanate (PZT) of millimeter and submillimeter dimensions in the plane. The choice of materials stems from the possibility of using electrodeposition technology to deposit thick layers of Ni to provide a sufficiently high magnetostriction in low magnetic fields. The first part of the work describes a method for fabricating Ni–PZT heterostructures in the form of separate stripes and a method for fabricating periodic structures in the form of a grating of Ni stripes on the surface of a PZT substrate, as well as measurement techniques. The second part presents the results of experimental studies of the ME characteristics of individual Ni–PZT stripes with linear dimensions of ~1–15 mm. In the third part of the work, the ME characteristics of Ni–PZT heterostructures with Ni-gratings with periods of 0.12–0.20 mm are described, including frequency, field, and amplitude dependences. According to the developed theory, the occurrence of a strong anisotropy is explained in terms of the ME effect in periodic structures taking into account the magnetic interaction between individual grating stripes. On the basis of the main conclusions, recommendations for future research are formulated.

MATERIALS AND METHODS

In order to experimentally study the influence of the linear dimensions of the ME structure on the characteristics of the direct resonant ME effect, structures of two types were fabricated. The first type consisted of two-layer composite heterostructures with layers of piezoelectric ceramics of lead zirconate titanate $PbZr_{0.52}Ti_{0.48}O_3$ (PZT) and Ni, whose schematic view and photographs are shown in Figs. 1a and 1b, respectively. Piezoceramic PZT was selected due to being a widely-available, isotropic and easily machined material. The ceramic piezoelectric modulus was $d_{31} \approx 175$ pC/m, and the permittivity $\varepsilon \approx 1700$. Ferromagnetic Ni layers have a high magnetostriction $\lambda_S = -30 \cdot 10^{-6}$ and saturate in low magnetic fields $H_S \approx 1$ kOe. The samples were fabricated using commercially available PZT disks of 25 mm in diameter and $a_p = 200$ μm thick with Ag electrodes of ~2-μm thick (Elpa Research Institute, Moscow, Russia). A layer of Ni with a thickness of $a_m \approx 10$ μm was deposited on one surface of the disk by electrolytic deposition from an aqueous solution of $NiCl_2$ and $NiSO_4$ salts [11]. At a current density of 1 A/cm^2, the Ni deposition rate was 1 μm/min. Stripes 1 mm wide were cut from the central part of the disk. Then structures with lengths L = 1.2, 2, 4, 6, 8, 10, 15, and 23 mm were fabricated from the stripes. By using the electrolytic deposition method, it was possible to fabricate monolithic structures with in-plane isotropic properties and good mechanical bonding between the layers.

ME structures of the second type comprised gratings of parallel Ni stripes deposited on the surface of a PZT substrate. The same disks of 25 mm in diameter and $a_p = 200$ μm thick with 2-μm thick Ag electrodes on the surfaces were used as the PZT substrate. A grating of Ni stripes was fabricated by the following method. First, both electrodes of the PZT disk were coated with

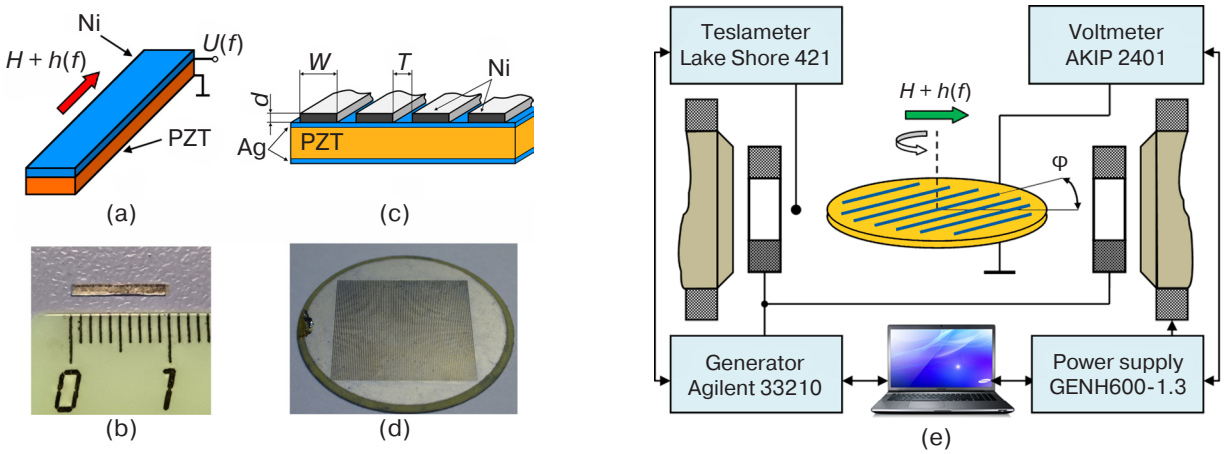

Fig. 1. View and schematics of researched composite Ni–PZT heterostructures (a)–(d) and block-diagram of the setup for measurements (e)

a layer of positive photoresist CRC Kontakt Chemie Positiv 20/200 (Belgium) having a thickness of ~2 μm. One of the surfaces was exposed through a 16 × 16 mm photomask in the form of parallel stripes to ultraviolet radiation for 60 s. Then, the exposed areas of the photoresist were removed with an aqueous solution of sodium hydroxide having a concentration of 6 g/L. After that, a Ni layer with a thickness of $a_m \approx 10$ μm was electrolytically deposited on the free sections of the Ag electrode. The cross section of the fabricated samples is shown schematically in Fig. 1c, while in Fig. 1d the visual appearance of one of the samples is depicted. This method was used to fabricate several structures with a grating of Ni stripes $w = 100$ μm wide and having a distance between stripes T = 20, 50, and 100 μm, respectively. For comparison, one of the surfaces of a sample was covered with a continuous layer ($T = 0$) of Ni having a thickness of $a_m \approx 10$ μm. The saturation magnetization of Ni measured on this sample was $M_S = 5900$ G; the saturation magnetostriction reached $\lambda_S = -30 \cdot 10^{-6}$ in the saturation field $H_S \approx 1$ kOe.

The block diagram of the setup for studying ME effects is shown in Fig. 1e. The samples were placed between Helmholtz coils with a radius of 15 cm connected to an Agilent 33210A generator (Agilent Technologies, USA). The coils generated an alternating exciting magnetic field $h\cos(2\pi ft)$ with a frequency f from 1 kHz to 2 MHz and an amplitude up to $h = 4$ Oe. A constant magnetic field H = 0–2 kOe was created using an electromagnet having a pole diameter of 50 mm connected to a TDK GENH600-1.3 power supply unit (TDK-Lambda Corporation, Germany). The H field was measured with a Lake Shore 421 Teslameter (Lake Shore Cryotronics, Westville, Ohio, USA). The fields h and H were applied in the plane of the structure and parallel to each other. In studying the anisotropy of the ME effect, the heterostructure with the Ni grating was rotated around the vertical axis by changing the angle φ between the fields and the axis of the Ni stripes. The voltage u, generated due to the ME effect between the electrodes of the PZT disk, was measured using an AKIP 2401 voltmeter having an input impedance of 10 MΩ. The dependences of the ME voltage on the excitation field frequency f and the bias field strength H were recorded for different orientations of the structure (angle φ). The setup was operated in automatic mode under the control of a specialized program in the *LabVIEW* environment[1]. The magnetostriction of the FM layer of the structure was measured using a strain gauge glued to the surface of the Ni film; the magnetization curves of the Ni film were measured using a Lake Shore 7407 vibrating magnetometer (Lake Shore Cryotronics, Westville, Ohio, USA).

MAGNETOELECTRIC EFFECT IN Ni–PZT STRIPES

At the first stage, the linear ME effect was studied in two-layer Ni–PZT heterostructures taking the form of stripes of different lengths L. Figure 2 shows the measured dependences of the ME voltage amplitude u on the frequency f of the exciting magnetic field with an amplitude h = 1.3 Oe for structures of different L. For each sample, the measurements were carried out in the optimal constant field H_m directed along the stripe axis at which the ME conversion is most efficient. As L decreases from 23 to 1.2 mm, the resonant frequency f_0 increases from 68.7 to 1380 kHz, while the signal amplitude at the resonant frequency drops by ~12 times. The quality factor of the resonances $Q = f_0/\Delta f$ (where Δf is the bandwidth at a level of 0.7) was $Q \approx 100$ for structures with L = 4–23 mm and then dropped to $Q \approx 67$ and $Q \approx 150$ as L decreased to 2.0 and 1.2 mm, respectively. Figure 2b shows the dependence

[1] The environment for creating applications for the collection, processing, and visualization of information received from instruments, laboratory facilities, process control and devices, was developed by National Instruments, USA. https://www.ni.com. Accessed November 22, 2021.

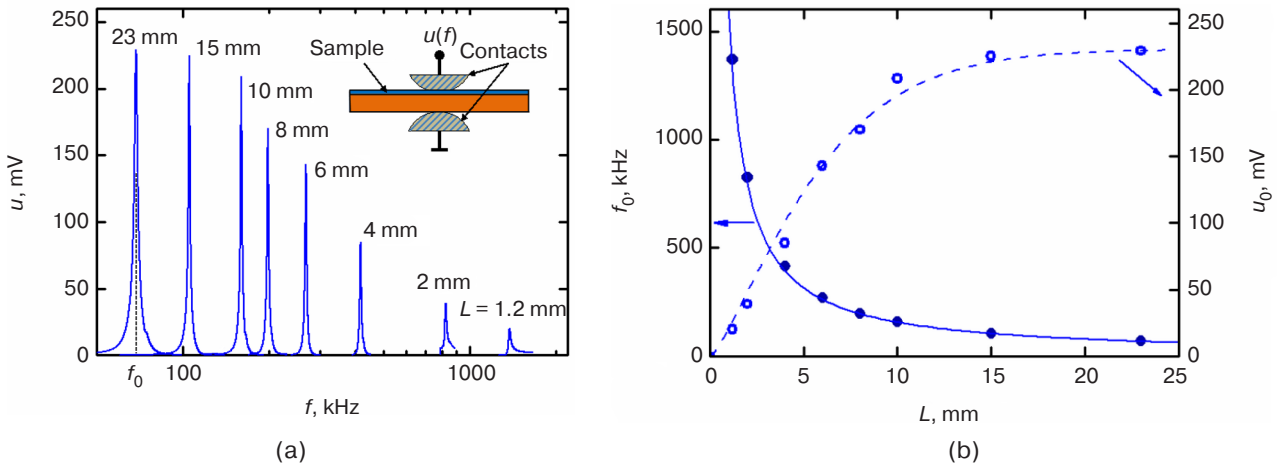

Fig. 2. (a) Dependences of the ME voltage amplitude u on the frequency f of the exciting magnetic field at a field amplitude h = 1.3 Oe for Ni–PZT stripes of different lengths L. The inset schematically shows the method of fixing the specimens; (b) Dependences of the resonant frequency f_0 and voltage u_0 generated at the frequency f_0 on the length of the Ni–PZT stripe L. The points are the experimental data, the solid line is the calculation by formula (1), the dashed line is the approximation

of the resonant frequency f_0 and the ME voltage at a given frequency u_0 on the length of the structure L. For a sample with a length L = 1.2 mm, the resonant frequency f_0 = 1380 kHz is almost 5 times higher than for a structure with a length of 5 mm described in [12]. The amplitude of the ME voltage, which remained constant at $u_0 \approx$ 230 mV for structures with a length L = 25–10 mm, then dropped approximately linearly to $u_0 \approx$ 19 mV as L decreased to 1.2 mm.

Figure 3 shows the dependences of the ME voltage u_0 on the constant magnetic field H for Ni–PZT stripes of different lengths L. The shape of the dependences is typical for the linear ME effect: initially, u_0 increases linearly with increasing H, subsequently reaching a maximum at H_m, which is different for each sample, then smoothly dropping to zero when the FM layer becomes saturated. As the stripe length decreases, the field H_m shifts to higher fields, while the voltage amplitude u_0 drops by a factor of ~12 at H_m.

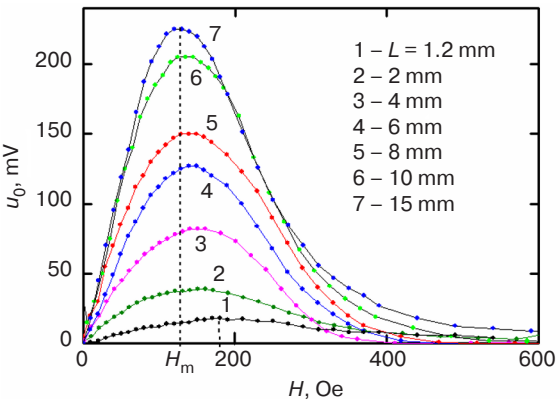

Fig. 3. Dependences of the ME voltage u_0 on the constant magnetic field H at h = 1.3 Oe for structures of various lengths L. The field H_m is only shown for a 15 mm long stripe

The most important characteristics of the ME effect in heterostructures are the resonant frequency f_0, the ME conversion coefficient at this frequency $\alpha_E = u(f_0)/(a_p h)$, and the magnitude of the optimal bias magnetic field H_m. The resonance frequency for the structures under study can be estimated from the formula for the frequency of the fundamental mode of acoustic oscillations of a free rod $f_0 = (1/2L)\sqrt{Y/\rho}$ [13]. The effective values of Young's modulus Y and density ρ for a Ni–PZT structure with two Ag-electrodes are obtained as $Y = \sum Y_k a_k / \sum a_k$ and $\rho = \sum \rho_k a_k / \sum a_k$, where Y_k, ρ_k, and a_k are Young's modulus, density, and thickness of the corresponding structure layer, respectively. Substituting the values of the layer parameters into the formula ($Y_m = 21.5 \cdot 10^{10}$ N/m^2, $Y_p = 7 \cdot 10^{10}$ N/m^2, $Y_{Ag} = 7.9 \cdot 10^{10}$ N/m^2; $\rho_m = 8.9 \cdot 10^3$ kg/m^3, $\rho_p = 7.7 \cdot 10^3$ kg/m^3, $\rho_{Ag} = 10.5 \cdot 10^3$ kg/m^3; a_m = 10 μm, a_p = 200 μm, a_{Ag} = 2 μm), we obtain the dependence of the resonance frequency on the sample length $f_0 = 1570/L$ kHz, where L is given in millimeters. The calculated dependence shown in Fig. 2b by a solid line satisfactorily describes the measurement data. We note that the frequency f_0 changed slightly (<1%) when the magnetic field H was tuned due to a change in the Young's modulus of the FM layer of the structure [14]. The maximum value of the ME coefficient for Ni–PZT stripes 15 mm long was $\alpha_E \approx$ 8.8 V/(Oe·cm). The observed increase in the optimal field H_m from ~120 to ~180 Oe along with a decrease in the length of the heterostructure from 15 to 1.2 mm is explained by the demagnetization effect [2]. The drop in the amplitude of the ME voltage with decreasing length L (and increasing frequency f_0) of the structure is mainly due to an increase in losses in the PZT layer caused by an increase in the resonance frequency. A decrease in the acoustic quality factor Q and the piezoelectric modulus d_{31} of the PZT layer with an increase in the resonance frequency can also lead to a voltage drop.

MAGNETOELECTRIC EFFECT IN PERIODIC Ni–PZT HETEROSTRUCTURES

At the second stage, the characteristics of the ME effect in periodic heterostructures with Ni-gratings were studied. As an example, Fig. 4 shows the dependences of the ME voltage u on the frequency f of the exciting field for structures in which the distance between the Ni stripes $T = 20$ μm and $T = 100$ μm for a field $h = 1$ Oe and a constant field $H = 90$ Oe is directed along the Ni stripes. The resonance peak near the frequency $f_0 \approx 2.74$ kHz with a quality factor $Q \approx 150$ at a level of 0.7 corresponds, as shown below, to the excitation of the lowest bending vibration modes of the structure. It can be seen that the amplitude of the peak u_0 decreases by several times, while the frequency f_0 increases slightly with greater distance between the Ni stripes. The value of the ME coefficient for a periodic structure with $T = 20$ μm at the resonance frequency was $\alpha_E \approx 1.0$ V/(Oe·cm), i.e., was of the same order as in structures with a continuous Ni layer [11].

Figure 5 demonstrates the transformation of the dependence $u_0(H)$ upon rotation of the direction of the field H in the plane of the structure for a structure with $T = 100$ μm. As the angle φ between the field H and the axis of the Ni stripes increases from zero to 90°, the value of H_m can be seen to increase from ~70 to ~230 Oe, while the maximum voltage amplitude $u_{max}(H_m)$ decreases monotonically from ~8 to ~ 2 mV.

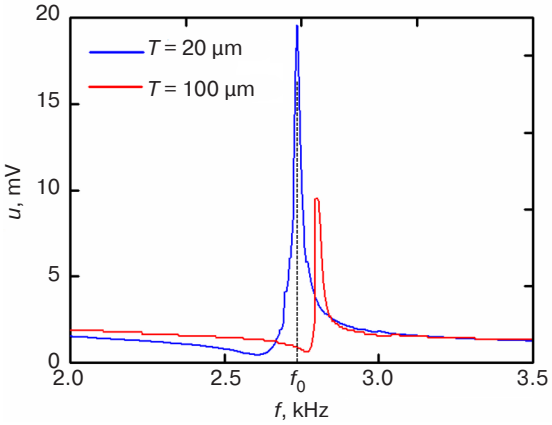

Fig. 4. Dependence of the ME voltage u on the frequency f of the exciting field for periodic Ni–PZT heterostructures with a distance between Ni stripes of 20 and 100 μm at a field $H = 90$ Oe directed along the Ni stripes

The angular dependences of the ME voltage u for the structure with $T = 100$ μm shown in Fig. 6 are constructed using data similar to those shown in Fig. 5. The curve demonstrates a strong anisotropy of the linear ME effect in the structure. Here the ME voltage can be seen to reach a maximum when the structure is magnetized along the Ni stripes (at φ = 0°) and drop by a factor of ~4 when magnetized across the stripes (at φ = 90°).

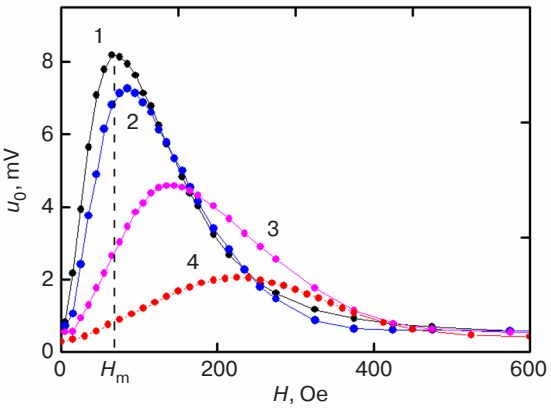

Fig. 5. Dependence of the voltage u_0 on the field H for a periodic Ni–PZT structure with $T = 100$ μm for different orientations of the field H: 1: φ = 0°, 2: φ = 30°, 3: φ = 60°, 4: φ = 90°

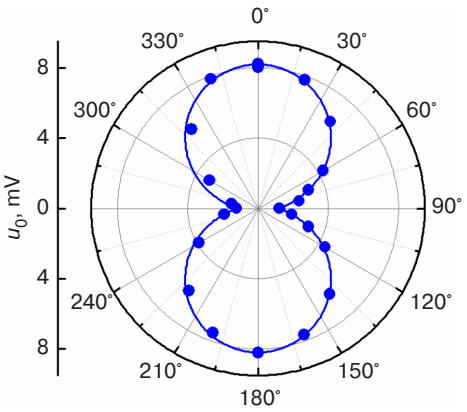

Fig. 6. Dependence of the voltage u_0 for a periodic Ni–PZT structure with $T = 100$ μm on the orientation angle φ of the field H in the plane. Points—experiment, solid line—calculation

In order to clarify the nature of the resonance peak shown in Fig. 4, the spatial structure of the Ni–PZT vibrational mode of the disk was visualized using the Chladni method. For this purpose, a thin layer of TiO_2 powder with a particle size of ~2–3 μm was poured onto the surface of a Ni–PZT disk excited at a resonance frequency $f_0 \approx 2.74$ kHz. The powder collected near the line of zero vertical displacement has the shape of a distorted circle as seen in Fig. 7a. The distribution of deformations of the disk flexural mode was also calculated using the *COMSOL Multiphysics*[2] software (COMSOL Group, Sweden). Figure 7b shows that the main oscillation mode has one nodal circle. The calculated frequency of this mode, $f_{cal} = 2.24$ kHz, agrees satisfactorily with the measured frequency of 2.74 kHz. The difference between the calculated and measured frequencies and the difference between the shape of the nodal diameter and the circle can be associated with the influence of the disk mounting location.

[2] The software for modeling constructions, devices, and processes in engineering, production, and scientific applications.

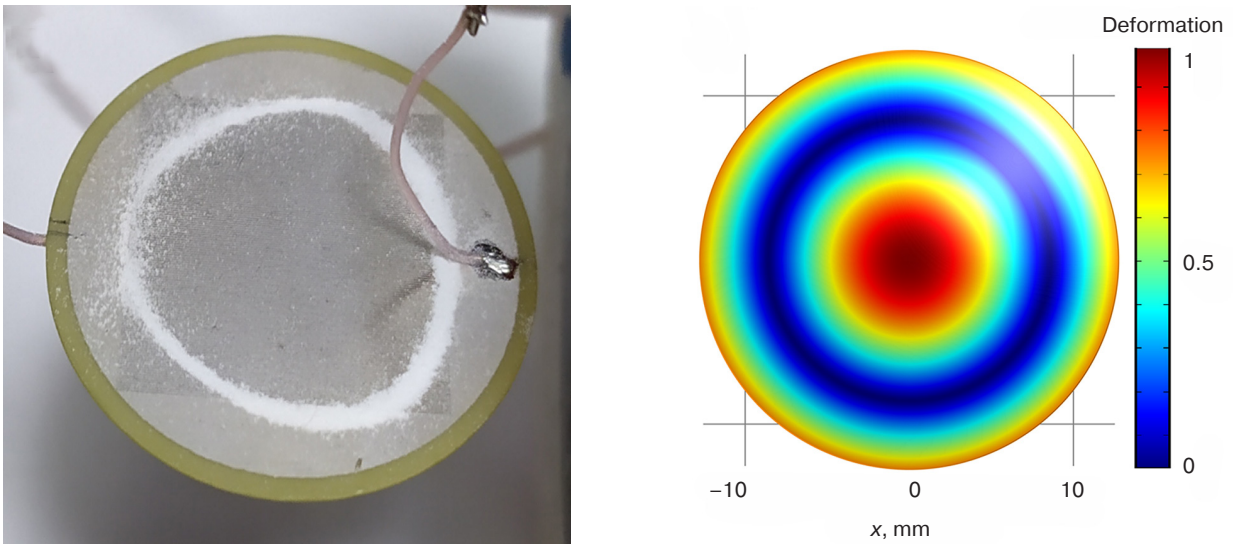

(a) (b)

Fig. 7. (a) Chladni figure for the Ni–PZT oscillation mode of the disk at the resonance frequency; (b) Ni–PZT disk flexural mode deformation distribution calculated in *COMSOL Multiphysics*

DISCUSSION OF RESULTS

To explain the characteristics of ME effects in stripes and periodic Ni–PZT heterostructures, we use the theory of the low-frequency linear ME effect in planar FM–PE structures [15]. The magnitude of the ME voltage generated by the structure at the resonance frequency is described by the simplified formula

$$u(H) \approx AQ\frac{d_{31}\lambda^{(1)}}{\varepsilon}h, \qquad (1)$$

where A is a constant coefficient depending only on the dimensions and mechanical parameters of the layers; Q is the quality factor of acoustic resonance; d_{31} and ε are the piezoelectric modulus and permittivity of the PE layer; $\lambda^{(1)}(H) = \partial\lambda / \partial H\big|_H$ is the piezomagnetic coefficient; $\lambda(H)$ is the field dependence of the magnetostriction of the FM layer; h is the amplitude of the exciting magnetic field. At the resonance frequency, the voltage amplitude increases by a factor of Q. It was observed in the experiment. The shape of the dependence $u_0(H)$ for the linear ME effect (see Fig. 3 and Fig. 5) is explained by the field dependence of the piezomagnetic coefficient $\lambda^{(1)}(H)$. The voltage reaches a maximum at the optimal field H_m corresponding to the maximum $\lambda^{(1)}$, and then drops due to a decrease in the piezomagnetic coefficient as the FM layer is saturated. The amplitude of the generated voltage u_0 increases linearly with the field h.

The anisotropy of the characteristics of the linear ME effect in the described structures arises due to demagnetization effects. Let us first consider the effect of demagnetization on the ME effect in one Ni stripe. It is known that in an FM sample of an ellipsoidal shape, the magnetic field inside the ferromagnetic H_{in} is related to the external field H by the relation [16]

$$H_{in} = H - NM(H_{in}), \qquad (2)$$

where N is the demagnetizing factor along the main axis of the ellipsoid; M is the magnetization of the ferromagnet.

For Ni, the relation $M = \chi H_{in} \approx \mu H_{in}$ is valid since the magnetic permeability $\mu = \chi + 1$ and the magnetic susceptibility χ are much greater than unity.

Then from (2) we obtain the relation

$$H_{in} \approx \frac{H}{1 + N\mu}, \qquad (3)$$

that is, due to demagnetization, the field H_{in} inside the ferromagnet decreases by a factor of $1 + N\mu$.

For a rectangular Ni stripe of ~20-mm long, 100-μm wide, and 10-μm thick, the calculation [17] gives demagnetizing factors $N_1 \approx 0.000002$ and $N_2 \approx 0.67$ when the field H is oriented in the plane along and across the stripe axis, respectively. Let us decompose the field H into two components $H_1 = H\cos\varphi$, parallel to the stripe axis, and $H_2 = H\sin\varphi$, perpendicular to the stripe axis. Relation (3) is applicable for each component separately.

The total field inside the stripe $H_{in} = \sqrt{H_{in1}^2 + H_{in2}^2}$. In this case, when the FM stripe is tangentially magnetized at an angle φ to its axis, the field inside the stripe can be found as

$$H_{in}(H,\varphi) = H\sqrt{\frac{\cos^2\varphi}{(1+N_1\mu)^2} + \frac{\sin^2\varphi}{(1+N_2\mu)^2}}. \qquad (4)$$

Differentiating (4) with respect to the magnetic field, we find the dependence of the piezomagnetic coefficient $\lambda^{(1)}(H, \varphi)$ on the magnitude of the field H and the angle φ specifying the orientation of the field with respect to the axis of the Ni stripes of the structure. It should also be taken into account that the value of the excitation field h_{in} inside the FM layer is similarly affected by demagnetization. Calculations have shown that with an increase in the angle φ, the optimal bias magnetic field H_m increases, while the magnitude of the ME voltage generated in this case $u_0(H_m)$ decreases; this is in agreement with the measurement data shown in Fig. 5. The angular dependence of the ME voltage amplitude $u_0(\varphi)$ calculated by the described method using expressions (1) and (4), the values of the parameters corresponding to the experiment, as well as the fitting coefficient $A_1 = 4.8 \cdot 10^{15}$ V^2/m, are shown by the solid line in Fig. 6. It can be seen that the proposed theory describes the results of the experiment well. Thus, by comparing the experimental data with the results of calculations taking into account the demagnetization in a single Ni stripe we conclude that the anisotropy of the linear ME effect can be qualitatively described in a periodic Ni–PZT heterostructure. Moreover, the magnitude of the anisotropy of the ME effect in structures with a grating-like Ni layer also depends on the distance between adjacent stripes. It was shown in [18–20] that the dipole–dipole interaction between neighboring FM stripes leads to a weakening of the demagnetization followed by an increase in the internal field in a ferromagnetic material.

To illustrate this point, a finite element simulation was carried out in the *COMSOL Multiphysics* software. The calculations were performed for a grating with dimensions in a plane of 16 × 16 mm, consisting of Ni stripes with a width W = 100 μm, a length L = 16 mm, and a thickness a_m = 10 μm. The distance between the stripes was changed from T = 0.5 μm to T = 100 μm. The magnitude of the external magnetic field and the relative magnetic permeability Ni were taken to be H = 90 Oe and μ = 350, respectively. The internal magnetic field H_{in} was calculated in the middle of the central Ni stripe of the grating. Figure 8 shows the calculated dependence of the field H_{in} on the distance T between the stripes when the grating is magnetized perpendicular to the stripe axis (curve 1).

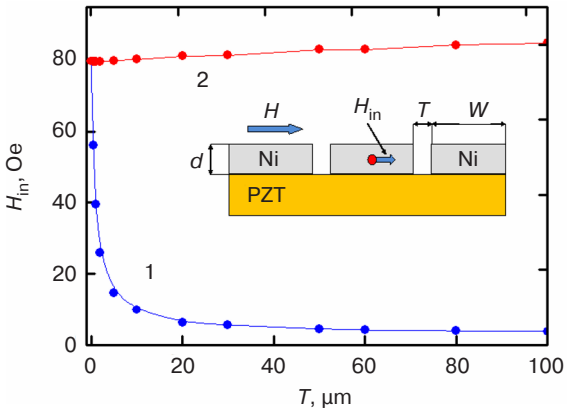

Fig. 8. Dependence of the internal field H_{in} in the middle of the central Ni stripe on the distance between the stripes of a grating magnetized in a field H = 90 Oe across (1) and along (2) the axis of the Ni stripes. The inset schematically shows the cross section of a Ni grating on a PZT substrate

At large distances $T >> a_m$, when each Ni stripe can be considered as isolated from the others, the field inside the central stripe is $H_{in} \approx H/(1 + \mu N_2) \approx 0.4$ Oe, i.e., the external field is weakened due to demagnetization. Figure 8 shows that the dipole–dipole interaction begins to manifest itself at $T \sim a_m = 10$ μm. As T decreases to zero (i.e., upon transition to a continuous Ni layer), the internal field becomes equal to $H_{in} \approx H/(1 + \mu N_3) \approx$ ≈ 79 Oe, where $N_3 \approx 0.0004$ is the demagnetizing factor for a continuous Ni layer with in-plane dimensions of 16 × 16 mm and a thickness of 10 μm [17]. When the structure is magnetized along the Ni stripes (curve 2 in Fig. 8), the internal field decreases insignificantly, from $H_{in} \approx H/(1 + \mu N_1) \approx 89.6$ Oe (isolated Ni stripe) to $H_{in} \approx H/(1 + \mu N_3) \approx 79$ Oe (solid Ni layer). Since the amplitude of the ME voltage depends on the internal field in the FM layer, a decrease in the distance between the Ni stripes leads to a decrease in the anisotropy of the linear ME effect. Thus, by changing the distance between the FM stripes in the grating, it is possible to control the magnitude of the internal field in the stripes, and, consequently, the anisotropy of the ME effect in periodic heterostructures. The described anisotropic ME effect in periodic heterostructures containing an FM layer in the form of a grating can be used to create magnetometers sensitive to the magnetic field orientation [21, 22].

CONCLUSIONS

It has been shown that the frequency of the resonant ME effect and the ME conversion coefficient in stripes based on Ni–PZT heterostructures are determined by the dimensions of the stripe in the plane. As the stripe length decreases from 23 to ~1 mm, the resonance frequency increases to ~1.4 MHz, while the ME conversion coefficient drops from $\alpha_E \approx 8.8$ V/(Oe·cm) to almost zero. In periodic heterostructures taking the form of a grating of Ni stripes on the surface of a PZT substrate, the frequency of the resonant ME effect is determined by the dimensions of the substrate in the plane, while the ME conversion coefficient depends on the width of the Ni stripes and the distance between the stripes. The ME coefficient for periodic heterostructures with a Ni stripe width of ~100 μm and a distance between them of 20–100 μm is ~1 V/(Oe·cm). Thus, in order to explain the anisotropy of the ME effect, it is necessary to change the

theory to take into account the effects of demagnetization when the orientation of the constant bias field relative to the stripe axis. The anisotropy of the ME effect in periodic heterostructures can be used to create sensors for constant magnetic fields that are sensitive to field orientation.

ACKNOWLEDGEMENTS

This study was supported by the Russian Science Foundation (grant No. 19-79-10128). Samples were produced with the financial support of the Grants Council of the President of the Russian Federation. Some of the measurements were carried out on the equipment of the Center for Collective Use at the MIREA – Russian Technological University.

Authors' contributions

F.A. Fedulov—conducting measurements, manufacturing samples.
D.V. Saveliev—conducting measurements.
D.V. Chashin—research methodology design.
V.I. Shishkin—processing of results.
Y.K. Fetisov—research concept development.

REFERENCES

1. Bichurin M., Petrov R., Sokolov O., Leontiev V., Kuts V., Kiselev D., Wang Y. Magnetoelectric magnetic field sensors: A review. *Sensors*. 2021;21(18):6322. https://doi.org/10.3390/s21186232
2. Gutierrez J., Lasheras A., Martins P., Pereira N., Barandiaran J.M., Lanseros-Mendes S. Metallic glass/PVDF magnetoelectric laminates for resonant sensors and actuators: A review. *Sensors*. 2017;17(6):1251. https://doi.org/10.3390/s17061251
3. Tu C., Chu Z.-Q., Spetzler B., et al. Mechanical-resonance-enhanced thin-film magnetoelectric heterostructures for magnetometers, mechanical antennas, tunable RF inductors, and filters. *Materials*. 2019;12(14):2259. https://doi.org/10.3390/ma12142259
4. Suchtelen van J. Product properties: a new application of composite materials. *Philips Res. Rep*. 1972;27:28–37.
5. Bichurin M., Filippov D., Petrov V., Laletsin V., Paddubnaya N., Srinivasan G. Resonance magnetoelectric effects in layered magneto-strictive-piezoelectric composites. *Phys. Rev. B*. 2003;68(13):10–13. https://doi.org/10.1103/PhysRevB.68.132408
6. Kopyl S., Surmenev R., Surmeneva M., Fetisov Y., Kholkin A. Magnetoelectric effect: principles and applications in biology and medicine – a review. *Mater. Today Bio*. 2021;12:100149. https://doi.org/10.1016/j.mtbio.2021.100149
7. Li L., Yao X., Gan L., Zhang X., Zhou J.-P. Magnetoelectric anisotropy in laminate composite for detecting magnetic field. *Func. Mater. Lett*. 2018;12(01):1850098. https://doi.org/10.1142/S1793604718500984
8. Vopsaroiu M., Stewart M., Fry T., Cain M., Srinivasan G. Tuning the magnetoelectric effect in multiferroic composites via crystallographic texture. *IEEE Trans. Magn*. 2008;44(11):3017–3020. https://doi.org/10.1109/TMAG.2008.2001649
9. Burdin D.A., Ekonomov N.A., Gordeev S.N., Fetisov Y.K. Anisotropy of ME effect in an amorphous ferromagnet-piezoelectric heterostructure. *J. Magn. Mag. Mater*. 2021;521(Part 2):167530. https://doi.org/10.1016/j.jmmm.2020.167530
10. Fetisov Y., Chashin D., Saveliev D., Fetisov L., Chamonin M. Anisotropic magnetoelectric effect in a planar heterostructure comprising piezoelectric ceramics and magnetostrictive fibrous composite. *Materials*. 2019;12(19):3228. https://doi.org/10.3390/ma12193228
11. Chashin D.V., Fetisov Y.K., Tafintseva E.V., Srinivasan G. Magnetoelectric effects in layered samples of lead zirconium titanate and nickel films. *Solid State Comm*. 2008;148(1–2):55–58. https://doi.org/10.1016/j.ssc.2008.07.015
12. Lasheras A., Gutierrez J., Barandiaran J.M. Quantification of size effects in the magnetoelectric response of metallic glass/PVDF laminates. *Appl. Phys. Lett*. 2016;108(22):222903. https://doi.org/10.1063/1.4953156
13. Timoshenko S. *Vibration Problems in Engineering*. NY: D. Van Nostrand Company Inc.; 1955. 468 p.
14. Nan T., Hui Y., Rinaldi M., Sun N.X. Self-biased 215 MHz magnetoelectric MEMS resonator for ultra-sensitive DC magnetic fields detection. *Sci. Rep*. 2013;3:1985. https://doi.org/10.1038/srep01985
15. Bichurin M., Petrov V., Srinivasan G. Theory of low-frequency magnetoelectric coupling in magnetostrictive-piezoelectric bilayers. *Phys. Rev. B*. 2003;68(5):1–13. https://doi.org/10.1103/PhysRevB.68.054402
16. Osborn J.A. Demagnetizing factors of the general ellipsoid. *Phys. Rev*. 1945;67(11–12):351–357. https://doi.org/10.1103/PhysRev.67.351
17. Chen D.X., Pardo E., Sanchez A. Demagnetizing factors of rectangular prisms and ellipsoids. *IEEE Trans. Magn*. 2002;38(4):1742–1752. https://doi.org/10.1109/TMAG.2002.1017766
18. Malkinski L.M., Yu M., Scherer II D.J. Magnetostatic interactions in two-dimensional arrays of magnetic strips. *Mater. Res. Symp. Proc*. 2010;1250:G08–03. https://doi.org/10.1557/PROC-1250-G08-03
19. Encinas-Oropesa A., Demand M., Piraux L., Huynen I., Ebels U. Dipolar interaction in arrays of nickel nanowires studied by ferromagnetic resonance. *Phys. Rev. B*. 2001;63(10):104415. https://doi.org/10.1103/PhysRevB.63.104415
20. Tartakovskaya E.V., Vovk A., Golub V. Dipolar interaction in ordered superlattices of ferromagnetic nanoparticles. *Phys. Stat. Sol. A*. 2008;205(8):1787–1789. https://doi.org/10.1002/pssa.200723610
21. Zhai J., Dong S., Xing Z., Li J., Viehland D. Geomagnetic sensor based on giant magnetoelectric effect. *Appl. Phys. Lett*. 2007;91(12):125513. https://doi.org/10.1063/1.2789391
22. Duc N.H., Tu B.D., Ngoc N.T., Lap V.D., Giang T.H. Metglas/PZT-magnetoelectric 2-D geomagnetic device for computing precise angular position. *IEEE Trans. Magn*. 2013;49(8):4839–4842. https://doi.org/10.1109/TMAG.2013.2241446

About the authors

Fedor A. Fedulov, Cand. Sci. (Eng.), Engineer, Scientific and Education Center "Magnetoelectric materials and devices," MIREA – Russian Technological University (78, Vernadskogo pr., Moscow, 119454 Russia). E-mail: ostsilograf@ya.ru. Scopus Author ID 57194284263, https://orcid.org/0000-0003-2188-0011

Dmitriy V. Saveliev, Postgraduate Student, Department of Nanoelectronics, Institute for Advanced Technologies and Industrial Programming, MIREA – Russian Technological University (78, Vernadskogo pr., Moscow, 119454 Russia). E-mail: dimsav94@gmail.com. Scopus Author ID 57196479660, ResearcherID D-8952- 2019, https://orcid.org/0000-0001-7762-9198

Dmitriy V. Chashin, Cand. Sci. (Eng.), Lead Engineer, Scientific and Education Center "Magnetoelectric materials and devices," MIREA – Russian Technological University (78, Vernadskogo pr., Moscow, 119454 Russia). E-mail: chashindv@ya.ru. Scopus Author ID 23977510200, https://orcid.org/0000-0002-1031-6696

Vladimir I. Shishkin, Cand. Sci. (Chem.), Assistant Professor, Deputy Director, Education and Science Association "Electronics," MIREA – Russian Technological University (78, Vernadskogo pr., Moscow, 119454 Russia). E-mail: shishkin@mirea.ru. https://orcid.org/0000-0002-2480-1182

Yuri K. Fetisov, Dr. Sci. (Phys.–Math.), Professor, Director, Scientific and Education Center "Magnetoelectric materials and devices," MIREA – Russian Technological University (78, Vernadskogo pr., Moscow, 119454 Russia). E-mail: fetisov@mirea.ru. Scopus Author ID 7003504213, https://orcid.org/0000-0002-8627-2730

Об авторах

Федулов Фёдор Александрович, к.т.н., инженер Научно-образовательного центра «Магнитоэлектрические материалы и устройства» ФГБОУ ВО «МИРЭА – Российский технологический университет» (119454, Россия, Москва, пр-т Вернадского, д. 78). E-mail: ostsilograf@ya.ru. Scopus Author ID 57194284263, https://orcid.org/0000-0003-2188-0011

Савельев Дмитрий Владимирович, аспирант кафедры наноэлектроники Института перспективных технологий и индустриального программирования ФГБОУ ВО «МИРЭА – Российский технологический университет» (119454, Россия, Москва, пр-т Вернадского, д. 78). E-mail: dimsav94@gmail.com. Scopus Author ID 57196479660, ResearcherID D-8952-2019, https://orcid.org/0000-0001-7762-9198

Чашин Дмитрий Владимирович, к.т.н., ведущий инженер Научно-образовательного центра «Магнитоэлектрические материалы и устройства» ФГБОУ ВО «МИРЭА – Российский технологический университет» (119454, Россия, Москва, пр-т Вернадского, д. 78). E-mail: chashindv@ya.ru. Scopus Author ID 23977510200, https://orcid.org/0000-0002-1031-6696

Шишкин Владимир Ильич, к.х.н., доцент, заместитель директора Учебно-научного объединения «Электроника» ФГБОУ ВО «МИРЭА – Российский технологический университет» (119454, Россия, Москва, пр-т Вернадского, д. 78). E-mail: shishkin@mirea.ru. https://orcid.org/0000-0002-2480-1182

Фетисов Юрий Константинович, д.ф.-м.н., профессор, директор Научно-образовательного центра «Магнитоэлектрические материалы и устройства» ФГБОУ ВО «МИРЭА – Российский технологический университет» (119454, Россия, Москва, пр-т Вернадского, д. 78). E-mail: fetisov@mirea.ru. Scopus Author ID 7003504213, https://orcid.org/0000-0002-8627-2730

Translated by E. Shklovskii
Edited for English language and spelling by Thomas Beavitt

Micro- and nanoelectronics. Condensed matter physics

Микро- и наноэлектроника. Физика конденсированного состояния

UDC 538.913, 538.958, 538.975
https://doi.org/10.32362/2500-316X-2022-10-3-74-84

RESEARCH ARTICLE

Polarization analysis of THz radiation using a wire grid polarizer and ZnTe crystal

Farkhad A. Zainullin [@], Dinar I. Khusyainov, Marina V. Kozintseva, Arseniy M. Buryakov

MIREA – Russian Technological University, Moscow, 119454 Russia
[@] Corresponding author, e-mail: madflyzero@gmail.com

Abstract

Objectives. Terahertz time domain spectroscopy (THz-TDS) is currently a promising research method in pharmacology and medicine due to the high sensitivity of terahertz radiation to the chemical composition and molecular structure of organic compounds. However, due to the chirality of many biomolecules, their analysis is performed by THz irradiation with circular dichroism. In particular, circular dichroism of THz radiation allows the study of "soft" vibrational movements of biomolecules with different chiralities. Therefore, when studying such biological materials, accurate control of THz radiation parameters is essential. The paper describes a method for characterizing THz radiation polarization on the example of a black phosphorus source material.

Methods. The analysis of polarization parameters of THz radiation experimentally obtained by THz-TDS and using terahertz polarizers was performed by mathematical modeling of the interaction between THz radiation and a ZnTe crystal as a detector.

Results. Two schemes of terahertz spectroscopy with the ZnTe crystal as the detector were discussed in detail. The polarization parameters were determined using one or two wire-grid THz polarizers. An expression for approximating the dependences of the peak-to-peak amplitude of THz radiation on the rotation angle of the wire-grid THz polarizer for these cases was derived. The impact of the terahertz electric field intensity value on the shape of polarization dependences was considered. The rotation angle of the polarization ellipse of THz radiation emitted by the surface of a bulk-layered black phosphorus crystal illuminated by femtosecond laser pulses was determined.

Conclusions. The amplitude of the THz radiation electric field intensity begins to impact the shape of polarization dependences when its value becomes comparable to or exceeds 40 kV/cm.

Keywords: time-resolved terahertz spectroscopy, ellipticity, polarization, electrooptic crystal, electrooptic sampling

• **Submitted:** 21.02.2022 • **Revised:** 13.04.2022 • **Accepted:** 26.04.2022

For citation: Zainullin F.A., Khusyainov D.I., Kozintseva M.V., Buryakov A.M. Polarization analysis of THz radiation using a wire grid polarizer and ZnTe crystal. *Russ. Technol. J.* 2022;10(3):74–84. https://doi.org/10.32362/2500-316X-2022-10-3-74-84

Financial disclosure: The authors have no a financial or property interest in any material or method mentioned.

The authors declare no conflicts of interest.

НАУЧНАЯ СТАТЬЯ

Анализ поляризации ТГц-излучения с помощью решетчатого поляризатора и кристалла ZnTe

Ф.А. Зайнуллин [@], Д.И. Хусяинов, М.В. Козинцева, А.М. Буряков

МИРЭА – Российский технологический университет, Москва, 119454 Россия
[@] Автор для переписки, e-mail: madflyzero@gmail.com

Резюме

Цели. Химический состав и молекулярная структура органических соединений обладают высокой чувствительностью к терагерцовому излучению. Поэтому терагерцовая спектроскопия во временно́й области в настоящее время является перспективным методом исследования в области фармакологии и медицины. Однако из-за того, что многие биомолекулы обладают хиральностью, их анализ проводится путем облучения ТГц-излучением с круговым дихроизмом. В частности, круговой дихроизм ТГц-излучения позволяет исследовать «мягкие» колебательные движения биомолекул с различной закрученностью. Точный контроль параметров этого излучения очень важен при исследовании биологических материалов. Цель работы – описать метод, позволяющий охарактеризовать поляризацию ТГц-излучения на примере использования черного фосфора в качестве источника.

Методы. Анализ параметров поляризации ТГц-излучения, экспериментально полученных методом спектроскопии временно́го разрешения, а также с использованием терагерцовых поляризаторов, проводился путем математического моделирования взаимодействия ТГц-излучения и кристалла ZnTe в качестве детектора.

Результаты. В работе подробно рассмотрены две схемы терагерцовой спектроскопии с кристаллом ZnTe в качестве детектора. Определение параметров поляризации выполнено с использованием одного или двух решетчатых ТГц-поляризаторов. Выведено выражение для аппроксимации зависимостей размаха амплитуды ТГц-излучения от угла поворота решетчатого ТГц-поляризатора для этих случаев. Рассмотрено влияние величины напряженности электрического поля терагерцового излучения на форму поляризационных зависимостей. Определен угол поворота эллипса поляризации ТГц-излучения, испускаемого поверхностью объемного слоистого кристалла черного фосфора при воздействии на него фемтосекундных лазерных импульсов.

Выводы. Амплитуда напряженности электрического поля ТГц-излучения начинает влиять на форму поляризационных зависимостей, когда ее величина становится сравнимой или превышает 40 кВ/см.

Ключевые слова: терагерцовая спектроскопия временно́го разрешения, эллиптичность, поляризация, электрооптический кристалл, электрооптическое стробирование

• **Поступила:** 21.02.2022 • **Доработана:** 13.04.2022 • **Принята к опубликованию:** 26.04.2022

Для цитирования: Зайнуллин Ф.А., Хусяинов Д.И., Козинцева М.В., Буряков А.М. Анализ поляризации ТГц-излучения с помощью решетчатого поляризатора и кристалла ZnTe. *Russ. Technol. J.* 2022;10(3):74–84. https://doi.org/10.32362/2500-316X-2022-10-3-74-84

Прозрачность финансовой деятельности: Авторы не имеют финансовой заинтересованности в представленных материалах или методах.

Авторы заявляют об отсутствии конфликта интересов.

INTRODUCTION

In recent years, the development of time-resolved THz spectroscopy technology has ensured an accurate and simple approach to analyzing material characteristics. Due to the non-ionizing interaction and strong penetrability of THz radiation, additional information on chemical composition or electron–phonon interaction in a sample may be obtained [1–3]. In contrast to infrared (IR) and Raman spectroscopy, THz spectroscopy is very sensitive to the molecular structure and intermolecular interactions in crystals, which is particularly valuable for medical research in pharmacology [4]. In addition, THz radiation excites longer wavelength vibrations, such as phonons in a semiconductor crystal or molecular vibrations in

organic matter, as compared to classical methods of mid-IR spectroscopy and X-ray diffraction. Therefore, it may ensure high reliability in identifying compounds that are difficult to distinguish by other methods [5]. The THz time-domain spectroscopy (THz-TDS) technique is used to analyze materials using THz radiation. This technique is applied to analyzing weak intermolecular interactions, such as lattice vibrations [6], hydrogen bonding [7], Van der Waals interaction [8], as well as collective vibrational modes determined by the molecular configuration, conformation, and general vibration of organic molecules [9]. In particular, THz pulses with elliptically polarized waves are of interest, both in terms of fundamental physics and technological applications. For example, many biomolecules have a chiral structure with rotational/vibrational modes in the terahertz energy range, whose interaction with elliptically polarized THz beams depends on the polarization of THz radiation and chirality of biomolecules. This allows, in particular, the study of "soft" vibrational modes of organic molecules having a different twist [10–12]. Therefore, in order to describe the interaction of THz pulse with the substance, the polarization parameters of THz radiation including ellipticity and rotation direction of the field vector should be obtained [13–15]. The electro-optical sampling technique involving the use of nonlinear optical ZnTe crystal (Russia) as a THz radiation detector in two detection versions based on phase- and amplitude modulation measurements is one of the most common THz-TDS method modifications [16].

Being one of the most promising components of THz devices in the layered semiconductor category, black phosphorus—BP (2dsemiconductors, USA)[1] crystallite was selected as the THz radiation source under study. This is primarily due to the fact that BP represents a "golden mean" between graphene (no bandgap) and semiconducting transition metal dichalcogenides (TMDs), such as molybdenum disulfide (MoS_2), which has a relatively large bandgap of about 2 eV [15]. Moreover, nanoscale films with band gap in the range from 1.5 eV to 0.53 eV may be obtained by varying the number of layers, from one to several [17]. The high carrier mobility of this material (much higher than in TMDs) is also dependent on the number of layers in the range from 299 to 3730 $cm^2/V{\cdot}c$ for electrons and from 337 to 10000 $cm^2/V{\cdot}c$ for holes [18, 19]. This allows THz radiation to be efficiently absorbed even though the photon energy is below the bandgap energy. It is also possible to tune (change) the bandgap width by applying a static electric field [17]. This dynamic bandgap tuning can be used not only to expand the operating wavelength range of BP based devices but also to pave the way for studying electrically tunable topological insulators and semimetals. In this case, the BP crystal allows elliptically polarized THz radiation to be obtained when exposed to linearly polarized femtosecond laser radiation [13].

In the present paper, two versions of polarization analysis of THz radiation are considered in detail. Analyzing in THz-TDS implies two wire-grid polarizers (WGP) used in the first version and one polarizer used in the second one.

METHODS

A variation of the THz-TDS technique allows THz radiation to be detected by electro-optical sampling. Polarization of the laser probe beam is modulated by the THz beam in the electro-optic ZnTe crystal. Using amplitude modulation [16], an optical polarizer crossed with the beam polarization direction is placed on the probe beam path after the ZnTe crystal and before the photodiode (ThorLabs, USA).[2] Under the action of the THz pulse, the beam polarization changes allowing a signal proportional to the amplitude of the THz radiation to be recorded on the diode. The detection method will be described further in more detail.

The electric displacement vector for a homogeneous medium is considered to describe the electro-optic effects in nonlinear optical crystals, as follows:

$$\mathbf{D} = \varepsilon_0 \varepsilon \mathbf{E}, \quad (1)$$

where ε_0 is the electric constant; ε is the dielectric permittivity being a direction-independent scalar quantity; and **E** is the electric intensity vector. In the crystal, permittivity may depend on the direction of the electric field relative to the crystallographic axes. In this case, dielectric permittivity is the symmetric tensor while the field **D** is generally not parallel to the electric field. Major axes may be transformed into the orthogonal coordinate system wherein **E** and **D** are related through a diagonal matrix, as follows:

$$\begin{pmatrix} D_1 \\ D_2 \\ D_3 \end{pmatrix} = \varepsilon_0 \begin{pmatrix} \varepsilon_1 & 0 & 0 \\ 0 & \varepsilon_2 & 0 \\ 0 & 0 & \varepsilon_3 \end{pmatrix} \cdot \begin{pmatrix} E_1 \\ E_2 \\ E_3 \end{pmatrix}. \quad (2)$$

Should diagonal elements ε_i be not all the same, as occurs in $CaCO_3$ [20], the crystal exhibits birefringence.

The energy density of the electric field is $\omega_e = \frac{1}{2}\mathbf{E} \cdot \mathbf{D}$. Using matrix (2), it may be shown that surfaces with constant energy density are ellipsoids in field **D**, written as follows:

[1] https://www.2dsemiconductors.com. Accessed December 22, 2019.

[2] https://www.thorlabs.com. Accessed December 22, 2019.

$$\varepsilon_0\omega_e = \mathbf{D}\cdot\hat{\varepsilon}^{-1}\cdot\mathbf{D} = \frac{D_1^2}{\varepsilon_1} + \frac{D_2^2}{\varepsilon_2} + \frac{D_3^2}{\varepsilon_3}. \quad (3)$$

Introducing non-dimensional vector **u** along direction **D** according to formula $\mathbf{u} = \frac{\mathbf{D}}{\sqrt{2\varepsilon_0\omega_e}}$, the following refractive index ellipsoid equation may be derived:

$$\frac{u_1^2}{n_1^2} + \frac{u_2^2}{n_2^2} + \frac{u_3^2}{n_3^2} = 1, \quad (4)$$

where $n_i = \sqrt{\varepsilon_i}$ for a non-magnetic material. The impermeability tensor may be defined as follows:

$$\hat{\boldsymbol{\eta}} = \hat{\varepsilon}^{-1}. \quad (5)$$

Using formula (5), equation (3) may be converted to the following ellipsoid equation:

$$\mathbf{u}\cdot\hat{\boldsymbol{\eta}}\cdot\mathbf{u} = 1. \quad (6)$$

Zinc telluride, which has a cubic crystal lattice, is optically isotropic in the absence of the applied electric field. This implies the possibility of replacing the permeability tensor by scalar ε^{-1} multiplied by unit matrix **I**. In the presence of the electric field, the impermeability tensor may be written as follows:

$$\hat{\boldsymbol{\eta}}(\mathbf{E}) = \varepsilon^{-1}\cdot\mathbf{I} + \mathbf{r}\cdot\mathbf{E}. \quad (7)$$

The second term (7) is described by the Pockels effect, where **r** is the tensor of electro-optic coefficients. The electro-optic Kerr effect being quadratic in the electric field may be neglected here, since it is negligible in ZnTe crystal as compared to the linear effect. Thus, having substituted (7) into equation (6), the ellipsoid equation can be written as follows:

$$\mathbf{u}\cdot\hat{\boldsymbol{\eta}}(\mathbf{E})\cdot\mathbf{u} = $$

$$= \sum_{i,j=1,2,3}\left(\varepsilon^{-1}\cdot\delta_{ij} + \sum_{k=1,2,3} r_{ijk}E_k\right)\mathbf{u}_i\mathbf{u}_j = 1. \quad (8)$$

Since tensor $\hat{\boldsymbol{\eta}}$ is symmetric, $r_{ijk} = r_{jik}$. It is conventional to replace the first two indices i, j of tensor **r** by a single index, as follows:

$$r_{11k} \to r_{1k},$$

$$r_{22k} \to r_{2k},$$

$$r_{33k} \to r_{3k},$$

$$r_{23k} = r_{32k} \to r_{4k},$$

$$r_{13k} = r_{31k} \to r_{5k},$$

$$r_{12k} = r_{21k} \to r_{6k}.$$

Zinc telluride crystallizes in the zincblende structure (zincblende comprises two face-centered cubic lattices shifted relative to each other by a quarter of the space diagonal) [21]. In the absence of the applied electric field, the refractive indices are equal, i.e., $n_1 = n_2 = n_3 = n_0$. In addition, **r** contains only one independent non-zero element $r_{41} = r_{52} = r_{63}$. Thus, ellipsoid equation (8) may be written in the following way:

$$\frac{1}{n_0^2}\left(u_1^2 + u_2^2 + u_3^2\right) + $$

$$+ 2r_{41}\left(E_1u_2u_3 + E_2u_3u_1 + E_3u_1u_2\right) = 1. \quad (9)$$

The ZnTe crystals used for detecting THz radiation have a crystallographic cut (1 1 0), as shown in Fig. 1. Since the THz pulse and the laser pulse fall perpendicular to this plane along the direction [−1 −1 0], their electric vectors lie in plane (1 1 0). The two-dimensional coordinate system (*X, Y*) is introduced in this plane in such a way that *X*-direction coincides with direction [−1 1 0] and *Y*-direction coincides with direction [0 0 1].

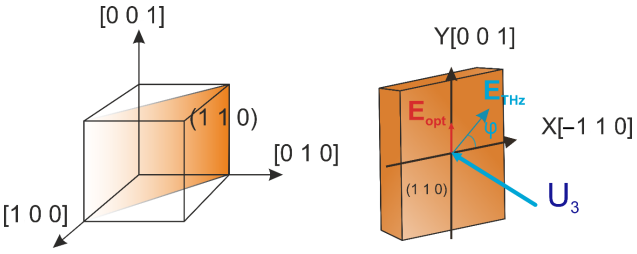

Fig. 1. Plane (1 1 0) (left) and coordinate system (*X, Y*) in this plane (right). The femtosecond laser probe pulse and the THz pump pulse are directed along vector $\mathbf{U_3}$ being the normal to plane (1 1 0)

Major axes should be transformed to obtain the refractive indices in the *XY* plane when applying the electric field.

Let the electric vector $\mathbf{E_{THz}}$ of THz pulse makes angle φ with the *X*-axis (axis [−1 1 0] of ZnTe crystal). Its components in the basis system of the cubic crystal lattice may be represented as follows:

$$\mathbf{E_{THz}} = E_{\mathrm{THz}}\begin{pmatrix} -\cos\varphi/\sqrt{2} \\ \cos\varphi/\sqrt{2} \\ \sin\varphi \end{pmatrix}. \quad (10)$$

In this case, equation (9) is written in the following way:

$$\mathbf{u}\cdot\hat{\boldsymbol{\eta}}\left(\mathbf{E_{THz}}\right)\cdot\mathbf{u}=1,$$

where $\hat{\boldsymbol{\eta}}(\mathbf{E_{THz}})$ is the impermeability tensor depending on field $\mathbf{E_{THz}}$, written in the following way:

$$\hat{\boldsymbol{\eta}}(\mathbf{E_{THz}})=\frac{1}{n_0^2}\begin{pmatrix}1&0&0\\0&1&0\\0&0&1\end{pmatrix}+$$

$$+\,r_{41}E_{\mathrm{THz}}\begin{pmatrix}0&\sin\varphi&\cos\varphi/\sqrt{2}\\\sin\varphi&0&-\cos\varphi/\sqrt{2}\\\cos\varphi/\sqrt{2}&-\cos\varphi/\sqrt{2}&0\end{pmatrix}. \quad (11)$$

Then, the eigenvalues for tensor $\hat{\boldsymbol{\eta}}(\mathbf{E_{THz}})$ may be found from formula (11) in the following way:

$$\lambda_{1,2}=\frac{1}{n_0^2}-\frac{r_{41}E_{\mathrm{THz}}}{2}\left(\sin\varphi\pm\sqrt{1+3\cos^2\varphi}\right),$$

$$\lambda_3=\frac{1}{n_0^2}+r_{41}E_{\mathrm{THz}}\sin\varphi. \quad (12)$$

In this case, the normalized eigenvectors may be written as follows:

$$\mathbf{U_1}=\frac{1}{2}\sqrt{1+\frac{\sin\varphi}{\sqrt{1+3\cos^2\varphi}}}\begin{pmatrix}-1\\1\\2\sqrt{2}\cos\varphi\Big/\left(\sqrt{1+3\cos^2\varphi}+\sin\varphi\right)\end{pmatrix},$$

$$\mathbf{U_2}=\frac{1}{2}\sqrt{1-\frac{\sin\varphi}{\sqrt{1+3\cos^2\varphi}}}\begin{pmatrix}-1\\1\\2\sqrt{2}\cos\varphi\Big/\left(\sqrt{1+3\cos^2\varphi}-\sin\varphi\right)\end{pmatrix},$$

$$\mathbf{U_3}=\frac{1}{\sqrt{2}}\begin{pmatrix}-1\\-1\\0\end{pmatrix}. \quad (13)$$

The directions of major axes coincide with those of the eigenvectors. The refractive indices may be determined by the following formula:

$$n_i=\frac{1}{\sqrt{\lambda_i}}.$$

Considering $r_{41}E_{\mathrm{THz}}\ll\frac{1}{n_0^2}$ the expressions for refractive indices corresponding to major axes may be written as follows:

$$n_1=n_0+\frac{n_0^3r_{41}E_{\mathrm{THz}}}{4}\left(\sin\varphi+\sqrt{1+3\cos^2\varphi}\right),$$

$$n_2=n_0+\frac{n_0^3r_{41}E_{\mathrm{THz}}}{4}\left(\sin\varphi-\sqrt{1+3\cos^2\varphi}\right), \quad (14)$$

$$n_3=n_0-\frac{n_0^3r_{41}E_{\mathrm{THz}}}{2}\sin\varphi.$$

It is clear (Fig. 1, direction $\mathbf{U_3}$) from equation (13) that the third major axis is perpendicular to the crystal plane (1 1 0). This direction coincides with the direction of the THz pump pulse and probe beam pulse propagation. Vector $\mathbf{U_1}$ lies in plane (1 1 0) forming angle ψ with the X-axis [−1 1 0], which can be calculated using the scalar product of vector $\mathbf{U_1}$ and the unit vector along the X-axis. Using the relation $\cos(2\psi)=2\cos^2\psi-1$, the following expression relating angle ψ and angle φ of THz polarization may be written:

$$\cos(2\psi)=\frac{\sin\varphi}{\sqrt{1+3\cos^2\varphi}}. \quad (15)$$

For $\varphi=\pi/2$, major axis U_1 is X-directed while axis U_2 is Y-directed. Therefore, when the electric field is applied to the ZnTe crystal (THz radiation), a refractive index ellipsoid having an ellipse in the XY section is formed (Fig. 2). The directions of the ellipse major axes correspond to the directions of vectors $\mathbf{U_1}$ and $\mathbf{U_2}$. The refractive indices are n_1 and n_2, and correspond to the first two major axes. The larger index (n_s) corresponds to the slower speed of light while the smaller one (n_f) corresponds to the faster speed. The refractive indices are generally denoted by $n_s=n_1$ and $n_f=n_2$.

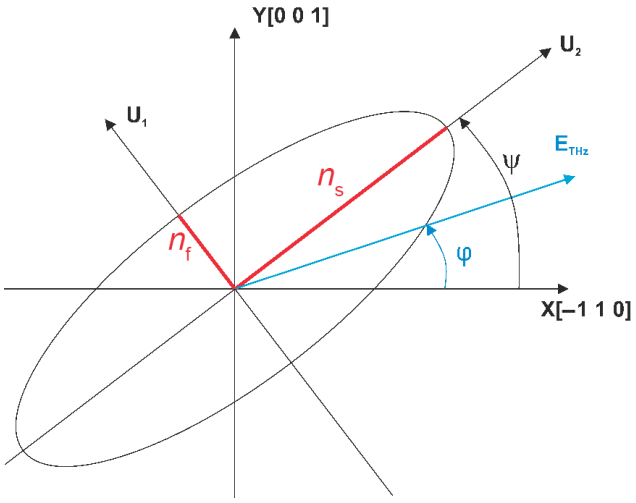

Fig. 2. Refractive index ellipsoid projected onto plane (1 1 0) of ZnTe crystal

The electric intensity vector $\mathbf{E_{THz}}$ makes angle φ with the *X*-axis = [−1 1 0] of ZnTe crystal, while the angle between the semi-major axis of the ellipse and the *X*-axis is ψ(φ). The THz pulse as well as the laser beam falls along the normal to plane (1 1 0) determined by unit vector $\mathbf{U_3} = \frac{1}{\sqrt{2}}\begin{pmatrix}-1\\-1\\0\end{pmatrix}$.

Since the laser beam falls on ZnTe crystal along the direction [−1 −1 0] (eigenvector $\mathbf{U_3}$), its electric vector $\mathbf{E_{opt}}$ lies in plane (1 1 0). In the crystal of thickness *d*, two $\mathbf{E_{opt}}$ components along major axes U_1 and U_2 have a relative phase shift written as follows:

$$\Gamma(\varphi) = \frac{\omega d}{2c} n_0^3 r_{41} E_{\mathrm{THz}} \sqrt{1+3\cos^2\varphi}, \quad (16)$$

where ω is the angular frequency of laser radiation, φ is the angle between $\mathbf{E_{THz}}$ and the *X*-axis, *d* is the ZnTe crystal thickness, and c is the speed of light.

The signal recorded by the photodiode may be described using the Jones matrix describing the linearly polarized laser beam passing through the birefringent crystal with an optical polarizer [22]. The *S*-polarized laser radiation may be described by the vector as follows:

$$\mathbf{E_{opt}} = E_{\mathrm{opt}}\begin{pmatrix}0\\1\end{pmatrix}, \quad (17)$$

where E_{opt} is the electric intensity of the laser probe beam. The polarization plane rotation by the angle ψ may be described by the matrix in the following way:

$$R(\psi) = \begin{pmatrix}\cos\psi & \sin\psi\\ -\sin\psi & \cos\psi\end{pmatrix}, \quad (18)$$

where $\psi = \frac{1}{2}\arccos\left[\frac{\sin\varphi}{\sqrt{1+3\cos^2\varphi}}\right]$ is the rotation angle of the beam polarization ellipse in ZnTe under the THz pulse action.

The birefringence matrix for ZnTe crystal may be written as follows:

$$\mathbf{Z(\varphi)} = \begin{pmatrix}\exp(-i\Gamma(\varphi)/2) & 0\\ 0 & \exp(i\Gamma(\varphi)/2)\end{pmatrix}. \quad (19)$$

The ZnTe impact on the probe beam may be written in the following form:

$$E_{\mathrm{opt}} R(-\psi) Z(\varphi) R(\psi)\begin{pmatrix}0\\1\end{pmatrix}.$$

Having passed ZnTe and the optical polarizer, the electric intensity of the probe beam may be described by the following formula:

$$E = (1 \quad 0)\, E_{\mathrm{opt}} R(-\psi) Z(\varphi) R(\psi)\begin{pmatrix}0\\1\end{pmatrix}.$$

The signal picked up by the photodiode is equal to the following expression:

$$S_x(\varphi) = K \cdot E_{\mathrm{opt}}^2 \sin^2\left(2\psi(\varphi)\right)\sin^2\left(\frac{\Gamma(\varphi)}{2}\right), \quad (20)$$

where *K* is the photodiode optoelectronic conversion.

Expressing $\sin^2(2\psi(\varphi)) = 1 - \cos^2(2\psi(\varphi))$ and substituting expressions (15) and (16) in (20), the resulting expression for approximation may be written as follows:

$$S_x(\varphi) = K \cdot E_{\mathrm{opt}}^2\left(1 - \frac{\sin^2\varphi}{1+3\cos^2\varphi}\right)\times$$
$$\times \sin^2\left(\frac{(\omega d/2c) n_0^3 r_{41} E_{\mathrm{THz}}\sqrt{1+3\cos^2\varphi}}{2}\right). \quad (21)$$

RESULTS AND DISCUSSION

In the study, the traditional THz-TDS experimental setup shown in Fig. 3 is used to determine polarization of THz radiation. A femtosecond titanium-sapphire laser with regenerative amplifier generating optical pulses, having a repetition frequency of 3 kHz, duration of 35 fs and central wavelength of 800 nm, is used as the laser source (Avesta Project, Russia).[3] The output optical beam is divided into a pump beam and a probe beam. The pump beam is focused on the BP crystallite surface at the angle of 45°, while the density of optical radiation on the sample surface is about 1 mJ/cm^2. The generated THz radiation is collimated by the parabolic mirror. Passing through two wire grid polarizers—WGPs (Specac Ltd, Great Britain),[4] the THz radiation is focused on the nonlinear optical ZnTe crystal detector by a parabolic mirror. The probe beam passes through the delay line to be focused onto ZnTe crystal in combination with the THz beam. The passing optical probe beam is recorded by photodiode. The electro-optic method based on amplitude modulation is used to record THz radiation [16]. The experiment is performed at room temperature.

[3] http://avesta.ru/. Accessed December 22, 2019 (in Russ.).
[4] https://www.specac.com. Accessed December 22, 2019.

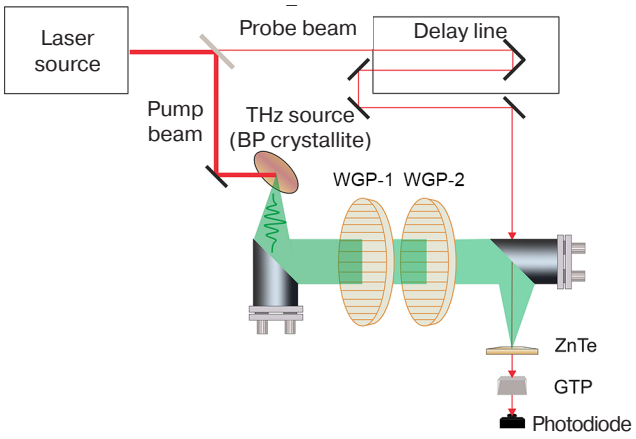

Fig. 3. THz-TDS experimental scheme.
GTP is the Glan–Taylor polarizer

The part of the experimental setup responsible for determining the polarization angle of THz radiation is shown in detail in Fig. 4. The angle between the WGP-2 analyzer axis coinciding with vector $\mathbf{E}_{\mathbf{THz}}$, and the X-axis is fixed and equal to φ_3. The WGP-1 polarizer is rotating. The angle between its axis coinciding with vector $\mathbf{E}'_{\mathbf{THz}}$ and the X-axis is φ_2.

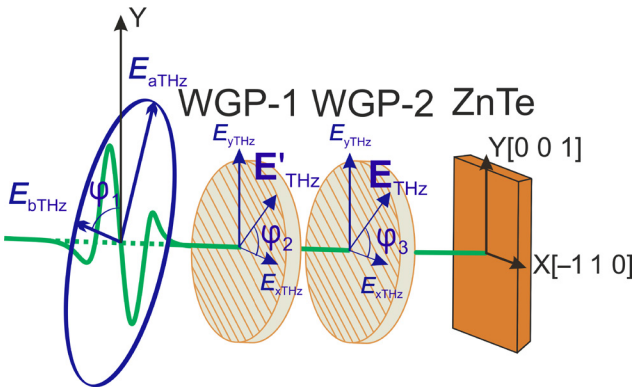

Fig. 4. Experimental setup geometry
when using two polarizers

The polarization ellipse of THz radiation lies in a plane parallel to the XY plane. Here, E_{aTHz} and E_{bTHz} are semi-axes of this ellipse; φ_1 is the angle between semi-minor axis and the Y axis; φ_2 and φ_3 are the angles between the X axis and the axes of the WGP-1 and WGP-2 polarizers, respectively.

According to the Malus law, the amplitude of THz radiation may be written in formula (16) in this case as follows:

$$E_{\text{THz}} = E'_{\text{THz}} \cos(\varphi_2 + \varphi_3), \qquad (22)$$

where $E'_{\text{THz}} = E_{\text{aTHz}} \sqrt{\cos^2(\varphi_1 + \varphi_2) + \varepsilon^2 \sin^2(\varphi_1 + \varphi_2)}$ is the THz pulse passed through the first polarizer WGP-1; $\varepsilon = \dfrac{E_{\text{bTHz}}}{E_{\text{aTHz}}}$ is the ellipticity of the pulse under study. Normalizing dependence (21) to the optical beam power taking formula (22) into account and recording the values of angles φ_1 and φ_3, the dependence for the normalized signal $f(\varphi_2)$ recorded by photodiode may be written as follows:

$$f(\varphi_2) = \frac{S_x\left(E_{\text{THz}}(\varphi_1,\varphi_2),\varphi_3\right)}{E_{\text{opt}}^2} = \sin^2(2\psi(\varphi_3))\sin^2\left(\frac{\Gamma\left(E_{\text{THz}}(\varphi_1,\varphi_2),\varphi_3\right)}{2}\right). \qquad (23)$$

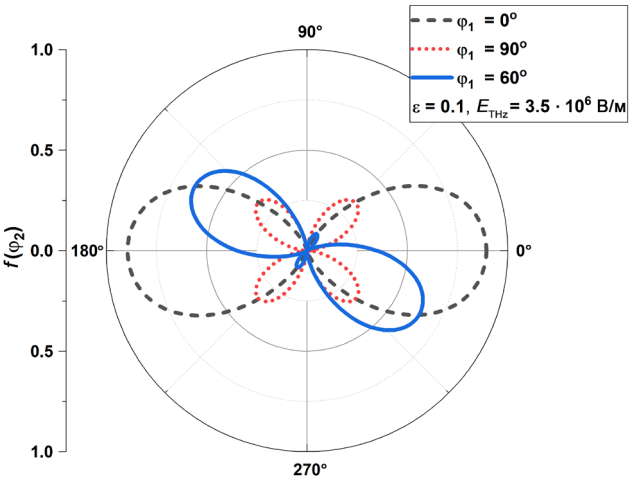

Fig. 5. Dependence plots for the recorded signal normalized to the optical radiation power of the probe beam

The dependence plots $f(\varphi_2)$ derived from expression (23) at different values for THz polarization angles φ_1 are shown in Fig. 5. The remaining parameters of THz radiation and WGP-2 polarizer position are $E_{\text{aTHz}} = 3.5 \cdot 10^6$ V/m; $\varepsilon = 0.1$; and $\varphi_1 = 0°$. Calculating at $\varphi_1 = 0°$ and $\varphi_1 = 90°$, a Dumbbell plot and a four-leaf clover shaped plot are derived, respectively; calculations at other angles, e.g., at $\varphi_1 = 60°$ result in the dependence being shaped transitionally between them. Since dependence $f(\varphi_2)$ is unique for each angle value, the experimental dependence can be easily approximated by expression (23), obtaining the actual parameters of THz radiation (polarization angle, ellipticity).

The smallness condition for the argument of sine $\dfrac{\Gamma(\varphi)}{2}$ is satisfied at $\dfrac{\omega d}{4c} n_0^3 r_{41} E_{\text{aTHz}} \le 0.35$ or at $E_{\text{aTHz}} \le 2 \cdot 10^6$ V/m. Since $\sin^2\left(\dfrac{\Gamma(\varphi)}{2}\right)$ in this case, the polarization dependencies comply with the Malus law when the polarized electromagnetic wave passes through two polarizers. Despite this limitation, the shape of dependences (Fig. 4) does not change up to values $E_{\text{aTHz}} \approx 4 \cdot 10^6$ V/m. When detecting THz wave at

$E_{aTHz} > 4 \cdot 10^6$ V/m, a distortion of the dependencies shown in Fig. 5 is observed. This is due to the phase difference between the ordinary and extraordinary optical beams becoming comparable or exceeding $\pi/2$.

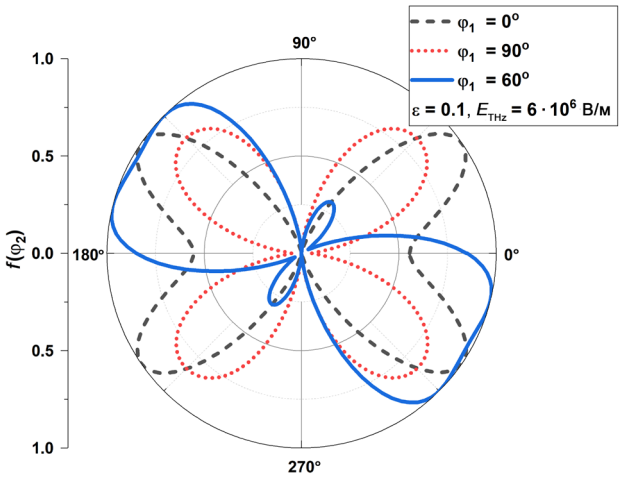

Fig. 6. Dependence plots for the recorded signal of THz pulse passed through two WG polarizers and normalized to the optical radiation power of the probe beam

The dependence plots $f(\varphi_2)$ (23) for $E_{aTHz} = 6 \cdot 10^6$ V/m at different polarization angles of THz radiation φ_1 and for values $\varepsilon = 0.1$, $\varphi_3 = 0$ are shown in Fig. 6. The shapes of dependencies begin to change significantly with increased amplitude of THz radiation. Thus, when $E_{aTHz} = 6 \cdot 10^6$ V/m, dependence $f(\varphi_2)$ is butterfly shaped at $\varphi_1 = 0°$ and four-leaf clover shaped at $\varphi_1 = 90°$ as in the case described above but with maximum values of the function being already comparable with those at the dependence at $\varphi_1 = 0°$; at other φ_1 values, there would be a transitional shape between "butterfly" and "clover."

We shall consider the experimental setup for analyzing THz radiation with one THz polarizer. Since the ZnTe crystal is sensitive to the THz pulse polarization, it could be simultaneously used as the polarization analyzer (Fig. 7).

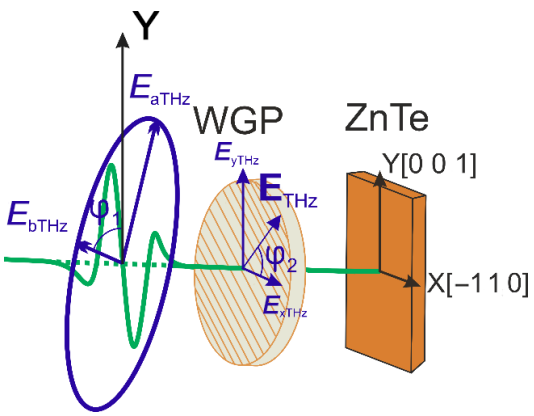

Fig. 7. Experimental setup geometry when using one polarizer

The polarization ellipse of THz radiation lies in the plane parallel to the XY plane. Here, E_{aTHz} and E_{bTHz} are semi-axes of the ellipse; φ_1 is the angle between semi-minor axis and the Y-axis; φ_2 is the angle between the X-axis and the polarizer axis.

In this case, the amplitude of the THz pulse passing through the WGP polarizer may be written in equation (16) in the following form:

$$E_{THz} = E_{aTHz}\sqrt{\cos^2(\varphi_1 + \varphi_2) + \varepsilon^2 \sin^2(\varphi_1 + \varphi_2)}. \quad (24)$$

Normalizing dependence (21) to the optical beam power, considering expression (24) and having the value for angle φ_1 recorded, dependencies $g(\varphi_2)$ at different polarization angles for the THz radiation under study similar in shape to previously derived dependencies (23) may be derived (Fig. 8) as follows:

$$g(\varphi_2) = \frac{S_x\left(E_{THz}(\varphi_1), \varphi_2\right)}{E_{opt}^2} =$$

$$= \sin^2\left(2\psi(\varphi_2)\right)\sin^2\left(\frac{\Gamma\left(E_{THz}(\varphi_1), \varphi_2\right)}{2}\right). \quad (25)$$

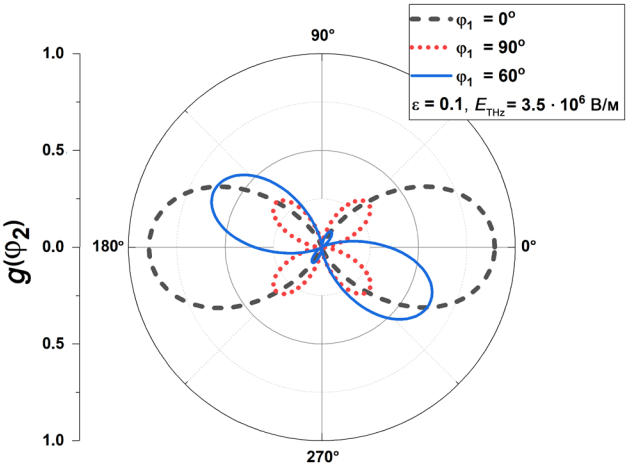

Fig. 8. Dependence plots for the recorded signal of THz pulse passed through WG polarizer and normalized to the optical radiation power of the probe beam

Dependence plots $g(\varphi_2)$ (25) at $E_{aTHz} = 3.5 \cdot 10^6$ V/m, different polarization angles of THz radiation φ_1 and $\varepsilon = 0.1$ are shown in Fig. 8. The plots coincide in shape with dependence plots (23) shown in Fig. 5, which indicates the possibility to analyze the polarization of THz radiation using one WGP. Should the electric intensity value E_{aTHz} exceed $4 \cdot 10^6$ V/m, the change in dependences (25) is observed, as in the case described above.

The BP crystallite used as the THz radiation source in the study has a radiation ellipticity of $\varepsilon = 0.77$ at the fixed angle of 90° between the field vector of the exciting

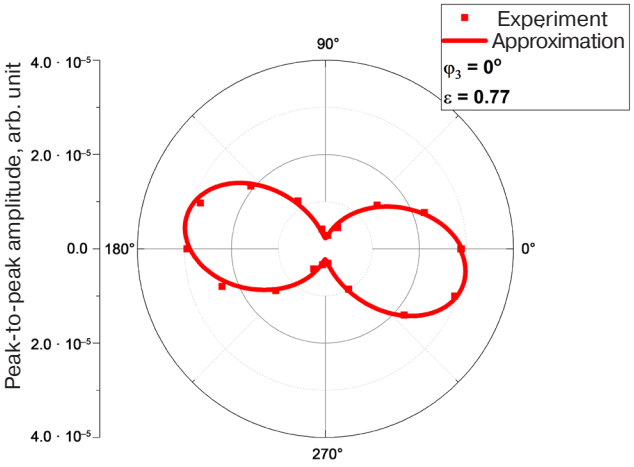

Fig. 9. Dependence plot of the THz peak-to-peak amplitude on the rotation angle of the WGP-1 polarizer

laser pump beam and the sample "zigzag" direction [13]. For analyzing the polarization, a scheme with two wire-grid polarizers is chosen (Fig. 4). The angle φ_3 for WGP-2 is fixed and equal to 0°. The resulting values for the recorded THz peak-to-peak amplitude at different WGP-1 polarizer axis angles φ_3 are shown in Fig. 9 along with the approximation of experimental data by expression (23). Using the approximation, the angle between semi-major axis of the THz polarization ellipse and the *X*-axis has been found to be 40°.

CONCLUSIONS

In the paper, a model describing the dependence of the peak-to-peak amplitude of THz radiation on the rotation angle of the WGP is considered and modified. The simulation results show that the dependences of the THz peak-to-peak amplitude on the polarizer rotation angle are similar in shape whether using two WGPs or one of them in the experimental setup. The possibility of using one polarizer in the analysis due to the ZnTe crystal sensitivity to the polarization of THz radiation is demonstrated. Since, having passed the ZnTe crystal under the THz pulse, the phase difference between the ordinary and extraordinary optical probe beams becomes comparable or exceeds $\pi/2$, dependences begin to differ only with a THz wave field intensity exceeding 40 kV/cm. The applicability of approximation is shown along with the angle $\varphi_1 = 40°$ between the semi-major axis of the THz polarization ellipse, while the *X*-axis is determined by the example of analyzing polarization of THz radiation emitted by the surface of BP crystallite under the femtosecond pump beam action.

ACKNOWLEDGMENTS

The study was supported by the Russian Science Foundation, grant No. 21-79-10353 "Controlled spintronic hybrid THz emitters and detectors." Experimental studies were carried out using the equipment of the Center for Collective Use at the MIREA – Russian Technological University.

Authors' contributions

F.A. Zainullin—mathematical modeling and experimental data processing.
D.I. Khusyainov—experiment.
M.V. Kozintseva—theory.
A.M. Buryakov—theory.

REFERENCES

1. Cui H., Zhang X.B., Yang P., Su J.F., Wei X.Y., Guo Y.H. Spectral characteristic of single layer graphene via terahertz time domain spectroscopy. *Optik* (*Stuttg*). 2015;126(14):1362–1365. https://doi.org/10.1016/j.ijleo.2015.03.032
2. Maamar N., Lazoul M., Latreche F.Y., Trache D., Coutaz J.L. Terahertz time-domain spectroscopy characterization of nitrocellulose in transmission and reflection configurations. *Optik* (*Stuttg*). 2020;224:165711. https://doi.org/10.1016/j.ijleo.2020.165711
3. Tu S., Wang Z., Liang G., Zhang W., Tang Y., She Y., Yi C., Bi X. A novel approach to discriminate transgenic soybean seeds based on terahertz spectroscopy. *Optik* (*Stuttg*). 2021;242:167089. https://doi.org/10.1016/j.ijleo.2021.167089
4. Tan N.Y., Zeitler J.A. Probing phase transitions in simvastatin with terahertz time-domain spectroscopy. *Mol. Pharm.* 2015;12(3):810–815. https://doi.org/10.1021/mp500649q
5. Ho L., Pepper M., Taday P. Signatures and fingerprints. *Nat. Photonics*. 2008;2(9):541–543. https://doi.org/10.1038/nphoton.2008.174
6. Wang W.N., Wang G., Zhang Y. Low-frequency vibrational modes of glutamine. *Chinese Phys. B*. 2011;20(12):123301. https://doi.org/10.1088/1674-1056/20/12/123301
7. Du S.Q., Li H., Xie L., Chen L., Peng Y., Zhu Y.M., Li H., Dong P., Wang J.T. Vibrational frequencies of anti-diabetic drug studied by terahertz time-domain spectroscopy. *Appl. Phys. Lett*. 2012;100(14):143702. https://doi.org/10.1063/1.3700808
8. Andersen J., Heimdal J., Mahler D.W., Nelander B., Wugt Larsen R. Communication: THz absorption spectrum of the CO_2–H_2O complex: Observation and assignment of intermolecular van der Waals vibrations. *J. Chem. Phys.* 2014;140(9):091103. https://doi.org/10.1063/1.4867901
9. Walther M., Plochocka P., Fischer B., Helm H., Uhd Jepsen P. Collective vibrational modes in biological molecules investigated by terahertz time-domain spectroscopy. *Biopolymers*. 2002;67(4–5):310–313. https://doi.org/10.1002/bip.10106
10. Tonouchi M. Cutting-edge terahertz technology. *Nat. Photonics*. 2007;1:97–105. https://doi.org/10.1038/nphoton.2007.3

11. Dadap J.I., Shan J., Heinz T.F. Circularly polarized light in the single-cycle limit: the nature of highly polychromatic radiation of defined polarization. *Opt. Express*. 2009;17(9):7431–7439. https://doi.org/10.1364/OE.17.007431
12. Yang X., Zhao X., Yang K., Liu Y., Liu Y., Fu W., et al. Biomedical applications of terahertz spectroscopy and imaging. *Trends Biotechnol*. 2016;34(10):810–824. https://doi.org/10.1016/j.tibtech.2016.04.008
13. Buryakov A., Zainullin F., Khusyanov D., Abdulaev D., Nozdrin V., Mishina E. Generation of elliptically polarized terahertz radiation from black phosphorus crystallites. *Opt. Eng*. 2021;60(08):082013. https://doi.org/10.1117/1.OE.60.8.082013
14. Khusyainov D., Ovcharenko S., Gaponov M., Buryakov A., Klimov A., Tiercelin N., Pernod P., Nozdrin V., Mishina E., Sigov A., Preobrazhensky V. Polarization control of THz emission using spin-reorientation transition in spintronic heterostructure. *Sci. Rep*. 2021;11(1):697. https://doi.org/10.1038/s41598-020-80781-5
15. Huang Y., Yartsev A., Guan S., Zhu L., Zhao Q., Yao Z., He C.,Zhang L., Bai J., Luo J., Xu X. Hidden spin polarization in the centrosymmetric MoS_2 crystal revealed via elliptically polarized terahertz emission. *Phys. Rev. B*. 2020;102(8):085205. https://doi.org/10.1103/PhysRevB.102.085205
16. Kovalev S.P., Kitaeva G.K. Two alternative approaches to electro-optical detection of terahertz pulses. *JETP Lett*. 2011;94(2):91–96 (in Russ.) https://doi.org/10.1134/S0021364011140074]
[Original Russian Text: Kovalev S.P., Kitaeva G.K. Two alternative approaches to electro-optical detection of terahertz pulses. *Pis'ma v Zhurnal Eksperimental'noi i Teoreticheskoi Fiziki*. 2011;94(2):95–100 (in Russ.).]
17. Deng B., Tran V., Xie Y., Jiang H., Li C., Guo Q., Wang X., Tian H., Koester S. J., Wang H., Cha J. J., Xia Q., Yang L., Xia F. Efficient electrical control of thin-film black phosphorus bandgap. *Nat. Commun*. 2017;8:14474. https://doi.org/10.1038/ncomms14474
18. Long G., Maryenko D., Shen J., Xu S., Hou J., Wu Z., Wong W.K., Han T., Lin J., Cai Y., Lortz R., Wang N. Achieving ultrahigh carrier mobility in two-dimensional hole gas of black phosphorus. *Nano Lett*. 2016;16(12):7768–7773. https://doi.org/10.1021/acs.nanolett.6b03951
19. Chen X., Wu Y., Wu Z., Han Y., Xu S., Wang L., Ye W., Han T., He Y., Cai Y., Wang N. High-quality sandwiched black phosphorus heterostructure and its quantum oscillations. *Nat. Commun*. 2015;6:7315. https://doi.org/10.1038/ncomms8315
20. Hossain F.M., Murch G.E., Belova I.V., Turner B.D. Electronic, optical and bonding properties of $CaCO_3$ calcite. *Solid State Commun*. 2009;149(29–30):1201–1203. https://doi.org/10.1016/j.ssc.2009.04.026
21. Soykan C., Kart S.Ö. Structural, mechanical and electronic properties of ZnTe polymorphs under pressure. *J. Alloys Compd*. 2012;529:148–157. https://doi.org/10.1016/j.jallcom.2012.02.170
22. Yariv A., Yeh P. *Photonics: optical electronics in modern communications*. Oxford University Press; 2007. 836 p.

About the authors

Farkhad A. Zainullin, Intern Researcher, Laboratory "Ultrafast Dynamics in Ferroics," Institute for Advanced Technologies and Industrial Programming, MIREA – Russian Technological University (78, Vernadskogo pr., Moscow, 119454 Russia). E-mail: madflyzero@gmail.com. Scopus Author ID 57226613215, https://orcid.org/0000-0002-1195-5166

Dinar I. Khusyainov, Postgraduate Student, Junior Researcher, Laboratory "Femtosecond Optics for Nanotechnologies," Institute for Advanced Technologies and Industrial Programming, MIREA – Russian Technological University (78, Vernadskogo pr., Moscow, 119454 Russia). E-mail: husyainov@mirea.ru. Scopus Author ID 57194467463, ResearcherID O-7241-2017, https://orcid.org/0000-0003-1332-4146

Marina V. Kozintseva, Cand. Sci. (Phys.-Math.), Assistant Professor, Department of Physics, Institute for Advanced Technologies and Industrial Programming, MIREA – Russian Technological University (78, Vernadskogo pr., Moscow, 119454 Russia). E-mail: kozintseva@mirea.ru. Scopus Author ID 6506049090, ResearcherID C-3826-2017, https://orcid.org/0000-0002-6277-4074

Arseniy M. Buryakov, Cand. Sci. (Phys.-Math.), Senior Researcher, Laboratory "Femtosecond Optics for Nanotechnologies," Institute for Advanced Technologies and Industrial Programming, MIREA – Russian Technological University (78, Vernadskogo pr., Moscow, 119454 Russia). E-mail: buryakov@mirea.ru. Scopus Author ID 55454206600, ResearcherID E-8283-2017, https://orcid.org/0000-0002-3347-9076

Об авторах

Зайнуллин Фархад Алмазович, стажер-исследователь специализированной учебно-научной лаборатории «Сверхбыстрая динамика ферроиков» Института перспективных технологий и индустриального программирования ФГБОУ ВО «МИРЭА – Российский технологический университет» (119454, Россия, Москва, пр-т Вернадского, д. 78). E-mail: madflyzero@gmail.com. Scopus Author ID 57226613215, https://orcid.org/0000-0002-1195-5166

Хусяинов Динар Ильгамович, аспирант, младший научный сотрудник учебно-научной лаборатории фемтосекундной оптики для нанотехнологий Института перспективных технологий и индустриального программирования ФГБОУ ВО «МИРЭА – Российский технологический университет» (119454, Россия, Москва, пр-т Вернадского, д. 78). E-mail: husyainov@mirea.ru. Scopus Author ID 57194467463, ResearcherID O-7241-2017, https://orcid.org/0000-0003-1332-4146

Козинцева Марина Валентиновна, к.ф.-м.н., доцент кафедры физики Института перспективных технологий и индустриального программирования ФГБОУ ВО «МИРЭА – Российский технологический университет» (119454, Россия, Москва, пр-т Вернадского, д. 78). E-mail: kozintseva@mirea.ru. Scopus Author ID 6506049090, ResearcherID C-3826-2017, https://orcid.org/0000-0002-6277-4074

Буряков Арсений Михайлович, к.ф.-м.н., старший научный сотрудник учебно-научной лаборатории фемтосекундной оптики для нанотехнологий Института перспективных технологий и индустриального программирования ФГБОУ ВО «МИРЭА – Российский технологический университет» (119454, Россия, Москва, пр-т Вернадского, д. 78). E-mail: buryakov@mirea.ru. Scopus Author ID 55454206600, ResearcherID E-8283-2017. https://orcid.org/0000-0002-3347-9076

Translated by K. Nazarov
Edited for English language and spelling by Thomas Beavitt

Micro- and nanoelectronics. Condensed matter physics
Микро- и наноэлектроника. Физика конденсированного состояния

UDC 538.951+ 538.955+538.956
https://doi.org/10.32362/2500-316X-2022-10-3-85-92

RESEARCH ARTICLE

Anisotropic magnetoelectric effect in lead zirconate titanate and magnetostrictive fiber composite structures

Dmitriy V. Saveliev, Leonid Y. Fetisov @, Vladimir I. Musatov, Mikhail V. Dzhaparidze

MIREA – Russian Technological University, Moscow, 119454 Russia
@ Corresponding author, e-mail: fetisovl@yandex.ru

Abstract

Objectives. The development of composite structures in which a strongly anisotropic magnetoelectric (ME) effect is observed is relevant for the creation of sensors that are sensitive to the direction of the magnetic field. Such an ME effect can arise due to the anisotropy of both the magnetic and the piezoelectric layers. In this work, a new anisotropic material named as a magnetostrictive fiber composite (MFC), comprising a set of nickel wires placed closely parallel to each other in one layer and immersed in a polymer matrix, is manufactured and studied. The study aimed to investigate the linear ME effect in a structure comprising of a new magnetic material, MFC, and lead zirconate titanate (PZT-19).

Methods. The magnetostriction for the MFC structure was measured using the strain-gauge method; the ME effect was determined by low-frequency magnetic field modulation.

Results. Structures with nickel wire diameters of 100, 150, and 200 μm were fabricated. The MFC magnetostriction field dependences were determined along with the frequency-, field-, and amplitude dependences of the ME voltage in the case of linear ME effect. Measurements were carried out at various values of the angle between the direction of the magnetic field and the wires. All samples demonstrated strong anisotropy with respect to the direction of the magnetic field. When the magnetic field orientation changes from parallel to perpendicular with respect to the nickel wire axes, the ME voltage decreases from its maximum value to zero.

Conclusions. The largest ME coefficient 1.71 V/(Oe · cm) was obtained for a structure made of MFC with a wire diameter of 150 μm. With increasing wire diameter, the resonance frequency increases from 3.5 to 6.5 kHz. The magnetostriction of the MFC is comparable in magnitude to that of a nickel plate having the same thickness.

Keywords: magnetoelectric effect, magnetostriction, fiber composites, piezoelectric effect, anisotropy

• **Submitted:** 03.12.2021 • **Revised:** 15.02.2022 • **Accepted:** 20.04.2022

For citation: Saveliev D.V., Fetisov L.Y., Musatov V.I., Dzhaparidze M.V. Anisotropic magnetoelectric effect in lead zirconate titanate and magnetostrictive fiber composite structures. *Russ. Technol. J*. 2022;10(3):85–92. https://doi.org/10.32362/2500-316X-2022-10-3-85-92

Financial disclosure: The authors have no a financial or property interest in any material or method mentioned.

The authors declare no conflicts of interest.

НАУЧНАЯ СТАТЬЯ

Анизотропный магнитоэлектрический эффект в структуре цирконат–титанат свинца / магнитострикционный волоконный композит

Д.В. Савельев, Л.Ю. Фетисов [@], В.И. Мусатов, М.В. Джапаридзе

МИРЭА – Российский технологический университет, Москва, 119454 Россия
[@] Автор для переписки, e-mail: fetisovl@yandex.ru

Резюме

Цели. Разработка композитных структур, в которых наблюдается сильно анизотропный магнитоэлектрический (МЭ) эффект, актуальна для создания датчиков, чувствительных к направлению магнитного поля. Такой МЭ эффект может быть обусловлен анизотропией как магнитного, так и пьезоэлектрического слоя. Авторами изготовлен новый анизотропный материал – магнитострикционный волоконный композит (МВК), представляющий собой набор никелевых проволок, расположенных вплотную параллельно друг к другу в один слой и погруженных в полимерную матрицу. Цель работы – исследование линейного МЭ эффекта в композитных структурах со слоями из МВК и керамики цирконата титаната свинца (ЦТС-19).

Методы. Магнитострикция МВК была измерена тензометрическим методом, МЭ эффект – методом низкочастотной модуляции магнитного поля.

Результаты. Были изготовлены структуры с диаметрами никелевых проволок 100, 150 и 200 мкм. Измерены полевые зависимости магнитострикции МВК, а также частотные, полевые и амплитудные зависимости МЭ напряжения для случая линейного МЭ эффекта при различной величине угла между направлением магнитного поля и проволоками. Показано, что все образцы обладают сильной анизотропией относительно направления магнитного поля. МЭ напряжение уменьшается от максимального значения до нуля при изменении направления магнитного поля с параллельного до перпендикулярного относительно волокон никеля.

Выводы. Наибольшим по величине МЭ коэффициентом, составляющим 1.71 В/(Э · см), обладает структура, изготовленная на основе МВК с диаметром проволоки 150 мкм. Частота резонанса растет от 3.5 кГц до 6.5 кГц с увеличением диаметра проволок. Величина магнитострикции МВК сопоставима по величине с магнитострикцией пластины никеля такой же толщины.

Ключевые слова: магнитоэлектрический эффект, магнитострикция, волоконные композиты, пьезоэффект, анизотропия

• **Поступила:** 03.12.2021 • **Доработана:** 15.02.2022 • **Принята к опубликованию:** 20.04.2022

Для цитирования: Савельев Д.В., Фетисов Л.Ю., Мусатов В.И., Джапаридзе М.В. Анизотропный магнитоэлектрический эффект в структуре цирконат–титанат свинца / магнитострикционный волоконный композит. *Russ. Technol. J*. 2022;10(3):85–92. https://doi.org/10.32362/2500-316X-2022-10-3-85-92

Прозрачность финансовой деятельности: Авторы не имеют финансовой заинтересованности в представленных материалах или методах.

Авторы заявляют об отсутствии конфликта интересов.

INTRODUCTION

Magnetoelectric (ME) effects in layered composite structures containing ferromagnetic (FM) and piezoelectric (PE) layers realize mutual conversion of magnetic and electric fields. This in turn forms a basis for the creation of alternating and constant magnetic fields sensors, energy harvesting devices, controlled electronic devices (inductors and transformers), antennas, new types of magnetic memory, etc. [1–3]. In such composite structures, ME effects arise as a result of a combination of the magnetostriction of the FM layer and the piezoelectric effect in the PE layer [4]. When an ME structure is placed in an external magnetic field, the FM layer is deformed due to magnetostriction. Such deformations through the mechanical connection between the layers are transmitted to the piezoelectric layers, generating an electric field *e* due to the piezoelectric

effect. In order to describe the efficiency of the ME effect, the corresponding coefficient $\alpha_E = e/h = u/(b \cdot h)$ was introduced, where b is the piezoelectric thickness; u is the electric voltage generated between the electrodes of the PE layer arising under the action of an alternating magnetic field h.

Particular attention was paid to the study of ME effects in isotropic layered composite structures, in which the magnitude of the effect does not depend on the direction of applied magnetic field H across the planar dimension of such structures. However, in some cases, for example, for magnetic field sensors that are sensitive to the direction of the magnetic field, the creation of anisotropic ME composites represents a topical problem, which can be solved either by means of FM layers with anisotropic magnetostriction or by means of the anisotropic piezoelectric effect occurring in PE layers. The anisotropic ME effect was observed in structures where a single crystal of cobalt ferrite $CoFe_2O_4$ [5] was used as a magnetic layer, while single crystals of lead magnioniobate titanate (PMN–PT) [6], lithium niobate $LiNbO_3$, or gallium phosphate $GaPO_4$ were used to form PE layers [7]. The anisotropy of magnetostriction can be artificially created during the fabrication of the structure. An anisotropic ME effect was also observed in heterostructures made from layers of piezoelectric ceramics of lead zirconate titanate (PZT, $Pb[Zr_xTi_{1-x}]O_3$, $0 \le x \le 1$) and FM ceramics $CoFe_2O_4$. Uniaxial magnetic anisotropy was created in the FM layer of such structures by applying external pressure to the layer during fabrication [8].

The anisotropy of the ME effect was also observed in structures that used piezo-fiber composites (PFC) manufactured by Smart Materials Corporation (Sarasota, Florida, USA) [9, 10]. PFCs comprise a set of rods made of piezoelectric ceramics arranged parallel to each other in a plane and placed in a polymer matrix. This material has become widespread due to the large size of the piezoelectric modulus, flexibility, and relatively low cost.

Recently, a new type of highly anisotropic magnetic material—magnetostrictive fiber composites (MFC)—has been proposed. This material comprises a set of wires made of a magnetic material (amorphous microwires or nickel) arranged parallel to each other at various distances and placed in a polymer matrix [11, 12]. The strongly anisotropic ME effect obtained by using this material as an FM layer in layered composites is due to the demagnetizing factor with respect to the direction of the external magnetic field (along the wires or across them).

In the present work, the authors fabricated several MFC samples based on nickel wires of different diameters and studied their magnetostrictive characteristics. The strongly anisotropic ME effect observed in MFC–PZT structures was analyzed in order to obtain the frequency-, field-, and angular dependences.

MATERIALS AND METHODS

Studies of the ME effect were carried out in two-layer composite structures containing layers of various MFCs and PZT piezoceramics. The MFC comprises a set of nickel wires closely arranged parallel to each other in a single layer and placed in a polymer matrix. Three MFC samples were made with wires of different diameters: 100 μm (sample 1), 150 μm (sample 2), and 200 μm (sample 3). BF-2 self-polymerizing adhesive based on formaldehyde resin was used as a matrix. The dimensions of the structures in the plane were 9.2 × 8.9 mm^2, 9.7 × 9.4 mm^2, and 8.4 × 8.3 mm^2, respectively. The MFC thicknesses were equal to the diameter of the wires. The appearance of the MFC is shown in Fig. 1a. The magnetostriction of all MFCs was ~$34 \cdot 10^{-6}$. When describing the results of measurements, subscripts 1, 2, and 3 are used in this work to denote MFCs having wire diameters of 100 μm, 150 μm, and 200 μm, respectively.

Commercially available $PbZr_{0.52}Ti_{0.48}O_3$ discs (Audiowell Electronics (Guangzhou) Co. Ltd., China) having a diameter of 16 mm and thickness of 200 μm were used as the PE layer. Silver electrodes were deposited on opposite sides of the disk and the disk was polarized in the transverse direction. Figure 1 presents photographs of the fabricated MFC and PZT–MFC structures. The layers of MFC and PZT were bonded

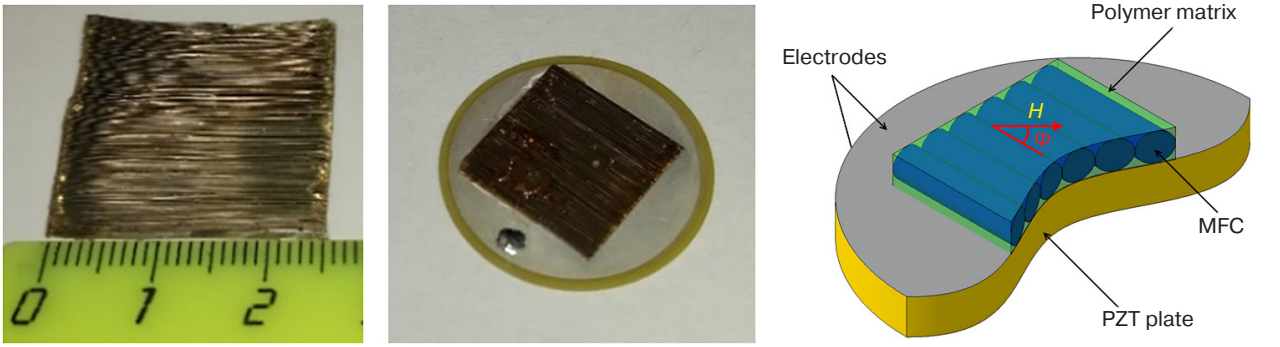

(a) (b) (c)

Fig. 1. Samples of MFCs (a), PZT–MFC with a diameter of 150 μm (b), and a schematic view of PZT–MFC structure (c)

using cyanoacrylate adhesive, while the structures were suspended in a magnetic field at two points located on opposite sides of the PZT disk using a special holder, allowing them to be rotated with respect to the direction of the magnetic field. According to the accepted classification of composites, the structures studied in the work belong to ME composites having a connectivity of "1–2" [13].

The ME effect in the structures was studied according to the method of low-frequency modulation of a magnetic field using the setup described in [12]. The structure was placed between the poles of an electromagnet in a constant magnetic field H in the range of ±1 kOe directed in the plane of the structure. The electromagnet was connected to a TDK Lambda GENH600-1.3 power supply (Japan). An exciting alternating magnetic field $h\cos(2\pi ft)$ with an amplitude of up to h = 0.8 Oe was created using Helmholtz coils connected to an Agilent 33210A arbitrary waveform generator (Agilent Technologies, Santa Clara, California, USA). The field h was parallel to the field H. The ME voltage $u(f)$ generated between the electrodes of the piezoceramic disk was measured using an AKIP 2401 voltmeter (China) with an input resistance of 10 MΩ at different values of f, h, φ, and H, as well as various orientations of H relative to the axis of the MFC wires. The dependences of the MFC magnetostriction on the magnetic field at different angles between the direction of the field and the direction of the fibers were measured by the tensometric method using the original setup described in [14].

RESULTS AND DISCUSSION

At first, the field and angular dependences of the MFC magnetostriction were studied. Figure 2 shows the field dependences of the MFC magnetostriction with different fiber diameters for cases when the magnetic field is directed along the wires. Within the measured range, it can be seen that samples 2 and 3

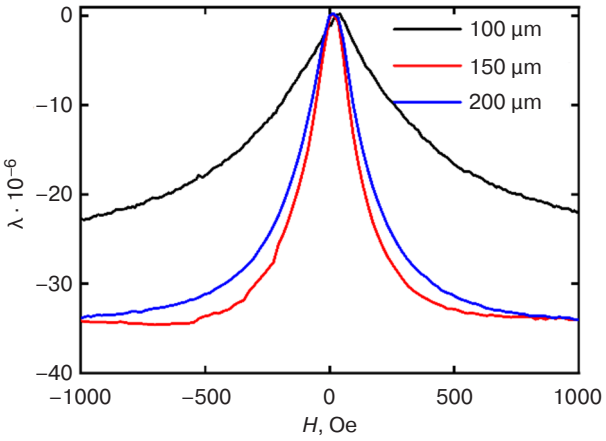

Fig. 2. Dependence of the magnetostriction for the fabricated MFC samples with different wire diameters on the magnetic field, H

reached saturation magnetostriction of ~$(-34 \cdot 10^{-6})$, while sample 1 has a value of ~$(-23 \cdot 10^{-6})$. Since the magnitude of the magnetostriction of sample 1 does not achieve saturation, it will be referred to as maximum in the text below. The saturation magnetic field decreases from more than 1 kOe to ~0.4 kOe as the fiber diameter increases from 100 μm to 200 μm. It can be seen that the magnitude of the magnetostriction of the MFC based on wires with a diameter of 150 μm increases faster than for a sample with a wire diameter of 200 μm. Here, the magnitude of the magnetostriction is apparently affected by both the demagnetizing factor and mechanical stresses from the matrix.

Figure 3 shows the measured dependences of the maximum magnetostriction on the angle between the direction of the magnetic field H and the nickel wires in fields up to 1 kOe. For all MFC samples, a strong anisotropy with respect to the direction of the magnetic field was observed. The maximum magnetostriction decreases almost to zero as the angle between the direction of the magnetic field and the wires increases to 90°. The dependence is symmetrical with respect to zero.

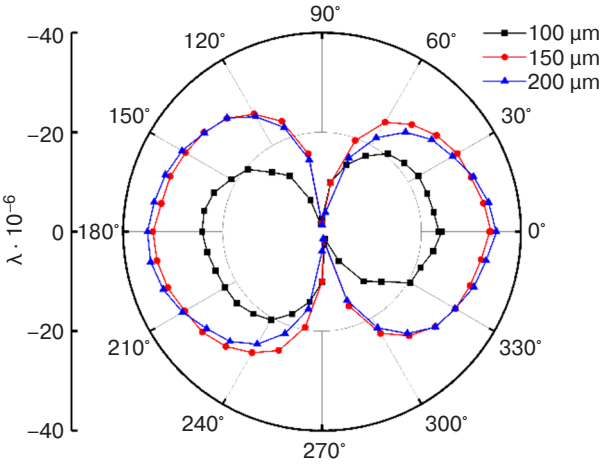

Fig. 3. Dependence of the MFC magnetostriction on the angle between the direction of the magnetic field and the direction of the wires for all samples

Next, measurements of the ME effect in the MFC–PZT structures were carried out. Figure 4 shows the frequency dependences of the ME voltage $u(f)$ obtained for all three structures. The measurements were carried out at h ~ 0.75 Oe and optimal values of the magnetic field strength H_m (H_m is the field in which the ME voltage value is maximum for each sample). The structures were magnetized along nickel wires.

The dependences show peaks at the frequencies of the bending resonance of the structures. For sample 1, the peak height was u_1 = 10.1 mV at a frequency $f_1 \approx$ 7.2 kHz; for sample 2, u_2 = 25.9 mV at a frequency $f_2 \approx$ 7.9 kHz; for sample 3, u_3 = 21.5 mV at a frequency $f_3 \approx$ 8.4 kHz. It can be seen that the resonant frequency of the structures increases with an increase in the diameter of the MFC

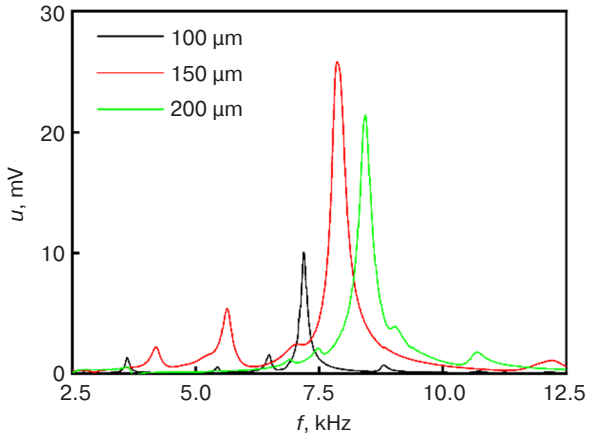

Fig. 4. Dependence of the ME voltage on the frequency measured in a magnetic field directed parallel to the wires

wires. The peak values are observed to increase linearly with an increase in the excitation field amplitude h. The quality factors of the resonances were $Q_1 \approx 72$, $Q_2 \approx 33$, $Q_3 \approx 32$. For each peak, the values of the ME coefficient were calculated using the formula $\alpha = u/(t \cdot h)$. Here u is the amplitude of the voltage generated by the ME structure; t is the thickness of the PZT layer; h is the amplitude of the alternating magnetic field. The calculated ME coefficients at resonant frequencies were $\alpha_1 = 0.61$ V/(Oe · cm), $\alpha_2 = 1.71$ V/(Oe · cm), and $\alpha_3 = 1.53$ V/(Oe · cm). While the obtained coefficients are comparable with the coefficients obtained in the PZT-nickel structures [15], they are significantly lower than the ME coefficients $\alpha_E \sim 10^2$ V/(Oe · cm) for the Metglas-AlN film structures [16]. The resonance parameters obtained from the data in Fig. 3 are given in Table.

Table. Parameters of resonant ME effect in MFC–PZT structures

Parameter	100 μm	150 μm	200 μm
ME voltage u, mV	10.1	25.9	21.5
ME coefficient α, V/(Oe · cm)	0.6	1.7	1.5
Resonance frequency f, kHz	7.2	7.9	8.4
Quality factor Q	72	33	32

Figure 5 shows the dependences of the ME voltage on the magnetic field H directed along the wires. The measurements were carried out at the corresponding resonant frequencies characteristic of each sample in an alternating magnetic field with an amplitude $h = 0.75$ Oe. For all samples, the dependences can be seen to have a typical form: the voltage initially increases with an increase in the field H, reaches a maximum in the field H_m corresponding to the maximum of the piezomagnetic coefficient ($q = d\lambda/dH|_H$), and then drops to almost zero when the magnetostriction is saturated. In the initial section, the field values H_m, which varied for each sample, were $H_{m1} \approx 70$ Oe, $H_{m2} \approx 50$ Oe, and $H_{m3} \approx 70$ Oe, respectively. All curves exhibited hysteresis. The maximum voltage amplitudes corresponded to the values shown in Fig. 4. The coercive fields H_c for samples 1–3 were $H_{c1} = 45$ Oe, $H_{c2} = 25$ Oe, and $H_{c3} = 35$ Oe, respectively.

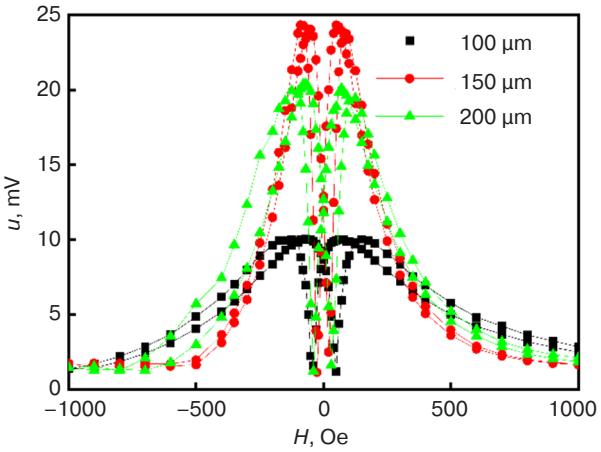

Fig. 5. Dependence of the ME voltage on the magnetic field H at the resonance frequency

At the next stage, we studied the dependences of the ME effect on the angle φ between the direction of the magnetic field and the axis of the wires ("angular dependences"), which was varied in the range from 0° to 360°. The measurements showed that, as this angle increases, the value of the maximum ME voltage decreases to practically reach zero at φ = 90°; this corresponds to the angular dependences of the magnetostriction shown in Fig. 3. The increase in the magnetic field H_m value at which the ME voltage reaches its maximum value, which is observed for each sample, is explained by the influence of the demagnetizing factor. Based on the obtained results, angular diagrams of the ME voltage in the field H_m at the resonance frequency are plotted

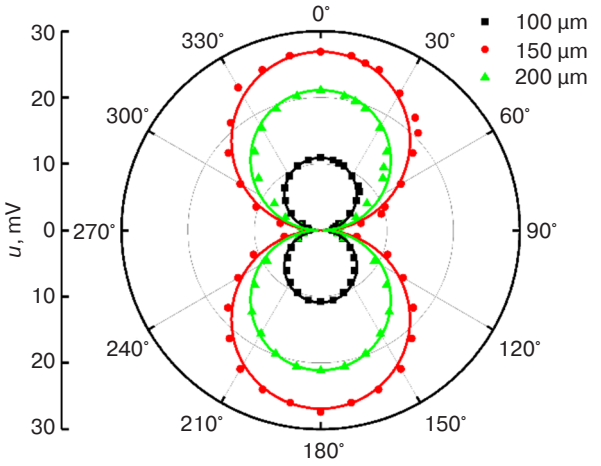

Fig. 6. Dependences of the ME voltage on the angle between the direction of the magnetic field and the axis of the wires

for all the studied samples (Fig. 6). It can be seen that the forms of dependences qualitatively coincide for all samples. The maximum voltage value was observed at the angle φ = 0°. With an increase in its value to 90° ME, the voltage decreased almost to zero. Thus, all samples demonstrate a strong anisotropy of the ME effect with respect to the direction of the magnetic field.

Figure 7 shows the dependences of the ME voltage on the amplitude of the alternating magnetic field, measured at the resonance frequency of the structures for the parallel orientation of the field H_m. Here, the dependences are linear over the entire range of amplitudes of alternating magnetic fields. The sensitivity of the structures to the magnetic field u/h was $u_1/h_1 \approx$ ≈ 12.4 mV/Oe for structure 1; $u_2/h_2 \approx 35.0$ mV/Oe for structure 2; $u_3/h_3 \approx 29.9$ mV/Oe for structure 3.

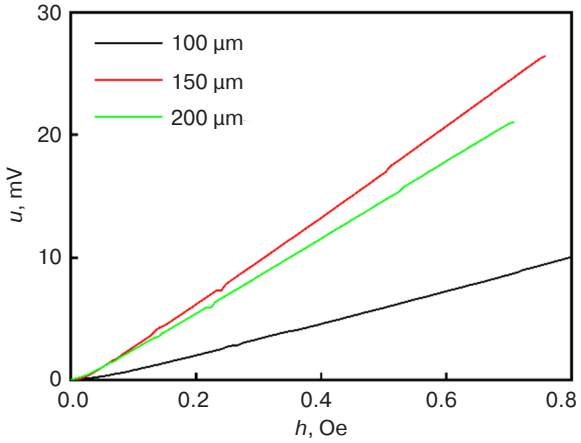

Fig. 7. Dependences of the ME voltage on the amplitude of the alternating magnetic field for samples based on MFC of various diameters

The frequencies of bending vibrations of a disk-shaped structure can be estimated using the following formula [17]:

$$f = k_{ns} \cdot \frac{a}{2\pi R^2}\sqrt{\frac{Y}{12\rho}}, \quad (1)$$

where k_{ns} is a constant, n is the number of nodal diameters, s is the number of nodal circles, a is the disk thickness, R is the disk radius, Y is Young's modulus, ρ is the density. Using the known values of the material parameters: Y_m = 210 GPa, $\rho_m = 8.9 \cdot 10^3$ kg/m^3, Y_p = 59.5 GPa, $\rho_m = 7.4 \cdot 10^3$ kg/m^3, and the dimensions of the structure, we obtain the frequencies $f_1 \approx 7$ kHz, $f_2 \approx 8.2$ kHz, and $f_3 \approx 8.3$ kHz. The frequencies determined in this way are in good agreement with the measured ones. Calculations showed that the resonant frequency increases with an increase in the diameter of the nickel wires, which also agrees with the measurements.

The amplitude of the ME voltage generated by the two-layer FM–PE structure in the linear mode is given by the formula [18, 19]:

$$u = AQ\frac{d_{31}}{\varepsilon}qh, \quad (2)$$

where A is the coefficient depending on the dimensions, mechanical and dielectric parameters of the layers of the structure, Q is the acoustic quality factor, d_{31} is the piezomodulus of the PE layer, $q = \lambda^{(1)} = \partial\lambda / \partial H\big|_H$ is the piezomagnetic coefficient, λ(H) is the dependence of the magnetostriction of the FM layer on the magnetic field, and ε is the permittivity of the PE layer. It follows from formula (2) that the shape of the dependence of the ME voltage $u(H)$ on the constant magnetic field is largely determined by the field dependence $\lambda^{(1)}(H)$. Therefore, the shape of the angular dependence of the ME voltage coincides with the shape of the angular dependence of the MFC magnetostriction.

Figure 8 shows the dependences of the piezomagnetic modulus q calculated by the method of numerical differentiation for three MFC samples, which have been plotted according to the data of Fig. 2. The maxima of the piezomagnetic moduli were $q_1 \approx 0.06$ Oe^{-1}, $q_2 \approx$ ≈ 0.21 Oe^{-1}, and $q_3 \approx 0.17$ Oe^{-1} in fields of 60–80 Oe, which resulted in the maximum value of the ME voltage u being observed for this sample (see Fig. 4)

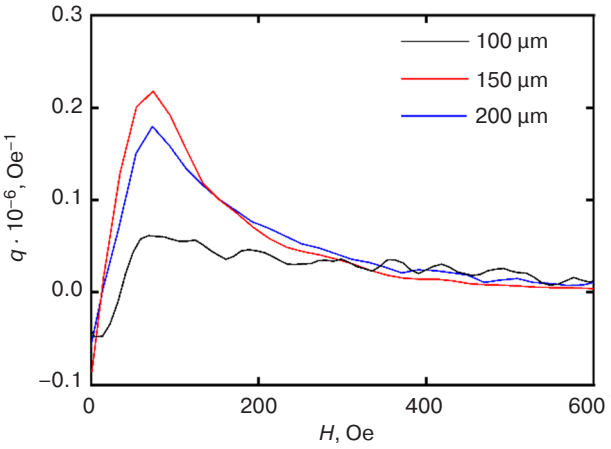

Fig. 8. Dependence of the piezomagnetic module of the MFC on the magnetic field for wires of different diameters

The anisotropy of the MFC magnetostriction is due to the demagnetizing factor. It is known that the field inside a ferromagnetic sample H_{in} is generally inhomogeneous and is related to the external field H as

$$H_{in} \approx H - N \cdot M(H_{in}), \quad (4)$$

where N is the demagnetizing factor depending on the shape of the sample and the direction of the field; M is the average magnetization of the sample, which depends on the field inside the FM layer H_{in} [20]. For a long nickel rod, when it is magnetized along the axis, the value is $N \approx 0$, and when it is magnetized across the axis, $N \approx 0.5$, i.e., when the nickel rod is magnetized along the axis, the

field H_{in} is practically equal to H, and when the nickel rod is magnetized across the axis, the field H_{in} is much smaller than H. Since the value of magnetostriction λ is determined precisely by the internal field H_{in}, a much larger field should be applied in order to achieve the maximum coefficient $\lambda^{(1)}(H)$ when it is magnetized across the axis of the nickel rod. In the general case, it is also necessary to take into account the dipole-dipole interaction between the wires inside the matrix, which depends on the distance between them.

We note that structures of this kind have a great advantage over traditional magnetic materials, since the characteristics of their ME effects can be controlled by changing the distance between the MFC wires, as well as their diameter and the materials used in the wires and matrix. These issues require further research.

CONCLUSIONS

Thus, a linear ME effect in MFC–PZT two-layer composite structures was determined and analyzed. The MFC samples comprised a set of nickel wires of different diameters arranged parallel to each other in a single layer in a polymer matrix. The frequency and field characteristics of structures with wires 100–200 μm in diameter were measured at the flexural resonance frequency. It was shown that the resonance frequency increases from 7.2 kHz to 8.4 kHz with increasing wire diameter. The highest ME coefficient of 1.7 V/(Oe · cm) obtained for a sample with a nickel wire diameter of 150 μm is comparable with the ME coefficient obtained for a structure of comparable thickness with an FM layer of polycrystalline nickel. The magnitude of the ME effect strongly depends on the orientation of the constant magnetic field H due to the anisotropy of the MFC magnetostriction.

AKNOWLEDGMENTS

The study was supported by the Russian Foundation for Basic Research, grant No. 20-32-90-190.

Authors' contributions

D.V. Saveliev—description of the research methodology, preparing test samples and installations, conducting research, data curation, visualization, and writing the text of the article.

L.Y. Fetisov—conceptualization, description of the research methodology, preparing test samples and installations, conducting research, validation, and writing the text of the article.

V.I. Musatov—preparing test samples and installations, conducting research, data curation, writing the text of the article.

M.V. Dzhaparidze—preparing test samples and installations and conducting research.

REFERENCES

1. Wang Y., Li J., Viehland D. Magnetoelectrics for magnetic sensor applications: status, challenges and perspectives *Mater. Today*. 2014;17(269):269–275. https://doi.org/10.1016/j.mattod.2014.05.004
2. Liang X., Matyushov A., Hayes P., Schell L., Dong C., Chen H., He Y., Will-Cole A., Quandt E., Martins P., McCord J., Medarde M., Lanceros-Mendez S., van Dijken S., Sun N.X., Sort J. Roadmap on magnetoelectric materials and devices. *IEEE Trans. Mag*. 2021;57(8).400157. https://doi.org/10.1109/TMAG.2021.3086635
3. He Y., Luo B., Sun N.-X. Integrated magnetics and magnetoelectrics for sensing, power, RF, and microwave electronics. *IEEE J. Microw*. 2021;4:908–929. https://doi.org/10.1109/JMW.2021.3109277
4. Nan C.-W., Bichurin M.I., Dong S., Viehland D., Srinivasan G. Multiferroic magnetoelectric composites: Historical perspective, status and future directions. *J. Appl. Phys*. 2008;103(3):031101. https://doi.org/10.1063/1.2836410
5. Oh Y.S., Crane S., Zheng H., Chu Y.H., Ramesh R., Kim K.H. Quantitative determination of anisotropic magnetoelectric coupling in $BiFeO_3$–$CoFe_2O_4$ nanostructures. *Appl. Phys. Lett*. 2010;97(5):052902. https://doi.org/10.1063/1.3475420
6. Vargas J.M., Gómez J. In-plane anisotropic effect of magnetoelectric coupled PMN-PT/FePt multiferroic heterostructure: Static and microwave properties. *APL Mater*. 2014;2(10):106105. https://doi.org/10.1063/1.4900815
7. Vidal J.V., Timopheev A.A., Kholkin A.L., Sobolev N.A. Anisotropy of the magnetoelectric effects in tri-layered composites based on single-crystalline piezoelectrics. *Vacuum*. 2015;122(B):286–292. https://doi.org/10.1016/j.vacuum.2015.06.022
8. Aubert A., Loyau V., Mazaleyrat F., LoBue M. Enhancement of the magnetoelectric effect in multiferroic $CoFe_2O_4$/PZT bilayer by induced uniaxial magnetic anisotropy. *IEEE Trans. Magn*. 2017;53(11):8109405. https://doi.org/10.1109/TMAG.2017.2696162
9. Bent A.A., Hagood N.W. Piezoelectric fiber composites with interdigitated electrodes. *J. Intell. Mater. Syst. Struct.* 1997;8(11):903–919. https://doi.org/10.1177/1045389X9700801101
10. Burdin D., Chashin D., Ekonomov N., Fetisov L., Fetisov Y., Shamonin M. DC magnetic field sensing based on the nonlinear magnetoelectric effect in magnetic heterostructures. *J. Phys. D: Appl. Phys*. 2016;49(37):375002. https://doi.org/10.1088/0022-3727/49/37/375002
11. Amirov A., Baraban I., Panina L., Rodionova V. Direct magnetoelectric effect in a sandwich structure of PZT and magnetostrictive amorphous microwires. *Materials*. 2020;13(4):916. https://doi.org/10.3390/ma13040916
12. Fetisov Y., Chashin D., Saveliev D., Fetisov L., Shamonin M. Anisotropic magnetoelectric effect in a planar heterostructure comprising piezoelectric ceramics and magnetostrictive fibrous composite. *Materials*. 2019;12(19):3228. https://doi.org/10.3390/ma12193228

13. Newnham R.E., Skinner D.P., Cross L.E. Connectivity and piezoelectric-pyroelectric composites. *Mater. Res. Bull*. 1978;13(5):525–536. https://doi.org/10.1016/0025-5408(78)90161-7
14. Chashin D.V., Burdin D.A., Fetisov L.Y., Ekonomov N.A., Fetisov Y.K. Precise measurements of magnetostriction of ferromagnetic plates. *J. Siberian Federal Univ. Math. & Phys*. 2018;11(1):30–34. https://doi.org/10.17516/1997-1397-2018-11-1-30-34
15. Feng M., Wang J.-J., Hu J.-M., Wang J., Ma J., Li H.-B., Shem Y., Lin Y.-H., Chen L.-Q., Nan C.-W. Optimizing direct magnetoelectric coupling in $Pb(Zr,Ti)O_3$/Ni multiferroic film heterostructures. *Appl. Phys. Lett*. 2015;106(7):072901. https://doi.org/10.1063/1.4913471
16. Greve H., Woltermann E., Quenzer H.J. Wagner B., Quandt E. Giant magnetoelectric coefficients in $(Fe_{90}Co_{10})_{78}Si_{12}B_{10}$-AlN thin film composites. *Appl. Phys. Lett*. 2010;96(18):182501. https://doi.org/10.1063/1.3377908
17. Timoshenko S. *Vibration Problems in Engineering*. New York: D. Van Nostrand Company, Inc.; 1961. 468 p.
18. Fetisov L.Y., Fetisov Y.K., Sreenivasulu G., Srinivasan G. Nonlinear resonant magnetoelectric interactions and efficient frequency doubling in a ferromagnetic-ferroelectric layered structure. *J. Appl. Phys*. 2013;113(11):116101. https://doi.org/10.1063/1.4798579
19. Bichurin M.I., Petrov V.M., Srinivasan G. Theory of low-frequency magnetoelectric coupling in magnetostrictive-piezoelectric bilayers. *Phys. Rev. B*. 2003;68(5):054402. https://doi.org/10.1103/PhysRevB.68.054402
20. Joseph R.I., Schlömann E. Demagnetizing field in nonellipsoidal bodies. *J. Appl. Phys*. 1965;36(5):1579–1593. https://doi.org/10.1063/1.1703091

About the authors

Dmitriy V. Saveliev, Postgraduate Student, Department of Nanoelectronics, Institute for Advanced Technologies and Industrial Programming, MIREA – Russian Technological University (78, Vernadskogo pr., Moscow, 119454 Russia). E-mail: dimsav94@gmail.com. Scopus Author ID 57196479660, ResearcherID D-8952-2019, https://orcid.org/0000-0001-7762-9198

Leonid Y. Fetisov, Dr. Sci. (Phys.–Math.), Associate Professor, Department of Nanoelectronics, Institute for Advanced Technologies and Industrial Programming, MIREA – Russian Technological University (78, Vernadskogo pr., Moscow, 119454 Russia). E-mail: fetisovl@yandex.ru. Scopus Author ID 26431336600, ResearcherID D-1163-2013, https://orcid.org/0000-0002-3699-4321

Vladimir I. Musatov, Student, Department of Nanoelectronics, Institute for Advanced Technologies and Industrial Programming, MIREA – Russian Technological University (78, Vernadskogo pr., Moscow, 119454 Russia). E-mail: musatov_vovak@mail.ru. Scopus Author ID 57416814900, https://orcid.org/0000-0002-2995-8824

Mikhail V. Dzhaparidze, Postgraduate Student, Department of Nanoelectronics Institute for Advanced Technologies and Industrial Programming, MIREA – Russian Technological University (78, Vernadskogo pr., Moscow, 119454 Russia). E-mail: mvd-1997@yandex.ru. Scopus Author ID 57395288400, https://orcid.org/0000-0001-7714-2742

Об авторах

Савельев Дмитрий Владимирович, аспирант кафедры наноэлектроники Института перспективных технологий и индустриального программирования ФГБОУ ВО «МИРЭА – Российский технологический университет» (119454, Россия, Москва, пр-т Вернадского, д. 78). E-mail: dimsav94@gmail.com. Scopus Author ID 57196479660, ResearcherID D-8952-2019, https://orcid.org/0000-0001-7762-9198

Фетисов Леонид Юрьевич, д.ф.-м.н., доцент кафедры наноэлектроники Института перспективных технологий и индустриального программирования ФГБОУ ВО «МИРЭА – Российский технологический университет» (119454, Россия, Москва, пр-т Вернадского, д. 78). E-mail: fetisovl@yandex.ru. Scopus Author ID 26431336600, ResearcherID D-1163-2013, https://orcid.org/0000-0002-3699-4321

Мусатов Владимир Иванович, студент кафедры наноэлектроники Института перспективных технологий и индустриального программирования ФГБОУ ВО «МИРЭА – Российский технологический университет» (119454, Россия, Москва, пр-т Вернадского, д. 78). E-mail: musatov_vovak@mail.ru. Scopus Author ID 57416814900, https://orcid.org/0000-0002-2995-8824

Джапаридзе Михаил Валерьевич, аспирант кафедры наноэлектроники Института перспективных технологий и индустриального программирования ФГБОУ ВО «МИРЭА – Российский технологический университет» (119454, Россия, Москва, пр-т Вернадского, д. 78). E-mail: mvd-1997@yandex.ru. Scopus Author ID 57395288400, https://orcid.org/0000-0001-7714-2742

Translated E. Shklovskii
Edited for English language and spelling by Thomas Beavitt

Analytical instrument engineering and technology

Аналитическое приборостроение и технологии

UDC 620.193
https://doi.org/10.32362/2500-316X-2022-10-3-93-102

RESEARCH ARTICLE

Contemporary approaches to reducing scale formation in heat-exchange equipment

Vladimir A. Golovin [1], Svetlana A. Tyurina [2, @], Vyacheslav A. Shchelkov [1]

[1] *Frumkin Institute of Physical Chemistry and Electrochemistry, Russian Academy of Sciences, Moscow, 119071 Russia*
[2] *MIREA – Russian Technological University, Moscow, 119454 Russia*
[@] *Corresponding author, e-mail: mgupi.tyurina@mail.ru*

Abstract

Objectives. Scale formation and corrosion are serious problems for heat and power equipment. These processes, when intense, can completely block the operation of the system, accelerating corrosion and leading to clogging, local overheating, and burnouts and ruptures of boilers and pipes, which in turn can lead to major environmental problems. Therefore, protecting surfaces from scale formation and corrosion is an important task. Promising methods for preventing the development of undesirable consequences include changing the composition of polymer coatings, e.g., by introducing microencapsulated corrosion inhibitors, as well as surface modification approaches, such as hydrophobization of the polymer coating surface. The purpose of the present work is to analyze methods for reducing scale formation and the rate of corrosion processes, as well as to study the efficiency of modification of paints and coatings by introducing microencapsulated corrosion inhibitors.

Methods. The study was based on the use of accelerated corrosion tests.

Results. Existing methods for reducing scale formation and corrosion rate on the surfaces of heat and power equipment were analyzed. The efficiency of modifying protective polymer materials by introducing microcapsules containing an active phosphonate additive was compared with approaches involving the surface modification of such protective materials.

Conclusions. It was determined that the modification of paints and coatings by introducing microencapsulated active additives can significantly reduce the rates of both scale formation and corrosion. By implementing state-of-the-art methods for modifying polymer coatings, a new generation of agents for efficiently preventing scale formation and corrosion processes can be developed for maintaining the high performance of heat-exchange equipment.

Keywords: scale formation, corrosion, inhibition, polymer coatings

• **Submitted:** 10.03.2022 • **Revised:** 25.03.2022 • **Accepted:** 28.04.2022

For citation: Golovin V.A., Tyurina S.A., Shchelkov V.A. Contemporary approaches to reducing scale formation in heat-exchange equipment. *Russ. Technol. J*. 2022;10(3):93–102. https://doi.org/10.32362/2500-316X-2022-10-3-93-102

Financial disclosure: The authors have no a financial or property interest in any material or method mentioned.

The authors declare no conflicts of interest.

НАУЧНАЯ СТАТЬЯ

Современные подходы к снижению накипеобразования в теплообменном оборудовании

В.А. Головин [1], С.А. Тюрина [2, @], В.А. Щелков [1]

[1] *Институт физической химии и электрохимии им. А.Н. Фрумкина Российской академии наук, Москва, 119071 Россия*
[2] *МИРЭА – Российский технологический университет, Москва, 119454 Россия*
[@] *Автор для переписки, e-mail: mgupi.tyurina@mail.ru*

Резюме

Цели. Процессы накипеобразования и коррозии являются серьезной проблемой для оборудования теплоэнергетического комплекса. Их активное развитие может полностью заблокировать работу системы, ускорить коррозию и привести к закупориванию, местным перегревам, прогарам и разрывам котлов и труб. Это, в свою очередь, может привести к катастрофическим последствиям и масштабным экологическим проблемам. Важной задачей является защита поверхностей от накипеобразования и коррозии. Перспективными методами предотвращения развития нежелательных последствий являются модификация состава полимерных покрытий за счет введения микрокапсулированных ингибиторов коррозии, а также поверхностная модификация, а именно, гидрофобизация поверхности полимерного покрытия. Целью работы являлся анализ методов снижения накипеобразования и скорости коррозионных процессов, а также исследование эффективности модификации лакокрасочных покрытий (ЛКП) посредством введения в их состав микрокапсулированных ингибиторов коррозии.

Методы. В работе использовались методы ускоренных коррозионных испытаний.

Результаты. Проанализированы существующие методы снижения накипеобразования и скорости коррозии на поверхностях теплоэнергетического оборудования. Исследована эффективность модифицирования защитных полимерных материалов за счет введения в их состав микрокапсул, содержащих активную фосфонатную добавку, а также их поверхностное модифицирование.

Выводы. Установлено, что модифицирование ЛКП за счет применения микрокапсулированных активных добавок позволяет существенно снизить скорость как накипеобразования, так и развития коррозионных процессов. Внедрение современных методов модифицирования полимерных покрытий позволяет получать составы нового поколения, эффективным образом препятствующие накипеобразованию, развитию коррозионных процессов, и дает возможность сохранять высокую производительность теплообменного оборудования.

Ключевые слова: накипеобразование, коррозия, ингибирование, полимерные покрытия

• **Поступила:** 10.03.2022 • **Доработана:** 25.03.2022 • **Принята к опубликованию:** 28.04.2022

Для цитирования: Головин В.А., Тюрина С.А., Щелков В.А. Современные подходы к снижению накипеобразования в теплообменном оборудовании. *Russ. Technol. J.* 2022;10(3):93–102. https://doi.org/10.32362/2500-316X-2022-10-3-93-102

Прозрачность финансовой деятельности: Авторы не имеют финансовой заинтересованности в представленных материалах или методах.

Авторы заявляют об отсутствии конфликта интересов.

INTRODUCTION

The formation of scale and corrosion on the internal sides of heat-transfer walls presents serious problems for heat and power equipment. A typical situation consists in the formation of a layer of scale, which comprises by corrosion products of metals used in water-cooling systems (circulating water pipelines, water chambers, and heat-exchanger tubes) along with limescale from water (both in the form of suspensions and dissolved salts). At an early stage, such buildups result in an increase in fuel consumption and a decrease in the reliability, efficiency, and operability of heat-exchange equipment and pipelines. At a more advanced stage, scale build-up can completely block the operation of the system, which accelerates corrosion processes leading to clogging, local overheating, and burnouts and ruptures of boilers and pipes. Ultimately, this can result in catastrophic consequences including major environmental problems [1, 2].

PRIMARY METHODS FOR REDUCING SCALE FORMATION AND CORROSION RATE

In a heat-exchange apparatus, e.g., the main steam condenser of the turbine of a nuclear power plant (NPP), the number of tubes can be very large, reach 100 000 or more. Therefore, the repair and reconstruction of such apparatuses present complex technical problems. In general, 2–5% of heat-exchanger tubes in such steam condensers have become unserviceable due to corrosion and erosion damage. Evaluation of the corrosion state of equipment at several thermal power plants (TPPs) and NPPs showed [3] that 30% of tubes are highly likely to form corrosion holes in the near future. Although these tubes can be plugged off, this will lead to an unacceptable decrease in the efficiency of the heat-exchanger equipment.

A successful solution of the problem of scale formation will ensure the cleanliness of the surfaces of water systems, helping to save fuel and energy resources, as well as preventing possible catastrophic consequences [4].

At present, the heat-exchange equipment of power systems is made mostly of copper–nickel alloys (MNZh 5-1, GOST 492-2006[1]), brass L68 (GOST 15527-2004[2]), stainless steel, and titanium alloys.

A significant variation in the conditions according to which corrosion processes develop in heat-exchange apparatuses of power plants is mainly due to the composition and temperature of the cooling water used. While NPPs typically either use natural freshwater from cooling ponds and rivers or seawater, the recycled water supply generally used for cooling TPPs is stored in cooling towers, allowing the use of special additives, e.g., for controlling the build-up of scale. Meanwhile the salt content of cooling water can differ considerably depending on the season and the cooling pond makeup conditions; in cooling water of enclosed water bodies, it can reach 100–3000 mg/L.

Based on the experience of repairing and inspection of heat-exchanger tubes of condensers of power plants, it can be concluded that the development of local corrosion is the main cause of leakage. However, local corrosion damage does not account for more than 70% of the total number of defects. Although the operating conditions and materials of heat exchangers differ, the following forms of corrosion damage are typical:

- destruction of tubes and tube sheets in the rolling zone by flow-accelerated corrosion and galvanic corrosion;
- development of unit corrosion pits or clusters of pits throughout the length of the internal surface of tubes (on the side of the cooling liquid). Pits can differ very widely in size and depth, all the way down to holes. This type of corrosion damage of tubes made of copper-nickel alloys, brasses, and stainless steels was detected both in both freshwater and seawater contexts [5].

Among the main types of corrosion damage of heat-exchanger tubes are the following:

- corrosion pits growing further into cracks due to the stress corrosion cracking mechanism;
- clusters of small-size pits (pitting) occurring primarily in the lower part of heat-exchanger tubes;
- intercrystalline, transcrystalline, and mixed-type cracking;
- corrosion over large-areas of insignificant depth.

In general, corrosion cracking of the metal of heat-exchanger tubes is caused by corrosive impurities in the form of chlorides and sulfates contained in the boiler water of steam generators [6].

The evaporation of some of the water circulating in the system from cooling towers and the surface of open ponds and water treatment facilities results in an increase in the concentration of salts and scale-forming compounds in the water. Significant quantities of corrosive compounds, mechanical suspensions, and microorganisms can accumulate in repeatedly reused water. All of this causes an intense scale build-up leading to local overheating, leading to corrosion of condensing and cooling equipment, impairing heat transfer, and weakening the mechanical strength of the metal of coil tubes and housings of apparatuses.

[1] GOST 492-2006. Interstate Standard. Nickel, nickel and copper-nickel alloys treated by pressure. Grades. Moscow: Standartinform; 2011 (in Russ.).

[2] GOST 15527-2004. Interstate Standard. Pressure treated copper zinc alloys (brasses). Grades. Moscow: IPK Izd. Standartov; 2004 (in Russ.).

Scale formation in demineralized water generator is inhibited by a number of methods, in particular:

- acidification of water and using scale control additives;
- addition of granular additives (seeds);
- contact stabilization;
- using special designs of evaporators with moving and self-cleaning heat-transfer surfaces;
- magnetic, ultrasonic, and radiation treatment of feed water.

The choice of one or another method for cleaning internal surfaces, which can be divided into chemical, mechanical, and physical approaches, is also largely determined by the type of scale.

Chemical methods of scale removal by possible simultaneous inhibition in different technological streams are typically performed by mixing a chemical treatment agent with a technological stream to ensure the treatment of hard-to-reach surfaces. However, chemical treatment methods that include the use of complex-forming agents and corrosion inhibitors are increasingly widely used due to a number of significant advantages.

The means by which complex-forming agents partially or fully convert insoluble scale into well-soluble salts or other compounds has been described in detail [7–9]. There are also methods based on the conversion of scale into substances that are insoluble in water but soluble in other chemical reagents [10–12].

A mixture of sodium tripolyphosphate and a nitrogen-containing compound (ethanolamine borate) has been recommended [13] as a water-soluble inhibitor; this can increase the efficiency of corrosion protection, decrease the salt deposition rate, and protect heat-exchange equipment made of ferrous metals from stress corrosion damage. It was determined that a combination of ethanolamine borate (EAB) and sodium tripolyphosphate (STPP) in a certain ratio (10.0–20.0 wt % EAB : 80.0–90.0 wt % STPP) gives rise to a synergistic increase in the washing, protective and water-displacement properties of the inhibitor.

The appropriate treatment methods, conditions, and reagents can be selected based on the results of chemical analysis of scale [14, 15]. One of the main methods for controlling the surface properties of materials is hydrophobization [16–19].

Water repellent coatings are highly important in many applications, including corrosion protection, self-cleaning, fouling protection, separation of oil from water, anti-icing, energy conversion, drug release, drag reduction in flowing liquids, and antibacterial adhesion, as well asproduction of antifouling paints for boats, windshields, architectural coatings, etc. [20, 21].

Along with hydrophobic coatings proper, a special group of superhydrophobic coatings can be identified. Bionic superhydrophobic coatings of surface attract attention owing to their characteristics and possibilities of application. In nature, superhydrophobic properties are present in the surfaces of some plants and animals, namely, lotus and rice leaves, shark skin, gecko foot, butterfly wing, penguin feather, and others [22, 23].

An efficient approach to reducing metal corrosion or improving metal waterproofing uses superhydrophobic materials to lower surface tension. However, the retention of an air layer as a barrier between the superhydrophobic metal support and the liquid limits the area of contact between the liquids and the surface, significantly decreasing the transfer of heat [24, 25]. Hydrophobic surfaces can be obtained by either creating a specific hierarchical surface roughness, or applying materials with low surface energy to a support. These approaches can be used both separately, and together [26, 27]. Superhydrophobic coatings produced using physical adsorption have short service life because of weak physical interaction [28]. High energies of interaction with a material are characteristic of coatings obtained using chemical adsorption of hydrophobic agents.

The curvature of a surface is one of the control factors. It has been determined that the contact angle on cylindrical and spherical surfaces is larger than that on a flat surface, whereas the contact angle on concave surfaces (nanopores, spherical cavities) is smaller than that on a flat surface of the same chemical composition [29].

At the Massachusetts Institute of Technology, Cambridge, MA, USA, a method was developed to coat the surfaces of a condensing apparatus with a monatomic graphene layer. By testing in a water vapor medium at 100°C, this coating was shown to ensure the transition from film to drop condensation and increase the heat transfer by a factor of 4 in comparison with metallic surfaces, where the condensate formed a water layer.

The short service life of most artificial superhydrophobic surfaces prohibits their widespread use in industry. Moreover, such surfaces tend to lose superhydrophobicity on exposure to an aggressive medium or under a mechanical action. In order to expand the range of application of superhydrophobic surfaces, solving these problems is highly important.

In order to maximize the service life of anti-scale coatings, the following complex properties should be ensured: thermodynamically stable heterogeneous conditions of surface wetting, chemical stability, high adhesion to support, and abrasion resistance.

Despite the above disadvantages and difficulties of obtaining superhydrophobic surfaces, the developed methods and superhydrophobic additives can be very useful for protecting heat-exchange equipment from scale formation and corrosion.

An efficient and widely used method for protecting and restoring tubes used in heat-exchange equipment is to apply a polymer protective coating (lining) to

the internal surface. This is due both to the successful development of polymer materials with a high thermal conductivity and to the development of the painting technology, which allows the application of an ultrathin lining to the undamaged surface of a tube in one pass while simultaneously placing reliable polymer plugs for fill both corrosion pits, and corrosion holes [30].

Metallic heat-transfer surfaces are converted to metal–polymer ones by applying a polymer composite lining to the internal surface of a metal tube. The efficiency of this conversion is determined by:

- a significant increase in the service life of the system of lined tubes owing to high chemical and abrasion resistance of polymer linings;
- blocks of corrosion sites, which can be scale formation nuclei;
- a substantially lower adhesion of scale to the polymer surface than to the metal of the tube. This is due to the smoother lining surface (especially in comparison with the surface of a tube with corrosion pits) and lower polarity of the inert polymer surface (in comparison with surface of the oxidized metal) and therefore the absence of conditions for chemical binding of scale;
- the possibility of controlled modification of the surface layer to impart additional anti-scale properties to the surface.

The following requirements are imposed on polymer materials for coating the heat-transfer surfaces of turbine condensers:

- the working temperature during normal operation should be 0 to +40°C with an option of a short-term increase to +240°C;
- the coating thickness should be no more than 50–60 μm according to the requirement of the minimum effect on heat transfer at a thermal conductivity of the material of the coating in a range of 1–2 W/(m · K);
- the linear thermal expansion coefficient should be close to that of the metal;
- the pull-off adhesion strength of the material to steel should be 50–60 MPa and remain unchanged during operation;
- the material should be resistant to abrasive wear at an abrasive concentration of 3–5% in a water flow;
- the coating should be smooth and gloss without drips and runs;
- the material should be readily manufacturable and inexpensive.

Many commercially-available polymer materials have some of the necessary characteristics. However, some have a limited operating temperature, while others have a high viscosity, resulting in the impossibility of applying a thin layer of polymer material to a metal substrate. If a coating is too thick, this inevitably leads to an increase in the thermal resistance. Polymer materials also differ significantly in terms of thermal and chemical stability, as well as their adhesion to various metals.

Despite all the difficulties, a wide range of polymer materials is currently used to protect the surfaces of heat-exchange equipment. Most materials require some form of modification, which can include hydrophobization of the surface to increase thermal conductivity and adhesion strength, improvement of thermal and chemical stability, abrasion resistance, etc.

At the Laboratory of Corrosion Protection of Metals and Alloys in Highly Aggressive Media at the Frumkin Institute of Physical Chemistry and Electrochemistry, Russian Academy of Sciences, Moscow, Russia, scale formation was successfully inhibited by introducing modifying (anti-scale) additives both as microcapsules to the bulk of a polymer corrosion protection coating, as well as to its surface.

Each of the microcapsules has the shape of a ball with a core made of a phosphonate modifying additive and a shell made of an epoxy polymer material. As a medium enters the microcapsules, the modifying additive is washed out. These microcapsules have been shown to significantly increase both the corrosion resistance and the duration of the anti-scale action of the modifying additives [31–34].

Testing showed that the adhesion of a scale layer to the modified polymer coatings remains very low. This leads to spontaneous peeling and cracking of scale following insignificant external actions or changes in technological parameters (Fig. 1).

Fig. 1. Photograph of a sample after scale formation testing. The upper part of the sample is protected by a polymer coating

Industrial tests have demonstrated that the coatings of this type minimize scale formation on tube sheets and the inlet portions of heat-exchanger tubes of steam condensers of TPPs and NPPs in long-term operation.

Importantly, the modified coatings have a high abrasion resistance (the sand concentration in the pulp is 5%; the flow velocity is 3 m/s), which allows the coatings

Fig. 2. Appearance of a protective coating on a part of the tube sheet and on a bundle of painted tubes of the horizontal network water heater at the Khabarovsk TPP after 7 months of operation

to be used in condenser tube cleaning systems. The wear rate was less than 0.5 μm in 1000 h. This ensures a service life of a 50-μm-thick coating of more than 10 years.

At the Balakovo NPP in Saratov oblast, Russia, coatings prevented scale and deposition formation in heat-exchanger tubes for 4 years. The coatings have no external damage, peels, or cracks. The color and luster of the surface of the coating were preserved; the anti-scale properties of the coating permitted transition to the batch operation of the condenser tube cleaning system [35].

Successful results were obtained in applying modified coatings to a network water heater at the Khabarovsk TPP. Before applying coatings, on tube sheets and the internal surface of tubes of the horizontal network water heater, a layer of deposited products of corrosion of the feeding water line intensely formed. After applying a polymer coating to the tube sheets and the internal surface of bundles of heat-exchanger tubes, the protected heat-transfer surfaces remained in the initial state without visible scale following 7 months of operation at temperatures up to 140°C (Fig. 2).

CONCLUSIONS

Modern methods of modification of polymer coatings by using active microencapsulated phosphonate additives produce agents of new generation that efficiently prevent scale formation and corrosion processes with retaining high performance of heat-exchange equipment. Along with a high functionality of protective coatings, one should note the availability of raw material and the economic efficiency of implementation of the presented approach for reducing scale formation in heat-exchange equipment. The minimum no-failure service life of the developed polymer protective coatings is estimated at 10 years.

Authors' contributions

V.A. Golovin—concept and methodology development, conducting research, collecting data, and scientific editing.

S.A. Tyurina—collecting data, conducting research, writing and editing the text of the article.

V.A. Shchelkov—methodology development, collecting data, and conducting research.

REFERENCES

1. Saremi M., Dehghanian C., Sabet M. The effect of molybdate concentration and hydrodynamic effect on mild steel corrosion inhibition in simulated cooling water. *Corros. Sci.* 2006;48(6);1404–1412. https://doi.org/10.1016/j.corsci.2005.06.009
2. *Betz Handbook of Industrial Water Conditioning:* 8th ed. BETZ Labratories Inc., USA; 1980. 440 p.
3. *Materialy konferentsii nachal'nikov turbinnykh tsekhov rossiiskikh i zarubezhnykh AES po povysheniyu nadezhnosti i effektivnosti turbinnogo oborudovaniya NTTs 2013* (*Materials of the conference of heads of turbine shops of Russian and foreign NPPs on improving the reliability and efficiency of turbine equipment STC 2013*). Moscow; 2013 (in Russ.).
4. Mwaba M.G., Golriz M.R., Gu. J. A semi-empirical correlation for crystallization fouling on heat exchange surfaces. *Appl. Therm. Eng.* 2006;26(4):440–447. https://doi.org/10.1016/j.applthermaleng.2005.05.021

СПИСОК ЛИТЕРАТУРЫ

1. Saremi M., Dehghanian C., Sabet M. The effect of molybdate concentration and hydrodynamic effect on mild steel corrosion inhibition in simulated cooling water. *Corros. Sci.* 2006;48(6);1404–1412. https://doi.org/10.1016/j.corsci.2005.06.009
2. *Betz Handbook of Industrial Water Conditioning:* 8th ed. BETZ Labratories Inc., USA; 1980. 440 p.
3. *Материалы конференции начальников турбинных цехов российских и зарубежных АЭС по повышению надежности и эффективности турбинного оборудования НТЦ-2013*. Москва; 2013.
4. Mwaba M.G., Golriz M.R., Gu. J. A semi-empirical correlation for crystallization fouling on heat exchange surfaces. *Appl. Therm. Eng.* 2006;26(4):440–447. https://doi.org/10.1016/j.applthermaleng.2005.05.021
5. Головин В.А., Печников Н.В., Щелков В.А., Цивадзе А.Ю. Оценка срока эксплуатации теплообменных трубок конденсаторов пара на основе статистического анализа локальной язвенной коррозии по данным вихретокового контроля. *Физикохимия поверхности и защита материалов.* 2018;54(45):14–26. https://doi.org/10.1134/S004418561806013X

5. Golovin V.A., Pechnikov N.V., Shchelkov V.A., Tsivadze A.Yu. Evaluation of the service life of heat exchange tubes of steam condensers based on statistical analysis of local ulcerative corrosion according to eddy current control data. *Fizikokhimiya poverkhnosti i zashchita materialov = Physical chemistry of the surface and protection of materials*. 2018. Vol. 54. P. 14–26 (in Russ.). https://doi.org/10.1134/S004418561806013X
6. Zhang H.H., Pang X., Meng Z., Chao L., Liang W., Gao K. The behavior of pre-corrosion effect on the performance of imidazoline-based inhibitor in 3 wt % NaCl solution saturated with CO_2. *Appl. Surf. Sci.* 2015;356:63–72. https://doi.org/10.1016/j.apsusc.2015.08.003
7. Avdeev Y.G., Kuznetsov Y.I. Inhibitory protection of steels from high-temperature corrosion in acid solutions. A review. Part 1. *Int. J. Corros. Scale Inhib*. 2020;9(2): 394–426. http://dx.doi.org/10.17675/2305-6894-2020-9-2-2
8. Bovt V.V., Mikov A.I. *Kompozitsiya na osnove nitrata karbamida i sposob polucheniya kompozitsii na osnove nitrata karbamida* (*Composition based on carbamide nitrate and method for producing a composition based on carbamide nitrate*): RF Pat. 2497941. Publ. 10.11.2013 (in Russ.).
9. Aptekman A.G., Beklemyshev V.I., Bolgov V.Yu., Makhonin I.I. *Promyvochnyi sostav dlya udaleniya nakipi* (*Flushing composition for descaling*): RF Pat. 2172301. Publ. 20.08.2001 (in Russ.).
10. Aliev Z.M., Magomedova D.Sh., Sup'yanova E.A., Yaldarov E.M. Using electrochemically synthesized anolyte for cleaning internal surfaces of pipelines from scale. *Vestnik Dagestanskogo gosudarstvennogo universiteta = Herald of Dagestan State University*. 2014;6:148–150 (in Russ.).
11. Linnikov O.D., Rodina I.V., Anokhina E.A., et al. *Sposob ochistki oborudovaniya ot otlozhenii s vysokim soderzhaniem medi* (*Method for cleaning equipment from deposits with a high copper content*): RF Pat. 2359196. Publ. 20.06.2009 (in Russ.).
12. Akhmedov G.Ya. *Sposob ochistki teploobmennika ot karbonatnykh otlozhenii* (*Method for cleaning the heat exchanger from carbonate deposits*) RF Pat. 2528776. Publ. 20.09.2014 (in Russ.).
13. Gaidar S.M. *Vodorastvorimyi ingibitor korrozii metallov* (*Water-soluble metals corrosion inhibitor*): RF Pat. 2355820. Publ. 20.05.2009 (in Russ.).
14. Artamonova I.V., Gorichev I.G. Ecological features of carbonate deposit removal from the surface of manufacturing equipment. *Izvestiya MGTU MAMI*. 2009;8(2):220–227 (in Russ.).
15. Shagiev N.G., Chichirova N.D., Abasev Yu.V., Lyapin A.I. Thermodynamic analysis of processes in water contours of power stations at chemical clearing with use of compositions based on a complexons. *Izvestiya vysshikh uchebnykh zavedenii. Problemy Energetiki = Power engineering: research, equipment, technology*. 2003;(11–12):82–88 (in Russ.).
16. Zhang P., Lv F.Y. A review of the recent advances in superhydrophobic surfaces and the emerging energy-related applications. *Energy*. 2015;82:1068–1087. https://doi.org/10.1016/j.energy.2015.01.061
17. Barati D.G., Aliofkhazraei M., Khorsand S., Sokhanvar S., Kaboli A. Science and engineering of superhydrophobic surfaces: review of corrosion resistance, chemical and mechanical stability. *Arab. J. Chem*. 2020;13(1): 1763–1802. https://doi.org/10.1016/j.arabjc.2018.01.013

6. Zhang H.H., Pang X., Meng Z., Chao L., Liang W., Gao K. The behavior of pre-corrosion effect on the performance of imidazoline-based inhibitor in 3 wt % NaCl solution saturated with CO_2. *Appl. Surf. Sci.* 2015;356:63–72. https://doi.org/10.1016/j.apsusc.2015.08.003
7. Avdeev Y.G., Kuznetsov Y.I. Inhibitory protection of steels from high-temperature corrosion in acid solutions. A review. Part 1. *Int. J. Corros. Scale Inhib*. 2020;9(2): 394–426. http://dx.doi.org/10.17675/2305-6894-2020-9-2-2

8. Бовт В.В., Миков А.И. *Композиция на основе нитрата карбамида и способ получения композиции на основе нитрата карбамида*: Пат. 2497941 РФ. Заявка № 201204930/04; заявл. 13.02.2012; опубл. 10.11.2013. Бюл. 31.
9. Аптекман А.Г., Беклемышев В.И., Болгов В.Ю., Махонин И.И. *Промывочный состав для удаления накипи*: Пат. 2172301 РФ. Заявка № 2000110279/12; заявл. 25.04.2000; опубл. 20.08.2001. Бюл. 23.
10. Алиев З.М., Магомедова Д.Ш., Супьянова Э.А., Ялдаров Э.М. Исследование электрохимически синтезированного анолита для очистки внутренних трубопроводов от накипи. *Вестник Дагестанского государственного университета*. 2014;6:148–150.
11. Линников О.Д., Родина И.В., Анохина Е.А. и др. *Способ очистки оборудования от отложений с высоким содержанием меди*: Пат. 2359196 РФ. Заявка № 2007134131/02; заявл. 12.09.2007; опубл. 20.06.2009. Бюл. № 17.
12. Ахмедов Г.Я. *Способ очистки теплообменника от карбонатных отложений*: Пат. 2528776 РФ. Заявка № 2013109835/06; заявл. 05.03.2013; опубл. 20.09.2014. Бюл. 26.
13. Гайдар С.М. *Водорастворимый ингибитор коррозии металлов*: Пат. 2355820 РФ. Заявка № 2008113753/02; заявл. 11.04.2008; опубл. 20.05.2009. Бюл. 14.
14. Артамонова И.В., Горичев И.Г. Экологические особенности удаления карбонатных отложений с поверхности теплотехнического оборудования. *Известия МГТУ «МАМИ»*. 2009;8(2):220–227.
15. Шагиев Н.Г., Чичирова Н.Д., Абасев Ю.В., Ляпин А.И. Термодинамический анализ процессов в водных контурах электростанций при химических очистках с использованием композиций на основе комплексонов. *Известия высших учебных заведений. Проблемы энергетики*. 2003;(11–12):82–88.

16. Zhang P., Lv F.Y. A review of the recent advances in superhydrophobic surfaces and the emerging energy-related applications. *Energy*. 2015;82:1068–1087. https://doi.org/10.1016/j.energy.2015.01.061
17. Barati D.G., Aliofkhazraei M., Khorsand S., Sokhanvar S., Kaboli A. Science and engineering of superhydrophobic surfaces: review of corrosion resistance, chemical and mechanical stability. *Arab. J. Chem*. 2020;13(1): 1763–1802. https://doi.org/10.1016/j.arabjc.2018.01.013

18. Latthe S.S., Sutar R.S., Kodag V.S., Bhosale A.K., Kumar A.M., Kumar Sadasivuni K., Xing R., Liu S. Self–cleaning superhydrophobic coatings: potential industrial applications. *Prog. Org. Coat*. 2019;128:52–58. https://doi.org/10.1016/j.porgcoat.2018.12.008
19. Cao L., Jones A.K., Sikka V.K., Wu J., Gao D. Anti-Icing superhydrophobic coatings. *Langmuir*. 2009;25(21): 12444–12448. https://doi.org/10.1021/la902882b

18. Latthe S.S., Sutar R.S., Kodag V.S., Bhosale A.K., Kumar A.M., Kumar Sadasivuni K., Xing R., Liu S. Self – cleaning superhydrophobic coatings: potential industrial applications. *Prog. Org. Coat.* 2019;128:52–58. https://doi.org/10.1016/j.porgcoat.2018.12.008
19. Cao L., Jones A.K., Sikka V.K., Wu J., Gao D. Anti-Icing superhydrophobic coatings. *Langmuir.* 2009;25(21): 12444–12448. https://doi.org/10.1021/la902882b
20. Mehmood U., Al-Sulaiman F.A., Yilbas B.S., Salhi B., Ahmed S.H.A., Hossain M.K. Superhydrophobic surfaces with antireflection properties for solar applications: a critical review. *Sol. Energy Mater. Sol. Cells*. 2016;157:604–623. https://doi.org/10.1016/j.solmat.2016.07.038
21. Gwon H.J., Park Y., Moon C.W., Nahm S., Yoon S.J., Kim S.Y., Jang H.W. Superhydrophobic and antireflective nanograss-coated glass for high performance solar cells. *Nano Res.* 2014;7(5):670–678. https://doi.org/10.1007/s12274-014-0427-x
22. Gao X.F., Jiang L. Biophysics: water-repellent legs of water striders. *Nature.* 2004;432(7013):36. https://doi.org/10.1038/432036a
23. Gao X., Yan X, Yao X., Xu L., Zhang J., Zhang K., Yang B., Jiang L. The dry-style antifogging properties of mosquito compound eyes and artificial analogues prepared by soft lithography. *Adv. Mater.* 2007;19(17):2213–2217. https://doi.org/10.1002/adma.200601946
24. Liu T., Chen S.G., Cheng S., Tian J.T., Chang X.T., Yin Y.S. Corrosion behavior of super-hydrophobic surface on copper in seawater. *Electrochim. Acta*. 2007;52(28): 8003–8007. https://doi.org/10.1016/j.electacta.2007.06.072
25. Yin Y.S., Liu T., Chen S.G., Liu T., Cheng S. Structure stability and corrosion inhibition of super-hydrophobic film on aluminum in seawater. *Appl. Surf. Sci.* 2008;255(5): 2978–2984. https://doi.org/10.1016/j.apsusc.2008.08.088
26. Hooda A., Goyat M.S., Pandey J.K., Kumar A., Gupta R. A review on fundamentals, constraints and fabrication techniques of super-hydrophobic coatings. *Prog. Org. Coat.* 2020;142:105557. https://doi.org/10.1016/j.porgcoat.2020.105557
27. Wang G., Zhang T.Y. Easy route to the wettability cycling of copper surface between superhydrophobicity and superhydrophilicity. *ACS Appl. Mater. Interfaces.* 2012;4(1):273–279. https://doi.org/10.1021/am2013129
28. Mortazavi V., Khonsari M. On the degradation of superhydrophobic surfaces: a review. *Wear.* 2017;372–373: 145–157. https://doi.org/10.1016/j.wear.2016.11.009
29. Boinovich L.B., Emelyanenko A.M. The prediction of wettability of curved surfaces on the basis of the isotherms of the disjoining pressure. *Colloids and Surfaces A: Physicochemical and Engineering Aspects.* 2011;383(1–3): 10–16. https://doi.org/10.1016/j.colsurfa.2010.12.020
30. Golovin V.A., Kaz'min A.N., Nemytova A.M. Experience gained from using protective coating of cooling tubes in the condensers at the Leningrad and the Smolensk nuclear power plants. *Term. Eng*. 2012;59(2):119–124. https://doi.org/10.1134/S0040601512020048
31. Ilyin A.B., Shchelkov V.A., Dobriyan S.A., Lukin V.B., Golovin V.A. Polymer coatings for protection of heat-exchange tubes of vapor condenser against corrosion and saltation. *Mezhdunarodnyi nauchno-issledovatel'skii zhurnal=InternationalResearchJournal*.2018;5(71):69–75 (in Russ.). https://doi.org/10.23670/IRJ.2018.71.037
20. Mehmood U., Al-Sulaiman F.A., Yilbas B.S., Salhi B., Ahmed S.H.A., Hossain M.K. Superhydrophobic surfaces with antireflection properties for solar applications: a critical review. *Sol. Energy Mater. Sol. Cells*. 2016;157:604–623. https://doi.org/10.1016/j.solmat.2016.07.038
21. Gwon H.J., Park Y., Moon C.W., Nahm S., Yoon S.J., Kim S.Y., Jang H.W. Superhydrophobic and antireflective nanograss-coated glass for high performance solar cells. *Nano Res.* 2014;7(5):670–678. https://doi.org/10.1007/s12274-014-0427-x
22. Gao X.F., Jiang L. Biophysics: water-repellent legs of water striders. *Nature.* 2004;432(7013):36. https://doi.org/10.1038/432036a
23. Gao X., Yan X, Yao X., Xu L., Zhang J., Zhang K., Yang B., Jiang L. The dry-style antifogging properties of mosquito compound eyes and artificial analogues prepared by soft lithography. *Adv. Mater.* 2007;19(17):2213–2217. https://doi.org/10.1002/adma.200601946
24. Liu T., Chen S.G., Cheng S., Tian J.T., Chang X.T., Yin Y.S. Corrosion behavior of super-hydrophobic surface on copper in seawater. *Electrochim. Acta*. 2007; 52(28):8003–8007. https://doi.org/10.1016/j.electacta.2007.06.072
25. Yin Y.S., Liu T., Chen S.G., Liu T., Cheng S. Structure stability and corrosion inhibition of super-hydrophobic film on aluminum in seawater. *Appl. Surf. Sci.* 2008;255(5):2978–2984. https://doi.org/10.1016/j.apsusc.2008.08.088
26. Hooda A., Goyat M.S., Pandey J.K., Kumar A., Gupta R. A review on fundamentals, constraints and fabrication techniques of super-hydrophobic coatings. *Prog. Org. Coat.* 2020;142:105557. https://doi.org/10.1016/j.porgcoat.2020.105557
27. Wang G., Zhang T.Y. Easy route to the wettability cycling of copper surface between superhydrophobicity and superhydrophilicity. *ACS Appl. Mater. Interfaces*. 2012;4(1):273–279. https://doi.org/10.1021/am2013129
28. Mortazavi V., Khonsari M. On the degradation of superhydrophobic surfaces: a review. *Wear.* 2017;372–373:145–157. https://doi.org/10.1016/j.wear.2016.11.009
29. Boinovich L.B., Emelyanenko A.M. The prediction of wettability of curved surfaces on the basis of the isotherms of the disjoining pressure. *Colloids and Surfaces A: Physicochemical and Engineering Aspects*. 2011;383(1–3):10–16. https://doi.org/10.1016/j.colsurfa.2010.12.020
30. Golovin V.A., Kaz'min A.N., Nemytova A.M. Experience gained from using protective coating of cooling tubes in the condensers at the Leningrad and the Smolensk nuclear power plants. *Term. Eng*. 2012;59(2):119–124. https://doi.org/10.1134/S0040601512020048
31. Ильин А.Б., Щелков В.А., Добриян С.А., Лукин В.Б., Головин В.А. Полимерные покрытия для защиты теплообменных трубок конденсаторов пара от коррозии и солеотложений. *Международный научно-исследовательский журнал*. 2018;5(71):69–75. https://doi.org/10.23670/IRJ.2018.71.037

32. Golovin V.A. Prevention of scale formation and corrosion of heat transfer surfaces of NPP condensers. In*: Proceeding of Conference of Heads of Turbine Shops of Russian and Foreign NPPs on Improving the Reliability and Efficiency of Turbine Equipment*. *Rosenergoatom Concern JSC*, February 13–15, 2018 (in Russ.)
33. Golovin V.A., Il'in A.B., Kuznec V.T., Vartapetjan A.R. *Sposob zashhity ot korrozii metallicheskih poverhnostej ingibirovannymi polimernymi kompozicijami i mikrokapsuly s ingibitorom korrozii* (*Method of protecting metal surfaces inhibited with polymer compositions from corrosion and micro-capsules with a corrosion inhibitor* (*versions*)): RF Pat. 2358036. Publ. 10.06.2009 (in Russ.).
34. Golovin V.A., Kuznets V.T., Kublitsky K.V., Ilin A.B. *Method for protection against corrosion and scale deposit and for restoring tubes of heat-exchanging equipment and device for carrying out said method*: US Pat. 7836844. Publ. 23.11.2010.
35. Golovin V.A., Ilyin A.B., Aliev A.D. Diffusion of phosphonic scale inhibitors for scale in epoxy matrices. *Mezhdunarodnyj nauchno-issledovatel'skij zhurnal = International Research Journal*. 2018;70(4):92–96 (in Russ.). https://doi.org/10.23670/IRJ.2018.70.033

32. Головин В.А. Предотвращение накипеобразования и коррозии теплопередающих поверхностей конденсаторов АЭС. *Труды конференции начальников турбинных цехов российских и зарубежных АЭС по повышению надежности и эффективности турбинного оборудования.* АО «Концерн Росэнергоатом», 13–15 февраля 2018.
33. Головин В.А., Ильин А.Б., Кузнец В.Т., Вартапетян А.Р. *Способ защиты от коррозии металлических поверхностей ингибированными полимерными композициями и микрокапсулы с ингибитором коррозии*: Пат. 2358036 РФ. Заявка № 2007148024/02; заявл. 25.12.2007; опубл. 10.06.2009.
34. Golovin V.A., Kuznets V.T., Kublitsky K.V., Ilin A.B. *Method for protection against corrosion and scale deposit and for restoring tubes of heat-exchanging equipment and device for carrying out said method*: US Pat. 7836844. Publ. 23.11.2010.
35. Головин В.А., Ильин А.Б., Алиев А.Д. Диффузия фосфоновых ингибиторов накипеобразования в эпоксидных матрицах. *Международный научно-исследовательский журнал.* 2018;70(4):92–96. https://doi.org/10.23670/IRJ.2018.70.033

About the authors

Vladimir A. Golovin, Dr. Sci. (Eng.), Head of the Laboratory of Metal and Alloy Protection from Corrosion in Highly Aggressive Media, Frumkin Institute of Physical Chemistry and Electrochemistry, Russian Academy of Sciences (31-4, Leninskii pr., Moscow, 119071 Russia). E-mail: golovin@corrosion.ru. Scopus Author ID 7006124188, ResearcherID S-1645-2018, https://orcid.org/0000-0001-9144-507X

Svetlana A. Tyurina, Cand. Sci. (Eng.), Associate Professor, Department of Digital and Additive Technologies, Institute for Advanced Technologies and Industrial Programming, MIREA – Russian Technological University (78, Vernadskogo pr., Moscow, 119454 Russia). E-mail: mgupi.tyurina@mail.ru. Scopus Author ID 57209980191, ResearcherID AGI-3957-2022, https://orcid.org/0000-0002-6671-1337

Vyacheslav A. Shchelkov, Cand. Sci. (Eng.), Senior Researcher, Laboratory of Metal and Alloy Protection from Corrosion in Highly Aggressive Media, Frumkin Institute of Physical Chemistry and Electrochemistry, Russian Academy of Sciences (31-4, Leninskii pr., Moscow, 119071 Russia). E-mail: tehnolog@rocor.ru. Scopus Author ID 6506074251, https://orcid.org/0000-0001-7437-5305

Об авторах

Головин Владимир Анатольевич, д.т.н., заведующий лабораторией защиты от коррозии металлов и сплавов в сильноагрессивных средах, Институт физической химии и электрохимии им. А.Н. Фрумкина Российской академии наук (119071, Россия, Москва, Ленинский пр-т, д. 31, корп. 4). E-mail: golovin@rocor.ru. Scopus Author ID 7006124188, ResearcherID S-1645-2018, https://orcid.org/0000-0001-9144-507X

Тюрина Светлана Александровна, к.т.н., доцент кафедры цифровых и аддитивных технологий Института перспективных технологий и индустриального программирования ФГБОУ ВО «МИРЭА – Российский технологический университет» (119454, Россия, Москва, пр-т Вернадского, д. 78). E-mail: mgupi.tyurina@mail.ru. Scopus Author ID 57209980191, ResearcherID AGI-3957-2022, https://orcid.org/0000-0002-6671-1337

Щелков Вячеслав Анатольевич, к.т.н., старший научный сотрудник лаборатории защиты от коррозии металлов и сплавов в сильноагрессивных средах, Институт физической химии и электрохимии им. А.Н. Фрумкина Российской академии наук (119071, Россия, Москва, Ленинский пр-т, д. 31, корп. 4). E-mail: tehnolog@rocor.ru. Scopus Author ID 6506074251, https://orcid.org/0000-0001-7437-5305

Translated by V. Glyanchenko
Edited for English language and spelling by Thomas Beavitt

Analytical instrument engineering and technology
Аналитическое приборостроение и технологии

UDC 628.95
https://doi.org/10.32362/2500-316X-2022-10-3-103-110

RESEARCH ARTICLE

Research and development of pulse electronic control devices with UV lamps

Olga Yu. Kovalenko [1], Svetlana A. Mikaeva [2, @], Yulia A. Zhuravleva [2]

[1] *Ogarev Mordovia State University, Saransk, 430005 Russia*
[2] *MIREA – Russian Technological University, Moscow, 119454 Russia*
[@] *Corresponding author, e-mail: mikaeva_s@mirea.ru*

Abstract

Objectives. When used in lighting installations with tubular low-pressure ultraviolet (UV) lamps, electronic ballasts should meet the following basic requirements: low cost, reliable ignition at low temperatures, as well as combining high energy efficiency with reliable lamp operation. As compared with electromagnetic ballasts, electronic ballasts allow the luminous efficiency and power factor of discharge lamps to be increased, reducing the consumption of scarce materials along with the weight of devices. In order to improve their energy efficiency, complete UV lamps are based on low-pressure discharge lamps with pulsed electronic ballasts supplying power at the frequency of 22–50 kHz. Various circuit designs include such basic units as mains filter, rectifier, power factor corrector, smoothing filter, high-frequency converter, ballast, and ignition device. The present study aimed to develop an electronic semiconductor circuit for switching on and powering a discharge lamp of increased energy efficiency using a pulsed electronic ballast.

Methods. Classical methods of mathematical research were applied for determining the flux of the 254-nm mercury resonance line using a structural electronic ballast diagram along with a mathematical description and adaptive model.

Results. Equations for determining the parameters of pulses formed by an envelope having the form of input voltage and current supplied at industrial frequency were formulated for different instants of time. A mathematical description is given for determining pulse duration and lamp current depending on the values of nominal and operating voltage, as well as nominal current. Diagrams for instantaneous voltage values at the high-frequency switch input and generated pulsed current are presented. The parameters of the 'UV lamp–electronic ballast' set were calculated using an adaptive model for determining the flux of the 254-nm mercury resonance line according to the condition of lamp power constancy.

Conclusions. Relative values for radiant efficiency of the 254-nm mercury line for UV lamps under study were determined. Theoretical research of electronic ballasts led to the development of a semiconductor switching and power supply circuit for the discharge lamp based on high-frequency rectangular pulses. The parameters of the element base were calculated along with selected basic initial characteristics of the blocking generator.

Keywords: electronic ballast, power, mathematical description, filter, converter, pulse, mercury resonance line, blocking generator

• **Submitted:** 20.10.2021 • **Revised:** 24.02.2022 • **Accepted:** 18.04.2022

For citation: Kovalenko O.Yu., Mikaeva S.A., Zhuravleva Yu.A. Research and development of pulse electronic control devices with UV lamps. *Russ. Technol. J.* 2022;10(3):103–110. https://doi.org/10.32362/2500-316X-2022-10-3-103-110

Financial disclosure: The authors have no a financial or property interest in any material or method mentioned.

The authors declare no conflicts of interest.

НАУЧНАЯ СТАТЬЯ

Исследование и разработка импульсных электронных пускорегулирующих аппаратов в комплекте с ультрафиолетовыми лампами

О.Ю. Коваленко [1], С.А. Микаева [2, @], Ю.А. Журавлёва [2]

[1] *Национальный исследовательский Мордовский государственный университет им. Н.П. Огарёва, Саранск, 430005 Россия*
[2] *МИРЭА – Российский технологический университет, Москва, 119454 Россия*
[@] *Автор для переписки, e-mail: mikaeva_s@mirea.ru*

Резюме

Цели. В облучательных приборах, работающих в светотехнических установках с трубчатыми ультрафиолетовыми (УФ) лампами низкого давления, к электронным пускорегулирующим аппаратам (ЭПРА) предъявляются следующие требования: невысокая стоимость, обеспечение надежного зажигания разрядных ламп низкого давления в условиях пониженных температур и надежная работа ламп при повышенной энергетической эффективности. По сравнению с электромагнитными пускорегулирующими аппаратами, ЭПРА обеспечивают повышение светоотдачи разрядных ламп и коэффициента мощности, снижение расхода дефицитных материалов, уменьшение массы. Для повышения энергетической эффективности УФ ламп в комплекте с ними целесообразно использовать импульсные ЭПРА, обеспечивающие питание на частоте 22–50 кГц. Различные схемные решения ЭПРА включают в себя такие основные узлы как сетевой фильтр, выпрямитель, корректор коэффициента мощности, сглаживающий фильтр, высокочастотный (ВЧ) преобразователь, балласт и зажигающее устройство. Целью работы является разработка электронной полупроводниковой схемы включения и питания разрядной лампы повышенной энергетической эффективности с импульсным ЭПРА.

Методы. Использованы классические методы математического исследования с применением структурной схемой ЭПРА, его математическим описанием и адаптивной модели для определения потока резонансной линии ртути с длиной волны 254 нм.

Результаты. Для разных моментов времени представлены уравнения определения параметров импульсов, образованных огибающей в форме входного напряжения и тока промышленной частоты. Дано математическое описание для определения длительности импульсов и тока лампы в зависимости от значений номинального и рабочего напряжения и номинального тока. Представлены диаграмма мгновенных значений напряжения на входе ВЧ ключа и диаграмма формируемого импульсного тока. В работе проведен расчет параметров комплекта «УФ лампа – импульсный ЭПРА» при условии постоянства мощности лампы и использовании адаптивной модели для определения потока резонансной линии ртути длиной волны 254 нм.

Выводы. В результате расчетов были определены относительные значения лучистой отдачи резонансной линии ртути исследуемых УФ ламп. Теоретические исследования ЭПРА позволили разработать электронную полупроводниковую схему включения и питания разрядной лампы прямоугольными импульсами высокой частоты. В ходе работы для предложенного схемного решения импульсного ЭПРА проведен расчет параметров элементной базы с выбранными основными исходными характеристиками блокинг-генератора.

Ключевые слова: электронный пускорегулирующий аппарат, мощность, математическое описание, фильтр, преобразователь, импульс, резонансная линия ртути, блокинг-генератор

• **Поступила:** 20.10.2021 • **Доработана:** 24.02.2022 • **Принята к опубликованию:** 18.04.2022

Для цитирования: Коваленко О.Ю., Микаева С.А., Журавлёва Ю.А. Исследование и разработка импульсных электронных пускорегулирующих аппаратов в комплекте с ультрафиолетовыми лампами. *Russ. Technol. J.* 2022;10(3):103–110. https://doi.org/10.32362/2500-316X-2022-10-3-103-110

Прозрачность финансовой деятельности: Авторы не имеют финансовой заинтересованности в представленных материалах или методах.

Авторы заявляют об отсутствии конфликта интересов.

INTRODUCTION

Recent advances in electrotechnical development involve the effective low-pressure ultraviolet (UV) lamps using electronic ballasts (EBs) [1, 2], which are used in disinfection systems and the control of unwanted odors in the air. Studies of UV radiation and the effectiveness of low-pressure UV lamps are presented in[1, 2, 3] [3–5]. When used in radiation sources for lighting installations based on tubular low-pressure UV lamps, EBs should meet the following basic requirements: low cost, reliable ignition of low-pressure discharge lamps at low temperatures, and ensuring the high energy efficiency of lamps without sacrificing reliability.

Compared with electromagnetic ballasts, EBs allow the luminous efficiency and power factor of discharge lamps to be increased, reducing the weight of units by 2–4 times along with the consumption of scarce materials. Currently available high-frequency (HF) EBs support additional functions, such as pre-heating of lamp electrodes, the ability to regulate radiation flux, etc.

In the present paper, a circuit design for EB with the lamp powered by HF rectangular pulses was proposed. The review of the published literature has revealed HF pulse power modes to be more effective than the sinusoidal ones [6, 7].

To improve the energy efficiency of UV lamps related to low-pressure discharge lamps, they should be completed with pulsed EB supplying power at the frequency of 22–50 kHz. Various EB circuit designs may include such basic units as a line filter, rectifier, power factor corrector, smoothing filter, HF converter, ballast, and ignition device [8–12].

RESEARCH AND MATHEMATICAL DESCRIPTION OF PULSED EB

The structural diagram shown in Fig. 1 has been used for implementing the pulsed EB practically.

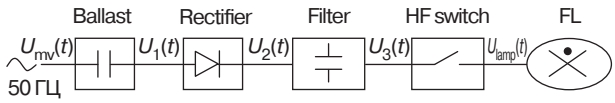

Fig. 1. Structural diagram of the pulsed EB. U_{mv}(t) is mains voltage (voltage at the pulsed EB input), $U_{lamp}(t)$ is a lamp operating voltage, and FL is a fluorescent lamp

Along with the instantaneous voltage values given in Fig. 2, the structural diagram shows that the amplitude of HF pulses may be limited by the mains voltage curve $U_1(t)$ transformed by the rectifier. At the HF switch input, a smoothing filter is located. The voltage begins to drop exponentially $U_3(t)$ at the point in the diagram (Fig. 2) at which the sinusoidal voltage $U_2(t)$ becomes lower than the filter capacitor voltage. Here, the dashed line indicates the smoothing filter input voltage while the solid line shows its output voltage.

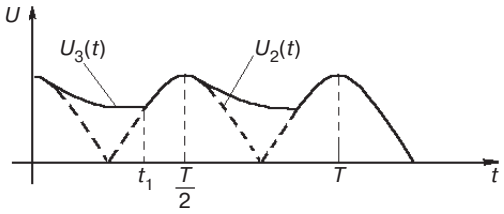

Fig. 2. Diagram for instantaneous values of the voltage at the HF switch input

Two equations describing the parameters of the pulses formed by the envelope in the form of the input voltage $U_{input}(t)$ and the industrial frequency current can be written for different instants of time. The HF switch output voltage has an amplitude corresponding to the amplitude of voltage $U_3(t)$, while the duration of pulses $t_{pulse}(t)$ (or pause $t_{pause}(t)$) depends on their amplitude. The value $t_{pulse}(t)$ is determined according to the lamp operating voltage $U_{lamp}(t)$ and empirical constant coefficients a, b.

The dependence of the lamp current on voltage is determined by its current voltage characteristic at known values of nominal voltage $U_{nom}(t)$ and current $I_{nom}(t)$, as well as the operating voltage $U_{lamp}(t)$.

The mathematical description may be represented by a system of equations, as follows:

$$\begin{cases} U_{lamp}(t) = U_m \exp\left(-\dfrac{1}{RC}t\right) \text{ at } 0 < t < t_1, \\ U_{lamp}(t) = U_m \cos 314t \text{ at } t_1 < t < \dfrac{T}{2}, \\ t_{pulse}(t) = \dfrac{a}{U_{lamp}(t) + b}, \\ i(t) = I_{nom} \exp\left(\dfrac{\ln U_{lamp}(t) - \ln U_{nom}(t)}{\rho}\right). \end{cases} \quad (1)$$

[1] Heathcote J. State of UV LED curing applications. *UV+EB Technology*. 2019;1. URL: https://uvebtech.com/articles/2019/state-of-uv-led-curing-applications/. Accessed October 1, 2021.

[2] Lawal O., et al. Proposed method for measurement of output of monochromatic (254 nm) low pressure UV lamps. *IUVA News*. 2008;10(1):14–17. URL: https://uvsolutionsmag.com/stories/pdf/archives/100103LawalEtAl_Article.pdf. Accessed October 1, 2021.

[3] Lee P. Advancements in UV LED curing technology and solutions for print. *UV+EB Technology*. 2015;1. URL: https://uvebtech.com/articles/2015/advancements-in-uv-led-curing-technology-and-solutions-for-print/. Accessed October 1, 2021.

Here, U_m is mains voltage amplitude, V; C is the smoothing filter capacity, F; R is an active component of the lamp resistance, Ohm; $i(t)$ is the current at the HF switch input, A; the angular frequency ω at signal frequency f = 50 Hz is equal to $\omega = 2\pi f = 314$ s^{-1}; ρ is the constant factor equal to 0.20–0.26; a and b are constant factors equal to 0.0025 s · V and 30 V, respectively.

The parameters of the 'UV lamp–EB' set on condition of the lamp power constancy were calculated for the UV lamps under study by equations (1) and using an adaptive model for determining the flux of the 254-nm mercury resonance line presented in the work of Kovalenko [4].

The main calculation results are shown in Table.

Table. Relative values for radiant efficiency of the 254-nm line for UV lamps complete with pulsed EB (ratio of radiant efficiency in pulsed (H_{pulse}) and stationary (H_{st}) modes). P_{av} is an average power of the lamp complete with pulsed EB

P_{av}, W	f, kHz	t_{pulse}, μs	Duty cycle	C, μF	H_{pulse}/H_{st}
30.1	23.1	25	2.35	30	0.687
30.0	23.7	25	2.42	50	0.822
30.0	41.0	6	1.32	50	0.927
29.9	43.8	10	1.77	50	0.975
40.0	23.6	25	2.41	50	0.746
39.9	43.6	10	1.77	50	0.880

The relative values for radiant efficiency of the 254-nm mercury line for the considered UV lamps (LE 30 and LER 40) complete with pulsed EB (ratio of radiant efficiency in pulsed and stationary modes) were determined on the basis of the calculation results. The lamp operating mode with a constant-voltage power supply was taken for stationary mode. However, despite its efficiency, stationary mode cannot be used for discharge lamps due to the cataphoresis phenomenon resulting in the decreased radiation flux of the lamp for a short period of time.

Table shows that the modes at a frequency of 41–44 kHz at a duty cycle of 1.77 may be considered the most effective ones for UV lamps complete with pulsed EB under study.

CIRCUIT DESIGN FOR PULSED EB

An electronic semiconductor switching and power supply circuit for the discharge lamp with selected original elements developed on the basis of theoretical EB research provides high stability of the radiant flux at unstable input voltages as a result of using feedback to determine the dependence of current pulse frequency $t_{pulse}(t)$ on the input voltage (Fig. 3).

The switching and power supply circuit for the discharge lamp shown in Fig. 3 is self-excited. The HF switch operating frequencies are above 25 kHz. A midfrequency transistor may be used as the power semiconductor element. Upon voltage being applied to the input, a voltage jump may occur at the collector of VT transistor; this is transmitted through the C5 capacitor to the primary winding of Tr transformer with a ferrite core having a hysteresis loop of rectangular shape.

When calculating the element parameters for the selected version of the pulsed EB, the lamp power values and HF power supply modes were selected.

Computational formulas and results of calculating main parameters for the circuit (Fig. 3) are presented taking the parameters of pulses—amplitudes of current and voltage, their duration, and frequency—into account.

The following basic initial parameters for calculating the blocking generator (HF switch) could be taken as an example:

$E_{C=}$ 150 V, t_{pulse} = 6–10 μs, f = 40–50 kHz, R_s = 239 Ohm,

I_{av} = 0.43 A, T^0 = 20–25 °C, R_d = 20 Ohm, R_b = 100 Ohm.

Here, E_C is an electromotive force in the transistor output circuit, R_s is the signal source resistance or output resistance of the previous stage, I_{av} is an average value of the lamp pulse current, T^0 is the transistor case temperature in operating mode, R_d is the damping circuit resistance, and R_b is the base volume resistance.

A KT809A transistor was selected considering such parameters as the collector power dissipation, collector voltage, and pulse duration.

The inductance L of the primary winding may be calculated from the following ratio:

$$L = \frac{\left(E_C - U_{CR}\right)t_{pulse}}{I_{CA} - \left(I_{IC} - 0.8E_C/r_{in}\right)}. \quad (2)$$

Here, U_{CR} is the collector residual voltage of saturated transistor (U_{CR} = 3 V); I_{CA} is the allowable collector current of transistor (I_{CA} = 5 A); I_{IC} is the initial current in collector circuit; and r_{in} is the input resistance of the transistor in the circuit with common radiator (r_{in} = 34 Ohm).

The maximum collector voltage may be determined by the following formula:

$$U_{Cm} = E_C\left(1 + \frac{t_{pulse}}{L}R_e\right), \quad (3)$$

[4] Kovalenko O.Yu. *Lighting installations for increasing the productivity of farm animals*. Dr. Sci. Thesis (Eng.). Saransk: Ogarev MSU; 2009 (in Russ.).

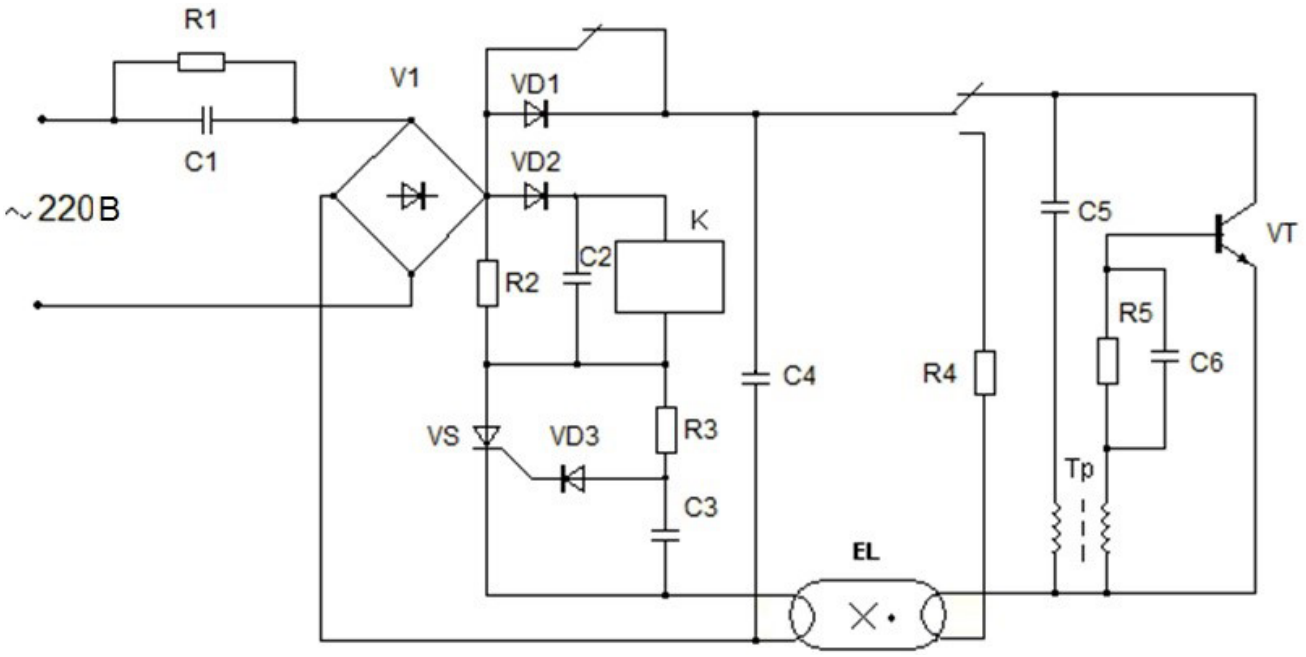

Fig. 3. Switching and power supply circuit for a discharge lamp with rated voltage 220 V

where R_e is the equivalent resistance of collector circuit written as follows:

$$R_e = \frac{R_s\left(R_d + r_d\right)}{R_s + R_d + r_d}. \quad (4)$$

Here, R_d is assumed to be equal to 20 Ohm; r_d is the forward resistance of diode (r_d = 5 Ohm).

When the temperature rises ($T^0 > T_1^e$), the value of thermal current generated by the collector residual voltage of a saturated transistor may be determined, as follows:

$$I_{CT} = I_{CT}\left(T_1^e\right)e^{0.08\left(T^0 - T_1^e\right)}. \quad (5)$$

Here, T_1^e is the environment temperature. The current I_{CT} (transition thermal current) may approximately double with the temperature increased by 10°C. Assuming the base potential (constant voltage source) $E_b = E_C$, capacitance C5 at resistance R_b = 100 Ohm may be determined in the following way:

$$C5 = \frac{\tau_{acc}}{\left(1 - \theta\frac{\tau_{acc}}{\tau_{pulse}}\right)\left(r_b + R_b\right)}. \quad (6)$$

Here, τ_{acc} is the accumulation time constant (for KT809A transistor, τ_{acc} = 28.9 μs); τ_{pulse} is the pulse duration, μs; r_b is the transistor base input resistance; and θ is the coefficient defined by the following formula:

$$\theta = \frac{t_{pulse}\left(\tau_{in} - \tau_{acc}\right)}{\tau_{in}\tau_{acc}}. \quad (7)$$

Here, τ_{in} is the capacity charging time constant characterized by the pulse leading edge time; τ_{in} = 40 μs.

The capacitor C6 required for compensating the inductive resistance of the transformer secondary winding and resistance R1, R_d is selected on the basis of calculations. The load resistance is taken as R_s = 349 Ohm. Diodes should be selected to account for the value of current through the load equal to the average value of the lamp pulse current I_{av} = 0.43 A.

The pulsation ratio K of the rectifying voltage is taken as equal to 0.3.

The smoothing filter capacity may be determined by the following formula:

$$C4 = \frac{1}{\omega R_s}\sqrt{\frac{1.68}{\text{arth}^2 K} - 4}. \quad (8)$$

The alternating current circuit capacitance at constant empirical coefficient m, depending on the rectifier type (for a double half-period rectifier, m = 0.34), is determined by the following formula:

$$C1 = \frac{(0.455K + 1.15)}{\omega R_s\sqrt{\frac{1}{m^2} - (1+K)^2\frac{K}{0.57}\left(2 - \frac{K}{0.57}\right)} - (1+K)\left(1 - \frac{K}{0.57}\right)}. \quad (9)$$

Thus, the following element base is defined on the basis of calculation results with selected main parameters for the blocking generator:

- Capacitors: C1, 5 μF × 250 V (KBG-MP); C4, 50.0 μF × 350 V (K-50-7), C5, 470 μF; C6, 5 μF;
- Resistors: R1 = 10 Ohm; R2 = 20 Ohm; R3 = 200 Ohm; R4 = 2 Ohm; R5 = 5.1 Ohm;
- Diodes: VD1–VD4, D 229 L; VD5, D 226 B;
- Transistor: VT, KT 809 A.

CONCLUSIONS

In the study, the relative values for radiant efficiency of the 254-nm mercury line have been calculated for the considered UV lamps complete with pulsed EB (ratio of radiant efficiency in pulsed and stationary modes). The most efficient modes were defined along with the circuit design for the pulsed EB allowing the HF switch operation to be controlled. The high stability of the radiant flux was ensured using feedback to control the duration of current and voltage pulses.

Authors' contributions

O.Yu. Kovalenko—overall supervision, planning and conducting research.

S.A. Mikaeva—conducting research, data collection and processing, and literature review.

Yu.A. Zhuravleva—conducting research, analysis of results, and writing the text of the article.

REFERENCES

1. Kovalenko O.Yu., Sarychev P.A., Mikaeva S.A., Mikaeva A.S. Improvement of the ultra-violet low pressure digit lamps. *Avtomatizatsiya i sovremennye tekhnologii = Automation and Modern Technologies*. 2011;12:13–15 (in Russ.).
2. Kovalenko O.Yu., Pil'shchikova Yu.A., Guseva E.D. Efficiency improvement and parameter checkout of emission sources of irradiation equipment in agriculture. *Fotonika = Photonics Russia*. 2017;8(68):68–73 (in Russ.). https://doi.org/10.22184/1993-7296.2017.68.8.68.73
3. Nikolaeva E.V., Alekseev Yu.V., Laryushin A.I., Sosnin E.A. Ultraviolet irradiation in the wavelength range 305–315 μm for treating a number of dermatological diseases. *Lazernaya meditsina = Laser Medicine*. 2014;18(4):51 (in Russ.). Available from URL: https://www.goslasmed.ru/wp-content/uploads/2016/09/Lazer-med_4_2014.pdf
4. Kowalski W. *Ultraviolet Germicidal Irradiation Handbook*. Berlin: Springer; 2009. 501 p. https://doi.org/10.1007/978-3-642-01999-9
5. Sankar G.U. A survey on wavelength based application of ultraviolet LED. *Int. J. Sci. Res. Sci. Eng. Technol*. 2016;2(6):23–24. Available from URL: https://ijsrset.com/paper/1986.pdf
6. Okhonskaya E.V. The efficiency of fluorescent lamps with high-frequency power supply. *Svetotekhnika = Light & Engineering*. 1987;2:10–12 (in Russ.).
7. Tsvetkov E.I. On the results of the study of a set of fluorescent lamp-pulsed semiconductor ballast. In: *Chelovek i svet*: Mezhvuzovskii sbornik nauchykh trudov (*Man and light*: Interuniversity collection of scientific papers). Saransk: Mordovia State University Publishing House; 1982. P. 86 (in Russ.).
8. Mikaeva S.A., Mikaeva A.S. *Eksperimental'nye issledovaniya kharakteristik perspektivnykh istochnikov sveta, priborov i system* (*Experimental study of characteristics of advanced light sources, devices and systems*). Moscow: RUSAINS; 2017. 136 p. (in Russ.). ISBN 978-5-4365-1785-8

СПИСОК ЛИТЕРАТУРЫ

1. Коваленко О.Ю., Сарычев П.А., Микаева С.А., Микаева А.С. Совершенствование ультрафиолетовых разрядных ламп низкого давления. *Автоматизация и современные технологии*. 2011;12:13–15.
2. Коваленко О.Ю., Пильщикова Ю.А., Гусева Е.Д. Повышение эффективности и контроль параметров источников излучения облучательных установок в сельском хозяйстве. *Фотоника*. 2017;8(68):68–73. https://doi.org/10.22184/1993-7296.2017.68.8.68.73
3. Николаева Е.В., Алексеев Ю.В., Ларюшин А.И., Соснин Э.А. Применение ультрафиолетового излучения в диапазоне длин волн 305–315 нм в терапии ряда дерматологических заболеваний. *Лазерная медицина*. 2014;18(4):51. URL: https://www.goslasmed.ru/wp-content/uploads/2016/09/Lazer-med_4_2014.pdf
4. Kowalski W. *Ultraviolet Germicidal Irradiation Handbook*. Berlin: Springer; 2009. 501 p. https://doi.org/10.1007/978-3-642-01999-9
5. Sankar G.U. A survey on wavelength based application of ultraviolet LED. *Int. J. Sci. Res. Sci. Eng. Technol*. 2016;2(6):23–24. URL: https://ijsrset.com/paper/1986.pdf
6. Охонская Е.В. Эффективность люминесцентных ламп при высокочастотном питании. *Светотехника*. 1987;2:10–12.
7. Цветков Е.И. О результатах исследования комплекта люминесцентная лампа – импульсный полупроводниковый ПРА. *Человек и свет*: Межвуз. сб. науч. трудов. Саранск: Изд-во Мордовского гос. ун-та; 1982. С. 86.
8. Микаева С.А., Микаева А.С. *Экспериментальные исследования характеристик перспективных источников света, приборов и систем*. М.: РУСАЙНС; 2017. 136 с. ISBN 978-5-4365-1785-8
9. Поляков В.Д., Смирнов Е.М. Характеристики люминесцентных ламп при управлении подогревом электрода с помощью ЭПРА. *Светотехника*. 2008;4:46–49.
10. Беспалов Н.Н., Ильин М.В., Капитонов С.С. Оборудование для испытаний управляющих устройств для светильников со светодиодами и ЭПРА для люминесцентных ламп. *Светотехника*. 2017;4:42–46.

9. Polyakov V.D., Smirnov E.M. Investigation the characteristics of luminescent lamps' cathode heating control by means of electron start-control devices (ESCD). *Light & Engineering*. 2008;16(4):43–47.
10. Bespalov N.N., Il'in M.V., Kapitonov S.S. Testing equipment for LED luminaire control devices and fluorescent lamp electron ballasts. *Light & Engineering*. 2017;25(4):86–91.
11. Malyshev A. New – well-forgotten old: nutritional features of bactericidal and fluorescent lamps and the choice of electronic ballasts for them. *Poluprovodnikovaya svetotekhnika = Solid – State Lighting*. 2021;6(74):26–30.
12. Terent'ev B. Electronic ballasts (EPRA): history, principle of operation, problems. Popular microcircuits for electronic ballasts. *Komponenty i tekhnologii = Components & Technologies*. 2008;5(82):106–110 (in Russ.). Available from URL: https://kit-e.ru/wp-content/uploads/2008_5_106.pdf
11. Малышев А. Новое – хорошо забытое старое: особенности питания бактерицидных и люминесцентных ламп и выбор ЭПРА для них. *Полупроводниковая светотехника*. 2021;6(74):26–30.
12. Терентьев Б. Электронные пускорегулирующие аппараты (ЭПРА): история, принцип работы, проблемы. Популярные микросхемы для ЭПРА. *Компоненты и технологии*. 2008;5(82):106–110. URL: https://kit-e.ru/wp-content/uploads/2008_5_106.pdf

About the authors

Olga Yu. Kovalenko, Dr. Sci. (Eng.), Associate Professor, Professor, Department of Metrology, Standardization and Certification, Institute of Electronics and Lighting Engineering, National Research Ogarev Mordovia State University (68, Bolshevistskaya ul., Saransk, 430005 Russia). E-mail: crystall2000@mail.ru. Scopus Author ID 57190227678.

Svetlana A. Mikaeva, Dr. Sci. (Eng.), Associate Professor, Professor, Department of Electronics Institute for Advanced Technologies and Industrial Programming, MIREA – Russian Technological University (78, Vernadskogo pr., Moscow, 119454 Russia). E-mail: mikaeva_s@mirea.ru. Scopus Author ID 57214070393, https://orcid.org/0000-0001-6992-455X

Yulia A. Zhuravleva, Cand. Sci., (Eng.), Assistant Professor, Assistant Professor, Department of Electronics, Institute for Advanced Technologies and Industrial Programming, MIREA – Russian Technological University (78, Vernadskogo pr., Moscow, 119454 Russia). E-mail: ulypil@mail.ru. Scopus Author ID 57217961848, https://orcid.org/0000-0003-3919-5127

Об авторах

Коваленко Ольга Юрьевна, д.т.н., доцент, профессор кафедры метрологии, стандартизации и сертификации Института электроники и светотехники ФГБОУ ВО «Национальный исследовательский Мордовский государственный университет им. Н.П. Огарёва» (430005, Россия, Саранск, Большевистская ул., д. 68). E-mail: crystall2000@mail.ru. Scopus Author ID 57190227678.

Микаева Светлана Анатольевна, д.т.н., доцент, профессор кафедры электроники Института перспективных технологий и индустриального программирования ФГБОУ ВО «МИРЭА – Российский технологический университет» (119454, Россия, Москва, пр-т Вернадского, д. 78). E-mail: mikaeva_s@mirea.ru. Scopus Author ID 57214070393, https://orcid.org/0000-0001-6992-455X

Журавлёва Юлия Алексеевна, к.т.н., доцент, доцент кафедры электроники Института перспективных технологий и индустриального программирования ФГБОУ ВО «МИРЭА – Российский технологический университет» (119454, Россия, Москва, пр-т Вернадского, д. 78). E-mail: ulypil@mail.ru. Scopus Author ID 57217961848, https://orcid.org/0000-0003-3919-5127

Translated by K. Nazarov
Edited for English language and spelling by Thomas Beavitt

Philosophical foundations of technology and society

Мировоззренческие основы технологии и общества

UDC 7.05
https://doi.org/10.32362/2500-316X-2022-10-3-111-120

RESEARCH ARTICLE

The concept of usability in terms of universal design

Irina Yu. Mamedova,
Anna E. Dryukova [@],
Natalia E. Milchakova

MIREA – Russian Technological University, Moscow, 119454 Russia
[@] Corresponding author, e-mail: dryukova@mirea.ru

Abstract

Objectives. The paper discusses usability as the concept underlying many contemporary design trends and accompanying technological development in various industrial, graphic and digital contexts. A formulation of the concept of usability in digital design contexts is advanced based on the evolution of industrial design.

Methods. Using the historical research method, usability is shown to be characterized by unification of form as applied to the relationship between a person and a design object. This conclusion has been applied to digital design using the analogy method. Basic principles of usability assessment in design are outlined, along with impacts on further development. Requirements for a designed product in terms of usability analysis should be fulfilled taking into account the principles of universality that constitute a basis for a universal design system.

Results. When developing UI/UX design objects, the usability of a digital product is considered in terms of universality based on rational visual image principles of industrial design and taking contemporary requirements in graphic, digital, and website design into account. Examples of industrial and digital design developments carried out by students using the concept of universal design are presented.

Conclusions. The usability of a design object can be shaped by using universal principles applying in both industrial and UI/UX design.

Keywords: usability, shaping, industrial design, digital design, universal design

• **Submitted:** 11.03.2022 • **Revised:** 29.03.2022 • **Accepted:** 25.04.2022

For citation: Mamedova I.Yu., Dryukova A.E., Milchakova N.E. The concept of usability in terms of universal design. *Russ. Technol. J*. 2022;10(3):111–120. https://doi.org/10.32362/2500-316X-2022-10-3-111-120

Financial disclosure: The authors have no a financial or property interest in any material or method mentioned.

The authors declare no conflicts of interest.

НАУЧНАЯ СТАТЬЯ

Концепция юзабилити с позиции универсального дизайна

И.Ю. Мамедова,
А.Э. Дрюкова [@],
Н.Е. Мильчакова

МИРЭА – Российский технологический университет, Москва, 119454 Россия
[@] Автор для переписки, e-mail: dryukova@mirea.ru

Резюме

Цели. В статье представлено понятие юзабилити как основополагающей концепции многих направлений современного дизайна: промышленного, графического, цифрового и т.д. с учетом развития технологий. Целью статьи является формулирование концепции юзабилити в цифровом дизайне на основании эволюции юзабилити в промышленном дизайне.

Методы. Использование исторического метода исследования показало, что юзабилити применительно к взаимосвязи между человеком и объектом дизайна характеризуется унификацией формы. С помощью метода аналогии этот вывод был применен и по отношению к цифровому дизайну. В статье приведены основные принципы оценки юзабилити в дизайне, а также характер ее влияния на дальнейшее развитие дизайна. Требования к проектируемому продукту с точки зрения анализа юзабилити рекомендовано выполнять с учетом принципов универсальности, являющихся основой системы универсального дизайна.

Результаты. Принимая во внимание принципы проектирования в промышленном дизайне и современные требования в области графического, цифрового и веб-дизайна, авторами предложено формировать юзабилити цифрового продукта с точки зрения универсальности и искать наиболее рациональные визуальные образы при проектировании объектов UI/UX дизайна. В статье приведены примеры разработок промышленного и цифрового дизайна, выполненных студентами с применением концепции универсального дизайна.

Выводы. Использование принципов универсальности как в промышленном, так и в UI/UX дизайне, позволяет сформировать юзабилити проектируемого объекта дизайна.

Ключевые слова: юзабилити, формообразование, промышленный дизайн, цифровой дизайн, универсальный дизайн

• **Поступила:** 11.03.2022 • **Доработана:** 29.03.2022 • **Принята к опубликованию:** 25.04.2022

Для цитирования: Мамедова И.Ю., Дрюкова А.Э., Мильчакова Н.Е. Концепция юзабилити с позиции универсального дизайна. *Russ. Technol. J.* 2022;10(3):111–120. https://doi.org/10.32362/2500-316X-2022-10-3-111-120

Прозрачность финансовой деятельности: Авторы не имеют финансовой заинтересованности в представленных материалах или методах.

Авторы заявляют об отсутствии конфликта интересов.

INTRODUCTION

A contemporary designer is confronted by a multilevel complex system of closely intertwined requirements, conditions, and frameworks, often involving contradiction and ambiguity. Today, one of the most important aspects of a designer's work involves developing products that have the property of usability. Usability is a property of a product's design that allows consumers to use it under specified conditions for achieving their goals with sufficient effectiveness, efficiency, and satisfaction. Since it allows an evaluation of the quality of the product design, the usability characteristic is of key importance. In industrial design contexts, usability is defined by the form of the designed object.

HISTORICAL BACKGROUND

Modern human beings perform many habitual actions, many of which have become second nature. As such, the nature of the household objects surrounding us

tends not to be reflected on. Whether we are considering a toothbrush, coffee cup, shoes, or comb, each of these objects has its own design history, which may not always be simple or uncontroversial (e.g., an ordinary table fork). The form of each everyday object perceived as a certain given has been shaped over time in accordance with various laws of evolution. Notwithstanding their multilevel nature and diversity, a certain regularity may be traced in the general principle of shaping material objects.

Many processes shaping human lives are cyclical in nature. In design contexts, the principle of shaping obeys the same laws as other processes occurring within the society. When analyzing the formal evolution of certain objects, relationships between historical eras—Gothic, Renaissance, Baroque, Classicism, and etc.—may be revealed. Along with features of scientific and technological progress in a given era, the nature of production is largely determined by the economic situation. Such historical changes result in the emergence of new art styles that influence the form of everyday objects.

Despite the technological paradigm, various craftwork skills still relevant today have been honed over the period of many centuries. During this time, significant attention has been focused on improving the forms of the most popular household items. Nevertheless, few attempts have been made to comprehend, scientifically justify, and describe the laws and principles according to which objects are shaped. Since craftwork does not generally involve explicit design, the centuries-old process of shaping of products has occurred more or less spontaneously. Behind each craft masterpiece lies the experience of generations preceding the master, involving lots of trial and error, unexpected findings, as well as inevitable failures. Thus, a more or less randomly obtained form combining convenience, functionality, and aesthetics "catches-on" in daily life, while inappropriate analogues gradually disappear in a process of evolution resulting in the unification of the form of the household object.

For primitive man, who lacked a variety of materials, the emergence of each new one has been a significant event; thus, the epochs of that time have the following distinctive names: "Stone Age," "Iron Age," and "Bronze Age." With a piece of clay accidentally falling into the fire, the previously mastered wood and stone have been supplemented with ceramics; seeing sparkling droplets emerging from a piece of ore in a fire, man discovered metal. Each time, the emergence of new materials and their processing technologies established a new development vector for artists, craftsmen, and architects. New materials and technologies gave rise to previously unseen objects and forms along with a rethinking of previous forms. Eventually, these processes again resulted in the unification of form within a new style, quite often involving a return to previous developments in the new round of progress (Fig. 1). However, the form is always strongly related to the production process.

(a) (b)

Fig. 1. Evolution of the mug form from antiquity (a) to the present day (b)

Among the many world-changing events associated with the historical period known as the Renaissance is the emergence of design as a discrete activity. While the difference between an idea and its realization may now be quite obvious, this approach represented a real innovation for the time; with the understanding that form exists separately from its material embodiment, craftwork started to lose its preeminent role in production. Scientists, artists, and architects—the precursors of modern engineers—invented various mechanisms, conducted experiments and calculations, as well as keeping records to build on the achievements of medieval science. Nevertheless, since form was not yet comprehended as an independent phenomenon, these changes in consciousness did not influence the shaping of traditional household items.

Although the first attempts to systematize principles of shaping were made during the period commonly referred to as the Industrial Revolution, this phenomenon in human history is also cyclical and obeys the same laws as all previous changes in the way of thinking.

The start of the Industrial Revolution has been associated with the invention of the steam engine during the late 18th century. This period has been described in textbooks on history, sociology, economics, and design as one of the key moments shaping the trajectory of modern society towards a global reorganization of the world. With the stealthy displacement of craftwork by the industrial paradigm, traditional forms typical were lost along with the elegance of lines, functionality, and convenience. In their attempts to conceal obvious shortcomings of new products in terms of their form, manufacturers resorted to so-called ornamentation, which involved decorating products to obscure the clumsiness of exterior forms and conjunctions with embossed overlays and coffers. This process coincided with the crucial shift towards

designing the form at a separate pre-primary stage rather than during the process of manufacture. Thus, it was necessary to develop a scientific understanding of the principles of shaping and identify its regularities based on a systematic approach. Here manufacturing was informed by design principles that had developed in architecture. The formation of the industrial design discipline is associated with such names as Gottfried Semper (German architect, 1803–1879) and Henry Cole (English artist and social activist, 1808–1882). By the end of the 19th century, design was already established as a discipline in its own right.

The transition to the 20th century may be characterized by a shift in industrial production to a new level. Household objects produced according to this paradigm have already become inexpensive, convenient and widely accessible to the public. The replacement of steam and water engines by electric equivalents, the invention of conveyor belts, as well as the development of transport, telegraph, telephone and radio gave rise to the Second Industrial Revolution.

The principle of shaping in design, encapsulated by the famous formulation "form follows function" by the architect Louis Sullivan in 1896, established the main direction for shaping in the 20th century. In industrial production, this brilliantly simple approach to shaping led to the establishment of industrial design schools based on Sullivan principle of functionalism (e.g., Bauhaus, Vkhutemas). Thus, the search for forms that maximize the function of products became the main strategy associated with the Second Industrial Revolution. Items produced during this period can be characterized a certain delicate elegance in terms of their functional simplicity and style. Therefore, the design concept of usability was defined by the relationship between form and function.

The end of World War II is associated with the third round of the industrial revolution. This period is marked by the more rapid pace of scientific and technological development with multifunctional electric devices moving from highly specialized areas of industrial production into the everyday lives of ordinary people. Private automobiles became widely available, electronics was actively developed and new materials based on polymers became widely used in production. The variety of forms produced in the 1960s–1980s is amazing.

During this time, the role of design in production significantly increased along with several trends in design associated with a rejection of functionalism as the ground for usability and based a post-modernistic rejection of the established principles of shaping. New trends in art-design were encapsulated in the slogans "form follows style," "form does not follow function," and "function is form," giving rise to a profusion of forms and products. Much of these have lost their relevance falling out of fashion with time. Again, there has been a trend towards the unification of form based already on the quality of the design concept rather than on the development and improvement over centuries.

Today, the unification of forms produced by the Second and the Third Industrial Revolutions may be witnessed. Here, we may cite the example of the automobile. Since the dawn of the automobile industry during the Second Industrial Revolution, the automobile form was dictated by its design and function, while the variety of these forms is limited by production capacity. With the development of material processing and assembly technologies, as well as improvements in aerodynamic and ergonomic testing during the third industrial revolution, the variety of forms employed in automotive engineering has increased significantly. Manufacturers have used all available means in an effort to impress the customer and increase sales; as a consequence, cars of various shapes, sizes, colors and versions have been rolling off the automaker assembly lines. An analysis of styles in car design for the second half of the 20th century should be the subject of a separate study. By the beginning of the 21st century, the design of the overwhelming majority of cars produced worldwide had been sufficiently unified enough to differ from each other by separate design details only: headlights, radiators and trunk shaping lines (Fig. 2). The overall shape has been reduced to the unified image dictated by the balance between aerodynamics, economic characteristics and ergonomics rather than by function. Thus, it is in a balance of characteristics that usability parameters are ultimately provided.

The late 20th century may be characterized by an emerging crisis in design. Having already come under attack during the second half of the 20th century, Sullivan's principle of form following function has become increasingly irrelevant in the production of objects functioning beyond the objective world. Today, humanity is in the midst of the Fourth Industrial Revolution placing an even heavier burden of responsibility on designers. This revolution is associated with formation of new expectations of quality of life, as well as with digitalization, development of artificial intelligence, and the replacement of conventional production technologies with the mass customization paradigm. Since there is insufficient time for unifying form in a natural manner, designers are obliged to shape the usability of objects guided by preferences that are yet to be manifested. For example, while the unification of automobile design took half a century, the unification of cell phones or computer mouse design occurred within 20 years (Fig. 3).

(a) (b)

(c) (d)

Fig. 2. Evolution of the car shape:
(a) 1958 Chevrolet Bel Air; (b) 1969 Ford Mustang Shelby GT500; (c) Toyota Auris 2008; (d) FORD Fiesta 2009

(a) (b)

Fig. 3. Shape evolution of the computer mouse:
(a) sample devices from the 1990s;
(b) modern computer mice

In this event, shaping in the context of usability requires a new approach to be considered not only in terms of function, but also the trend towards future unification due to the demand and quality of design. The development of modern usability in design may be characterized most thoroughly by the "form follows ergonomics" principle. Modern digital products are often no longer intended to be directly manipulated. For example, the function of modern headphones is not essentially different from the function of those in the past; however, their operation principle and the human-computer interaction technology have changed dramatically. Their shape may vary now within a very wide range, from familiar to bionic ones [1–6].

RESEARCH RESULTS

In industrial design, the concept of usability is intimately associated with form evolution and product shaping. However, universality principles should be considered when designing and constructing industrial facilities. In contrast to industrial products, the development of digital technology has resulted in the creation of digital products depending to a greater extent on usability. Shaping in digital design implies a search for harmonious color combinations, defining the style of elements (including defining the form of these elements) to create a harmonious composition. However, the most important criterion in digital design is usability (ease of use). Therefore, developers carry out thorough pre-project research before starting developing a website or mobile application design. Usability in user interface (UI) design is related to user experience (UX)

design research, implying the development of user interface designs that combined user convenience with a harmonious interface appearance.

Digitalization in the contemporary world accompanies the transformation of socio-technical structures previously provided by non-digital products and relations into structures mediated by digital products and relations with embedded new digital capabilities. While the development of digitalization and digital technologies has influenced the creation of new so-called "non-digital" products, since this involves the creation and development of digital products, the contemporary designer is required to master digital competencies and skills in order to create them.

Digital skills involve mastering a set of capabilities for digital devices, communication applications, and networks for accessing and managing information. Thus, digital skills and competencies should be mastered in the following areas: programming and web development, application development, digital design, project management, digital marketing, and data analytics.

The main advantages of creating digital products are the following:

1. *Low overhead costs*. Digital designing certainly involves the cost of purchasing computer hardware and licensed professional software. However, in contrast to the industrial production, the creation of each unit of a digital product (digital identity, landing page, etc.) does not imply purchasing raw materials for their creation.
2. *High profitability*. Since there are no recurring costs for materials when developing a digital product, profit can be made without use of consumables. Nevertheless, costs must be allocated to payments for labor, electricity, etc.
3. *Automated development process*. When developing various digital products, many processes may be automated to accelerate the process of completion.
4. *Flexible digital product transport*. Advanced cloud and associated technologies allow the storage and transportation of digital products to consumers without involving their physical transportation.

Thus, ergonomics, ease of use, and usability come to the fore in creating successful and competitive digital products. In digital design, the product—e.g., developing the design of website or its mobile version—undergoes a rather long process of UI/UX design testing. Although this process has common roots with evolutionary shaping in industrial design, web designers try to obtain maximum user feedback on each element of the digital product performance. Then, an analysis of user experience is carried out along with troubleshooting of the website or mobile application.

Before starting the layout, the user route for "wandering" within the developed graphical user interface should be plotted to provide a framework for the work (Fig. 4). After the route has been discussed, the development of architecture along with layout is performed (Fig. 5). The interface visualization is an important outcome of the work (Fig. 6) [7–9].

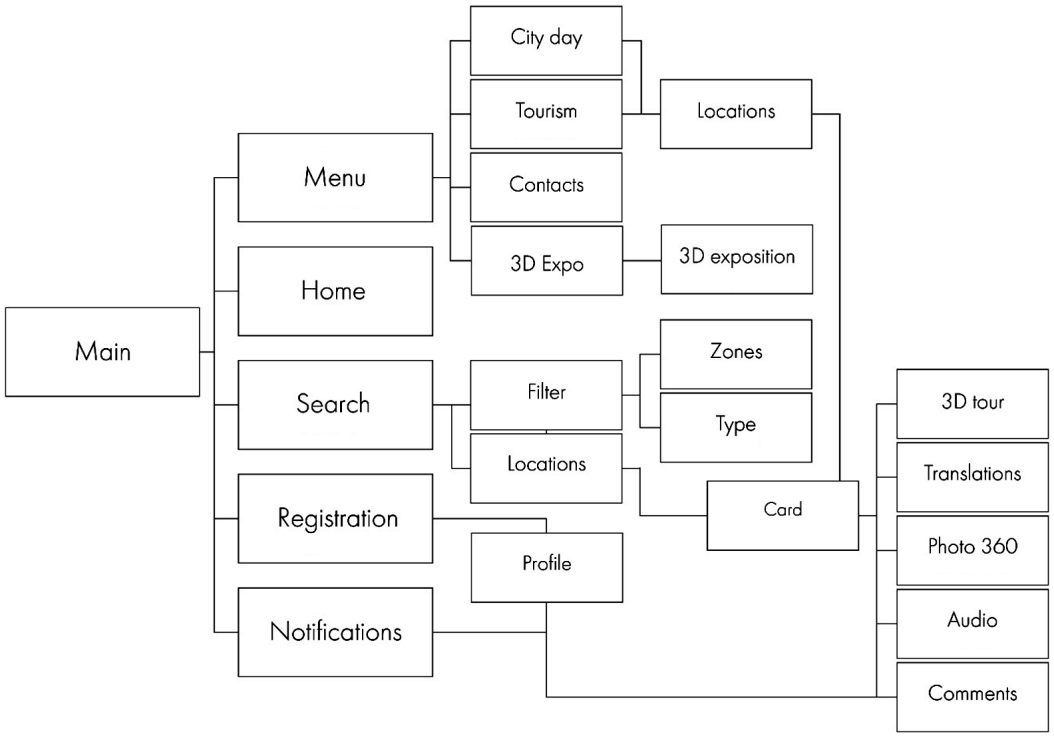

Fig. 4. Developing the user route for the exhibition website

Fig. 5. Designing the website layout

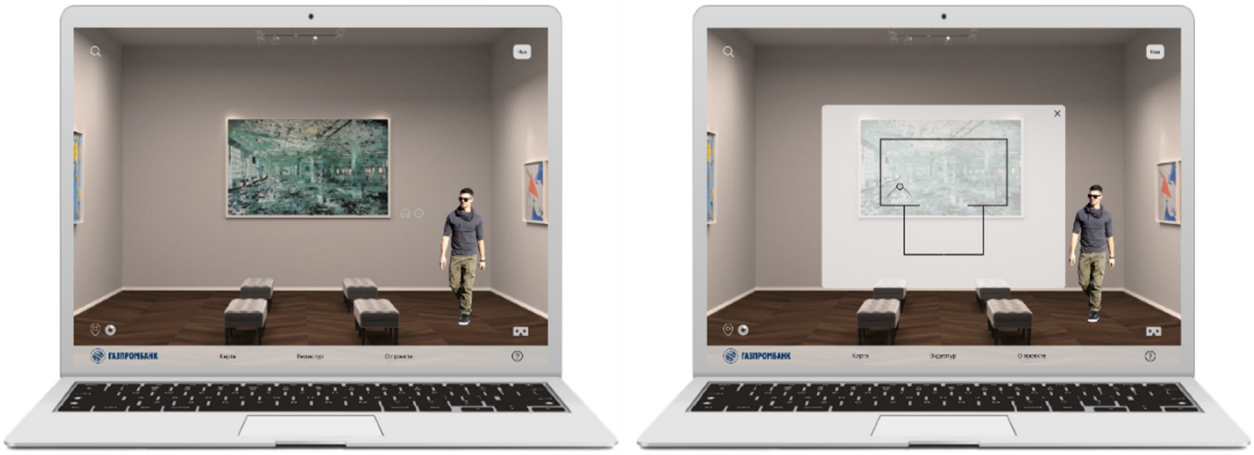

Fig. 6. Visualizing website design

In today's world, principles of universality are referred to in industrial design and architecture. Universality of design allows designers to navigate rapidly changing trends. This trend, which originally involves the development of projects taking ergonomics requirements into account, is based on inclusivity principles and intended for a wide range of users. Universal design shapes the object-spatial environment accessible to people with different abilities and physical traits [10–14]. Products designed according to versality principles should be adapted to a wide range of individual preferences and capabilities, as well as being easy to use and intuitive. Object design transmits information to the user as well as minimizing risks and the adverse consequences of accidental or unintended actions. Universal design ensures that objects may be used efficiently, comfortably and with minimal fatigue. The focus on ergonomics specifies sizes for objects and environments to ensure their usability regardless of the user's body size, condition, or mobility. Due to the original universality of such objects, their shape does not require unification.

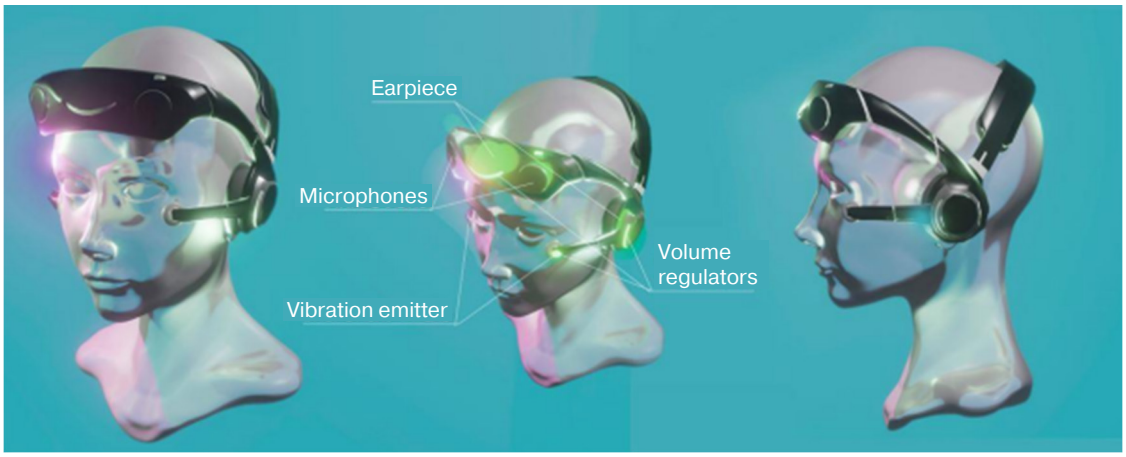

Fig. 7. The concept of a bionic helmet phone for people with disabilities

Digital product usability also requires universality principles to be considered since people with disabilities actively use digital technologies. Therefore, for example, whether developing a desktop or mobile version of a website, a version for blind or visually impaired individuals should be developed.

The possibilities of universal design are the research area being developed by the Department of Computer Design at the Institute for Advanced Technologies and Industrial Programming, MIREA – Russian Technological University [13–15].

Since the design of objects and environments based on universal principles is an essential aspect of training students at the department, students of the Department of Computer Design are actively involved in researching universal design possibilities.

The design of a helmet phone comprising a hearing device with air and bone conduction capabilities may be mentioned as an example of the developments of the department considering the universal design principles in both industrial and digital spheres (Fig. 7). This device facilitates the enhanced perception of sounds for people with hearing loss. The distinctive feature of the device consists in its design based entirely on professiographic methods for the ergonomic study of the human body. Studies have shown that vibration emitters intended for perceiving sounds through bones are located in the cheekbone area having maximum bone conduction. In order to keep the device on the user's head, a system of fastening arcs has been developed [15].

A scientific and practical conference "Universal Design – Equal Opportunities – Comfortable Environment," which examines various trends in modern design in terms of inclusiveness and universality, has been hosted at the University since 2016.

CONCLUSIONS

The evolution of usability is cyclical in nature. Each stage of scientific and technological progress produces a lot of new objects and forms, most of them losing relevance over time to be perceived as archaic and obsolete. Those passing the test of time are reduced to a single form and typically used for decades. Principles of versatility considering primarily ergonomics, safety, and usability help to avoid errors in product design. The evolution of digital design and web technologies define the developed product usability (ease of use). This promotes the transition from complex forms to simpler ones in design and shaping of digital products for a wide range of users and people with disabilities.

Authors' contributions

I.Yu. Mamedova—concept development, literary analysis, and writing the text of the article.

A.E. Dryukova—conducting a historical and comparative analysis of the usability development in design.

N.E. Milchakova—formulation of the concept of usability in the field of UI/UX design taking into account the historical context and principles of universality, drawing conclusions.

REFERENCES

1. Sokolova M.L., Kukhta M.S., Lobatskaya R.M., Chernykh M.M., Mil'chakova N.E. *Dizain* (*Design*). Textbook. Moscow: MGUPI; 2013. 142 p. (in Russ.). ISBN 978-5-8068-0523-3
2. Kukhta M.S., Kumanin V.I., Sokolova M.L., Gol'dshmidt M.G. *Promyshlennyi dizain* (*Industrial Design*). Textbook. Tomsk: TPU; 2013. 312 p. (in Russ.). ISBN 978-5-4387-0205-4
3. Runge V.F. *Istoriya dizaina, nauki i tekhniki* (*History of design, science and technology*). Moscow: Arkhitektura-S; 2006. 368 p. (in Russ.). ISBN 5-9647-0090-X
4. Kumanin V.I., Kukhta M.S. (Eds.). *Dizain. Materialy. Tekhnologii: entsiklopedicheskii slovar'* (*Design. Materials. Technologies: Encyclopedic Dictionary*). Tomsk: TPU; 2011. 320 p. (in Russ.). ISBN 978-5-98298-774-7
5. Kumanin V.I. Anti-design. *Trudy Akademii tekhnicheskoi estetiki i dizaina = Proceedings of the Academy of Technical Aesthetics and Design*. 2015;2:5–6 (in Russ.).
6. Kumanin V.I. The evolution of design in Russia during the last century. *Trudy Akademii tekhnicheskoi estetiki i dizaina = Proceedings of the Academy of Technical Aesthetics and Design*. 2013;1:29–30 (in Russ.).
7. Lukovskii M.A. Modern technologies for the development and development of websites based on the principles of emotional design. *Nauka i sovremennost' = Science and Modernity*. 2014;27:66–69 (in Russ.).
8. Milchakova N.E. Design of visual communications. *Trudy Akademii tekhnicheskoi estetiki i dizaina = Proceedings of the Academy of Technical Aesthetics and Design*. 2013;1:22–24 (in Russ.).
9. Morozov M.D., Romanov V.V. Role of aesthetics in web design. *Vestnik Astrakhanskogo gosudarstvennogo tekhnicheskogo universiteta = Vestnik of the Astrakhan State Technical University*. 2019;2(68):77–80 (in Russ.).
10. Albagachiev A.Yu., Mammadova I.Yu., Sokolova M.L., Milchakova N.E. Industrial design and universality principles application in the process of technical products engineering. *Vestnik mashinostroeniya = Russian Engineering Research*. 2017;11:84–86 (in Russ.).
11. Sokolova M.L., Milchakova N.E., Zhigunova A.I. The concept of responsibility as the modern outlook of designer. *Russian Technological Journal*. 2020;8(2): 109–121 (in Russ.). https://doi.org/10.32362/2500-316X-2020-8-2-109-121
12. Gertsik Yu.G., Gertsik Yu.G. Using the concept of universal design to improve the effectiveness of medical devices screening, correction of hearing loss and speech disorders. In: *The second Russian scientific and practical conference with international participation "Universal design – equal opportunities – a comfortable environment*." Collection of conference reports. Moscow: MIREA; 2018. P. 62–67 (in Russ.).
13. Sokolova M.L., Denisyuk T.V. Areas of application of universal and disciplinary design. In: *The second Russian scientific and practical conference with international participation "Universal design – equal opportunities – a comfortable environment*." Collection of conference reports. Moscow: MIREA; 2018. P. 212–215 (in Russ.).

СПИСОК ЛИТЕРАТУРЫ

1. Соколова М.Л., Кухта М.С., Лобацкая Р.М., Черных М.М., Мильчакова Н.Е. *Дизайн*: учебник для вузов. М.: МГУПИ; 2013. 142 с. ISBN 978-5-8068-0523-3
2. Кухта М.С., Куманин В.И., Соколова М.Л., Гольдшмидт М.Г. *Промышленный дизайн*: учебник. Томск: Изд-во ТПУ; 2013. 312 с. ISBN 978-5-4387-0205-4
3. Рунге В.Ф. *История дизайна, науки и техники*. М.: Архитектура-С; 2006. 368 с. ISBN 5-9647-0090-X
4. Куманин В.И., Кухта М.С. (под ред.) *Дизайн. Материалы. Технологии:* энциклопедический словарь. Томск: Изд-во ТПУ; 2011. 320 с. ISBN 978-5-98298-774-7
5. Куманин В.И. Антидизайн. *Труды Академии технической эстетики и дизайна*. 2015;2:5–6.
6. Куманин В.И. Эволюция дизайна в России в последнее столетие. *Труды Академии технической эстетики и дизайна*. 2013;1:29–30.
7. Луковский М.А. Современные технологии развития и разработки веб-сайтов на основе принципов эмоционального дизайна. *Наука и современность*. 2014;27:66–69.
8. Мильчакова Н.Е. Дизайн визуальных коммуникаций. *Труды Академии технической эстетики и дизайна*. 2013;1:22–24.
9. Морозов М.Д., Романов В.В. Роль эстетики в веб-дизайне. *Вестник Астраханского государственного технического университета*. 2019;2(68):77–80.
10. Албагачиев А.Ю., Мамедова И.Ю., Соколова М.Л., Мильчакова Н.Е. Промышленный дизайн и применение принципов универсальности при проектировании технических изделий. *Вестник машиностроения*. 2017;11:84–86.
11. Соколова М.Л., Мильчакова Н.Е., Жигунова А.И. Концепция ответственности как современное мировоззрение дизайнера. *Российский технологический журнал*. 2020;8(2):109–121. https://doi.org/10.32362/2500-316X-2020-8-2-109-121
12. Герцик Ю.Г., Герцик Ю.Г. Использование концепции универсального дизайна для повышения эффективности медицинских изделий скриннинга, коррекции тугоухости и речевых нарушений. *Вторая российская научно-практическая конференция с международным участием «Универсальный дизайн – равные возможности – комфортная среда, 2018»*. Сборник докладов конференции. М.: РТУ МИРЭА; 2018. С. 62–67.
13. Соколова М.Л., Денисюк Т.В. Области применения универсального и дисциплинарного дизайна. *Вторая российская научно-практическая конференция с международным участием «Универсальный дизайн – равные возможности – комфортная среда, 2018»*. Сборник докладов конференции. М.: РТУ МИРЭА; 2018. С. 212–215.
14. Соколова М.Л. Современные проблемы направления «Технология художественной обработки материалов». *Российский технологический журнал*. 2017;5(1):50–56. https://doi.org/10.32362/2500-316X-2017-5-1-50-56
15. Дадин М.В., Соловьев Я.В., Иванов А.М., Калинин А.В. Разработка дизайна слухового аппарата с возможностями воздушной и костной проводимости. *Сборник докладов Третьей Национальной научно-практической конференции с международным участием «Универсальный дизайн – равные возможности – комфортная среда, 2019»*. Сборник докладов конференции. М.: РТУ МИРЭА; 2019. Р. 171–173.

14. Sokolova M.L. Modern problems of the course of "Technology for the decorative processing of materials." *Russian Technological Journal*. 2017;5(1):50–56 (in Russ.). https://doi.org/10.32362/2500-316X-2017-5-1-50-56
15. Dadin M.V., Soloviev Ya.V., Ivanov A.M., Kalinin A.V. Design development of a hearing aid with air and bone conduction capabilities. In: *Reports of the Third National Scientific and Practical Conference with international participation "Universal design – equal opportunities – a comfortable environment, 2019*." Moscow: MIREA; 2019. P. 171–173 (in Russ.).

About the authors

Irina Yu. Mamedova, Cand. Sci. (Eng.), Head of Department of Computer Design, Institute for Advanced Technologies and Industrial Programming, MIREA – Russian Technological University (78, Vernadskogo pr., Moscow, 119454 Russia). E-mail: i_mamedova@mirea.ru. Scopus Author ID 57215912459.

Anna E. Dryukova, Cand. Sci. (Eng.), Associate Professor, Department of Computer Design, Institute for Advanced Technologies and Industrial Programming, MIREA – Russian Technological University (78, Vernadskogo pr., Moscow, 119454 Russia). E-mail: dryukova@mirea.ru.

Natalia E. Milchakova, Cand. Sci. (Eng.), Associate Professor, Department of Computer Design, Institute for Advanced Technologies and Industrial Programming, MIREA – Russian Technological University (78, Vernadskogo pr., Moscow, 119454 Russia). E-mail: milchakova@mirea.ru. ResearcherID AAE-2051-2019, https://orcid.org/0000-0003-3662-087X

Об авторах

Мамедова Ирина Юрьевна, к.т.н., доцент, заведующий кафедрой компьютерного дизайна Института перспективных технологий и индустриального программирования ФГБОУ ВО «МИРЭА – Российский технологический университет» (119454, Россия, Москва, пр-т Вернадского, д. 78). E-mail: i_mamedova@mirea.ru. Scopus Author ID 57215912459.

Дрюкова Анна Эдуардовна, к.т.н., доцент, доцент кафедры компьютерного дизайна Института перспективных технологий и индустриального программирования ФГБОУ ВО «МИРЭА – Российский технологический университет» (119454, Россия, Москва, пр-т Вернадского, д. 78). E-mail: dryukova@mirea.ru.

Мильчакова Наталья Егоровна, к.т.н., доцент, доцент кафедры компьютерного дизайна Института перспективных технологий и индустриального программирования ФГБОУ ВО «МИРЭА – Российский технологический университет» (119454, Россия, Москва, пр-т Вернадского, д. 78). E-mail: milchakova@mirea.ru. ResearcherID AAE-2051-2019, https://orcid.org/0000-0003-3662-087X

Translated by K. Nazarov
Edited for English language and spelling by Thomas Beavitt

MIREA – Russian Technological University.
78, Vernadskogo pr., Moscow, 119454 Russian Federation.
Publication date May 31, 2022.
Not for sale.

МИРЭА – Российский технологический университет.
119454, РФ, г. Москва, пр-т Вернадского, д. 78.
Дата опубликования 31.05.2022 г.
Не для продажи.

https://www.rtj-mirea.ru


МИРЭА
Российский
технологический
университет